

A MECHANISTIC MODELING OF CO₂ CORROSION OF MILD STEEL IN THE
PRESENCE OF H₂S

A dissertation presented to

the faculty of the

Fritz J. and Dolores H. Russ
College of Engineering and Technology
of
Ohio University

In partial fulfillment

of the requirements for the degree

Doctor of Philosophy

Kun-Lin John Lee

November 2004

This thesis entitled
A MECHANISTIC MODELING OF CO₂ CORROSION OF MILD STEEL IN THE
PRESENCE OF H₂S

by
Kun-Lin J. Lee

has been approved for
the Department of Chemical Engineering
and the Russ College of Engineering and Technology by

Srdjan Nesic
Professor of Chemical Engineering

Dennis Irwin
Dean, Russ College of Engineering and Technology

LEE, KUN-LIN J. Ph.D. NOVEMBER 2004. Chemical Engineering

A MECHANISTIC MODELING OF CO₂ CORROSION OF MILD STEEL IN THE PRESENCE OF H₂S (220 pages.)

Director of Thesis: Srdjan Nesic

A mechanistic model CO₂/H₂S corrosion of mild steel in the presence of trace amount of H₂S has been developed. The model predicts accurate solution chemistry at the metal surface and it is capable of predicting the rate of iron sulfide and iron carbonate film growth, the change in morphology and composition of the film with respect to space and time, as well as the resulting corrosion rate time evolution.

The model has been successfully calibrated against data from a large number of carefully controlled corrosion experiments under different environmental parameters in the presence of trace amount of H₂S, in both film free and film forming conditions. Parametric testing of the model has been done in order to gain insight into the effect of various environmental parameters on mixed films formation and the resulting corrosion rate. The trends shown in the predictions agreed well with the general understanding of the CO₂/H₂S corrosion process in the presence of iron carbonate and iron sulfide films.

Approved: Srdjan Nesic

Professor of Chemical Engineering

DEDICATION

To

Kuo-Ching Lee and Hsiu-Li Wang (my parents)

and

Emily Lee (my sister)

ACKNOWLEDGEMENTS

I would like to thank Dr. Srdjan Nestic, who formed part of my vision and taught me things that really matter in life. I am very fortunate that I have met Srdjan in my life. During the last eight years I have known Srdjan as a sympathetic man with integrity and immense patience. His enthusiasm on research and his mission for providing only high-quality work has made a deep impression on me. Srdjan's breadth of knowledge never ceases to amaze me. Besides being the "bestest" academic advisor, Srdjan is a father and a close friend to me, who has given me invaluable lessons about life throughout the years. Srdjan, I owe you a lot of gratitude for having suffered from my lack of responsibility in the first two years of my study, yet you never gave up on me. Moving to America with you was definitely one of the best decisions in my life

I would also like to acknowledge my indebtedness to the staff at the Institute for Corrosion and Multiphase Technology, including Mr. Al Schubert, Mr. Bruce Brown and Mr. John Goettge for their assistance in technical matters; Dr. Gulino, Dr. Gu and Dr. Cai for their invaluable advices; and Wei Sun for her assistance in research and coursework.

I am very grateful to Gloria Chou, for her love, patience and support during my study. We have grown dependent on each other during this enjoyable journey. Her companionship made my life in Athens the most unforgettable experience.

TABLE OF CONTENTS

CHAPTER 1: INTRODUCTION	12
CHAPTER 2: LITERATURE REVIEW	15
2.1 CO ₂ corrosion.....	15
2.2 The effect of pH	16
2.3 The effect of temperature.....	17
2.4 The effect of CO ₂ partial pressure	17
2.5 The effect of flow.....	18
2.6 Effect of Supersaturation	19
2.7 Corrosion product film formation.....	19
2.8 The effect of H ₂ S	22
2.8.1 H ₂ S dominated system (sour regime)	23
2.8.2 CO ₂ dominated system (sweet regime).....	24
2.9 Nature of iron sulfide films.....	25
2.9.1 Mackinawite.....	25
2.9.2 Cubic FeS.....	26
2.9.3 Troilite.....	27
2.9.4 Pyrrhotite.....	27
2.9.5 Pyrite	28
2.9.6 Greigite	29
2.10 Mechanism of iron sulfide film formation in CO ₂ /H ₂ S corrosion	30
2.10.1 Effect of brine on iron sulfide film in Pure H ₂ S solutions.....	30
2.10.2 Transformation of iron sulfide in pure H ₂ S solutions at pH4	31
2.10.3 Iron sulfide stability diagram using Pourbaix diagrams	32
2.10.4 Mechanism of pyrite in pure H ₂ S solutions	32
2.10.5 Mechanism of Mackinawite in CO ₂ /H ₂ S solutions.....	33
2.11 CO ₂ Corrosion Models.....	34
2.11.1 de Waard Model.....	35
2.11.2 Gray et al.....	36
2.11.3 Nesic et al.....	37
CHAPTER 3: RESEARCH OBJECTIVES.....	42
3.1 Research objectives.....	42
3.2 Research milestones.....	42
CHAPTER 4: MECHANISTIC MODELING OF CO ₂ CORROSION IN FILM-FREE CONDITIONS	46
4.1 Introduction.....	46
4.2 Physico-Chemical Model.....	46
4.2.1 Chemical Reactions	46
4.2.2 Electrochemical reactions at the steel surface	49
4.2.3 Transport processes.....	51
4.3 Mathematical model.....	53
4.3.1 Chemical reactions.....	54
4.3.2 Electrochemical reactions at the steel surface	57
4.3.3 Transport processes.....	60
4.3.4 Initial and boundary conditions	64

4.4 Numerical Techniques	65
4.5 Verification and parametric study	68
4.5.1 The effect of pH	68
4.5.2 The effect CO ₂ partial pressure	69
4.5.3 The effect of temperature	71
4.5.4 The Effect of Flow	71
4.6 Summary	72
CHAPTER 5: MECHANISTIC MODELING CO ₂ CORROSION ACCOMPANIED BY IRON CARBONATE FILM FORMATION	74
5.1 Introduction	74
5.2 Physico-Chemical Model	74
5.3 Numerical Techniques	81
5.4 Verification and Parametric Study	82
5.4.1 Experimental setting and procedure	83
5.4.2 Comparison case #1	85
5.4.3 Comparison case #2	91
5.4.4 The effect of pH	96
5.4.5 The effect of temperature	99
5.4.6 The effect of CO ₂ partial pressure	102
5.4.7 The effect of Fe ²⁺ concentration	104
5.5 Summary	107
CHAPTER 6: MODELING OF CO ₂ /H ₂ S CORROSION IN FILM FREE CONDITIONS	109
6.1 Introduction	109
6.2 Physico-Chemical Model	110
6.2.1 Experiments	112
6.2.2 Experimental equipments	113
6.2.3 Material	114
6.2.4 Experimental Procedure	115
6.2.5 Results and discussion of mechanisms	116
6.2.6 Surface Analysis	123
6.3 Mathematical Model	126
6.4 Verification	127
6.5 Summary	128
CHAPETER 7: MECHANISTIC MODEL OF CO ₂ /H ₂ S CORROSION ACCOMPANIED BY SIMULTANEOUS IRON CARBONATE AND IRON SULFIDE FILM GROWTH	129
7.1 Introduction	129
7.2 Physico-Chemical Model	129
7.3 Verification and Parametric Study	134
7.3.1 Corrosion rate comparison	135
7.3.2 Film comparison	136
7.4 parametric testing	141
7.4.1 The effect of H ₂ S concentration	142
7.4.2 The effect of pH	147
7.4.3 The effect of CO ₂ partial pressure	153

CHAPTER 8: CONCLUSIONS	158
CHAPTER 9: RECOMMENDATION AND FUTURE WORK	160
REFERENCES	161
APPENDIX A: CORROSION MONITORING TECHNIQUES.....	172
<i>Potentiodynamic sweep</i>	175
<i>Linear Polarization Resistance (LPR)</i>	179
<i>Electrochemical Impedance Spectroscopy (EIS)</i>	181
APPENDIX B: VAPOR-LIQUID EQUILIBRIUM MODEL.....	182
<i>Open system conditions</i>	182
<i>Closed system conditions</i>	185
<i>Numerical techniques</i>	186
<i>Results and discussion</i>	187
APPENDIX C: MECHANISTIC EIS ANALYTICAL MODEL.....	194
Modeling.....	194
<i>Physical model of Cathodic reaction</i>	194
<i>Mathematical model</i>	196
Charge-transfer overvoltage.....	197
Diffusion overvoltage	200
Reaction overvoltage	203
Double layer capacitance	204
Derivation of reaction impedance in a finite boundary layer	206

LIST OF TABLES

Table 1. Chemical reactions accounted for in the model and their equilibrium constants. ¹⁵	47
Table 2. Equilibrium (K), forward (k_f) and backward (k_b) reaction rate coefficients (note: $K = k_f/k_b$). ¹⁵	56
Table 3. Electrochemical parameters for the reactions included in the model which fit the general rate equation (18)	59
Table 4. Species accounted for in the present version of the model and the corresponding reference molecular diffusion coefficient. ¹⁵	63
Table 5. Liquid properties as a function of temperature (source: CRC Handbook of Chemistry and Physics ⁹⁹).	63
Table 6. Experimental conditions for CO ₂ film forming experiments.....	84
Table 7. Predicted supersaturation, scaling tendency, film thickness and corrosion rate at various pH for T=80°C, $P_{CO_2} = 0.54$ bar, $c_{Fe^{2+}} = 250$ ppm, $v=1$ m/s.....	96
Table 8. Predicted supersaturation, scaling tendency, film thickness and corrosion rate at various temperatures for pH 6.6, $P_{CO_2} = 0.54$ bar, $c_{Fe^{2+}} = 250$ ppm, $v=1$ m/s.	100
Table 9. Predicted supersaturation, scaling tendency, film thickness and corrosion rate at various CO ₂ partial pressures for T=80°C, pH 6.6, $c_{Fe^{2+}} = 250$ ppm, $v=1$ m/s.	103
Table 10. Predicted supersaturation, scaling tendency, film thickness and corrosion rate at various Fe ²⁺ concentrations for T=80°C, pH 6.6, $P_{CO_2} = 0.54$ bar, $v=1$ m/s.	106
Table 11. Chemical composition of the API 5L X65 carbon steel used for the working electrode (mass%).....	114
Table 12. Experimental conditions for CO ₂ /H ₂ S film-free corrosion study	116
Table 13. Experimental Test Matrix for CO ₂ /H ₂ S flow loop in film-forming conditions.....	135

LIST OF FIGURES

Figure 1. Corrosion regimes in CO ₂ /H ₂ S corrosion defined by Pots, et al. ⁵⁸	23
Figure 2. The structure of mackinawite, image taken from L. A. Taylor and L. W. Finger, “Structure Refinement and Composition of Mackinawite” ⁶²	25
Figure 3. The structure of cubic FeS. Image taken from J. S. Smith and J. D. A. Miller, “Nature of Sulfides and Their Corrosive Effect on Ferrous Metals: A Review” ⁶¹ ..	26
Figure 4. The structure of troilite. Image taken from J. S. Smith and J. D. A. Miller, “Nature of Sulfides and Their Corrosive Effect on Ferrous Metals: A Review” ⁶¹ ..	27
Figure 5. The structure of pyrrhotite. Image taken from J. S. Smith and J. D. A. Miller, “Nature of Sulfides and Their Corrosive Effect on Ferrous Metals: A Review” ⁶¹ ..	28
Figure 6. The structure of pyrite. Image taken from J. S. Smith and J. D. A. Miller, “Nature of Sulfides and Their Corrosive Effect on Ferrous Metals: A Review” ⁶¹ ..	29
Figure 7. The structure of greigite. Image taken from J. S. Smith and J. D. A. Miller, “Nature of Sulfides and Their Corrosive Effect on Ferrous Metals: A Review” ⁶¹ ..	29
Figure 8. Reaction scheme of the mechanisms of iron sulfide formation ²⁷	31
Figure 9. Thermodynamic boundary conditions that separate various corrosion products in CO ₂ /H ₂ S solutions ⁷⁶	33
Figure 10 Sketch of the computational domain and the control volume used for discretization of the computational domain. ¹⁵	60
Figure 11. Sketch of the computational grid and the control volumes used for discretization of the computational domain. The concentrations, the potential and the chemical reaction terms are all computed in the centre of the control volume while the fluxes are computed on the interfaces.	66
Figure 12. Predicted and experimentally measured corrosion rates showing the effect of pH in the absence of iron carbonate films. Test conditions: 20°C, $P_{CO_2} = 1$ bar, 1 m/s, $c_{Fe^{2+}} < 2$ ppm. Model of Nescic et al. ¹⁰⁵ was used. Experimental data taken from Nescic et al. ¹⁰⁶	69
Figure 13. Predicted and experimentally measured corrosion rates showing the effect of CO ₂ partial pressure P_{CO_2} . Test conditions: 60°C, pH5, 1 m/s. Data taken from Wang et al. ¹⁰⁷ Corrosion rates were measured both by linear polarization resistance (LPR) and weight loss (WL). Error bars denote maximum and minimum values and the figure above the bars is the number of repeated experiments. OU V 3.0 is the model of Nescic et al. ¹⁰⁵ , Electrochemical is the model of George et al. ¹⁰⁸	70
Figure 14. Predicted and experimentally measured corrosion rates showing the effect of temperature. Test conditions: pH4, $P_{CO_2} = 1$ bar, $c_{Fe^{2+}} < 5$ ppm, 100 ppm acetic species ($HAc + Ac^-$) $v=0.5$ m/s. Data taken from Wang et al. ¹⁰⁷ Corrosion rates were measured both by linear polarization resistance (LPR) and weight loss (WL). OU V 3.0 is the model of Nescic et al. ¹⁰⁵ , Electrochemical is the model of George et al. ¹⁰⁸	71
Figure 15. Predicted and experimentally measured corrosion rates showing the effect of velocity in the absence of iron carbonate films. Test conditions: 20°C, $P_{CO_2} = 1$ bar, $c_{Fe^{2+}} < 2$ ppm. Model of Nescic et al. ¹⁰⁵ was used. Experimental data taken from Nescic et al. ¹⁰⁶	72

Figure 16. Schematic of a glass cell: 1. Reference electrode; 2. Temperature probe; 3. Luggin capillary; 4. Working electrode; 5. Hot plate; 6. Condenser; 7. Bubbler for gas; 8. pH electrode; 9. Counter electrode.....	83
Figure 17. Comparison between experimental data (points) and model predictions (line) for $T=80^{\circ}\text{C}$, $\text{pH } 6.6$, $P_{\text{CO}_2} = 0.54 \text{ bar}$, $c_{\text{Fe}^{2+}} = 250 \text{ ppm}$, $v=1 \text{ m/s}$	86
Figure 18. Surface area-to-volume ratio A/V as a function of porosity ε for a control volume of $\Delta x \propto 10^{-7} \text{ m}$	87
Figure 19. The predicted porosity change of different iron carbonate film layers with respect to time. Each layer is $0.16 \mu\text{m}$ thick. Conditions: $T=80^{\circ}\text{C}$, $\text{pH } 6.6$, $P_{\text{CO}_2} = 0.54 \text{ bar}$, $c_{\text{Fe}^{2+}} = 250 \text{ ppm}$, $v=1 \text{ m/s}$	88
Figure 20. Predicted iron carbonate film growth with respect to time for $T=80^{\circ}\text{C}$, $\text{pH } 6.6$, $P_{\text{CO}_2} = 0.54 \text{ bar}$, $c_{\text{Fe}^{2+}} = 250 \text{ ppm}$, $v=1 \text{ m/s}$. Black depicts a 100% dense ($\varepsilon=0$) iron carbonate film and white means no film ($\varepsilon=1$).....	89
Figure 21. SEM image of a cross section of a steel specimen including an iron carbonate film. Exposed for 10 hours at $T=80^{\circ}\text{C}$, $\text{pH } 6.6$, $P_{\text{CO}_2} = 0.54 \text{ bar}$, $c_{\text{Fe}^{2+}} = 250 \text{ ppm}$, $v=1 \text{ m/s}$	90
Figure 22. Comparison between experimental data (points) and model predictions (line) for $T=80^{\circ}\text{C}$, $\text{pH } 6.6$, $P_{\text{CO}_2} = 0.54 \text{ bar}$, $c_{\text{Fe}^{2+}} = 5 \text{ ppm}$, $v=1 \text{ m/s}$	92
Figure 23. The predicted porosity change of different iron carbonate film layers with respect to time. Each layer is $0.16 \mu\text{m}$ thick. Conditions: $T=80^{\circ}\text{C}$, $\text{pH } 6.6$, $P_{\text{CO}_2} = 0.54 \text{ bar}$, $c_{\text{Fe}^{2+}} = 5 \text{ ppm}$, $v=1 \text{ m/s}$	93
Figure 24. Predicted iron carbonate film growth with respect to time for $T=80^{\circ}\text{C}$, $\text{pH } 6.6$, $P_{\text{CO}_2} = 0.54 \text{ bar}$, $c_{\text{Fe}^{2+}} = 5 \text{ ppm}$, $v=1 \text{ m/s}$. Black depicts a 100% dense ($\varepsilon=0$) iron carbonate film and white means no film ($\varepsilon=1$).....	94
Figure 25. SEM image of a cross section of a steel specimen including an iron carbonate film. Exposed for 48 hours at $T=80^{\circ}\text{C}$, $\text{pH } 6.6$, $P_{\text{CO}_2} = 0.54 \text{ bar}$, $c_{\text{Fe}^{2+}} = 5 \text{ ppm}$, $v=1 \text{ m/s}$	95
Figure 26. The predicted effect of pH on the corrosion rate for $T=80^{\circ}\text{C}$, $P_{\text{CO}_2} = 0.54 \text{ bar}$, $c_{\text{Fe}^{2+}} = 250 \text{ ppm}$, $v=1 \text{ m/s}$. Corresponding film thickness and porosity are shown in Figure 27. Predicted supersaturation and scaling tendency are listed in Table 7.	97
Figure 27. The predicted film thickness and porosity as a function of pH after 30 hours of exposure at $T=80^{\circ}\text{C}$, $P_{\text{CO}_2} = 0.54 \text{ bar}$, $c_{\text{Fe}^{2+}} = 250 \text{ ppm}$, $v=1 \text{ m/s}$. Black depicts a 100% dense ($\varepsilon=0$) iron carbonate film and white means no film ($\varepsilon=1$). The corresponding corrosion rate curves are shown in Figure 26. Predicted supersaturation and scaling tendency are listed in Table 7.....	98
Figure 28. The predicted effect of temperature on the corrosion rate for $\text{pH } 6.6$, $P_{\text{CO}_2} = 0.54 \text{ bar}$, $c_{\text{Fe}^{2+}} = 250 \text{ ppm}$, $v=1 \text{ m/s}$. Corresponding film thickness and porosity are shown in Figure 29. Predicted supersaturation and scaling tendency are listed in Table 8.	99

- Figure 29. The predicted film thickness and porosity as a function of temperature after 30 hours of exposure at pH 6.6, $P_{CO_2}=0.54$ bar, $c_{Fe^{2+}}=250$ ppm, $v=1$ m/s. Black depicts a 100% dense ($\varepsilon=0$) iron carbonate film and white means no film ($\varepsilon=1$). The corresponding corrosion rate curves are shown in Figure 28. Predicted supersaturation and scaling tendency are listed in Table 8. 101
- Figure 30. The predicted effect of CO_2 partial pressure on the corrosion rate for $T=80^\circ C$, pH 6.6, $c_{Fe^{2+}} = 250$ ppm, $v=1$ m/s. Corresponding film thickness and porosity are shown in Figure 31. Predicted supersaturation and scaling tendency are listed in Table 9. 102
- Figure 31. The predicted film thickness and porosity as a function of CO_2 partial pressure after 5 hours of exposure at $T=80^\circ C$, pH 6.6, $c_{Fe^{2+}} =250$ ppm, $v=1$ m/s. Black depicts a 100% dense ($\varepsilon=0$) iron carbonate film and white means no film ($\varepsilon=1$). The corresponding corrosion rate curves are shown in Figure 30. Predicted supersaturation and scaling tendency are listed in Table 9. 104
- Figure 32. The predicted effect of Fe^{2+} concentration on the corrosion rate for $T=80^\circ C$, pH 6.6, $P_{CO_2} = 0.54$ bar, $v=1$ m/s. Corresponding film thickness and porosity are shown in Figure 33. Predicted supersaturation and scaling tendency are listed in Table 10. 105
- Figure 33. The predicted film thickness and porosity as a function of Fe^{2+} ion concentration after 30 hours of exposure at $T=80^\circ C$, pH 6.6, $P_{CO_2} =1$ bar, $v=1$ m/s. Black depicts a 100% dense ($\varepsilon=0$) iron carbonate film and white means no film ($\varepsilon=1$). The corresponding corrosion rate curves are shown in Figure 32. Predicted supersaturation and scaling tendency are listed in Table 10. 107
- Figure 34. Effect of H_2S concentration in single phase flow for $T=60^\circ C$, $p(CO_2)=7.7$ bar, pH4, $v=1.92$ m/s, $V_{sg}=3.0$ m/s. Data taken from Brown and Lee.⁸² 111
- Figure 35 Schematic of the experimental test cell: 1-Ag/AgCl reference electrode, 2-gas rotameter, 3- H_2S scrubber (gas absorbent) , 4-Luggin capillary, 5-graphite counter electrode, 6-rotator, 7-pH electrode, 8-working electrode, 9-gas out, 10-gas in, 11-temperature control unit/stirrer. 114
- Figure 36. Effect of 3 ppm gaseous H_2S on the Nyquist impedance diagram for carbon steel X65 in pH 5 saturated CO_2 solution of water + 3% NaCl, $p = 1$ bar, $t = 20^\circ C$, $\omega = 1000$ rpm at corrosion potential (vs. Ag/AgCl). 117
- Figure 37. Effect of gaseous H_2S concentration on the steady-state Nyquist impedance 119
- Figure 38. Effect of H_2S gaseous concentration on the final stabilized corrosion rate (measured by LPR and EIS) of carbon steel X65 in pH 5 saturated CO_2 solution, water + 3% NaCl, $p = 1$ bar, $t = 20^\circ C$, $\omega = 1000$ rpm. Experiments were repeated for each H_2S concentration. 120
- Figure 39. Normalised corrosion rate obtained under various environmental parameters in film free conditions: pH<5 $p = 1$ to 7 bar, $t = 20-80^\circ C$, $v=$ stagnant to 3 m/s. 121
- Figure 40. Effect of immersion time on Nyquist impedance diagram of carbon steel X65 in pH 5 saturated CO_2 solution with 340 ppm gaseous H_2S , water + 3% NaCl, $p = 1$ bar, $t = 20^\circ C$, $\omega = 1000$ rpm at corrosion potential. 122

- Figure 41. Survey scan on the carbon steel X65 surface after 72 hours of immersion in pH 5 saturated CO₂ solution with 340 ppm gaseous H₂S, water + 3% NaCl, p = 1 bar, t = 20°C, ω = 1000 rpm..... 124
- Figure 42. Narrow scans of Fe(2p_{3/2}) spectrum on the carbon steel X65 surface after 72 hours of immersion in pH 5 saturated CO₂ solution with 340 ppm gaseous H₂S, water + 3% NaCl, p = 1 bar, t = 20°C, ω = 1000 rpm , including fitted curves. 125
- Figure 43. Narrow scans of S(2p) spectrum on the carbon steel X65 surface after 72 hours of immersion in pH 5 saturated CO₂ solution with 340 ppm gaseous H₂S, water + 3% NaCl, p = 1 bar, t = 20°C, ω = 1000 rpm, including fitted curves..... 126
- Figure 44. Comparison between model prediction and experimental data on the effect of trace amount of H₂S on CO₂ corrosion rate in the absence of iron sulfide films. ppm refers to the concentration in the gas phase. 127
- Figure 45. First attempt at the comparison between the model prediction and the measured corrosion rate from the flow loop experiment in the presence of trace amount of H₂S at film forming conditions: pH 6 saturated CO₂ solution with 120 ppm gaseous H₂S, water + 1% NaCl, P_{CO₂} = 7.7 bar, t = 60°C, Fe²⁺=17ppm..... 136
- Figure 46. Cross section MP 25 day exposure of X65(2) coupon, (next to metal surface) layer #1: 60 um, layer #2: 60 um, and layer #3: 30 um. Layer #1 EDS is [32.4% Fe, 0.0% S, 13.4% C, 26.5% O], the interface between layer #1 and layer #2 EDS is [35.4% Fe, 12.9% S, 14.0% C, 9.5% O], and the EDS of layer #2 is [31.2% Fe, 15.0% S, 20.8% C, 11.2% O]. 137
- Figure 47. First attempt at predicting film thickness and composition of film without modification of kinetics of iron sulfide precipitation. After 25 days of exposure at c_{H₂S}=120 ppm, T=60°C, P_{CO₂} = 7.7bar, pH 6.0, c_{Fe²⁺}=17 ppm, v=1 m/s..... 138
- Figure 48. Second attempt at predicting film thickness and composition of film after modification of kinetics of iron sulfide precipitation. 25 days of exposure at c_{H₂S}=120 ppm, T=60°C, P_{CO₂} = 7.7bar, pH 6.0, c_{Fe²⁺}=17 ppm, v=1 m/s..... 140
- Figure 49. Second attempt at predicting film thickness and porosity of film after modification of kinetics of iron sulfide precipitation. 25 days of exposure at c_{H₂S}=120 ppm, T=60°C, P_{CO₂} = 7.7bar, pH 6.0, c_{Fe²⁺}=17 ppm, v=1 m/s. Porosity ε=1 means no film..... 140
- Figure 50. After modification of iron sulfide precipitation kinetics, second attempt at the comparing the model prediction and the measured corrosion rate from the flow loop experiment in the presence of trace amount of H₂S at film forming conditions: pH 6 saturated CO₂ solution with 120 ppm gaseous H₂S, water + 1% NaCl, P_{CO₂} = 7.7 bar, t = 60°C, Fe²⁺=17ppm. 141
- Figure 51. The predicted effect of H₂S concentration on the corrosion rate for T=60°C, pH 6.0, P_{CO₂} = 7.7 bar, c_{Fe²⁺}=17 ppm, v=1 m/s. Corresponding film thickness and porosity are shown in Figure 52..... 143
- Figure 52. The predicted effect of H₂S concentration on the film thickness and porosity after 100 hours of exposure at T=60°C, P_{CO₂} = 7.7bar, pH 6, c_{Fe²⁺}=17 ppm, v=1 m/s. Porosity ε=1 means no film. 144

Figure 53. The predicted film thickness and composition of film after 100 hours of exposure at $c_{H_2S}=50$ ppm, $T=60^\circ\text{C}$, $P_{CO_2} = 7.7\text{bar}$, $\text{pH } 6.0$, $c_{Fe^{2+}} = 17$ ppm, $v=1$ m/s.	144
Figure 54. The predicted film thickness and porosity of film after 100 hours of exposure at $c_{H_2S}=50$ ppm, $T=60^\circ\text{C}$, $P_{CO_2} = 7.7\text{bar}$, $\text{pH } 6.0$, $c_{Fe^{2+}} = 17$ ppm, $v=1$ m/s. Porosity $\varepsilon=1$ means no film.	145
Figure 55. The predicted film thickness and composition of film after 100 hours of exposure at $c_{H_2S}=120$ ppm, $T=60^\circ\text{C}$, $P_{CO_2} = 7.7\text{bar}$, $\text{pH } 6.0$, $c_{Fe^{2+}} = 17$ ppm, $v=1$ m/s. Porosity $\varepsilon=1$ means no film.	145
Figure 56. The predicted film thickness and porosity of film after 100 hours of exposure at $c_{H_2S}=120$ ppm, $T=60^\circ\text{C}$, $P_{CO_2} = 7.7\text{bar}$, $\text{pH } 6.0$, $c_{Fe^{2+}} = 17$ ppm, $v=1$ m/s. Porosity $\varepsilon=1$ means no film.	146
Figure 57. The predicted film thickness and composition of film after 100 hours of exposure at $c_{H_2S}=250$ ppm, $T=60^\circ\text{C}$, $P_{CO_2} = 7.7\text{bar}$, $\text{pH } 6.0$, $c_{Fe^{2+}} = 17$ ppm, $v=1$ m/s. Porosity $\varepsilon=1$ means no film.	146
Figure 58. The predicted film thickness and porosity of film after 100 hours of exposure at $c_{H_2S}=250$ ppm, $T=60^\circ\text{C}$, $P_{CO_2} = 7.7\text{bar}$, $\text{pH } 6.0$, $c_{Fe^{2+}} = 17$ ppm, $v=1$ m/s. Porosity $\varepsilon=1$ means no film.	147
Figure 59. The predicted effect of pH on the corrosion rate for $T=60^\circ\text{C}$, $c_{H_2S}=120$ ppm, $P_{CO_2} = 7.7$ bar, $c_{Fe^{2+}} = 17$ ppm, $v=1$ m/s. Corresponding film thickness and porosity are shown in Figure 60.	148
Figure 60. The predicted effect of pH on the film thickness and porosity after 66 hours of exposure at $T=60^\circ\text{C}$, $c_{H_2S}=120$ ppm, $P_{CO_2} = 7.7$ bar, $c_{Fe^{2+}} = 17$ ppm, $v=1$ m/s. Porosity $\varepsilon=1$ means no film.	149
Figure 61. The predicted film thickness and composition of film after 66 hours of exposure at $\text{pH } 6.3$, $c_{H_2S}=120$ ppm, $T=60^\circ\text{C}$, $P_{CO_2} = 7.7$ bar, $c_{Fe^{2+}} = 17$ ppm, $v=1$ m/s.	149
Figure 62. The predicted film thickness and porosity of film after 66 hours of exposure at $\text{pH } 6.3$, $c_{H_2S}=120$ ppm, $T=60^\circ\text{C}$, $P_{CO_2} = 7.7$ bar, $c_{Fe^{2+}} = 17$ ppm, $v=1$ m/s. Porosity $\varepsilon=1$ means no film.	150
Figure 63. The predicted film thickness and composition of film after 66 hours of exposure at $\text{pH } 6$, $c_{H_2S}=120$ ppm, $T=60^\circ\text{C}$, $P_{CO_2} = 7.7$ bar, $c_{Fe^{2+}} = 17$ ppm, $v=1$ m/s.	151
Figure 64. The predicted film thickness and porosity of film after 66 hours of exposure at $\text{pH } 6$, $c_{H_2S}=120$ ppm, $T=60^\circ\text{C}$, $P_{CO_2} = 7.7$ bar, $c_{Fe^{2+}} = 17$ ppm, $v=1$ m/s. Porosity $\varepsilon=1$ means no film.	151
Figure 65. The predicted film thickness and composition of film after 66 hours of exposure at $\text{pH } 5.7$, $c_{H_2S}=120$ ppm, $T=60^\circ\text{C}$, $P_{CO_2} = 7.7$ bar, $c_{Fe^{2+}} = 17$ ppm, $v=1$ m/s.	152

Figure 66. The predicted film thickness and porosity of film after 66 hours of exposure at pH 5.7, $c_{H_2S}=120$ ppm, $T=60^\circ\text{C}$, $P_{CO_2}=7.7$ bar, $c_{Fe^{2+}}=17$ ppm, $v=1$ m/s. Porosity $\varepsilon=1$ means no film.....	152
Figure 67. The predicted effect of P_{CO_2} on the corrosion rate for $T=60^\circ\text{C}$, $c_{H_2S}=120$ ppm, pH=6, $c_{Fe^{2+}}=17$ ppm, $v=1$ m/s. Corresponding film thickness and porosity are shown in Figure 68.....	153
Figure 68. The predicted effect of P_{CO_2} on the film thickness and porosity after 300 hours of exposure at $T=60^\circ\text{C}$, $c_{H_2S}=120$ ppm, pH=6, $c_{Fe^{2+}}=17$ ppm, $v=1$ m/s. Porosity $\varepsilon=1$ means no film.	154
Figure 69. The predicted film thickness and composition of film after 300 hours of exposure at $P_{CO_2}=1$ bar, $c_{H_2S}=120$ ppm, $T=60^\circ\text{C}$, pH 6, $c_{Fe^{2+}}=17$ ppm, $v=1$ m/s.	155
Figure 70. The predicted film thickness and porosity of film after 300 hours of exposure at $P_{CO_2}=1$ bar, $c_{H_2S}=120$ ppm, $T=60^\circ\text{C}$, pH 6, $c_{Fe^{2+}}=17$ ppm, $v=1$ m/s. Porosity $\varepsilon=1$ means no film.....	155
Figure 71. The predicted film thickness and composition of film after 300 hours of exposure at $P_{CO_2}=3$ bar, $c_{H_2S}=120$ ppm, $T=60^\circ\text{C}$, pH 6, $c_{Fe^{2+}}=17$ ppm, $v=1$ m/s.	156
Figure 72. The predicted film thickness and porosity of film after 300 hours of exposure at $P_{CO_2}=3$ bar, $c_{H_2S}=120$ ppm, $T=60^\circ\text{C}$, pH 6, $c_{Fe^{2+}}=17$ ppm, $v=1$ m/s. Porosity $\varepsilon=1$ means no film.....	156
Figure 73. The predicted film thickness and composition of film after 300 hours of exposure at $P_{CO_2}=7.7$ bar, $c_{H_2S}=120$ ppm, $T=60^\circ\text{C}$, pH 6, $c_{Fe^{2+}}=17$ ppm, $v=1$ m/s.	157
Figure 74. The predicted film thickness and porosity of film after 300 hours of exposure at $P_{CO_2}=7.7$ bar, $c_{H_2S}=120$ ppm, $T=60^\circ\text{C}$, pH 6, $c_{Fe^{2+}}=17$ ppm, $v=1$ m/s. Porosity $\varepsilon=1$ means no film.....	157
Figure 75. Polarization curve from potentiodynamic sweep technique. Source: DC electrochemical test methods from Corrosion testing made easy series. NACE...	177
Figure 76. Obtaining R_p from Linear Polarization Resistance technique. Source: DC electrochemical test methods from Corrosion testing made easy series. NACE...	180
Figure 77. Comparison between our model and OLI model prediction on the species concentration with respect to pH in open system, solid line = our model, dash line = OLI model prediction.....	187
Figure 78. pH effect on the concentration of carbonic species for 25°C , atmospheric pressure in closed system.....	188
Figure 79. Comparison of open system and closed system with gas to volume ratio 100:1 at 60°C and 7.9bar.....	189
Figure 80. Effect of pH on the concentration of sulfuric species, solid line= H_2S flow loop system with gas to liquid volume ratio of 1004:946, dash line = open system.	190
Figure 81. H_2S flow loop system concentration of all the species in the presence of 3 ppm H_2S at $T=60^\circ\text{C}$, $p(\text{CO}_2)=7.9$ bar with gas to liquid ratio of 1004:946.....	191

Figure 82. Closed flow loop system concentration of all the species in the presence of 20%(200000ppm) H ₂ S at T=60°C, p(CO ₂)=7.7 bar with gas to liquid ratio of 1004:946	192
Figure 83. Effect of 20% H ₂ S concentration on the carbonic species, solid line= 20% H ₂ S in the system, dash line = no H ₂ S presence.	193
Figure 84. Comparison between calculated electrochemical impedance of H ⁺ ions for a finite-thickness diffusion boundary layer, $\delta_{B.L.}=0.003\text{m}$ and infinite-thickness diffusion boundary layer, also known as Warburg impedance, for T=20°C, $[H^+]_{bulk}=1\times 10^{-5}$ mol/liter.	202
Figure 85. Effect of the thickness of diffusion boundary layer on the characteristics of electrochemical impedance of H ⁺ ions for T=20°C, $[H^+]_{bulk}=1\times 10^{-5}$ mol/liter.....	202
Figure 86. The equivalent circuit of the EIS model. Rs = solution resistance, CPEDl = constant phase elements describing double layer capacitance, Z_{total} = total impedance, R.E. = reference electrode, W.E. = working electrode.....	205

CHAPTER 1: INTRODUCTION

CO₂/H₂S combined internal corrosion attack has been a recognised problem in oil and gas industry for many years. Although various research efforts have tried to analyse it in order to develop predictive models, the underlying corrosion mechanisms are still not fully understood.

Engineers in the oil and gas industry nowadays employ various models for CO₂ corrosion¹⁻¹⁷. Depending on how firmly they are based on theory these predictive models can be classified into three categories: mechanistic, semi-empirical and empirical models. Even for “pure CO₂” corrosion, most research effort on the modelling are either semi-empirical or empirical¹⁻¹¹, that is, they are aimed at predicting the corrosion rate, but neglect the physics behind it. Only some of the more recent models have been based on mechanistic descriptions of the processes underlying CO₂ corrosion.¹²⁻¹⁷ In the case of H₂S corrosion and CO₂/H₂S corrosion, experimental investigations have been performed in various studies.¹⁸⁻³¹ These studies included the effect of H₂S on cathodic and anodic processes and the formation of various crystalline forms of iron sulfide scales. Several research efforts^{24,27-31} have attempted to elucidate the mechanism of CO₂/H₂S corrosion. However, the predictive models for combined CO₂/H₂S corrosion attack are not only primitive but also unable to meet the demands of the industry.

Several models exist that calculate equilibrium thermodynamics of Fe/CO₂/H₂S/H₂O chemistry system.^{17,32,33} There are no models existing for the interpretation of corrosion, transport and scaling phenomena in this system. A research project was here undertaken with an aim to develop an integrated *mechanistic* model of

CO₂/H₂S corrosion that includes all the important processes occurring such as: the electrochemical and chemical reactions, the transport processes within the boundary layer and the scale formation.

Several studies³⁴⁻³⁷ have demonstrated that the electrochemical behaviour of iron in the acidic solutions containing H₂S can be investigated by means of AC impedance measurement together with the potentiodynamic sweep technique. This research project will follow similar methodology to conduct a systematic investigation on the influence of H₂S concentration on the mechanism of iron dissolution in CO₂/H₂S solution.

A vapor-liquid equilibrium model for dilute aqueous solutions of CO₂/H₂S at different temperature has been developed with the aim to calculate the species concentrations in the presence of H₂S. Although similar model has been built previously,³⁸⁻⁴⁰ it was essential to develop a model of our own to provide more flexibility and applicability of input because the equilibrium concentrations are used as initial and boundary conditions for the mechanistic corrosion model. The equilibrium model is also a practical tool in experimental analysis as it enables important parameter such as pH and H₂S concentration to be compared and verified against the experimental measurements.

Film formation due to the presence of H₂S and its effect on corrosion of mild steel is the main focus of this research as the formation of stable and metastable iron sulfide species are difficult to predict when taking various environmental factors into account.

In order to model the corrosion process on theoretically plausible grounds, one of the most fundamental problems to be solved is the transport processes of all the species in the system, such as H⁺, Fe²⁺, H₂CO₃, and CO₂, with appropriate boundary conditions. The solution of the transport process will determine the concentration of these species in

the near wall region, which enables more accurate prediction for the morphology of the film and its effect on the corrosion of the mild steel.

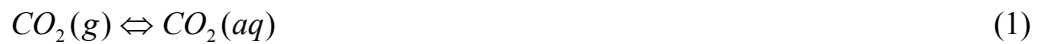
The ability of the mechanistic electrochemical/transport coupled model^{13,15} to calculate the concentration profile near the metal surface proves to be a strong advantage over other existing models and will be used as a basis for the future development of the combined CO₂/H₂S model. This research project includes addition of new species, chemical and electrochemical reactions arising from the presence of H₂S.

Overall, this research project not only provides the insight of the fundamental understanding of CO₂/H₂S corrosion with the inclusion of film formation, but also has a great practical tool for predicting corrosion in the oil gas transportation and other related areas.

CHAPTER 2: LITERATURE REVIEW

2.1 CO₂ corrosion

Carbon dioxide corrosion or “sweet corrosion” of carbon steel is a major problem in the oil and gas industry. The presence of dry CO₂ gas or only oil is itself not corrosive. However, it is the contact of the aqueous phase with the surface of the metal that leads to corrosion and subsequent failures. The basic CO₂ corrosion reactions have been well understood and accepted throughout the work done in the past few decades.¹⁻¹⁷ The major chemical reactions include CO₂ dissolution and hydration to form carbonic acid,



It then dissociates into bicarbonate and carbonate ions in two steps:



CO₂ corrosion is an electrochemical reaction with the overall reaction given by:



Thus, CO₂ corrosion leads to the formation of a corrosion product, FeCO₃, which when precipitated could form a protective or a non-protective scale depending on the environmental conditions.⁴¹⁻⁴³

The electrochemical reactions at the steel surface include the anodic dissolution of iron:^{49,50}



and two cathodic reactions. The cathodic reactions are proton reduction reaction and the direct reduction of carbonic acid:



Despite more than three decades of intense research, it is still not known which of the two reactions actually prevails on the surface.^{1,5,44} Hence, many have taken the net cathodic current to be the sum of the currents of the two reactions.⁴⁴ It has been suggested that the direct reduction of bicarbonate ion becomes important at higher pH.⁴⁵

Having outlined the mechanism, one can anticipate that there are many environmental factors such as solution chemistry, flow velocity, temperature, pressure, pH etc., affect the uniform CO₂ corrosion rate of mild steel. The formation of the corrosion product scales due to the environmental conditions could also have a significant impact on the corrosion rate of the metal. The effect of some of the important factors on CO₂ corrosion in the oil and gas industry will be discussed in the following paragraphs.

2.2 The effect of pH

pH is an indication of the H⁺ ion concentration in the solutions, which is one of the main species involved in cathodic reaction of CO₂ corrosion process. It has been illustrated both experimentally^{44,45} and computationally¹⁵ that corrosion rate changes significantly with respect to pH. At low pH (pH<4) and low CO₂ partial pressure (≤1 bar), a flow sensitive direct reduction of H⁺ (equation 7) dominates the cathodic reaction.¹³ On the other hand, at higher pH (pH>5) and higher CO₂ partial pressure (≥1

bar) the cathodic reaction is controlled by the direct reduction of H_2CO_3 , (equation 8), which is related to the amount of dissolved CO_2 .¹³

However, it is the indirect effect of pH on the formation of protective films (such as iron carbonate) that is the most important. Higher pH leads to a decreased solubility of iron carbonate and thus results in an increased precipitation rate, faster formation of protective films and hence reduction of the corrosion rate.¹⁶

2.3 The effect of temperature

Temperature accelerates all the processes involved in CO_2 corrosion including transport of species, chemical reactions in the bulk of the solutions and electrochemical reactions at the metal surface. Depending on whether the solubility of protective films (such as iron carbonate or other salts) is exceeded, temperature can either increase or decrease the corrosion rate.^{16,46} In the case of corrosion where protective films do not form (typically at low pH), corrosion rate increases with increasing temperature. However, at a higher pH where solubility of protective films is likely to be exceeded, increased temperature would accelerate the kinetics of precipitation and facilitate protective films formation, thus decreasing the corrosion rate. The corrosion rate usually peaks somewhere in between 60°C and 80°C depending on flow conditions and water chemistry.

2.4 The effect of CO_2 partial pressure

In the absence of protective films, an increase in CO_2 partial pressure will result in an increase of corrosion rate, because with increased CO_2 partial pressure, the direct

reduction of H_2CO_3 (equation 8) will be accelerated due to an increase of H_2CO_3 concentration.¹³ However, when other conditions are favorable for formation of protective iron carbonate films, increased CO_2 partial pressure may help to facilitate the film formation. At a given high enough constant pH, an increase in CO_2 partial pressure results in an increase of CO_3^{2-} concentration and a higher supersaturation, thus speeding up precipitation and film formation.¹⁶

2.5 The effect of flow

Flow affects corrosion through the mass transport process involved in CO_2 corrosion. Higher flow rates usually means higher turbulence and more effective mixing in the solution.¹³ Depending on whether other conditions are beneficial for protective film formation, flow affects CO_2 corrosion in a number of ways. Without protective films, turbulent flow accelerates the transport of species towards and away from the metal surface, which may result in an increase of corrosion rate given that transport is the rate determining factor. On the other hand, when other conditions are conducive to formation of protective iron carbonate films, species transport in turbulent flow affects the surface concentration of species and consequently the precipitation rate of iron carbonate; in many cases less protective films are being formed at higher flow velocities.¹⁶ In some cases where flow velocities are extremely high, flow can even mechanically remove the protective films that are already in place, resulting in an increase of corrosion rate.

2.6 Effect of Supersaturation

During the transport the oil and gas in the pipeline, the water phase will accumulate dissolved ferrous ions, Fe^{2+} due to corrosion of the mild steel pipe wall. So there can be considerable amount of Fe^{2+} in the downstream portion of the pipeline, which could have an influence on the formation of the iron carbonate scale. Increased Fe^{2+} concentration can lead to higher supersaturation, which could increase the precipitation rate of iron carbonate and lead to more protective scale formation.¹⁶

Corrosion also leads to an increase in pH which results in an increase in the CO_3^{2-} ion concentration. This in turn leads to the increase in the supersaturation that could lead to formation of iron carbonate film.

2.7 Corrosion product film formation

CO_2 corrosion of a metal is strongly dependent on the type of corrosion product film formed on the surface of the metal during the corrosion process. The stability, protectiveness, precipitation rate and the adherence of these films determine the nature of (localized/ uniform) and the rate of corrosion. Depending on the environmental factors, corrosion films can be divided into following major classes:

a) Iron carbide (Fe_3C)

Iron carbide is the undissolved component of the mild steel, which is left behind from the corrosion process. It is conductive, very porous and non-protective. Iron carbide films can significantly affect the corrosion process by either decreasing the corrosion rate by acting as a diffusion barrier or increasing the corrosion due to:⁴⁷

- Galvanic coupling of the film to the metal.
- Increase in the true specimen surface area
- Acidification of the solution inside the corrosion product film

b) Iron carbonate (FeCO_3):

The reaction for formation of solid iron carbonate is given by:



The precipitation of solid iron carbonate occurs when the product of concentrations of Fe^{2+} and CO_3^{2-} exceed a certain limit known as the solubility limit. However, the rate of precipitation of iron carbonate is so slow that most often the precipitation kinetics comes into consideration rather than the thermodynamics.

The equation for the rate of precipitation of the iron carbonate ($R_{\text{FeCO}_3(s)}$) is given as :⁴⁶

$$R_{\text{FeCO}_3(s)} = \frac{A}{V} \cdot f(T) \cdot K_{sp_{\text{FeCO}_3}} \cdot f(S_{\text{FeCO}_3}) \quad (10)$$

Where Supersaturation S is defined as:

$$S_{\text{FeCO}_3} = \frac{c_{\text{Fe}^{2+}} c_{\text{CO}_3^{2-}}}{K_{sp_{\text{FeCO}_3}}} \quad (11)$$

With A/V = the surface area-to-volume ratio and $K_{sp_{\text{FeCO}_3}}$ = solubility limit of FeCO_3

Since CO_3^{2-} ion concentration is dependent on the pH, it can be deduced that:

$$S = f(\text{Fe}^{2+}, \text{pH}) \quad (12)$$

When iron carbonate precipitates at the steel surface, it decreases the corrosion rate by:^{16, 41}

- Presenting a diffusion barrier for the species involved in the corrosion process
- Blocking a portion of the steel and preventing electrochemical reactions from occurring.

The most important factors affecting the precipitation of iron carbonate are supersaturation and the temperature.

c) Iron sulfide (FeS):

The formation of iron sulfide only occurs in the presence of H₂S. The reaction for formation of solid iron carbonate is given by:



It is assumed that the precipitation of solid iron sulfide occurs when the product of concentrations of Fe²⁺ and S²⁻ exceed a the solubility limit of FeS. The equation for the rate of precipitation of the iron carbonate ($R_{FeS(s)}$) is given as:⁴⁸

$$R_{FeCO_3(s)} = \frac{A}{V} \cdot f(T) \cdot Ksp_{FeS} \cdot f(S) \quad (14)$$

Where Supersaturation S_{FeS} is defined as:

$$S_{FeS} = \frac{c_{Fe^{2+}} \cdot c_{S^{2-}}}{Ksp_{FeS}} \quad (15)$$

With Ksp_{FeS} = solubility limit of FeS

It is assumed that iron sulfide affects the CO₂ corrosion in the same way as iron carbonate (by being a diffusion barrier and surface blockage). However, iron sulfide films are semi-conductive; in some cases it has been observed that the presence of iron sulfide may lead to localized corrosion and the cause is still not clear.^{52,53}

2.8 The effect of H₂S

The internal CO₂ corrosion of mild steel in the presence of hydrogen sulfide (H₂S) represents a significant problem for both oil refineries and natural gas treatment facilities. In the recent years the problem has become more important as the available reserves of oil possess a considerable amount of H₂S. Although the interaction of H₂S with low-carbon steels have been published by various authors,⁵³⁻⁵⁷ the understanding of the effect of H₂S on CO₂ corrosion is still limited because the nature of the interaction with carbon steel is complicated.

In the presence of H₂S, additional chemical reactions occurring in the bulk of the solution include:

Dissociation of dissolved H₂S:



Dissociation of HS⁻ ion:



Although H₂S gas is about three times more soluble than CO₂ gas, the acid created by the dissociation of H₂S is about three times weaker than carbonic acid. Hence, the effect of H₂S gas on decreasing the solution pH is approximately the same as CO₂ gas. Unlike dissolved CO₂, dissolved H₂S does not need to undergo the slow hydration step in order to become an acid.

Generally, three regimes in CO₂/H₂S system can be classified based on the concentration of H₂S as shown in figure below:⁵⁸

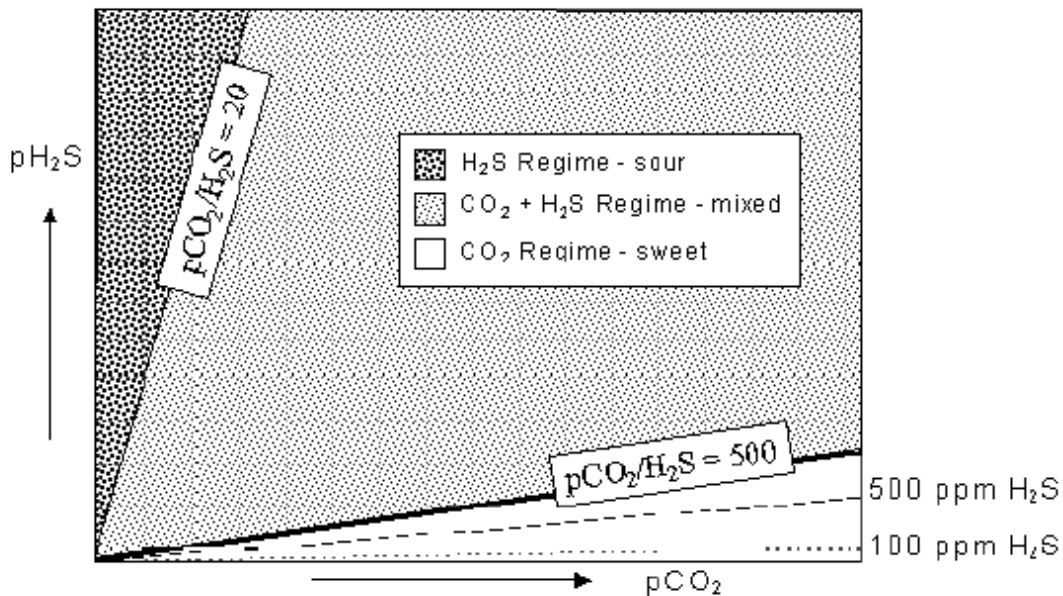


Figure 1. Corrosion regimes in CO₂/H₂S corrosion defined by Pots, et al.⁵⁸

2.8.1 H₂S dominated system (sour regime)

Dissolved H₂S is a weak acid like carbonic acid. As a result, not only does H₂S lower the solution pH, but also it can increase the corrosion rate in a similar way as carbonic acid, by providing an extra cathodic reaction:⁵³



However, this direct reduction of H₂S is only feasible if the amount of H₂S is high enough, which means the system has to be either H₂S dominated system, (sour regime) or CO₂/H₂S mixed system.

Moreover, elemental sulfur is often associated with high concentration of H₂S and very little is known about the complex interactions taking place in the presence of elemental sulfur. Although H₂S may also lead to corrosion problems associated with hydrogen blistering and sulfide stress cracking in sour regime, it will not be covered in

the literature review as it is not within the scope of this study. This study will primarily focus on the CO₂ corrosion mechanism in the presence of trace amount (<500ppm) of H₂S, which is in the “sweet regime”.

2.8.2 CO₂ dominated system (sweet regime)

Ignoring the cracking aspects of corrosion problems associated with the "sour regime", trace amount of H₂S can affect CO₂ corrosion in various ways. The majority of open literatures^{52,57} have reported that the trace amount of H₂S does reduce the corrosion rate at ambient temperatures. On the other hand, the presence of H₂S can also lead to formation of iron sulfide films according to equation (13).

Depending on various environmental factors, different types of iron sulfide can be formed. In some cases iron sulfide films can be nonprotective and result in localised attack. Understanding the mechanisms of the formation of various forms of iron sulfide films and its effect on CO₂ corrosion process are the major challenges in modelling CO₂/H₂S corrosion.

In the following section a description of the nature, composition and structure of several distinctive iron sulfide films, as well as the mechanism of formation and transformation of various types of iron sulfide films are reviewed.

2.9 Nature of iron sulfide films

2.9.1 Mackinawite

Mackinawite is a tetragonal sulfur-deficient iron sulfide with a composition of either FeS_{1-x} ($0 < x < 0.07$) or Fe_{1+x}S ($0.057 < x < 0.064$)⁶¹. Mackinawite was considered unstable relative to troilite (described below) based on standard free energy considerations. The crystal structure of mackinawite is illustrated below in one-dimension and three-dimension:^{62, 63}

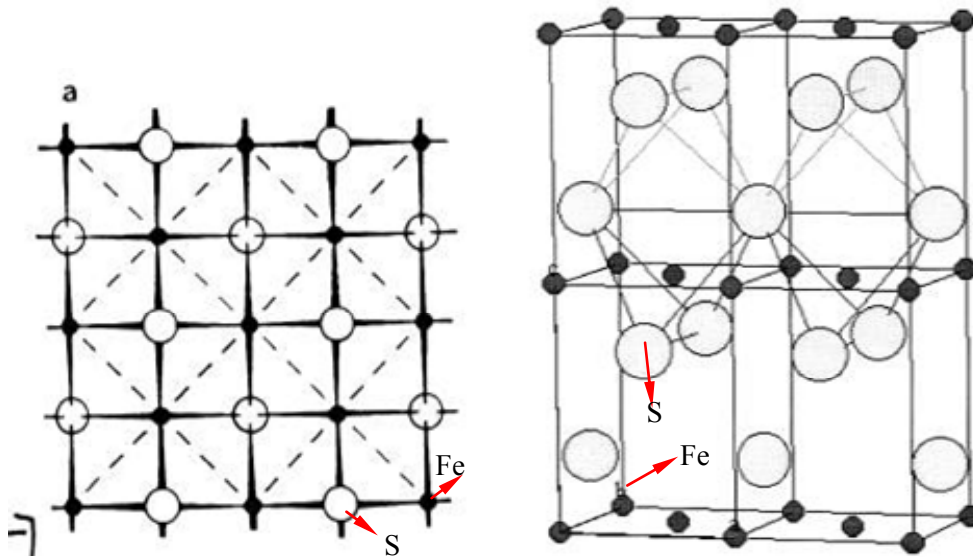


Figure 2. The structure of mackinawite, image taken from L. A. Taylor and L. W. Finger, "Structure Refinement and Composition of Mackinawite"⁶²

The structure of mackinawite consists of a distorted cubic-packed array of sulfur atoms with iron in some of the tetrahedral interstices. Iron atoms are at the center of slightly distorted tetrahedral sharing edges to form sheets. These atoms are held together with only weak Van der Waals forces.

Mackinawite is a main corrosion product on the surface of carbon steel in saturated $\text{CO}_2/\text{H}_2\text{S}$ solution. There are two ways of forming mackinawite:

1. Precipitation of aqueous Fe^{2+} and S^{2-} (equation 13)
2. Direct chemical reaction of dissolved H_2S with the metallic iron with. (solid state formation)

2.9.2 Cubic FeS

Cubic FeS has a cubic stoichiometric crystal structure and is only encountered as a corrosion product.⁶¹

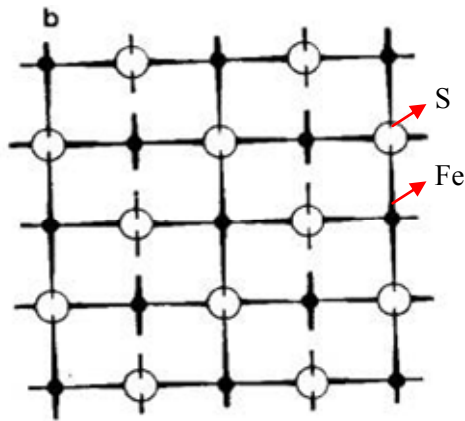


Figure 3. The structure of cubic FeS. Image taken from J. S. Smith and J. D. A. Miller, “Nature of Sulfides and Their Corrosive Effect on Ferrous Metals: A Review”⁶¹

Within cubic FeS there are no Fe-Fe bonds and the structure of cubic FeS shows a striking resemblance to that of mackinawite, which accounts for the fact that the transformation of Cubic FeS to mackinawite occurs spontaneously at room temperature. Hence Cubic FeS is considered as only a metastable species.

2.9.3 Troilite

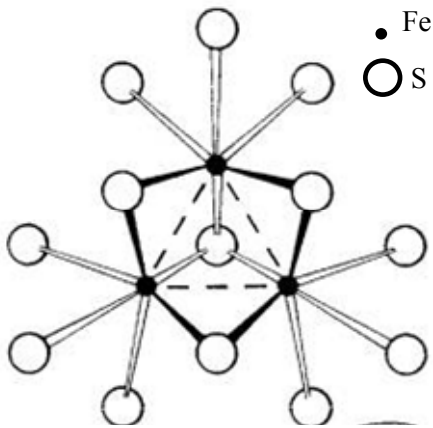


Figure 4. The structure of troilite. Image taken from J. S. Smith and J. D. A. Miller, “Nature of Sulfides and Their Corrosive Effect on Ferrous Metals: A Review”⁶¹

The above schematic drawing is a crystal structure of troilite⁶². The formula of troilite is stoichiometric FeS. Both Fe and S are six-coordinate, and iron atoms are drawn together as triangular clusters. Dashed lines show Fe-Fe interactions. It was found that troilite appears as a corrosion product on carbon steel surface in aqueous H₂S at low temperatures, due to high local iron concentrations at the corroding surface.²⁷

2.9.4 Pyrrhotite

Pyrrhotite is more stable than mackinawite and it is an iron-deficient iron sulfide with a composition ranging from Fe₇S₈ to stoichiometric troilite, FeS.⁶¹

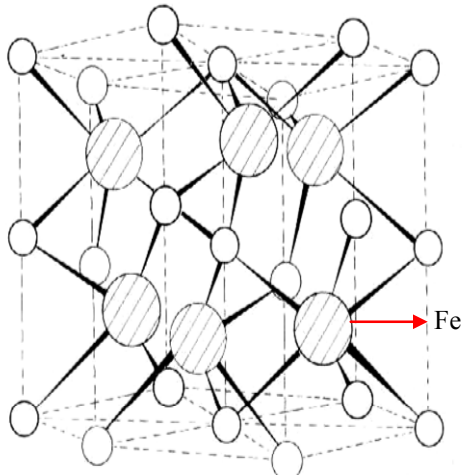


Figure 5. The structure of pyrrhotite. Image taken from J. S. Smith and J. D. A. Miller, "Nature of Sulfides and Their Corrosive Effect on Ferrous Metals: A Review"⁶¹

The above crystal structure of pyrrhotite illustrated that it is an ordered defect hexagonal structure, with one vacancy in every four metal positions, confined to every second layer.

2.9.5 Pyrite

Pyrite has a cubic crystal structure^{61,62}; the sulfur is present as the polysulfide species, S_2^{2-} . The sulfur-to-sulfur bond lengths almost equal the sulfur molecule. Pyrite is the most stable iron sulfide and the structure of pyrite is shown below:

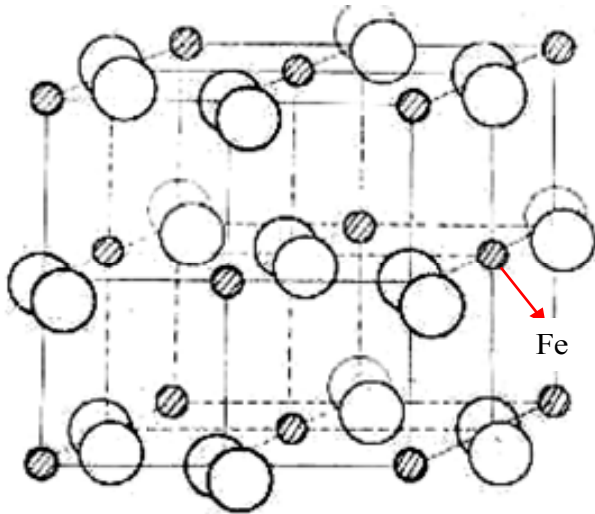


Figure 6. The structure of pyrite. Image taken from J. S. Smith and J. D. A. Miller, “Nature of Sulfides and Their Corrosive Effect on Ferrous Metals: A Review”⁶¹

2.9.6 Greigite

Greigite is a thio-spinel of iron⁶¹, Fe_3S_4 , consisting of sulfur in cubic close packing with eight iron ions in tetrahedral co-ordination and sixteen iron ions in octahedral coordination:

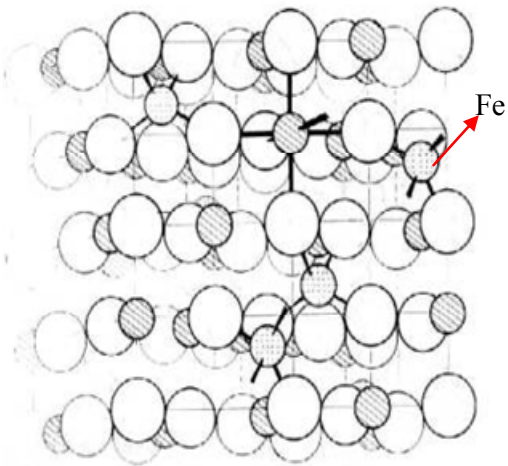


Figure 7. The structure of greigite. Image taken from J. S. Smith and J. D. A. Miller, “Nature of Sulfides and Their Corrosive Effect on Ferrous Metals: A Review”⁶¹

Greigite is thermodynamically unstable relative to troilite and pyrite. In addition, greigite will form as corrosion product only if oxygen or sulfur is introduced into the solutions.

2.10 Mechanism of iron sulfide film formation in CO₂/H₂S corrosion

Mechanism of scale formation in CO₂/H₂S corrosion is very complicated because various types of iron sulfides can form under different conditions. Various published explanations on mechanisms of film growth and transformation of different iron sulfide films in CO₂/H₂S solutions are summarized below. Iron sulfide film growth can occur by means of solid-state reaction or precipitation due to local supersaturation. The type of iron sulfide formed may be metastable and later transforms into a more stable form of iron sulfide. This section will be focused on the mechanism and the effect of iron sulfide films on CO₂/H₂S corrosion.

2.10.1 Effect of brine on iron sulfide film in Pure H₂S solutions

Having conducting experiments using saturated H₂S solutions, Meyer et al.⁶⁴ have observed that the corrosion rates and the corrosion product are strongly influenced by some ionic species in the presence of brine.⁶⁴ When iron was immersed in pure saturated H₂S solutions (in the absence of oilfield brine), the initially formed mackinawite would first convert into a mackinawite scale and soon covered by protective pyrrhotite and pyrite films.

On the other hand, under exactly the same experimental conditions but with the presence of brine, a porous mackinawite film would transform into a mackinawite scale. However, no protective pyrrhotite-pyrite scale would be formed during the 20 weeks of the experiment.

2.10.2 Transformation of iron sulfide in pure H_2S solutions at pH4

Shoesmith et al.²⁷ systematically studied on the nature of corrosion products formed on iron exposed to pure aqueous H_2S (in the absence of CO_2) at pH 4. The initial corrosion of iron or carbon steel by hydrogen sulfide saturated water at low temperatures involves the formation of mackinawite (tetragonal FeS_{1-x}), cubic ferrous sulfide, and troilite (stoichiometric hexagonal FeS). Solubility measurements^{65,71} and interconversion studies^{67,68} indicate that the stability of iron sulfide is in the order of troilite > mackinawite > cubic ferrous sulfide. The qualitative elucidation of the mechanisms of the formation of iron sulfides is depicted by the reaction scheme shown below:

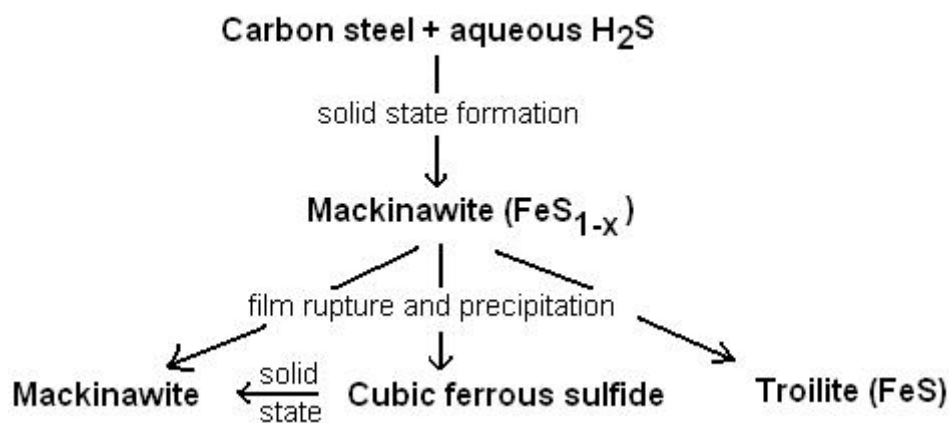


Figure 8. Reaction scheme of the mechanisms of iron sulfide formation²⁷

Initially a layer of mackinawite is produced by solid state formation. Solid state formation is a chemical reaction in which a solid reacts with another solid, a liquid or a gas to form a solid product (an intermetallic, a silicide, an oxide, a salt etc.) at the interface between initial substances. The initial mackinawite layer is easily cracked and pitted, which leads to high local iron dissolution and release of iron ions. Hence cubic ferrous sulfide and smaller amount of troilite is then formed by precipitation. Although troilite is the most stable of the three phases, the nucleation of troilite is difficult and requires long immersion time (> 96 hours).

2.10.3 Iron sulfide stability diagram using Pourbaix diagrams

Anderko and Shuler⁷²⁻⁷³ developed a program for generating iron sulfide stability diagrams that combine the principles of the Pourbaix (potential vs. pH) diagrams with an advanced water chemistry model. It is claimed that the validity of the model ranges from dilute to concentrated (non-ideal) solutions with an extensive range of temperature (up to 300°C) and pressure (up to 1kbar). The model claims that it is able to predict the conditions that favor the stability of various iron sulfide species, both stable and metastable products. However, one needs to bear in mind that the Pourbaix diagrams are based on thermodynamics and it can not predict the kinetics (rate) of formation of various iron sulfide species.

2.10.4 Mechanism of pyrite in pure H₂S solutions

Experimental results⁷⁴ have proven that mackinawite can be stable for up to four months at low temperature. In pure saturated H₂S solutions, the rate of pyrite formation

from a precursor mackinawite is low at temperature below 100°C. With controlled, intentional oxidation experiments below 100°C and over a wide range of pH (3.3-12), it was proved that mackinawite only serves as a precursor to pyrite formation in slightly oxidizing environments. The formation of pyrite is a multi-step process involving an initial solid-state reaction of mackinawite from aqueous sulfide species, and the transformation of mackinawite to pyrite via the intermediate metastable greigite.

2.10.5 Mechanism of Mackinawite in $\text{CO}_2/\text{H}_2\text{S}$ solutions

S. N. Smith^{30,75,76} proposed a model based on the formation of mackinawite and defined boundary conditions that separate various corrosion products in $\text{CO}_2/\text{H}_2\text{S}$ solutions as shown below:

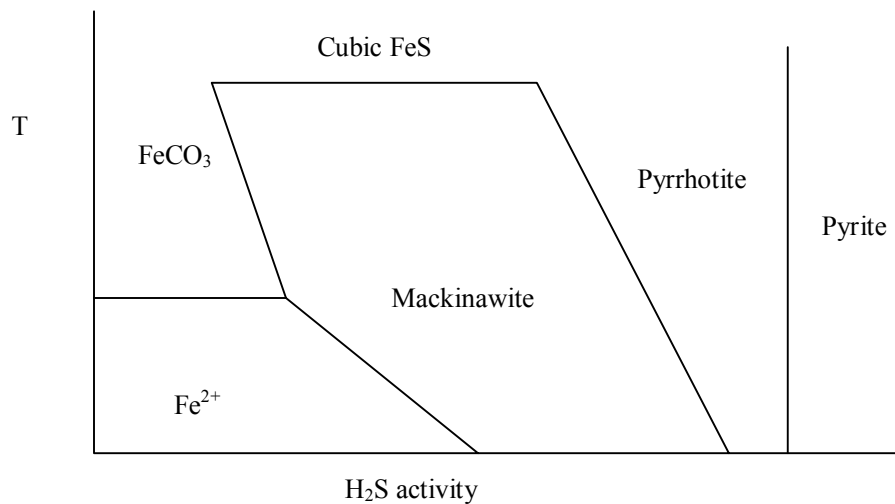


Figure 9. Thermodynamic boundary conditions that separate various corrosion products in $\text{CO}_2/\text{H}_2\text{S}$ solutions⁷⁶

Although pyrrhotite and pyrite are more stable than mackinawite as iron sulfide films from thermodynamic point of view, mackinawite is always the initial corrosion

product due to its rapid kinetics of formation. Mackinawite is usually expected to form under conditions where the combined bulk activity of Fe^{2+} and H_2S is inadequate to exceed the solubility limit of FeS , yet H_2S activity is sufficient to form mackinawite provided that the Fe^{2+} activity on the steel surface is assumed to be 1.0. The proposed mechanism assumes that H_2S diffuses to the metal surface and reacts with the steel surface (via solid state reaction) to first form an adsorbed FeS which then combines to form mackinawite. However, mackinawite immediately begins to dissolve to form $\text{Fe}(\text{HS})^+$ and HS^- because the solubility limit in the bulk solution has not been exceeded. As $\text{Fe}(\text{HS})^+$ diffuses away, a fresh steel surface is exposed and is available for an immediate reaction with H_2S to form more mackinawite. Therefore a very thin tarnish of mackinawite is produced which repeatedly forms and dissolves. Assuming the above mechanism holds true, the corrosion rate of a mackinawite covered surface can then be determined by the dissolution of mackinawite and the rate of mackinawite diffusing away from the metal surface.

Despite various attempts in clarifying the mechanism of $\text{CO}_2/\text{H}_2\text{S}$ corrosion, very little quantitative information is available. Published laboratory work has not been conclusive, indicating that it is necessary to conduct a detailed investigation, in order to elucidate the mechanism of CO_2 corrosion in the presence of trace amount of H_2S .

2.11 CO_2 Corrosion Models

Several important models that had significant contributions to development of CO_2 corrosion modeling are reviewed in this section.

2.11.1 de Waard Model

The model proposed by de Waard and his coworkers¹⁻⁴ is the most widely accepted CO₂ corrosion model in oil and gas industry for the past two decades. Initially it was a mechanistic model based on the assumption of direct reduction of H₂CO₃ and the correlation with glass cell laboratory data. The initial model¹ (published in 1975) only included the effect of partial CO₂ pressure and temperature as shown below:

$$\log V_{cor} = 7.96 - \frac{2320}{T + 273} - 5.55 \times 10^{-3} T + 0.67 \log p_{co_2} \quad (19)$$

where V_{cor} = corrosion rate (mm/year)

T = temperature (°C)

P_{CO_2} = partial pressure of CO₂ (bar)

The temperature function in the above equation (19) was determined by assuming an Arrhenius type dependence for a charge transfer controlled process. On the other hand, the CO₂ partial pressure function was obtained by assuming that all the H⁺ ions in solution originate from dissociation of carbonic acid, which is only valid for pure saturated CO₂ solution in the absence of brines. Moreover, the model falsely assumed that the anodic dissolution of iron is strongly influenced by concentration of OH⁻ (This well-known pH dependent mechanism⁷⁹ is only valid in strong acid solution pH<4).

The revised versions²⁻⁴ implemented various correction factors into the original equation to account for high pH in brines, corrosion product films, total pressure, oil wetting, top of line corrosion, inhibitor, glycol, velocity, etc. However, the addition of correction factors had violated the assumptions under which the original equation was derived, thus the model was no longer mechanistic, but rather had become semi-empirical.

This semi-empirical model was successfully calibrated with a large and reliable experimental database. However, user should be very careful when the application is extrapolated outside the experimental range because it can lead to unreliable and sometimes physically unrealistic results. Moreover, predictions made by this model are considered to be worst case scenario, especially under film forming conditions, i.e. at high temperature or high pH. Correction factors must be applied in order for this model to predict corrosion product films and the corresponding corrosion rates under film forming conditions. Although weighed down by numerous theoretical deficiencies, this semi-empirical model is a practical tool that can be extended to areas where inadequate theoretical knowledge can be compensated by with empirical correlations.

2.11.2 Gray et al.

In order to investigate the mechanisms of CO₂ corrosion, a more complete mechanistic electrochemical model was proposed by Gray et al.^{44,45} The model constants had a physical meaning and were either available in the literature or determined from conducted experiments. The treatment of the electrochemical reactions occurring at the metal surface was legitimate as it was adopted from literature and its implementation into the overall model was a huge step forward in terms of its approach in the field of CO₂ corrosion modeling. The only drawback of this model was its overly ambitious attempt to cover a very broad range of parameters (pH 2-11, T=25-125°C) with only one set of mechanisms. Unfortunately this well-established theoretical approach was not appreciated by most of Gray's contemporaries as most researchers were reluctant to

either accept the more difficult mechanistic approach or renounce the informal standard approach dominated by semi-empirical and empirical models.

2.11.3 Nesic et al.

Inspired by the approach of Gray et al.,^{44,45} Nesic et al.¹³ also presented an electrochemical model of CO₂ corrosion. However, the range of parameters covered was narrowed down to more realistic CO₂ corrosion conditions (pH 3-6, T=20-80°C). Physical constants appearing in the model were determined from the literature, or obtained from numerous rotating cylinder glass cell experiments if the constants were not available from literature. The predictions made with the model were successfully compared with independent pipe-flow glass-loop experiments. This mechanistic model has proved its ability to extrapolate successfully outside the experimental range.

In both of the mechanistic electrochemical models mentioned above, the corrosion rate can be obtained by determining the rate of the underlying electrochemical reactions such as:

- Fe oxidation
- H⁺ reduction
- H₂CO₃ reduction
- H₂O reduction

The electrochemical reaction rate can be expressed as a current density (A m⁻²). For each of the cathodic species, the cathodic current i_c is expressed as:

$$\frac{1}{i_c} = \frac{1}{i_{ct}} + \frac{1}{i_{lim}} \quad (20)$$

where i_{ct} = cathodic charge transfer controlled current

i_{lim} = limiting current.

The cathodic charge transfer controlled current can be written for all cathodic reactions and is a function of the corrosion potential E at the metal surface:

$$i_{ct} = i_o \cdot 10^{-\frac{E-E_{rev}}{b_c}} \quad (21)$$

where i_o = exchange current density ($A\ m^{-2}$)

E_{rev} = reversible potential (V)

b_c = cathodic Tafel slope (V)

The values of i_o , E_{rev} and b_c are all characteristic for a particular electrochemical reaction and depend on the temperature and the concentration of species involved in the reaction at the metal surface. Some of these parameters are usually not available in the literature and must be obtained from the experimental study.

In the case of H^+ reduction, the limiting current comes from the mass transfer limitation for H^+ reduction:

$$i_{lim(H^+)}^d = k_m F \cdot [H^+]_b \quad (22)$$

where k_m = mass transfer coefficient

F = Faraday's constant

$[H^+]_b$ = bulk concentration of H^+ ion

The mass transfer coefficient k_m can be calculated from a correlation for the given flow geometry.

In the case of direct H_2CO_3 reduction, the limiting current is a consequence of a slow CO_2 hydration step (88) and can be found as:

$$i_{\text{lim}(H_2CO_3)}^r = F \cdot [CO_2]_b \cdot (D_{H_2CO_3} K_{hyd} k_{hyd}^f)^{0.5} \quad (23)$$

where $[CO_2]_b$ = bulk concentration of dissolved carbon dioxide

$D_{H_2CO_3}$ = diffusion coefficient for H_2CO_3 in water

K_{hyd} = equilibrium constant for CO_2 hydration reaction

k_{hyd}^f = forward reaction rate for CO_2 hydration reaction

The above equation (23) was derived for a stagnant condition, where the boundary layer is semi-infinite. In order to account for the flow effect on the chemical reaction limiting current, Nesic et al.⁸¹ later proposed a theoretical multiplier f for the above equation (23):

$$f = \coth \xi \quad (24)$$

where ξ = ratio of the thickness of the diffusion and reaction boundary layers.

For the case of direct H_2O reduction there is no limiting current, because H_2O is abundant throughout the solutions.

For the anodic dissolution of iron, pure Tafel behaviour was assumed close to the corrosion potential and the anodic current:

$$i_a = i_{o(Fe)} \cdot 10^{\frac{E - E_{rev}}{b_a}} \quad (25)$$

where $i_{o(Fe)}$ = exchange current density for Fe

b_a = anodic Tafel slope

E_{rev} = reversible potential

The unknown corrosion potential E at the metal surface in the (25) equation above can be determined from the charge balance equation which states that the sum of cathodic currents equals the sum of anodic currents at the metal surface:

$$\sum i_c = \sum i_a \quad (26)$$

Although this type of mechanistic electrochemical model comprehensively describes the electrochemical processes occurring on the metal surface, it is not applicable to corrosion in the presence of protective films because the electrochemical processes were not coupled properly with the transport processes and chemical processes in the boundary layer. In corrosion, certain species in the solution are produced the metal surface (e.g. Fe^{2+}) while others are depleted (e.g. H^+) by the electrochemical reactions, which results in concentration gradients and diffusion of these species towards and away from the surface. Not only does the rate of electrochemical processes depend on the concentration of species at the surface, but the concentration of species at the metal surface can also be very different from the ones in the bulk when the electrochemical process is much faster than the diffusion process. Hence there is a mutual coupling between electrochemical processes at the metal surface and the transport of species. On the other hand, the chemical reactions also have an intricate interaction with both the transport and electrochemical processes, especially for the case of protective film formation. In addition, since the water solution is always flowing in most practical services, the effect of turbulent convection also contributes to the transport of species to and from the surface, thus increasing the rate of electrochemical process and the corresponding corrosion rate.

Therefore a more sophisticated transport model coupling with electrochemical model was later proposed by Nescic et al.¹⁵ by solving the transport processes of all the species in the system, with fluxes due to electrochemical reactions as boundary conditions. The solution of the transport process will determine the concentration of

these species in the near wall region, which enables more accurate prediction for the morphology of the film and its effect on the corrosion of the mild steel. Numerical techniques are used in order to obtain solution of the complicated equations leading to more accurate predictions.

Detailed explanation of coupled electrochemical/transport model which was used as a starting point for the present study is discussed in Chapter 4.

From the preceding discussion, a lack of understanding regarding the interaction between the scale and corrosion process in the presence of trace amount of H₂S is evident. Moreover, the necessity to implement a mechanistic model of CO₂ corrosion in the presence of H₂S is realized.

CHAPTER 3: RESEARCH OBJECTIVES

3.1 Research objectives

The understanding of CO₂ corrosion in the presence of trace amount of H₂S is limited and no predictive mechanistic models have been published in the open literature for H₂S or CO₂/H₂S corrosion. Also no models existed that mechanistically covered the corrosion in the presence of surface films. Therefore the purpose of the present research project was to make the following contribution to the area of modelling of CO₂ corrosion in the presence of H₂S:

"Build and implement a mechanistic model covering the effect of H₂S traces on CO₂ corrosion including the formation of protective films and starting from the mechanistic CO₂ corrosion model of Nesic et al.¹⁵"

3.2 Research milestones

In order to achieve the above objective, the following milestones need to be accomplished because they served as fundamental building blocks for the final model. All of the milestones listed below were achieved and published either as Board report or papers.

- Implementation of implicit electrochemical boundary conditions to the original CO₂ corrosion model of Nesic et al¹⁵. This model served as a basis for all future developments.

- Small-scale CO₂ experiment in film forming conditions (high temperature and pH) in order to obtain missing physical constants for iron carbonate film growth model.¹⁶ (Corrosion monitoring techniques are described in Appendix A)
- Implementation of FeCO₃ film growth model.¹⁶
- Development of a vapor-liquid equilibrium model for dilute aqueous solutions of CO₂/H₂S at different temperature with the aim to calculate the species concentrations in the presence of H₂S for both open and closed system.⁸² These conditions were used as initial and bulk boundary conditions for all future developments of the model. (Described in detail in Appendix B)
- Small-scale glass cell CO₂/H₂S experiments in film free conditions using Electrochemical Impedance Spectroscopy (EIS) and Linear Polarization Resistance (LPR) techniques.⁸³
- Development of an analytical EIS model to interpret the EIS data collected on CO₂/H₂S corrosion.⁸⁴ (Detailed description is included in Appendix C)
- Addition of new species, chemical reactions and electrochemical reactions arising from the presence of H₂S into CO₂ corrosion model from Nescic et al.⁸⁵
- Implementation of FeS film growth model and parametric study to gain insights of CO₂/H₂S corrosion in film forming conditions.⁸⁶
- Calibration and verification of the overall performance of the model with large-scale experimental results.⁸⁷

The following chapters are laid out in a sequence that assists the readers to understand the mechanistic modeling of CO₂ corrosion of mild steel in the presence of

H₂S in detail. Since the mechanistic model of CO₂ corrosion of mild steel was already developed by Netic et al.¹⁵ as the work on this project was beginning, it was used as a well-established platform for all future developments. Therefore, the original version¹⁵ of the mechanistic model of CO₂ corrosion (without H₂S) of mild steel in film free conditions must be comprehensively reviewed first in Chapter 4 in order to appreciate the complexity of the model and the challenges that were faced.

Since the original version of CO₂ corrosion model lacked the prediction of the morphology of iron carbonate films and its effect on corrosion rate, an immediate major improvement was accomplished by the present author to implement iron carbonate film growth¹⁶ into the original model and is discussed in Chapter 5. Having completed the package for CO₂ corrosion model, the investigation of CO₂/H₂S corrosion could then be pursued.

The investigation and modeling of CO₂/H₂S corrosion was executed with caution because the underlying corrosion mechanisms were not fully understood. After having studied the growth of iron carbonate films and its effect on CO₂ corrosion, the present author realized that the presence of surface films significantly alters the way that the environmental parameters affect the corrosion process. Thus the initial study of the effect of trace amount H₂S must be performed in film free conditions in order to elucidate the fundamental mechanisms (see Chapter 6).

After having elucidated the CO₂/H₂S corrosion mechanisms in film-free conditions, finally the objective of this Ph.D. study was accomplished with an investigation of CO₂/H₂S corrosion in film forming conditions (Chapter 7).

In each of the four above mentioned chapters, a similar format was used in laying out the subject matter in order to help readers to better understand of the material presented in this study.

- **Introduction.** Every section starts with a subsection that briefly describes the background information.
- **Physico-chemical model.** The qualitative description of the physico-chemical processes is presented in the next subsection .
- **Mathematical model.** Once the basic concepts are grasped, they were transformed into equations, which is shown in the subsequent subsection.
- **Numerical techniques.** The next subsection discusses means of solving these equations.
- **Verification and parametric study.** Once any of the models was completed, it required *verification* in order to display how the model predictions compared with results of experimental laboratory studies. Once the validity of the model was demonstrated, the *parametric study* was performed to help gain the insight into the effect of various parameters and the complex interplay at work.
- **Summary.** Each chapter finishes with a discussion that summarizes the accomplishment and points toward the the next step.

CHAPTER 4: MECHANISTIC MODELING OF CO₂ CORROSION IN FILM-FREE CONDITIONS

4.1 Introduction

In order to model the phenomena of CO₂ corrosion in film-free conditions, one needs to understand the mechanisms of CO₂ corrosion, which is qualitatively described in the following subsection on the *physico-chemical model*. All the important processes underlying CO₂ corrosion such as: the electrochemical and chemical reactions, the transport processes within the boundary layer and porous films, are discussed in detail.

4.2 Physico-Chemical Model

Based on the experimental observations and literature research, it is commonly accepted that aqueous CO₂ corrosion of carbon steel is an electrochemical process involving the anodic dissolution of iron and the cathodic reactions. The overall reaction is described as:



This overall reaction can be broken down into several major chemical and electrochemical reactions.

4.2.1 Chemical Reactions

The main chemical reactions occurring in the bulk of the solution include CO₂ dissolution and hydration to form carbonic acid (H₂CO₃):



Carbonic acid is a weak acid compared to mineral acid since it does not fully dissociate, but partially dissociates in two steps:



In practical CO₂ corrosion situations many other species are present in the water solution. Therefore a large number of additional chemical reactions can occur. The full list of the chemical reactions accounted for in the present version of the model is shown in Table 1.

Table 1. Chemical reactions accounted for in the model and their equilibrium constants. ¹⁵

	Reaction	Equilibrium constant
Dissolution of carbon dioxide	$CO_2(g) \Leftrightarrow CO_2$	$K_{sol} = c_{CO_2} / p_{CO_2}$
Water dissociation	$H_2O \underset{k_{b,wa}}{\overset{k_{f,wa}}{\Leftrightarrow}} H^+ + OH^-$	$K_{wa} = c_{H^+} c_{OH^-}$
Carbon dioxide hydration	$CO_2 + H_2O \underset{k_{b,hy}}{\overset{k_{f,hy}}{\Leftrightarrow}} H_2CO_3$	$K_{hy} = c_{H_2CO_3} / c_{CO_2}$
Carbonic acid dissociation	$H_2CO_3 \underset{k_{b,ca}}{\overset{k_{f,ca}}{\Leftrightarrow}} H^+ + HCO_3^-$	$K_{ca} = c_{H^+} c_{HCO_3^-} / c_{H_2CO_3}$
Bicarbonate anion dissociation	$HCO_3^- \underset{k_{b,bi}}{\overset{k_{f,bi}}{\Leftrightarrow}} H^+ + CO_3^{2-}$	$K_{bi} = c_{H^+} c_{CO_3^{2-}} / c_{HCO_3^-}$

Table 1 continued

Dissolution of hydrogen sulphide	$H_2S(g) \rightleftharpoons H_2S$	$K_{H_2S,sol} = c_{H_2S} / p_{H_2S}$
Hydrogen sulphide dissociation	$H_2S \underset{k_{b,H_2S}}{\overset{k_{f,H_2S}}{\rightleftharpoons}} H^+ + HS^-$	$K_{H_2S} = c_{H^+} c_{HS^-} / c_{H_2S}$
Hydrogen sulphide anion dissociation	$HS^- \underset{k_{b,HS^-}}{\overset{k_{f,HS^-}}{\rightleftharpoons}} H^+ + S^{2-}$	$K_{H_2S} = c_{H^+} c_{S^{2-}} / c_{HS^-}$
Acetic acid dissociation	$HAc \underset{k_{b,ac}}{\overset{k_{f,ac}}{\rightleftharpoons}} H^+ + Ac^-$	$K_{HAc} = c_{H^+} c_{Ac^-} / c_{HAc}$
Hydrogen sulphate anion dissociation	$HSO_4^- \underset{k_{b,HSO_4^-}}{\overset{k_{f,HSO_4^-}}{\rightleftharpoons}} H^+ + SO_4^{2-}$	$K_{HSO_4^-} = c_{H^+} c_{SO_4^{2-}} / c_{HSO_4^-}$

In order to preserve chemical equilibrium in the solution, sometimes chemical reactions are very fast compared to all other processes (such as electrochemical reactions or transport of species) happening at the same time. On the other hand, when the slow chemical reaction of H_2CO_3 hydration (equation 88) lags behind the other processes, local non-equilibrium can be created in the solution. In both case, chemical reactions can change the rate of electrochemical processes at the surface and hence the corrosion rate.

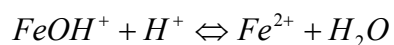
4.2.2 Electrochemical reactions at the steel surface

Anodic Reaction

The anodic dissolution of iron in a water solution is the dominant anodic reaction in CO_2 corrosion:

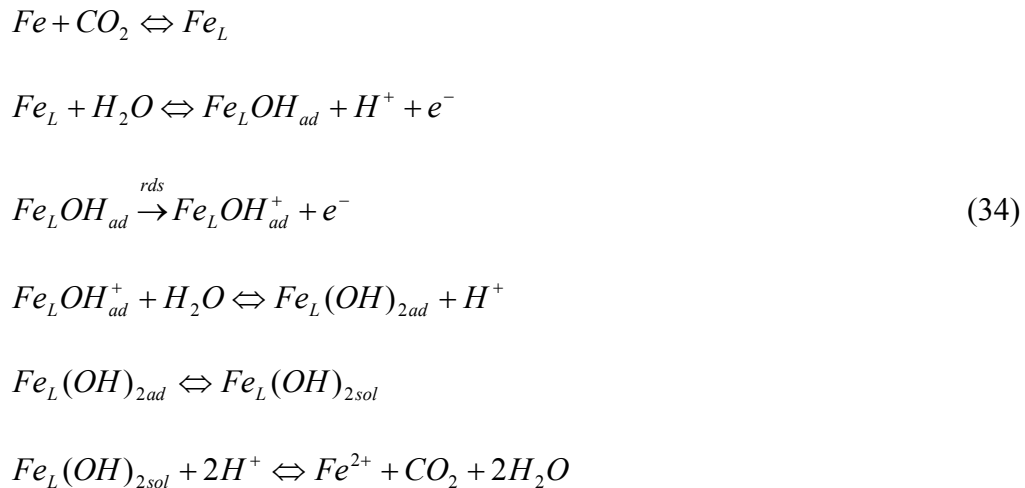


In order to elucidate diverse experimental findings, Bockris, Drazic and Despic (BDD)⁷⁹ proposed the multi-step mechanism for iron dissolution in strong acid:



A reaction order with respect to OH^{-} equal to one is described in this well-known mechanism and it has been regularly taken for granted in CO_2 solutions application. However, most abusers overlooked the fact that this mechanism is only valid below pH 4, while CO_2 corrosion usually occurs between pH 4 and pH 7.

On the other hand, Nescic et al.⁸⁸ have reported that the presence of CO₂ does indeed affect the anodic dissolution of iron, as the kinetics of iron dissolution in CO₂ solutions was found to be different from that of strong acid solutions. In CO₂ saturated solutions, it was proposed that the Chemical ligand Fe_L=Fe-CO₂ is formed as an adsorbed species at the metal surface and catalyzing the dissolution of iron. In order to explain various experimental findings at pH>5, the following detailed multi-step mechanism was proposed:



Cathodic Reaction

It is believed that the presence of CO₂ increases the rate of corrosion of mild steel in aqueous solutions by increasing the rate of the hydrogen evolution reaction. The presence of H₂CO₃ enables hydrogen evolution at a high rate even at pH > 5. Hence the presence of CO₂ leads to a higher corrosion rate than what would be found in a solution of a strong acid at the given pH. It is not conclusive whether H₂CO₃ serves as an additional reservoir of H⁺ ions⁵ or that H₂CO₃ is directly electrochemically reduced.^{1,44,89}

Many have assumed that these two reactions are independent and the net cathodic current is the sum of the currents from these two electrochemical cathodic reactions⁴⁴:



Schmitt and Rothman⁸⁰ have observed that the hydration of dissolved CO₂ (equation 88) is the slowest step in the chemical reactions in the bulk of the solution. This rate determining step is responsible for the slow replenishment of H₂CO₃ and thus explains the fact that the limiting current for hydrogen evolution in saturated aqueous CO₂ solution is only slightly affected by the flow velocity, and even less flow dependence at the higher pH.

At lower potentials the direct reduction of water becomes significant, especially at pH>5 and very low partial pressures of CO₂.^{13,90}



Having briefly described the CO₂ corrosion mechanism above, it comes as no surprise that various environmental factors such as temperature, pH, CO₂ partial pressure, and flow etc., affect the uniform CO₂ corrosion rate of mild steel.

4.2.3 Transport processes

According to electrochemical processes, species such as Fe²⁺ will be produced in the solution at the metal surface while others such as H⁺ will be depleted at the metal surface. Therefore concentration gradients will be established, which results in molecular diffusion of the species towards and away from the surface. The change in species concentration at the metal surface will be small when the diffusion processes are much

faster than the electrochemical processes. However, when the rate of the diffusion process is slower than that of the electrochemical reactions, the concentration of species at the metal surface can become very different from the ones in the bulk solution. Moreover, the rate of the electrochemical processes depends on the species concentrations at the surface. Therefore a mutual coupling exists between the electrochemical processes at the metal surface (due to corrosion) and processes in the adjacent solution layer (due to diffusion in the boundary layer). Similarly, chemical reactions also interact with both the transport and electrochemical processes in a complex way as described below.

The conduction of ionic species in an electrolyte has been well treated in the literature for electrochemical systems such as electrolysis. In these situations an applied potential aids in the movement of the charged species. This produces potential gradients, and hence, an electric current in the solution. In the corrosion system there are no applied potential gradients (other than in experiments when corrosion rate is measured by electrochemical means). However, a potential gradient may still exist in spontaneous corrosion. This is considered to be due to differences in diffusion coefficients allowing species to flux at different rates. As ionic species try to assert their independence from one another, electrostatic attraction between the particles produces an electric field which couples all the charged species in solution. The potential gradient acts to slow down the faster moving species and speed up the slower in an effort to minimize any charge separation, and hence maintain an electroneutral solution. However, it has been proven by Nescic et al.¹⁵ that the contribution of electromigration to the overall flux of species is small and can be neglected in spontaneous corrosion.

The effect of convection on transport processes cannot be ignored because the water solution moves with respect to the metal surface in most practical systems. Time-averaged convection is parallel to the surface and does not contribute much to the transport of species near solid surfaces and in the boundary layer. However, transient turbulent eddies can penetrate deep into the boundary layer and significantly alter the rate of species transport to and from the surface. There is no turbulence very close to the surface and the species are transported only by diffusion.

4.3 Mathematical model

A mathematical model is described below which covers all of the above processes:

- Homogenous chemical reactions in the bulk of a water solution;
- Electrochemical reactions at the steel surface;
- Transport of species to and from the bulk, including convection and diffusion through the boundary layer and the porous films as well as migration due to establishment of potential gradients;

Fundamental physico-chemical laws and resulting equations are applied in order to mathematically model these processes. Parameters for the different equations, such as equilibrium constants, reaction rate constants and diffusion coefficients, are obtained from the open literature.

4.3.1 Chemical reactions

A variety of homogeneous chemical reactions accompanies the CO₂ corrosion process and it is regarded as local sources or sinks of species in the solution. By affecting the surface concentrations of species, chemical reactions can significantly alter the rate of electrochemical processes at the steel surface and the rate of corrosion.

Assuming ideal dilute solutions, the rate of a homogeneous chemical reaction (shown in Table 2) can be conveniently expressed as:

$$R_j = k_f \prod_{r=1}^{n_r} c_r - k_b \prod_{p=1}^{n_p} c_p \quad (38)$$

where k_f and k_b are the forward and backward reaction rate constants while c_r and c_p are the concentrations of reactants and products involved.

In order to explain the calculation of the rates of homogenous chemical reactions in detail, the first and second dissociation steps of carbonic acid will be used as an example:



The net rate of change of carbonic acid concentration due to the first dissociation step - reaction (39) is:

$$R_{H_2CO_3} = -\left(k_{f,ca}c_{H_2CO_3} - k_{b,ca}c_{H^+}c_{HCO_3^-}\right) \quad (41)$$

where $k_{f,ca}$ and $k_{b,ca}$ are the forward and backward reaction rate constants and $c_{H_2CO_3}$, c_{H^+} and $c_{HCO_3^-}$ are the concentrations of species involved. According to the law of

mass conservation, the net rates of change of H^+ and HCO_3^- species concentrations, due to the first dissociation step - reaction (39), are given by:

$$R_{H^+} = R_{HCO_3^-} = -R_{H_2CO_3} \quad (42)$$

The net rates of change R_j of the concentrations of the three species: H^+ , HCO_3^- , and CO_3^{2-} involved in the second dissociation step - reaction (40), can be described similarly.

All the chemical reaction terms can be conveniently grouped by using a matrix form as:¹⁵

$$\begin{bmatrix} R_{H_2CO_3} \\ R_{H^+} \\ R_{HCO_3^-} \\ R_{CO_3^{2-}} \end{bmatrix} = \begin{bmatrix} -1 & 0 \\ 1 & 1 \\ 1 & -1 \\ 0 & 1 \end{bmatrix} \begin{bmatrix} \left(k_{f,ca} c_{H_2CO_3} - k_{b,ca} c_{H^+} c_{HCO_3^-} \right) \\ \left(k_{f,bi} c_{HCO_3^-} - k_{b,bi} c_{H^+} c_{CO_3^{2-}} \right) \end{bmatrix} \quad (43)$$

For any set of k chemical reactions involving j species one can write in a compact form:

$$R_j = a_{jk} r_k \quad (44)$$

The subscripts a_{jk} is the stoichiometric matrix using a tensor notation where row j represents the j -th species, column k represents the k -th chemical reaction, and r_k is the reaction rate vector. This technique results in a flexible framework that enables any number of homogenous chemical reactions to be implemented to the model without difficulty. All the net rates of change R_j are equal to zero at equilibrium. However, unlike other models, this chemical reaction model does not prescribe whether any particular reaction will be locally or globally in equilibrium in advance. When the homogenous chemical reaction rates k_f and k_b for a particular reaction are very large, the net reaction term R_j will be much larger than the other terms in transport equations below

(47), which means that the concentrations of the species involved will be at equilibrium irrespective of other processes. On the other hand, in the case of slow chemical reactions (such as CO₂ hydration reaction 88) the concentrations of species involved will be strongly influenced by other terms (such as diffusion or migration) in transport equations (47) resulting in a non-equilibrium concentration field. The equilibrium, forward and backward reaction rates coefficients for reactions included in the current model, defined in Table 1, are listed in Table 2.

Table 2. Equilibrium (K), forward (k_f) and backward (k_b) reaction rate coefficients (note: $K = k_f/k_b$).¹⁵

Constant	Source
$K_{sol} = \frac{14.5}{1.00258} \times 10^{-(2.27+5.65 \times 10^{-3} T_f - 8.06 \times 10^{-6} T_f^2 + 0.075 I)}$ molar/bar	Oddo and Tomson ⁹¹
$K_{H_2S,sol} = 10^{-0.71742672 - 0.012145427 \cdot T_C + 5.6659982 \times 10^{-5} \cdot T_C^2 - 8.1902716 \times 10^{-8} \cdot T_C^3}$ molar/bar	IUPAC data ⁹²
$K_{wa} = 10^{-(29,3868 - 0.0737549 \cdot T_K + 7.47881 \times 10^{-5} \times T_K^2)}$ molar ²	Kharaka et al. ⁹⁴
$k_{b,wa} = 7.85 \cdot 10^{10} \quad M^{-1} s^{-1}$	Delahay ⁹⁰
$K_{hy} = 2.58 \times 10^{-3}$	Palmer and van Eldik ⁹⁵
$k_{f,hy} = 10^{\frac{329.85 - 110.541 \cdot \log T_K - 17265.4}{T_K}}$ s ⁻¹	Palmer and van Eldik ⁹⁵
$K_{ca} = 387.6 \cdot 10^{-(6.41 - 1.594 \times 10^{-3} T_f + 8.52 \times 10^{-6} T_f^2 - 3.07 \times 10^{-5} p - 0.4772 I^{1/2} + 0.1180 I)}$ molar	Oddo and Tomson ⁹¹
$k_{f,ca} = 10^{5.71 + 0.0526 \times T_C - 2.94 \times 10^{-4} \times T_C^2 + 7.91 \times 10^{-7} \times T_C^3}$ s ⁻¹	Comprehensive Chemical Kinetics ⁹⁶
$K_{bi} = 10^{-(10.61 - 4.97 \times 10^{-3} T_f + 1.331 \times 10^{-5} T_f^2 - 2.624 \times 10^{-5} p - 1.166 I^{1/2} + 0.3466 I)}$ molar	Oddo and Tomson ⁹¹
$k_{f,bi} = 10^9 \text{ s}^{-1}$	estimated

Table 2 continued

$K_{H_2S} = 10^{-(15.345-0.045676 \times T_K + 5.9666 \times 10^{-5} \times T_K^2)}$	<i>molar</i>	Kharaka et al. ⁹⁴
$k_{f,H_2S} = 10^4 \text{ s}^{-1}$		estimated
$K_{HS^-} = 10^{-(23.93-0.030446 \times T_K + 2.4831 \times 10^{-5} \times T_K^2)}$	<i>molar</i>	Kharaka et al. ⁹⁴
$k_{f,HS^-} = 1 \text{ s}^{-1}$		estimated
$K_{HAc} = 10^{-(6.66104-0.0134916 \times T_K + 2.37856 \times 10^{-5} \times T_K^2)}$	<i>molar</i>	Kharaka et al. ⁹⁴
$k_{f,HAc} = 3.2 \cdot 10^5 \text{ s}^{-1}$		Vetter ¹⁴⁴
$K_{HSO_4^-} = 10^{1.54883-0.00998 \times T_K - 5.9254 \times 10^{-6} \times T_K^2}$	<i>molar</i>	Kharaka et al. ⁹⁴
$k_{f,HSO_4^-} = 1 \text{ s}^{-1}$		estimated

Note: in the table above T_f is temperature in degrees Fahrenheit, T is absolute temperature in Kelvin, T_c is temperature in degrees Celsius, I is ionic strength in molar and p is the pressure in psi.

4.3.2 Electrochemical reactions at the steel surface

It is reported¹⁵ that the electrical potential of the surface, the surface concentrations of species involved in those reactions and temperature all affect the rates of the electrochemical reactions at the metal surface. Since exchange of electrons are involved in electrochemical reactions, the reaction rate can be conveniently expressed as a rate at which the electrons are “consumed or released”, that is, in terms of an electrical current density i . Fundamental rate equations of electrochemistry relate i to the potential at the metal surface E , via an exponential relationship:¹⁵

$$i = \pm i_o \cdot 10^{\pm \frac{E-E_{rev}}{b}} \quad (45)$$

where i_o = exchange current density ($A \text{ m}^{-2}$)

E_{rev} = reversible potential (V)

b_c = cathodic Tafel slope (V)

The values of i_o , E_{rev} and b_c are all characteristic for a particular electrochemical reaction and depend on the temperature and the concentration of species involved in the reaction at the metal surface. Some of these parameters are usually not available in the literature and must be obtained from the experimental study. The calculation of these parameters is summarized in Table 3. Equation (77) can be written down for each of the electrochemical reactions involved in a corrosion process such as (77, 35, 36 and 37). The + sign applies for anodic reactions such as (77) while the – sign applies for cathodic reactions such as (35-37).

Since the electrical potential E at the metal surface is unknown for a spontaneous corrosion process, the charge balance equation at the metal surface can be applied to obtain E :¹⁵

$$\sum_1^{n_a} i_a = \sum_1^{n_c} i_c \quad (46)$$

where n_a and n_c are the total number of anodic and cathodic reactions respectively. On the other hand, the potential E is a known value in situations where external polarisation is applied (e.g. potentiodynamic experiments, cathodic protection or in electrochemical reactors).

Table 3. Electrochemical parameters for the reactions included in the model which fit the general rate equation (18), where the

exchange current density is¹⁵: $i_o = i_{oref} \left(\frac{c_{H^+}}{c_{H^+ref}} \right)^{a_1} \left(\frac{c_{CO_2}}{c_{CO_2ref}} \right)^{a_2} \left(\frac{c_{H_2CO_3}}{c_{H_2CO_3ref}} \right)^{a_3} \cdot e^{\frac{-\Delta H}{R} \left(\frac{1}{T} - \frac{1}{T_{ref}} \right)}$

	i_{oref}	a_1	c_{H^+ref}	a_2	c_{CO_2ref}	a_3	$c_{H_2CO_3ref}$	ΔH	T_{ref}	E_{rev}	b
	$\frac{A}{m^2}$		molar		molar		molar	$\frac{kJ}{mol}$	$^{\circ}C$	V	V
$2H^+ + 2e^- \rightarrow H_2$	0.05	0.5	10^{-4}	0	N/A	0	N/A	30	25	$-\frac{2.3RT}{F} pH$	$\frac{2.3RT}{2F}$
$2H_2CO_3 + 2e^- \rightarrow H_2 + 2HCO_3^-$	0.06	-0.5	10^{-5}	0	N/A	1	10^{-4}	50	20	$-\frac{2.3RT}{F} pH$	$\frac{2.3RT}{2F}$
$Fe \rightarrow Fe^{2+} + 2e^-$	1	1 for $p_{CO_2} < 1bar$ 0 for $p_{CO_2} \geq 1bar$	10^{-4}	2 for pH<4 1 for 4<pH<5 0 for pH>5	0.0366	0	N/A	37.5	25	-0.488	0.03 for pH<4 0.08 for 4<pH<5 0.12 for pH>5

Note: ΔH is activation energy and T_{ref} is the reference temperature. Data and mechanisms were taken from reference¹³ for the

cathodic reaction and the reference¹⁵ for the anodic reaction.

4.3.3 Transport processes

With appropriate boundary conditions, the corrosion process is modeled by using the transient species conservation equation. A one-dimensional species transport domain is adequate to describe uniform corrosion process:

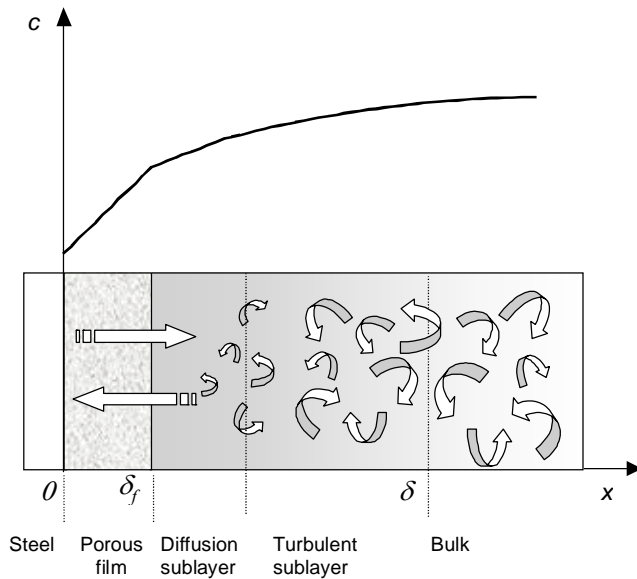


Figure 10 Sketch of the computational domain and the control volume used for discretization of the computational domain.¹⁵

The domain stretches from the steel surface through the pores of a corrosion product film and the mass transfer boundary layer and eventually ends in the turbulent bulk of the solution. It is assumed that the transport of species on the bulk side of the boundary layer is dominated by turbulent mixing because the flow field is turbulent in the bulk solution. Whereas the transport of species in the sublayer closer to the surface and in the pores of the surface film is governed by means of molecular diffusion. Different rates of transport are observed in these three regions, fast in the turbulent boundary layer,

intermediate in the molecular diffusion dominated boundary layer and slow in the porous film.

Irrespective of whether the species are involved in the electrochemical reactions at the metal surface or in the chemical reactions, the concentration of each and every species is governed by a species conservation equation. A universal one-dimensional form of the equation which describes transport for species j in the presence of chemical reactions, (valid both for the liquid boundary layer¹⁰¹ and the porous film¹⁰²) is: ¹⁵

$$\underbrace{\frac{\partial(\varepsilon c_j)}{\partial t}}_{\text{accumulation}} = \underbrace{\frac{\partial}{\partial x} \left(\varepsilon^{1.5} D_j^{eff} \frac{\partial c_j}{\partial x} \right)}_{\text{net flux}} + \underbrace{\varepsilon R_j}_{\substack{\text{source or sink} \\ \text{due to chemical reactions}}} \quad (47)$$

where c_j = concentration of species j (kmol m^{-3})

ε = porosity of the film (equal to one outside the film – in the boundary layer)

t = time (s)

x = spatial coordinate (m)

D_j^{eff} = effective diffusivity coefficient = ($D_j^m + D_j^t$)

D_j^m = molecular diffusivity coefficient ($\text{m}^2 \text{s}^{-1}$)

D_j^t = turbulent diffusivity coefficient ($\text{m}^2 \text{s}^{-1}$)

R_j = the source or sink of species j due to chemical reactions ($\text{kmol m}^{-3} \text{s}^{-1}$)

Transport by molecular diffusion is well known, and its implementation into the model is straightforward. The only physical constants required are the diffusion coefficients for the various species in solution and these are readily available in the

literature. A full list of species included in the present version of the model, along with their diffusion coefficients, is displayed in Table 4.

Currently the convection effect is modeled by using “turbulent diffusivity” term¹⁰³ via empirical relationships which are modeled similar to molecular diffusion. This approach is not uncommon. It allows the molecular diffusion and turbulent diffusion to be lumped together as an effective diffusion. Making this approximation greatly reduces the computational effort and provides an adequate alternative to modeling the convective component of the flux until more comprehensive models can be added. The turbulent diffusion coefficient D_t , is a function of the distance from the metal or film surface and is given by¹⁰³:

$$D_t = \begin{cases} 0 & \text{for } x < \delta_f \\ 0.18 \left(\frac{x - \delta_f}{\delta - \delta_f} \right)^3 \frac{\mu}{\rho} & \text{for } x > \delta_f \end{cases} \quad (48)$$

It is assumed that there is no fluid flow within the porous film (for $x < \delta_f$). The liquid boundary layer thickness is typically a function of the Reynolds number. For pipe flow it reads¹⁰³:

$$\delta - \delta_f = 25Re^{-7/8}d \quad (49)$$

where d is the hydraulic diameter, $Re = \rho U d / \mu$ is the Reynolds number, U is bulk velocity, ρ is the density, and μ is dynamic viscosity. The density and viscosity are modeled as a function of temperature as shown in Table 5.

Table 4. Species accounted for in the present version of the model and the corresponding reference molecular diffusion coefficient.¹⁵

Species	Diffusion coefficient (m ² /s)	Source
CO ₂	1.96 · 10 ⁻⁹	Perry ⁹⁷
H ₂ CO ₃	2.00 · 10 ⁻⁹	Kvarekvål ⁹⁸
HCO ₃ ⁻	1.105 · 10 ⁻⁹	Newman ¹⁰¹
CO ₃ ²⁻	0.92 · 10 ⁻⁹	Kvarekvål ⁹⁸
H ⁺	9.312 · 10 ⁻⁹	Newman ¹⁰¹
OH ⁻	5.26 · 10 ⁻⁹	Newman ¹⁰¹
Fe ²⁺	0.72 · 10 ⁻⁹	Kvarekvål ⁹⁸
Cl ⁻	2.032 · 10 ⁻⁹	Newman ¹⁰¹
Na ⁺	1.334 · 10 ⁻⁹	Newman ¹⁰¹
Ca ²⁺	0.792 · 10 ⁻⁹	Newman ¹⁰¹
Ba ²⁺	0.847 · 10 ⁻⁹	Newman ¹⁰¹
Sr ²⁺	0.791 · 10 ⁻⁹	Newman ¹⁰¹
HAc	1.24 · 10 ⁻⁹	Perry ⁹⁷
Ac ⁻	1.089 · 10 ⁻⁹	Newman ¹⁰¹
H ₂ S	1.61 · 10 ⁻⁹	Perry ⁹⁷
HS ⁻	2.00 · 10 ⁻⁹	estimated
S ²⁻	2.00 · 10 ⁻⁹	estimated
HSO ₄ ⁻	1.33 · 10 ⁻⁹	Newman ¹⁰¹
SO ₄ ²⁻	1.065 · 10 ⁻⁹	Newman ¹⁰¹

Table 5. Liquid properties as a function of temperature (source: CRC Handbook of Chemistry and Physics⁹⁹).

Dynamic viscosity	$\mu = 0.001002 \cdot 10^{\frac{1.3277(293.15-T) - 0.001053(298.15-T)^2}{T-168.15}}$	kg/ms
Density	$\rho = (753.596 + 1.87748 \cdot T - 0.003564 \cdot T^2)$	kg/m ³
Dielectric constant	$\xi = \frac{10^{-9}}{36\pi} \times (249.21 - 0.79069 \times T + 0.00072997 \times T^2)$	
Diffusion coefficient (subscript <i>ref</i> denotes reference values, see Table 4)	$D_i = D_{ref} \frac{T}{T_{ref}} \frac{\mu_{ref}}{\mu}$	

4.3.4 Initial and boundary conditions

The boundary conditions essentially define the corrosion process. The modelling of the species transport equation has been undertaken in numerous studies of electrochemical systems, but its application to the corrosion situation has been limited. Therefore, extensive use has been made of the electrochemical literature in completing the corrosion code to date. The difference between the two situations arises in the boundary conditions, mainly in the fact that no potential, or current, is applied to the corrosion system. Electrochemical reactions are still occurring on the corrosion surface, yet they are self-sustaining. The initial conditions for the concentration profiles are considered to be bulk concentrations which are calculated from a prior equilibrium calculation.

The corrosion system also adds to the complexity in that the corrosion surface is changing in time, in terms of its physical location (it corrodes i.e. "disappears"), as well as in terms of rates of the anodic or cathodic conditions.

At the metal surface zero flux $N_j = 0$ is specified for the species not involved in electrochemical equation. For species j involved in an electrochemical reactions at the metal surface, the flux at the metal surface can be determined from:¹⁵

$$N_j = -\frac{i_j}{n_j F} \quad (50)$$

In order to obtain the partial current i_j for a given species from equation (77), the corrosion potential E must be obtained beforehand by applying the charge balance equation at the metal surface (46); n_j is the number of moles of electrons exchanged per

mol of species j participating in a particular electrochemical reaction. (e.g. $n_{H^+} = 1 \text{ mol}_e / \text{mol}_{H^+}$ for reaction (35)); F is the Faraday's constant.

4.4 Numerical Techniques

One equation (47) is written for each species in the solution. The resulting set of equations is solved simultaneously in space and time. The boundary conditions for this set of partial differential equations are:

- at the steel surface: flux of species obtained from the rate of the electrochemical reactions according to equation (50)
- In the bulk: equilibrium concentrations of species as obtained by solving the set of equilibria listed in Table 1. Assuming that all species are thoroughly mixed by turbulence.

Once the set of equations is solved for any given time step, the corrosion rate, CR, can be simply calculated as the flux of Fe^{2+} ions at the metal surface (reaction (77)) by using equation (50).

In this model, there are n equations for n species in the solution because there is a transport equation (47) for each species. Since all the equations are strongly and nonlinearly coupled through the chemical reaction, all these equations must be solved simultaneously together with the boundary conditions including the nonlinear surface charge balance equation (46).

The differential transport equations (47) were discretized using a finite difference method and a non-uniform grid as sketched in Figure 11.¹⁵

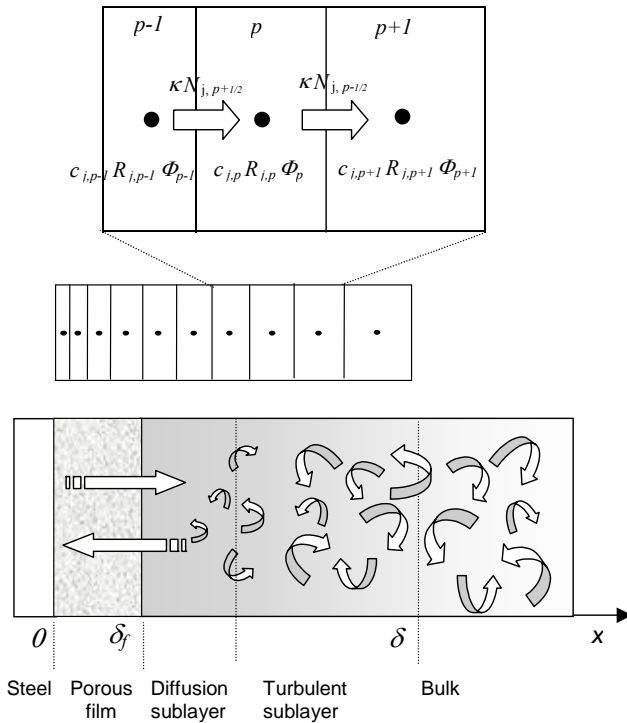


Figure 11. Sketch of the computational grid and the control volumes used for discretization of the computational domain. The concentrations, the potential and the chemical reaction terms are all computed in the centre of the control volume while the fluxes are computed on the interfaces.

The finite difference approximation of the transport equations (47) for species j in control volume p is given by:

$$\varepsilon_p \frac{c_{j,p}^{n+1} - c_{j,p}^n}{\Delta t} \Delta x_p = -\kappa_{p+1/2} N_{j,p+1/2}^{n+1} + \kappa_{-1/2,p} N_{j,p-1/2}^{n+1} + \varepsilon_p R_{j,p}^{n+1} \Delta x_p \quad (51)$$

Superscripts $n+1$ and n denote new and old points in time, respectively, Δx_p is the size of the control volume p . All the terms are calculated in the center of the control volumes except the fluxes which are evaluated at the control volume boundaries (see Figure 11). In order to avoid instability, a fully implicit time discretization scheme is used in which all the variables on the right hand side of equation (51) are taken at the new

time $n+1$. When there is an sudden change at the interface between the fluid and the film, most interpolation schemes would lead to large numerical errors, therefore a conservative harmonic averaging is used to calculate these fluxes based on values of the variables at the nodal points $p-1$, p and $p+1$ on both side of the boundaries. On the other hand, all the nonlinear terms such as the fluxes, the chemical reaction rate terms and all the terms in the surface charge balance equation are spatially linearized by applying Taylor series expansion around the known solution and by keeping only the constant and the linear term. As an illustration, the chemical reaction terms can be linearized as:

$$R_{j,p}^{n+1} = a_{jk} r_k^{n+1} = a_{jk} \left(r_k^{n'} + \frac{\partial r_k^{n'}}{\partial c_j} (c_{j,p}^{n+1} - c_{j,p}^{n'}) \right) \quad (52)$$

where superscript n' denotes the known solution. The implicit boundary condition for the electrochemical reactions has been implemented by the author to improve the stability of the model. Since the current term in boundary condition at the metal surface is a function of both potential and the concentration of involved species, the current term can be linearized as:

$$i_i^{n+1} = i_i^n + \sum_{j=1}^n \frac{\partial i_i^{n'}}{\partial c_j} (c_j^{n+1} - c_j^{n'}) + \frac{\partial i_i^{n'}}{\partial E} (E^{n+1} - E^{n'}) \quad (53)$$

The discretization procedure described above converts the set of nonlinear partial differential equations for species transport (47) into a set of linear equations in the form $Ax = b$. The matrix A is block tri-diagonal and a LU solver¹⁰⁴ Is applied to solve these equations.

In order to increase the speed of the lengthy calculations, Fortran programming language was used in the model. On the other hand, Microsoft Excel/Visual Basic was

used for the user interface in order to take advantage of the user-friendly features of this package including input/output dialogs and plotting capabilities.

4.5 Verification and parametric study

The film-free CO₂ corrosion model is verified by comparing the predictions with the large experimental database from CO₂ corrosion and multiphase flow at Ohio University. One needs to bear in mind that all the experiments shown in this section were conducted in film free conditions. The ability of the model to capture fundamental behavior of the CO₂ corrosion process in the absence of iron carbonate films is shown in the comparisons below.

While direct comparisons with experiments will be made in this section, the effect of different environmental parameters on CO₂ corrosion is discussed and the performance of the model will be contrasted against the general understanding of the CO₂ corrosion process in the absence of iron carbonate films.

4.5.1 The effect of pH

It was proven previously both experimentally and computationally¹⁵ that pH has a strong influence on the corrosion rate. Typical pH in pure/condensed water is less or equal to pH 4. Whereas it is usually within the range of $5 < \text{pH} < 7$ in buffered brines. As previously discussed in the section of *Physico-chemical* model, direct reduction of H⁺ ions (reaction (35)) is important at pH 4 or below, especially at lower partial pressure of CO₂. As indicated in Figure 12, pH has a direct effect on the corrosion rate.

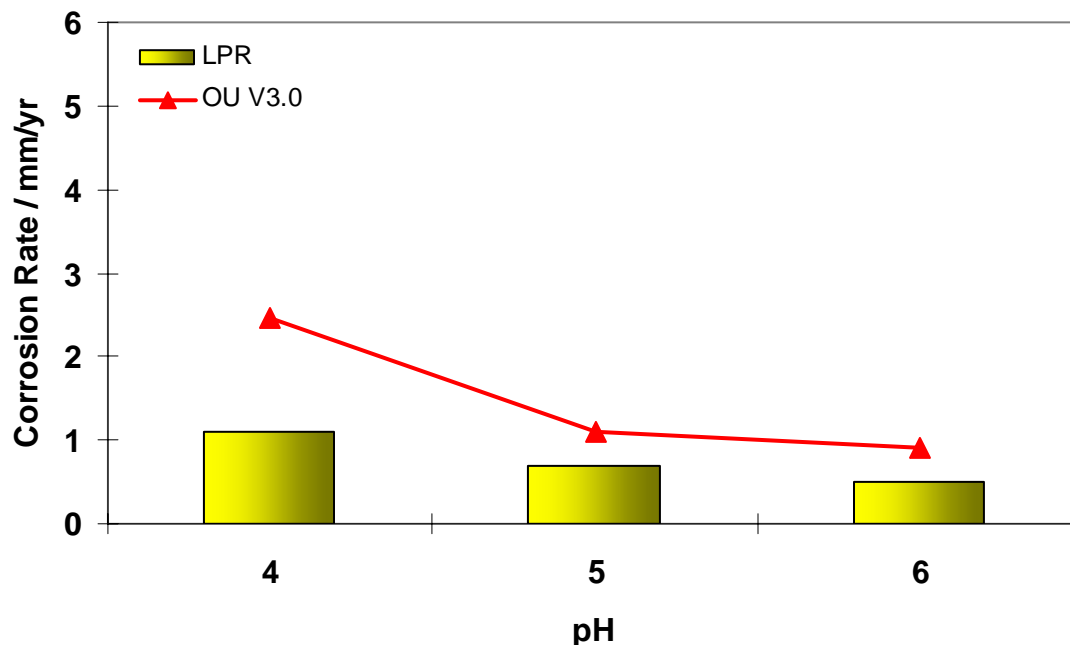


Figure 12. Predicted and experimentally measured corrosion rates showing the effect of pH in the absence of iron carbonate films. Test conditions: 20°C, $P_{CO_2} = 1$ bar, 1 m/s, $c_{Fe^{2+}} < 2$ ppm. Model of Nescic et al.¹⁰⁵ was used. Experimental data taken from Nescic et al.¹⁰⁶

4.5.2 The effect CO_2 partial pressure

Figure 13 illustrates that, in the case of film-free CO_2 corrosion, an increase of CO_2 partial pressure (P_{CO_2}) typically leads to an increase in the corrosion rate because the concentration of H_2CO_3 increases with P_{CO_2} , which leads to the acceleration of the cathodic direction carbonic acid reduction (reaction (36)), and ultimately results in the increase of the corrosion rate.

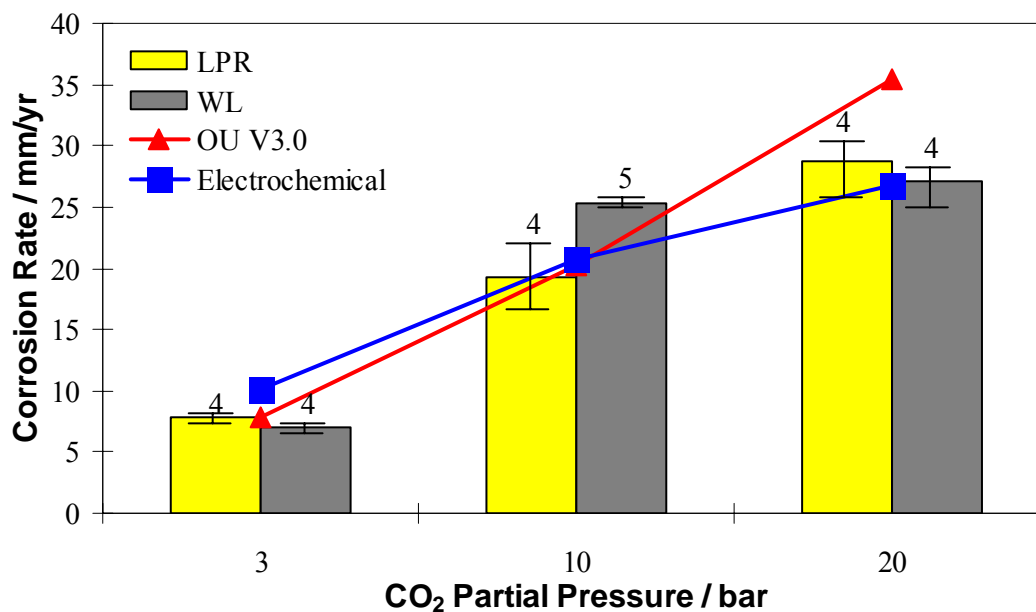


Figure 13. Predicted and experimentally measured corrosion rates showing the effect of CO₂ partial pressure P_{CO_2} . Test conditions: 60°C, pH5, 1 m/s. Data taken from Wang et al.¹⁰⁷ Corrosion rates were measured both by linear polarization resistance (LPR) and weight loss (WL). Error bars denote maximum and minimum values and the figure above the bars is the number of repeated experiments. OU V 3.0 is the model of Nesic et al.¹⁰⁵, Electrochemical is the model of George et al.¹⁰⁸

4.5.3 The effect of temperature

In the case at low pH when precipitation of iron carbonate or other protective films does not occur, temperature accelerates the kinetics of all the processes involved in corrosion: electrochemical, chemical, transport, etc. Hence the corrosion rate also increases with temperature in film free conditions as indicated in Figure 14.

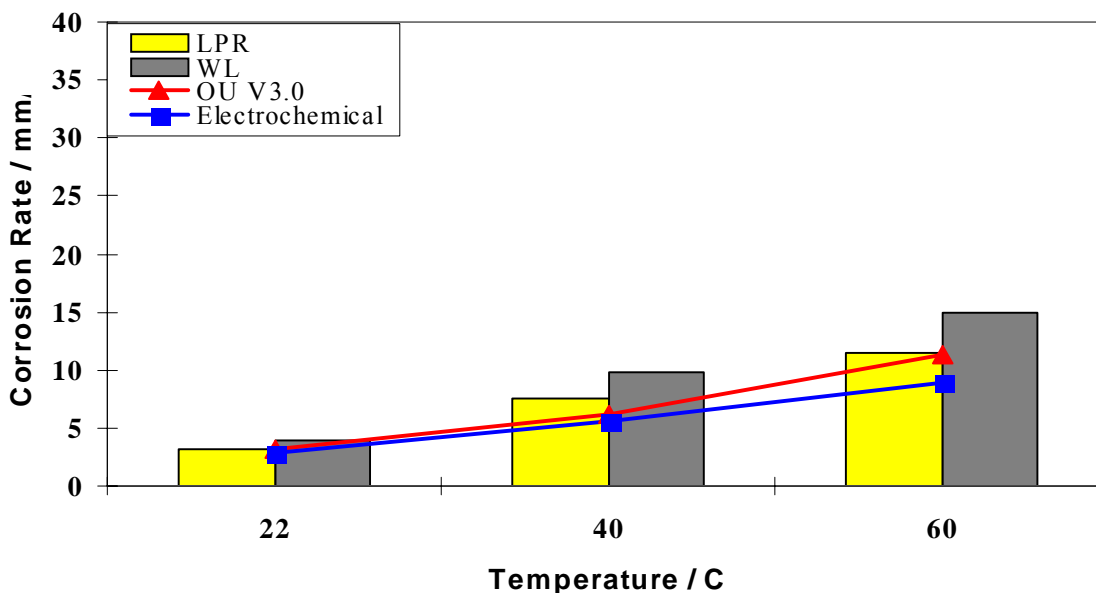


Figure 14. Predicted and experimentally measured corrosion rates showing the effect of temperature. Test conditions: pH4, $P_{CO_2} = 1$ bar, $c_{Fe^{2+}} < 5$ ppm, 100 ppm acetic species ($HAc + Ac^-$) $v=0.5$ m/s. Data taken from Wang et al.¹⁰⁷ Corrosion rates were measured both by linear polarization resistance (LPR) and weight loss (WL). OU V 3.0 is the model of Nesic et al.¹⁰⁵, Electrochemical is the model of George et al.¹⁰⁸

4.5.4 The Effect of Flow

In film free conditions, transport of species towards and away from the metal surface is enhanced by the turbulent flow, which results in an increase in the corrosion rate as shown in Figure 15.

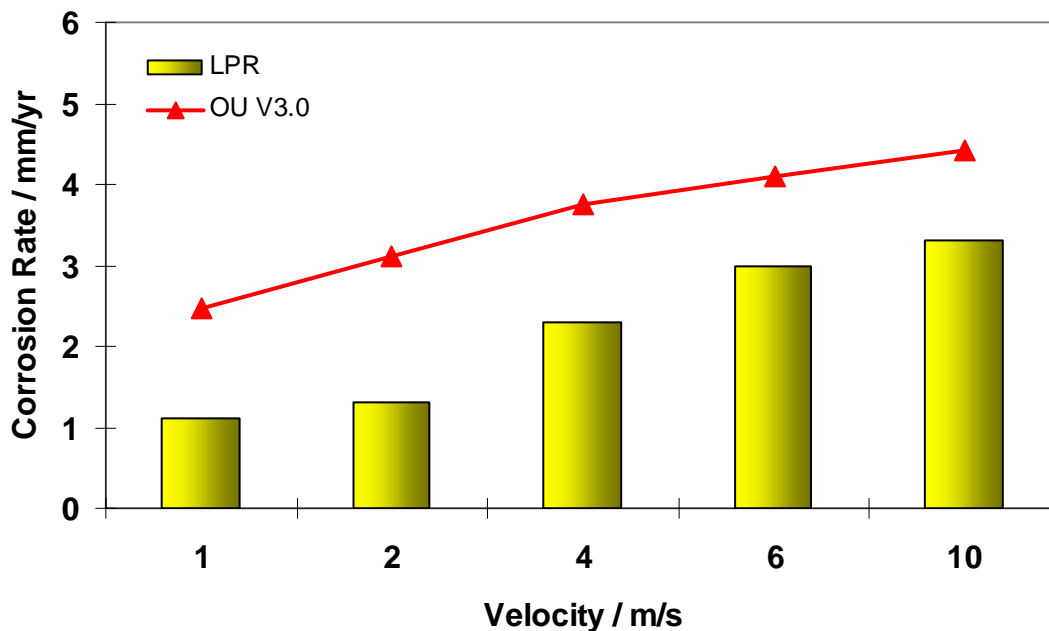


Figure 15. Predicted and experimentally measured corrosion rates showing the effect of velocity in the absence of iron carbonate films. Test conditions: 20°C, $P_{CO_2} = 1$ bar, $c_{Fe^{2+}} < 2$ ppm. Model of Nescic et al.¹⁰⁵ was used. Experimental data taken from Nescic et al.¹⁰⁶

4.6 Summary

The film-free CO₂ corrosion mechanistic model covers most of the processes important in uniform CO₂ corrosion in the absence of iron carbonate films: electrochemical reactions at the steel surface, the transport processes within the liquid boundary layer and porous films and homogenous chemical reactions. The majority of the model is mechanistic in nature, fully transparent and based on solid theoretical knowledge. The model simulates the corrosion rate and has the ability to calculate transient species concentration profile near the metal surface, which provides a solid

foundation and will be used as a basis for the future development of the combined CO₂/H₂S corrosion model.

Comparisons with laboratory experiments have revealed the strengths of the model such as its ability to gain the insights of the complex processes taking place during corrosion in the absence of surface films. However, it is recognised that the properties of protective iron carbonate corrosion product films are crucial in predicting the actual corrosion rate in film forming conditions (i.e. higher temperatures and pH).

Hence, the mechanistic modelling of the morphology of the corrosion films and its effect on corrosion became the immediate task which was accomplished by the author, and which will be described in the following chapter.

The foundation has been laid out in this chapter and it should be emphasized that the contributions of the author will be described in detail starting from Chapter 5.

CHAPTER 5: MECHANISTIC MODELING CO₂ CORROSION ACCOMPANIED BY IRON CARBONATE FILM FORMATION

5.1 Introduction

Although the mechanistic model described in chapter 4 offers an insight into the various complex processes occurring in CO₂ corrosion - from a practical point of view it is just another worst-case CO₂ corrosion prediction model. Admittedly, it does go one step further than other similar CO₂ models as it enables prediction of conditions leading to protective film formation, as well as the effect of protective films once they are in place. However, there is a missing link: it cannot predict the kinetics of film growth, neither can it predict the morphology of the growing films. Hence an additional development was needed required to fill this gap, i.e. the mechanistic model of Nescic et al.¹⁵ was used as a basis and extended to cover the iron carbonate film growth process.

5.2 Physico-Chemical Model

In CO₂ corrosion of carbon steel, when the concentrations of Fe²⁺ and CO₃²⁻ ions exceed the solubility limit, they can precipitate to form solid iron carbonate according to:



When iron carbonate precipitates at the steel surface, it can slow down the corrosion process by presenting a diffusion barrier for the species involved in the corrosion process

but also by blocking (covering) a portion of the steel surface and preventing the underlying steel from further dissolution.

Iron carbonate film growth depends primarily on the precipitation rate R_{FeCO_3} . Nucleation of crystalline films is a very difficult process to model mathematically. In addition in many corrosion situations the rate of precipitation is believed to be controlled by the crystal growth rate rather than nucleation rate. As more iron carbonate precipitates the film grows in density as well as thickness. However, the steel surface corrodes under the film, continuously creating a “void” between the film and the steel surface (here called “film undermining”). As soon as it is created the void starts filling by the ongoing precipitation. When the rate of precipitation at the steel surface equals or exceeds the rate of corrosion (film undermining) dense protective films form - sometimes very thin but still protective. Vice versa when the corrosion process undermines the newly formed film faster than precipitation can fill in the voids, a porous and unprotective film forms - which can be sometimes very thick. This phenomenon has been previously quantified through the use of a non-dimensional parameter termed “scaling tendency”⁴⁶:

$$ST = \frac{R_{FeCO_3}}{CR} \quad (55)$$

which describes the relative rates of precipitation and corrosion expressed in the same volumetric units. For $ST \ll 1$ porous and unprotective films are likely to form, and conversely when $ST \geq 1$ conditions become favorable for formation of dense protective iron carbonate films. However, the use of scaling tendency is not as straightforward as it appears. Strictly speaking one needs to compute the scaling tendency at the steel surface

where the films form (surface scaling tendency - *SST*). Therefore one needs information about the solution chemistry at the steel surface which can be very different from the one in the bulk, particularly if some sort of surface film is already in place (e.g. iron carbide, mill scale). Further, the scaling tendency changes with time as the corrosion and precipitation rate change. The model shown below does not explicitly use the concept of scaling tendency even if the physical processes underlying it (precipitation and undermining) are accounted for. The surface and bulk scaling tendencies are computed in the model in order to check their validity as an effective indicator of protective film formation.

Mathematical Model

The proposed equation describing the film growth kinetics is rather simple: it is a mass balance for the solid iron carbonate:

$$\underbrace{\frac{\partial c_{FeCO_3(s)}}{\partial t}}_{\text{local change}} = \underbrace{R_{FeCO_3(s)}}_{\text{precipitation rate}} - \underbrace{CR \frac{\partial c_{FeCO_3(s)}}{\partial x}}_{\text{undermining rate}} \quad (56)$$

expressing the fact that the amount of solid iron carbonate found at any location, $c_{FeCO_3(s)}$ in kmol/m^3 will increase over time because of precipitation and/or will decrease due to the undermining effect.

The last term on the right hand side in equation (56) above needs a clarification. Corrosion of the steel causes the steel surface shown in Figure 10 to move to the left. Within the framework of a fixed grid (in space) this is a moving boundary problem. If the whole domain is to be covered at all times, it appears that the fixed grid needs to be

continuously extended to the left in order to “cover” the voids created by the corrosion process. This is not easy and would require a lot of interpolation and complex bookkeeping. Another simpler option is to assume that the grid is “attached” to the steel surface which is moving to the left with a velocity equal to the corrosion rate CR . The advantage of this option is that in this case one does not have to keep extending the grid. However, in a moving frame of reference it appears as if the whole computational domain shown in Figure 10 moves to right, as corrosion proceeds. In other words, a convective-like term appears in all the transport equations (47) for the species as well as in equation (56) for solid iron carbonate. This term appears to sweep everything away from the steel surface with a velocity CR what has the same effect as the surface of the steel moving in the opposite direction with the same velocity*. Hence the convective-like term on rhs of equation (56) describing the undermining effect.

Another aspect of equation (56) deserves a comment. Physically, precipitation of crystalline films (such as iron carbonate) goes through two phases: nucleation and crystal growth. In most cases when there is a solid steel surface present with all its imperfections being good candidates for nuclei formation, the nucleation phase is over relatively fast and can be disregarded. It can be assumed that the rate of precipitation is controlled by the crystal growth rate. Generally crystals grow from a large number of discrete nuclei into dendritic structures which may or may not join, forming a porous film. A discrete lattice growth modelling approach has been employed in the past to

* The sweeping effect is not very significant for transport of the dissolved species in the solution as the sweeping velocity CR is at least a few orders of magnitude smaller than the diffusional velocity. For example a corrosion rate of the order of 1 mm/y amounts to a sweeping velocity of the order of 1 nm/min. Diffusional velocity for a typical species in the solution is of the order of 1 mm/min.

model the film growth process¹⁰⁹⁻¹¹¹. However, for the purposes of the present model, it would be computationally costly and mathematically difficult to model a three-dimensional discrete film growth process and couple it to the existing one-dimensional transport model for all the other species. It seemed more appropriate to persist with the one-dimensional control volume approach in describing the film growth as expressed by equation (56). In a control volume approach, all properties are assumed to be constant within a control volume and therefore it appears that some detailed information about the film can be lost - smeared over the control volume. This can be avoided by using very fine grids - small control volume sizes of the order of $\Delta x \propto 10^{-7}$ m which is still a few orders of magnitude larger than the length scale of the dendrites. In this way it can be assumed that any averaging of the film properties across such small control volumes will not lead to a significant loss of detailed information. After all, the present model is not aimed at elucidating the fine points of crystalline iron carbonate film growth, but attempts to capture the overall effect these films have on the CO₂ corrosion process.

It is convenient to express the morphology of iron carbonate films via the distribution of volumetric porosity ε since it is used as the principal film parameter affecting transport of species. Tortuosity and permeability of the film which appear in the original transport equation have already been expressed in terms of porosity (see equation 47)¹⁵. Volumetric porosity is defined as:

$$\varepsilon = \frac{V_{void}}{V_{total}} = \frac{(V_{total} - V_{FeCO_3(s)})}{V_{total}} = 1 - \frac{V_{FeCO_3(s)}}{V_{total}} \quad (57)$$

Rearranging film growth equation (56) to express it in terms of porosity yields:

$$\frac{\partial \varepsilon}{\partial t} = -\frac{M_{FeCO_3(s)}}{\rho_{FeCO_3(s)}} R_{FeCO_3(s)} - CR \frac{\partial \varepsilon}{\partial x} \quad (58)$$

where $M_{FeCO_3(s)} = 115.847$ kg/kmol is the molecular mass and $\rho_{FeCO_3(s)} = 3900$ kg/m³ is the density of iron carbonate.

The rate of precipitation $R_{FeCO_3(s)}$ in equation (69) has been published by two studies^{51, 46} who have proposed rather different expressions for the precipitation (crystal growth) rate, and both have been tested in the present model:

$$\text{Johnson and Tomson}^{51}: \quad R_{FeCO_3} = A \cdot e^{54.8 - \frac{123.0 \text{ kJ/mol}}{RT}} \cdot K_{sp(FeCO_3)} \cdot (S_{FeCO_3}^{1/2} - 1)^2 \quad (59)$$

$$\text{van Hunnik et. al.}^{46}: \quad R_{FeCO_3} = A \cdot e^{52.4 - \frac{119.8 \text{ kJ/mol}}{RT}} \cdot K_{sp(FeCO_3)} \cdot (S_{FeCO_3} - 1)(1 - S_{FeCO_3}^{-1}) \quad (60)$$

Supersaturation is defined as:

$$S_{FeCO_3} = \frac{c_{Fe^{2+}} c_{CO_3^{2-}}}{K_{sp(FeCO_3)}} \quad (61)$$

where the solubility product $K_{sp(FeCO_3)}$ for $FeCO_3$ is calculated as:^{59,92}

$$K_{sp(FeCO_3)} = 10^{(-10.13 - 0.0182 \cdot T) / (0.0115 \cdot I - 0.6063)}$$

with temperature(T) in °C and ionic strength(I) in mol/L.

From the two different expressions describing the kinetics of iron carbonate precipitation proposed by Johnson and Tomson⁵¹ and Van Hunnik et al.⁴⁶, the latter is used in conjunction with the film growth model, because it is believed to give more realistic results especially at higher supersaturation.

It is assumed iron carbonate precipitation can occur on the steel surface or within the pores of a given porous surface film. Within the context of the present model, the surface area-to-volume ratio A/V is defined locally - as a function of the film porosity in a particular control volume. The two studies mentioned above^{51,46} offered no guidance on what values for A/V to use in such a case. Using simple asymptotic analysis it can be deduced that in the bulk solution where there is no film, $\varepsilon=1$ and $A/V=0$. Implicitly this means that homogeneous precipitation in the bulk solution does not occur no matter how high the local supersaturation and temperature. On the other end of the scale, in 100% dense films, $\varepsilon=0$ and $A/V=0$. In between these extremes, for $0<\varepsilon<1$ the surface area-to-volume ratio can become very large. There is some information in the open literature on how A/V changes with porosity^{112,113} based on simple geometrical models which usually fail at one of the extremes. After much trial and error, by using geometrical as well as physical arguments, and through comparison with CO₂ corrosion experiments (described below), it has been concluded that the area-to-volume ratio depends on porosity as:

$$\frac{A}{V} \propto \frac{\varepsilon^2(1-\varepsilon)}{\Delta x} \quad (62)$$

where Δx is the width of the control volume.

The solubility product K_{sp} for iron carbonate is modeled as a function of temperature (°C) and ionic strength based on the IUPAC data⁹² and in-house calculations done with the Thermo-Calc program⁹³.

Repeated observations were made that crystals usually dissolve much faster than they grow: a factor of 5 is not uncommon¹¹⁴. In most cases it can be assumed that the rate of dissolution is controlled by the rate of mass transfer of the solvated species from the

surface of the crystal into the bulk solution¹¹⁴. In the present version of the model dissolution is not included.

Iron carbonate precipitation has been implemented in the model as a chemical reaction taking place at the steel surface, in the porous corrosion film and on the film surface. The precipitation reaction acts as a sink for Fe^{2+} and CO_3^{2-} ions, influencing the fluxes and concentration gradients for both the ions and all other carbonic species.

5.3 Numerical Techniques

The film growth equation (69) was discretized using a finite difference method. An explicit time discretization scheme was used to simplify the coupling with the rest of the model which was discretized fully implicitly in order to maintain stability. This can easily be justified by the wide disparity of the time scales: relaxation time for the species transport equations (47) is of the order of seconds while the for the film growth equation (69) it is of the order of hours or even days. In other words film precipitation happens so slowly, compared to the other processes in CO_2 corrosion, that it can be calculated by using an explicit time discretization scheme without risking instability.

In equation (69), the film undermining term $CR \cdot \partial \varepsilon / \partial x$ is of a convective nature as discussed previously. A first order upwinding method is commonly used (in lieu of central differences) for spatial discretization of convective terms in order to achieve numerical stability. However, in the absence of any physical diffusion (iron carbonate films do not diffuse) simple upwinding led to large numerical diffusion and unacceptable level of numerical errors. This is due to the hyperbolic nature of equation (69) and the

very small CFL number ($CFL=CR\Delta t/\Delta x\approx 10^{-3}$). Exact solution of hyperbolic equations is obtained only for $CFL=1$.^{115,116} Therefore, a more accurate Koren's flux limiter scheme¹¹⁷ was used to discretize the film undermining term..

A typical initial condition for equation (69) used below was $\varepsilon=1$ throughout the solution - i.e. no initial film case, although any other porosity profile could have been used instead to simulate the presence of a carbide film or a mill scale. Boundary conditions for equation (69) were $\varepsilon=0$ at the steel surface and $\varepsilon=1$ in the bulk solution.

All the results of the simulations shown below were numerically tested by performing temporal and spatial grid refinement studies. The data shown in the figures below are all grid and time step independent. Uniform control volume size and time steps were used to improve the order of accuracy of the interpolation schemes.

5.4 Verification and Parametric Study

In order to verify and “fine-tune” the performance of the model described above, accurate CO_2 corrosion experiments in the presence of iron carbonate films were needed. There are a number of such experiments to be found in the open literature, however upon closer inspection all had to be rejected, because there was some relevant information which was not reported in each of them. Therefore custom designed glass cell experiments were conducted using a rotating cylinder electrode (see Figure 16). Conditions were chosen to enable rapid protective iron carbonate film formation in a relatively short time frame (one day), so that the reproducibility of the measurements could be easily established.

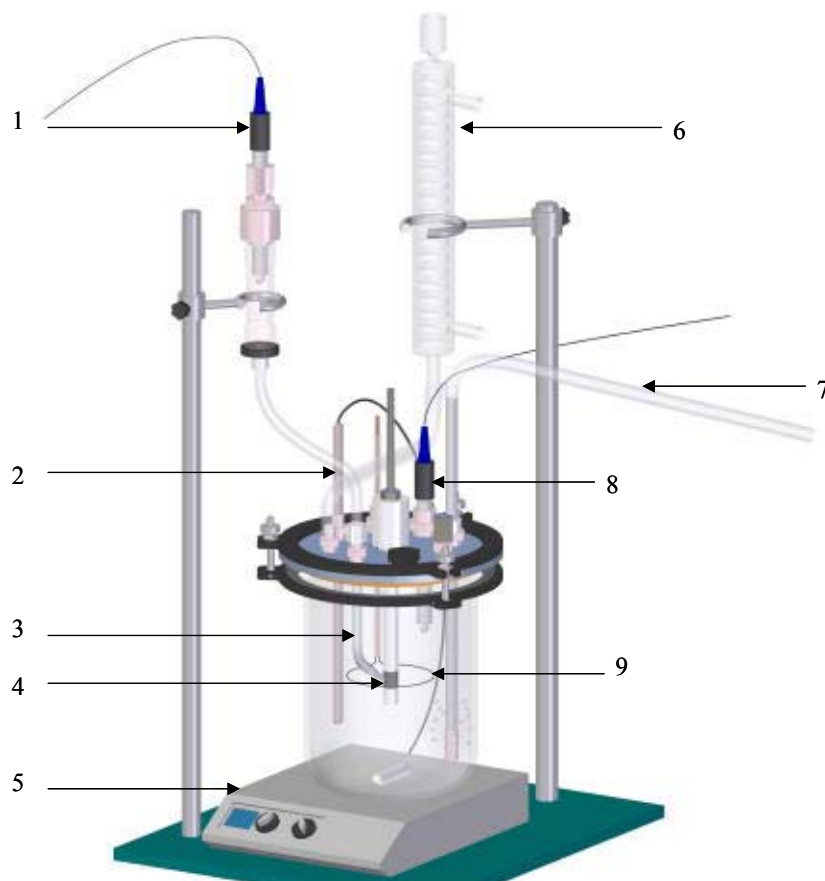


Figure 16. Schematic of a glass cell: 1. Reference electrode; 2. Temperature probe; 3. Luggin capillary; 4. Working electrode; 5. Hot plate; 6. Condenser; 7. Bubbler for gas; 8. pH electrode; 9. Counter electrode

5.4.1 Experimental setting and procedure

The glass cell was filled up with 2.5 liters of electrolyte which was made up of distilled water and 1.0 wt% sodium chloride. At the beginning, the solution was deaerated by bubbling CO₂ gas for 1 hour. The cell was sealed tightly to prevent oxygen contamination, and CO₂ gas bubbling was continued throughout the experiment, hence it can be assumed that water vapor and CO₂ were the only gas constituents. Subsequently the solution was heated to 80°C. Since the cell was operating at atmospheric pressure,

partial pressure of CO₂ was approximately 0.54 bar. The desired pH of 6.6 was then adjusted by adding sodium hydrogen carbonate (NaHCO₃). A cylindrical 1020 mild steel specimen with a ferritic-pearlitic microstructure was sanded using 1000 grit silicon carbide (SiC) paper, then washed with ethanol and dried before immersion into the solution. The rotating speed of the cylindrical specimen was adjusted to give the peripheral velocity of the steel surface of 1 m/s. The electrochemical corrosion measurements were performed by using a potentiostat connected to a PC. The corrosion rate was measured every hour using the linear polarization resistance (LPR) method, by polarizing the working electrode ± 5 mV vs. the open circuit potential at a rate of 0.1 mV/s. At the end of the experiment, after the specimen was removed from the cell it was immediately rinsed with ethanol in order to avoid film contamination with oxides. It was then allowed to dry and mounted in a low viscosity epoxy resin in order to fix the film. The specimen was cross sectioned, polished, platinum coated and observed using Scanning Electron Microscopy (SEM) and Energy Dispersive Spectroscopy (EDS).

Table 6. Experimental conditions for CO₂ film forming experiments

Test solution	Water + 1 mass% NaCl
Test material	1020 mild carbon steel
Temperature	80°C
CO ₂ partial pressure	0.54 bar
pH	6.6
Fe ⁺⁺	5, 250 ppm
Velocity	1000 rpm
Polarization resistance	From -5 to +5 mV vs. E _{oc}
Sweep rate	0.1 mV/s
Test duration	10 – 48 hours

5.4.2 Comparison case #1

The measured and predicted corrosion rates are compared for an experiment conducted at atmospheric pressure, temperature $T=80^{\circ}\text{C}$, pH 6.6, partial pressure of CO_2 $P_{\text{CO}_2}=0.54$ bar, velocity $v=1$ m/s. In order to form protective FeCO_3 films via precipitation in a short time frame, steel wool was placed at the bottom of the glass cell at the very beginning of the experiment in order to provide an ample source of Fe^{2+} ions. Based on pH 6.26 (measured once the pH reading stabilized), it was estimated via equilibrium calculations that the bulk concentration of Fe^{2+} was approximately 250 ppm leading to a bulk supersaturation $S=576$ and a surface scaling tendency of $SST=9.7$ at the steel surface prior to any film formation. As expected under these conditions, the corrosion rate was reduced sharply as iron carbonate protective films formed. The experiment was stopped after 10 hours when the corrosion rate was lower than 0.03 mm/year. The agreement between measured and predicted values shown in Figure 17 is very good given the complexity of the processes.

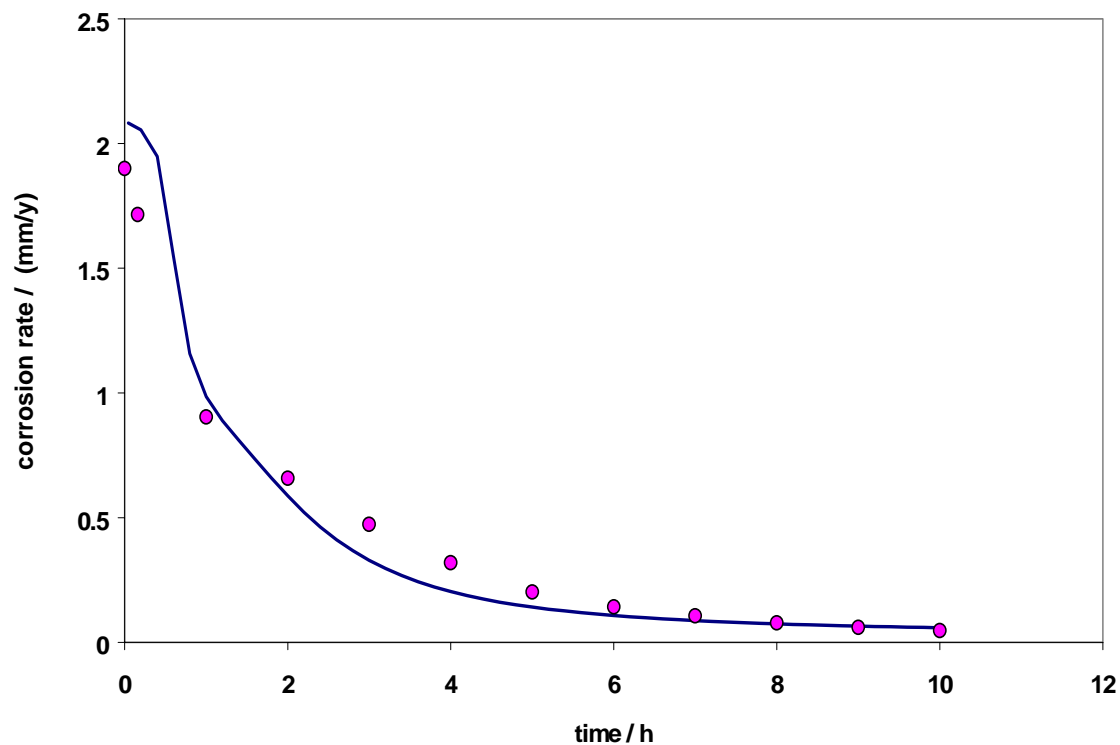


Figure 17. Comparison between experimental data (points) and model predictions (line) for $T=80^{\circ}\text{C}$, $\text{pH } 6.6$, $P_{\text{CO}_2} = 0.54 \text{ bar}$, $c_{\text{Fe}^{2+}} = 250 \text{ ppm}$, $v=1 \text{ m/s}$.

In order to achieve such agreement the only freely adjustable parameter in the model was the unknown proportionality constant between the surface area-to-volume ratio and the porosity of the film in equation (62). By trial and error it was found to be of the order of 10^{-3} . The resulting relationship is depicted in Figure 18 as shown below:

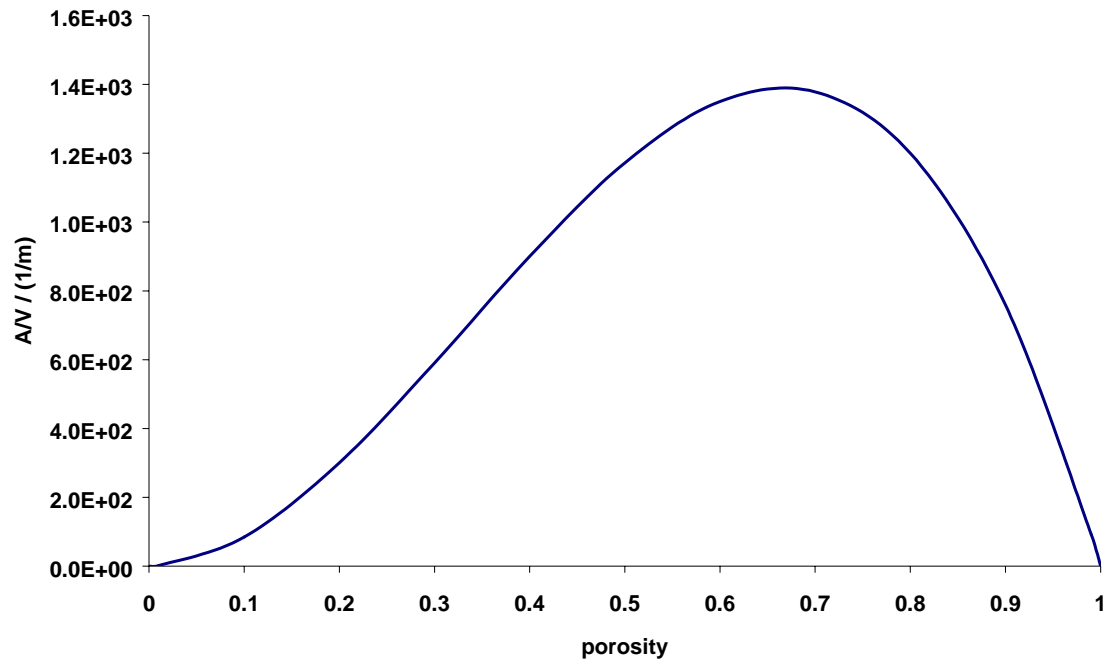


Figure 18. Surface area-to-volume ratio A/V as a function of porosity ε for a control volume of $\Delta x \propto 10^{-7}$ m.

The predicted film growth process is shown in Figure 19 as a change of porosity in each control volume with respect to time.

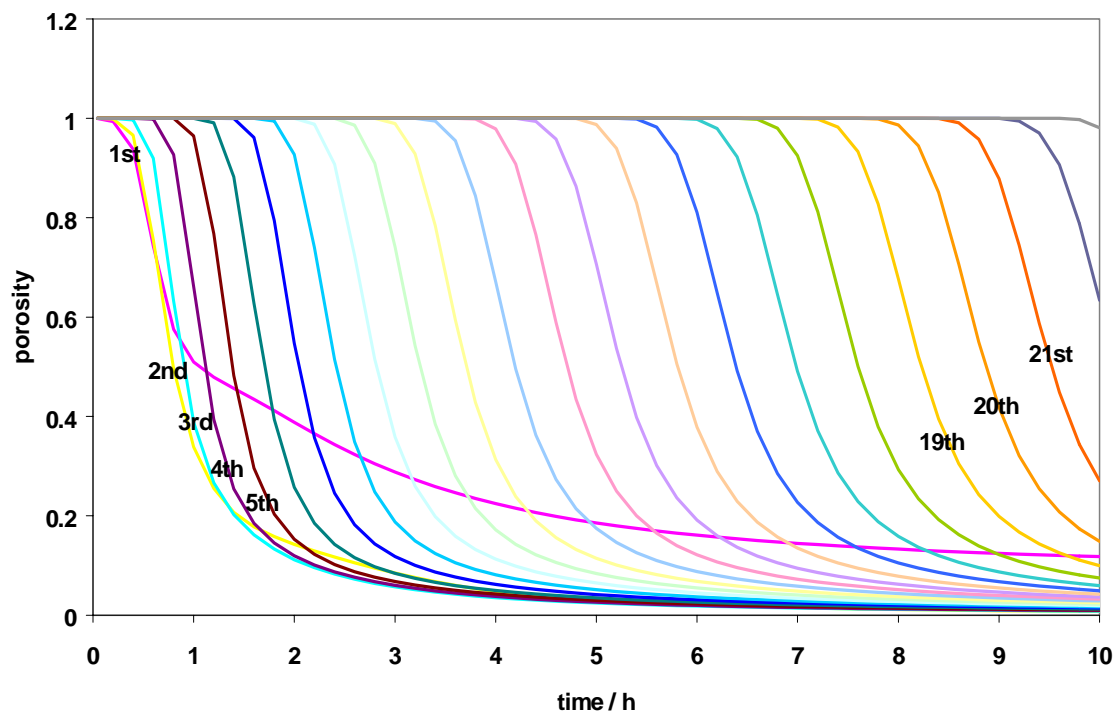


Figure 19. The predicted porosity change of different iron carbonate film layers with respect to time. Each layer is $0.16 \mu\text{m}$ thick. Conditions: $T=80^\circ\text{C}$, $\text{pH } 6.6$, $P_{\text{CO}_2} = 0.54$ bar, $c_{\text{Fe}^{2+}} = 250$ ppm, $v=1$ m/s.

It can be seen that the porosity decrease i.e. film buildup was initially sharpest in the first layer adjacent to the steel surface what is to be expected as highest supersaturation is reached there. However as the steel surface corroded under the film and undermined it, the second layer away from the steel surface (at a distance of $0.23\mu\text{m}$) experienced fastest film buildup, followed by the third layer etc. After 10 hours a very dense and protective film formed close to the steel surface. Since the bulk supersaturation was very high the film kept on growing in thickness. It is interesting to

note that the first layer adjacent to the steel surface never reached the same high density of the other layers above it due to the undermining effect by corrosion.

Another more intuitive way of looking at the same film growth process is depicted in Figure 20.

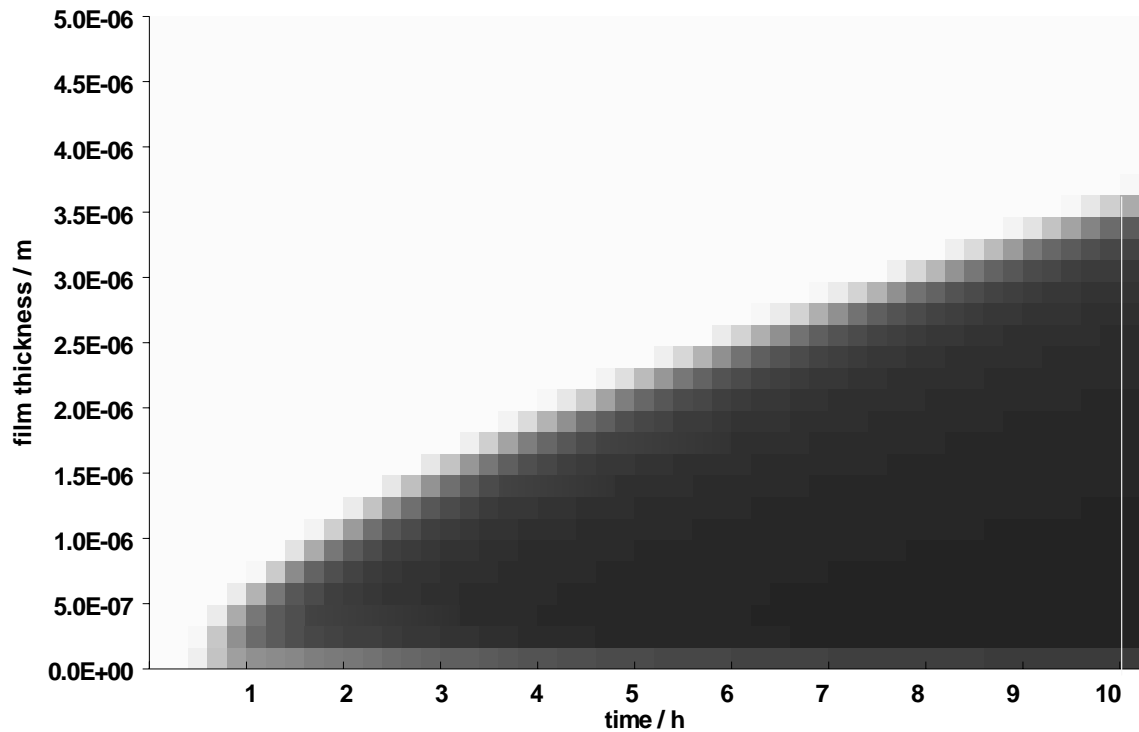


Figure 20. Predicted iron carbonate film growth with respect to time for $T=80^{\circ}\text{C}$, $\text{pH } 6.6$, $P_{\text{CO}_2} = 0.54 \text{ bar}$, $c_{\text{Fe}^{2+}} = 250 \text{ ppm}$, $v=1 \text{ m/s}$. Black depicts a 100% dense ($\varepsilon=0$) iron carbonate film and white means no film ($\varepsilon=1$).

Here, a change of porosity of the film is shown in time and space by using different shades of gray, black depicting a 100% dense ($\varepsilon=0$) iron carbonate film and white meaning no film ($\varepsilon=1$).

Scanning Electron Microscopy (SEM) image of the cross section of the steel specimen from the experiment described above (exposed for 10 hours) is shown in Figure 21.

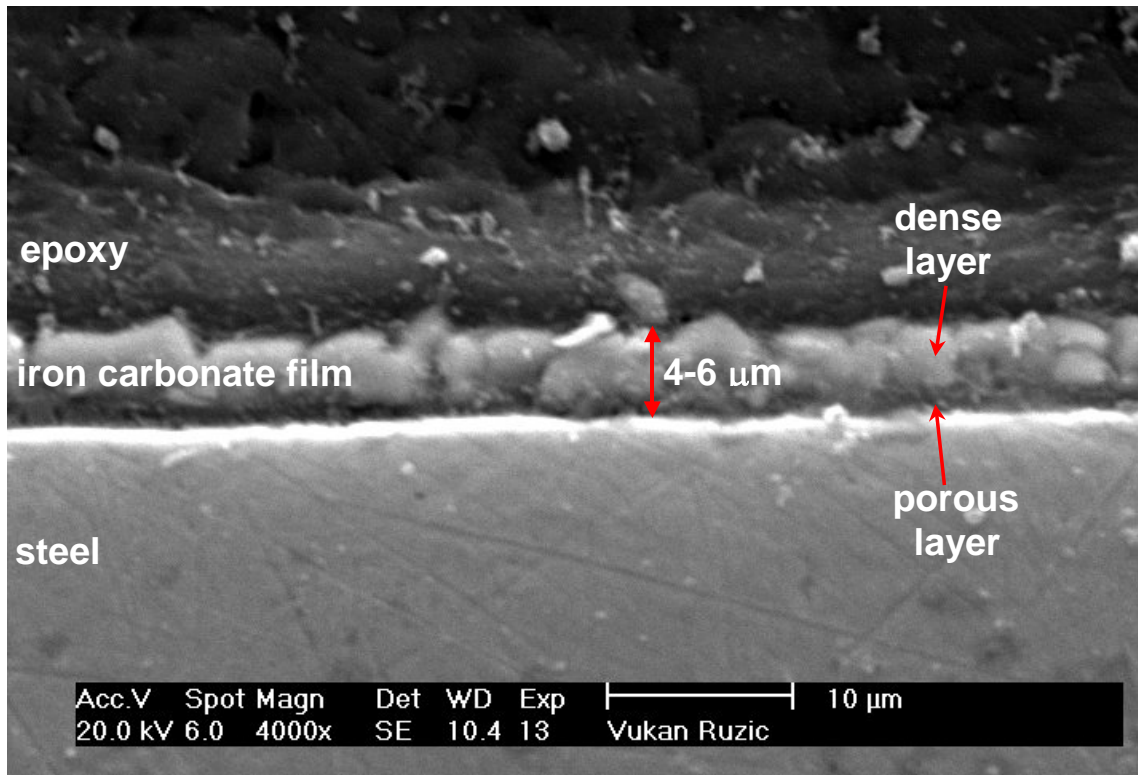


Figure 21. SEM image of a cross section of a steel specimen including an iron carbonate film. Exposed for 10 hours at $T=80^{\circ}\text{C}$, $\text{pH } 6.6$, $P_{\text{CO}_2} = 0.54 \text{ bar}$, $c_{\text{Fe}^{2+}} = 250 \text{ ppm}$, $v=1 \text{ m/s}$.

When comparing the film thickness and morphology with the predicted values (highlighted by the white rectangle in Figure 20) it is seen that the agreement is good for the thickness of film (measured: $4\text{-}6\mu\text{m}$, predicted: $3.7\mu\text{m}$). Indeed the SEM image shows a fairly uniformly dense film with a more porous layer of iron carbonate adjacent

to the steel surface just as predicted. During the experiment less than 1 μm of steel was lost to the corrosion process.

5.4.3 Comparison case #2

The next test of the model was to compare its performance using a different set of environmental conditions. It was particularly interesting to evaluate if the newly established relationship between the surface area-to-volume ratio and the porosity of the film depicted in Figure 11 would apply without adjustment - what would build confidence in its generality. A second set of experiments used for verification was conducted under the same condition as the previous set ($T=80^{\circ}\text{C}$, $\text{pH } 6.6$, $P_{\text{CO}_2}=0.54$ bar, $v=1$ m/s) with the exception of the steel wool which was not used - resulting in a much lower Fe^{2+} concentration. Using equilibrium calculations, based on $\text{pH } 4.6$ measured at the beginning of the experiment, it was estimated that the Fe^{2+} concentration was approximately 5-10 ppm throughout most of the experiment. The value of pH was adjusted to 6.6 by adding NaHCO_3 what resulted in a bulk supersaturation $S=10$ to 23 and a surface scaling tendency of $SST=0.25$ to 0.47 prior to any film formation. Base on the high supersaturation it was expected that some precipitation would occur however, the low value of the surface scaling tendency suggested that the film might have troubles attaching to the surface.

The experiment was stopped after two days without achieving protective film formation. In Figure 22 measured and predicted corrosion rate were compared and both show that no protective films were formed after 48 hours.

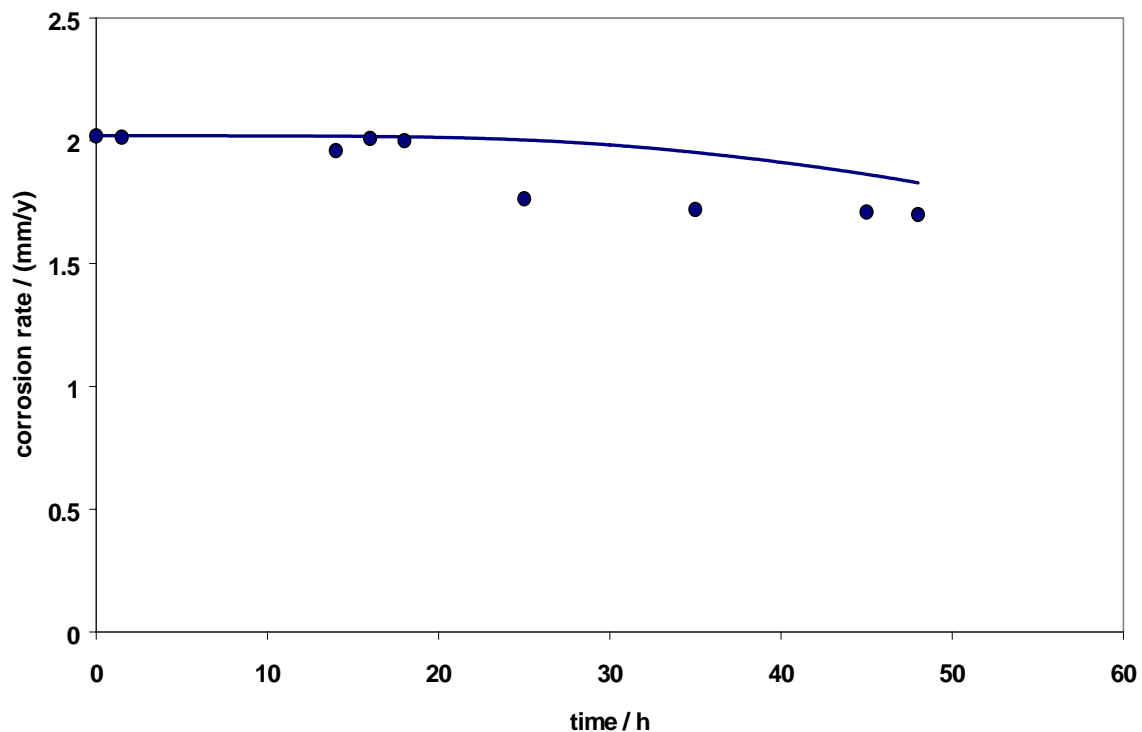


Figure 22. Comparison between experimental data (points) and model predictions (line) for $T=80^{\circ}\text{C}$, $\text{pH } 6.6$, $P_{\text{CO}_2} = 0.54 \text{ bar}$, $c_{\text{Fe}^{2+}} = 5 \text{ ppm}$, $v=1 \text{ m/s}$.

The agreement is rather good given that no further adjustment of the model was made.

In Figure 23 the prediction showed that some precipitation occurred, however the film layer adjacent to the rapidly corroding steel surface remained very porous due to undermining while a more dense film grew at some distance away from the steel surface.

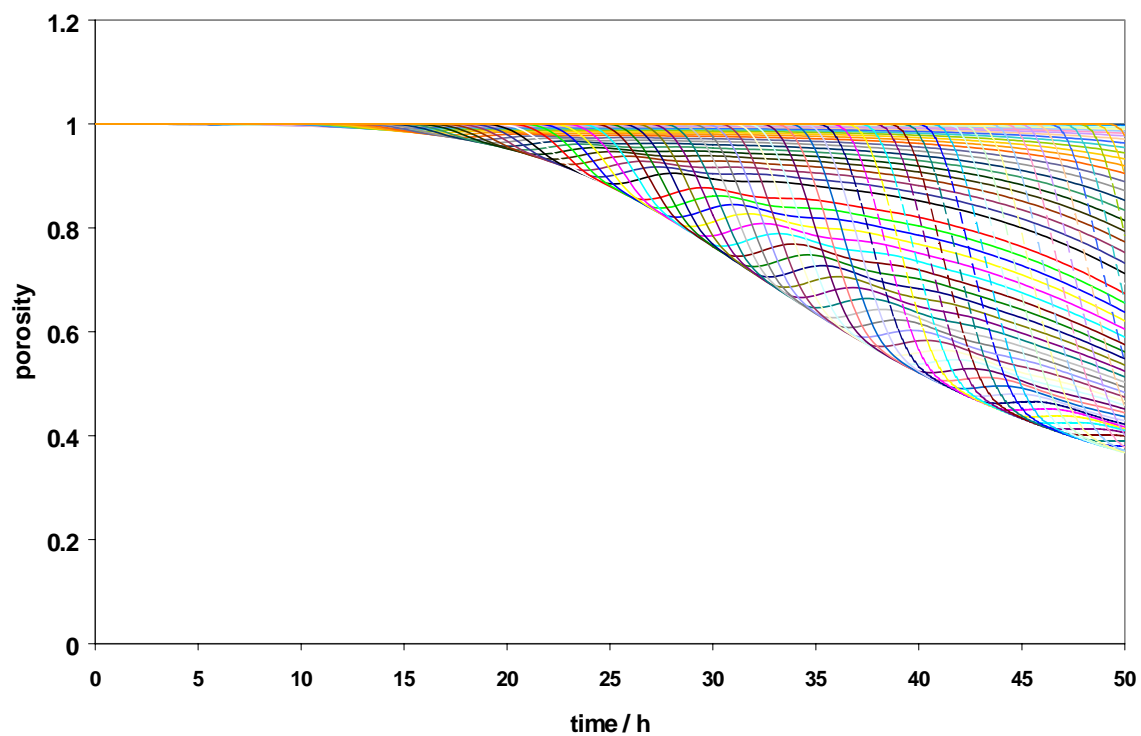


Figure 23. The predicted porosity change of different iron carbonate film layers with respect to time. Each layer is $0.16 \mu\text{m}$ thick. Conditions: $T=80^\circ\text{C}$, $\text{pH } 6.6$, $P_{\text{CO}_2} = 0.54$ bar, $c_{\text{Fe}^{2+}} = 5$ ppm, $v=1$ m/s.

The same is shown in Figure 24 showing that a relatively dense film formed at approximately $5 \mu\text{m}$ away from the surface after 48 hours of exposure.

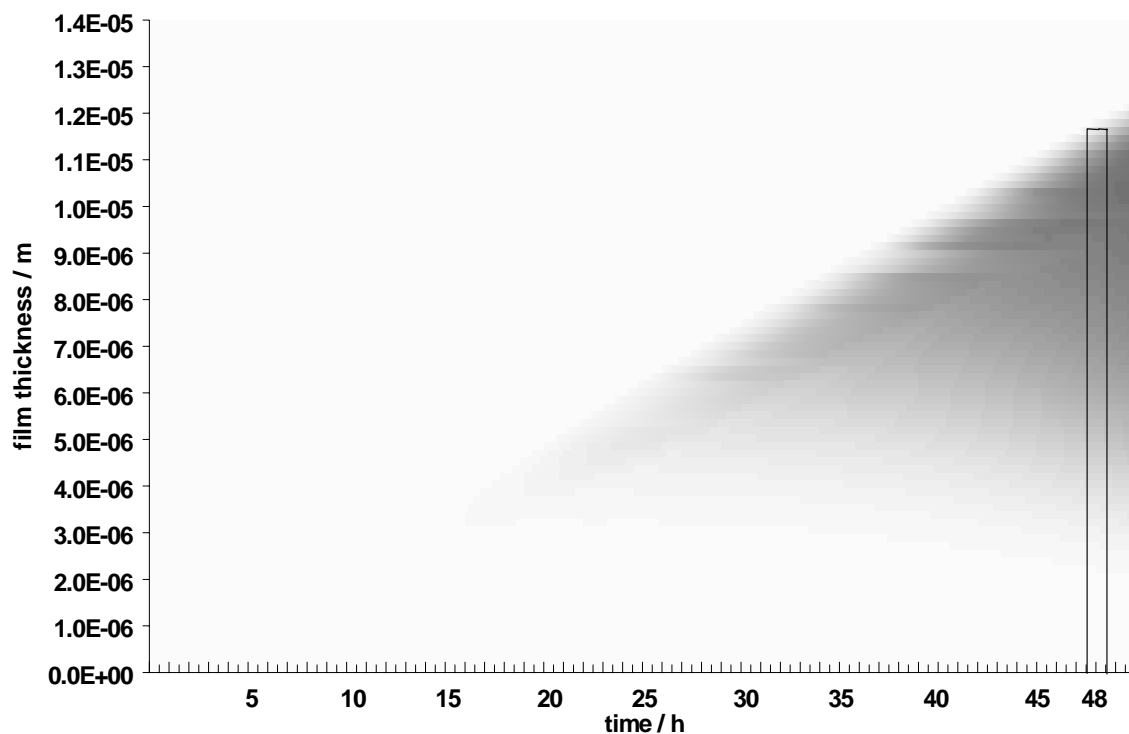


Figure 24. Predicted iron carbonate film growth with respect to time for $T=80^{\circ}\text{C}$, $\text{pH } 6.6$, $P_{\text{CO}_2} = 0.54 \text{ bar}$, $c_{\text{Fe}^{2+}} = 5 \text{ ppm}$, $v=1 \text{ m/s}$. Black depicts a 100% dense ($\varepsilon=0$) iron carbonate film and white means no film ($\varepsilon=1$).

Qualitatively this agreed well with the cross section examination conducted by using SEM, as shown in Figure 25, where a totally detached layer of iron carbonate can be seen approximately 10-20 μm away from the steel surface. During the experiment approximately 10 μm of steel was lost to the corrosion process.

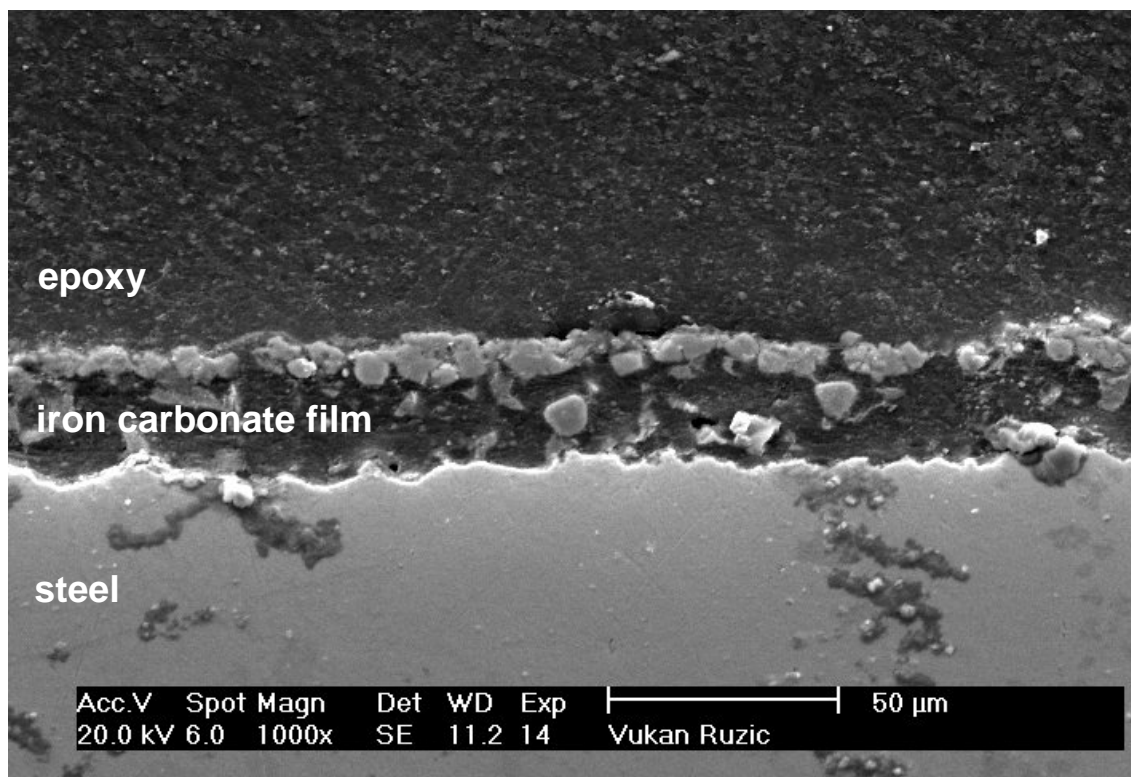


Figure 25. SEM image of a cross section of a steel specimen including an iron carbonate film. Exposed for 48 hours at $T=80^{\circ}\text{C}$, $\text{pH } 6.6$, $P_{\text{CO}_2} = 0.54 \text{ bar}$, $c_{\text{Fe}^{2+}} = 5 \text{ ppm}$, $v=1 \text{ m/s}$.

Clearly one can be satisfied with the qualitative as well as quantitative predictions made by the model, however some more fine-tuning is needed, requiring a new set of dedicated CO_2 corrosion experiments conducted under a variety of environmental conditions leading to iron carbonate film growth. This is a task for the immediate future.

In the parametric study that was performed the model was used to predict CO_2 corrosion under broadly varying environmental conditions in order to establish its more general applicability. No direct comparisons with experiments will be made in this section, however performance of the model will be contrasted against the general understanding of the CO_2 corrosion process in the presence of iron carbonate films. As

shown in the previous section (comparison case #1), the model was successful in predicting CO₂ corrosion and film formation in an experiment conducted at T=80°C, pH=6.6, $P_{CO_2} = 0.54$ bar, $c_{Fe^{2+}} = 250$ ppm, $v=1$ m/s, and therefore this set of conditions will be used as a baseline case when varying the different parameters, one at a time.

5.4.4 The effect of pH

It was shown previously both experimentally¹¹⁸, and computationally¹⁵ that pH has a strong influence on the conditions leading to the formation of iron carbonate films. High pH results in a decreased solubility of iron carbonate, increased supersaturation and consequently higher precipitation rate and surface scaling tendency. In Table 7 the predicted supersaturation, scaling tendency, film thickness and a corrosion rate after 30 hours of exposure at various pH are shown.

Table 7. Predicted supersaturation, scaling tendency, film thickness and corrosion rate at various pH for T=80°C, $P_{CO_2} = 0.54$ bar, $c_{Fe^{2+}} = 250$ ppm, $v=1$ m/s.

pH	Supersaturation (prior to any film formation)		Scaling Tendency (prior to any film formation)		Film thickness* (after 30 hours) in μ m	Corrosion rate* (after 30 hours) in mm/y
	Surface	bulk	Surface	Bulk		
5.8	63	11	0.41	0.06	6.2	1.6
6.0	154	29	1.03	0.18	4.95	0.13
6.26	464	104	3.03	0.66	4.8	0.04
6.6	1595	576	9.70	3.35	8.4	0.03

* Film thickness as well as porosity are shown in Figure 27.

* Corresponding corrosion rate vs. time curves are shown in Figure 26.

Judging by the high supersaturation alone, one could expect that protective film should form in all cases, given that the temperature is relatively high (80°C). However the surface scaling tendency seems to suggest that protective film formation might be very difficult at pH 5.8 (as $SST < 1$) and probably slow at pH 6.0 ($SST \approx 1$). The predictions of the corrosion rate at varying pH confirmed this as shown in Figure 26.

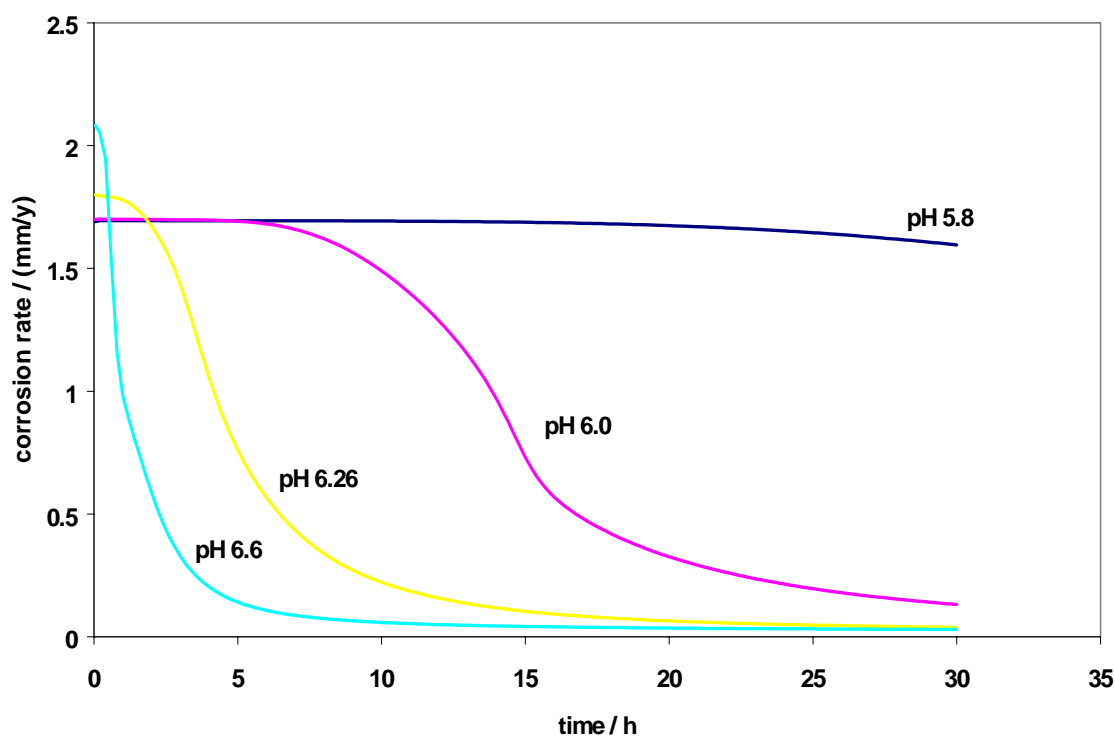


Figure 26. The predicted effect of pH on the corrosion rate for $T=80^{\circ}\text{C}$, $P_{\text{CO}_2}=0.54$ bar, $c_{\text{Fe}^{2+}}=250$ ppm, $v=1$ m/s. Corresponding film thickness and porosity are shown in Figure 27. Predicted supersaturation and scaling tendency are listed in Table 7.

At pH 5.8 the corrosion rate is not reduced by a significant amount after 30 hours reflecting the fact that a relatively porous, detached and unprotective film formed as shown in Figure 27.

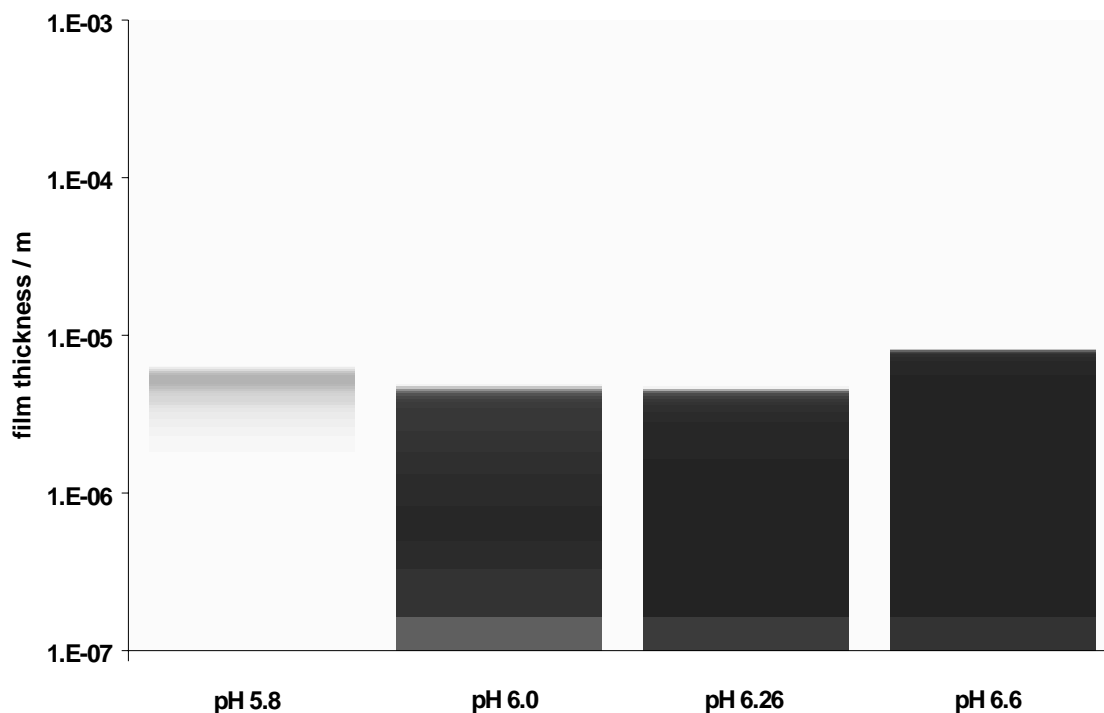


Figure 27. The predicted film thickness and porosity as a function of pH after 30 hours of exposure at $T=80^{\circ}\text{C}$, $P_{\text{CO}_2}=0.54$ bar, $c_{\text{Fe}^{2+}}=250$ ppm, $v=1$ m/s. Black depicts a 100% dense ($\varepsilon=0$) iron carbonate film and white means no film ($\varepsilon=1$). The corresponding corrosion rate curves are shown in Figure 26. Predicted supersaturation and scaling tendency are listed in Table 7.

However a downward trend in the corrosion rate is evident as the porous film slowly fills up with iron carbonate. A clear trend can be observed in Figure 26: higher pH resulted in faster formation of more protective films, as expected. From Figure 27 one can deduce that as the pH 5.8 was increased to pH 6.0 and then 6.26 the resulting film was of similar thickness but progressively became more dense and protective. The pH 6.6 has resulted in a much thicker and dense iron carbonate film.

5.4.5 The effect of temperature

It is known that increased temperature aids iron carbonate film formation by accelerating the kinetics of precipitation. The predicted temperature effect on CO_2 corrosion is illustrated in Figure 28 for the baseline case.

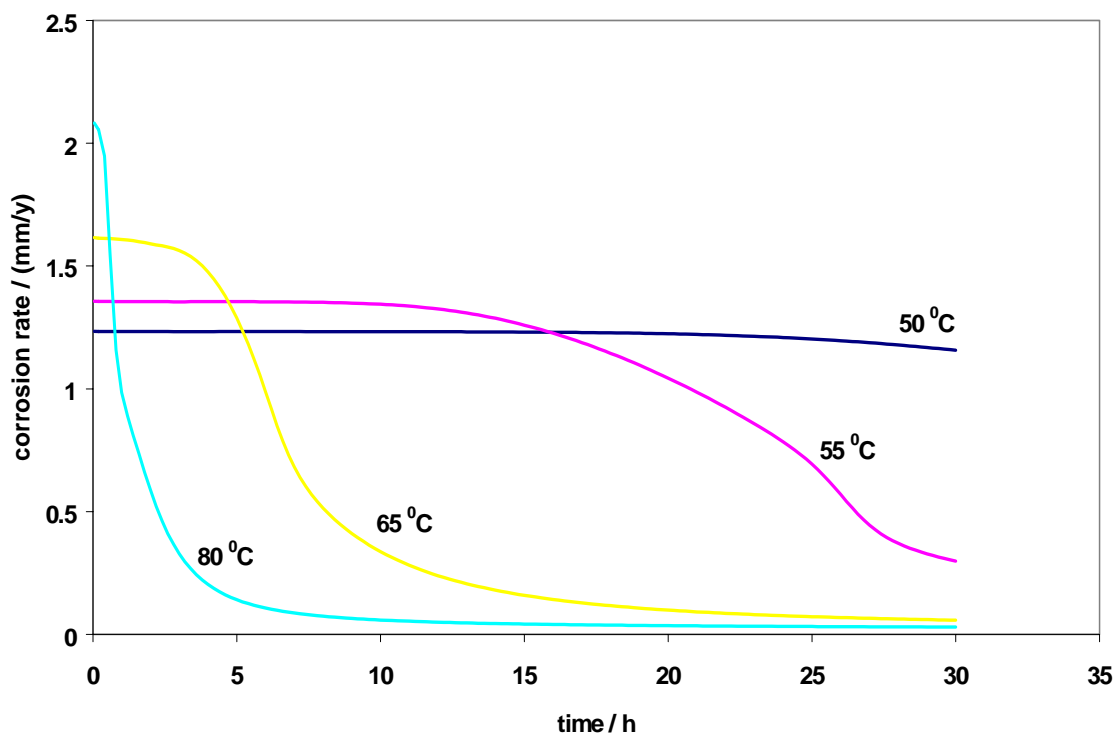


Figure 28. The predicted effect of temperature on the corrosion rate for pH 6.6, $P_{\text{CO}_2} = 0.54$ bar, $c_{\text{Fe}^{2+}} = 250$ ppm, $v=1$ m/s. Corresponding film thickness and porosity are shown in Figure 29. Predicted supersaturation and scaling tendency are listed in Table 8.

Prior to any film formation the corrosion rate increases with temperature. While very protective films form rapidly at 80°C , already at 65°C and 55°C the kinetics of film formation is very much slower while at 50°C only porous film formation can be detected. It is rather striking how under certain conditions a difference of 5°C can lead to two very

different corrosion scenarios. At 55°C iron carbonate films form which would eventually offer good protection while at 50°C there is a detached, porous layer of iron carbonate film which offers little protection. Calculated data shown in Table 8 support this conclusion, where very high supersaturation is obtained at all temperatures, however the surface scaling tendency is smaller than unity for 50°C.

Table 8. Predicted supersaturation, scaling tendency, film thickness and corrosion rate at various temperatures for pH 6.6, $P_{CO_2} = 0.54$ bar, $c_{Fe^{2+}} = 250$ ppm, $v = 1$ m/s.

T in °C	Supersaturation (prior to any film formation)		Scaling Tendency (prior to any film formation)		Film thickness [♦] (after 30 hours) in μm	Corrosion rate [♥] (after 30 hours) in mm/y
	Surface	bulk	Surface	Bulk		
50	562	245	0.43	0.19	4.9	1.16
55	675	290	0.76	0.32	5.1	0.3
65	969	387	2.22	0.87	5.1	0.06
80	1595	576	9.70	3.35	8.4	0.03

♦ Film thickness as well as porosity are shown in Figure 29.

♥ Corresponding corrosion rate vs. time curves are shown in Figure 28.

By looking at Figure 29 it can be seen that the film thickness at 55°C and 65°C is similar however the film formed at 55°C is more porous particularly close to the metal surface due to the undermining effect. At 80°C a very dense and thick protective film is obtained.

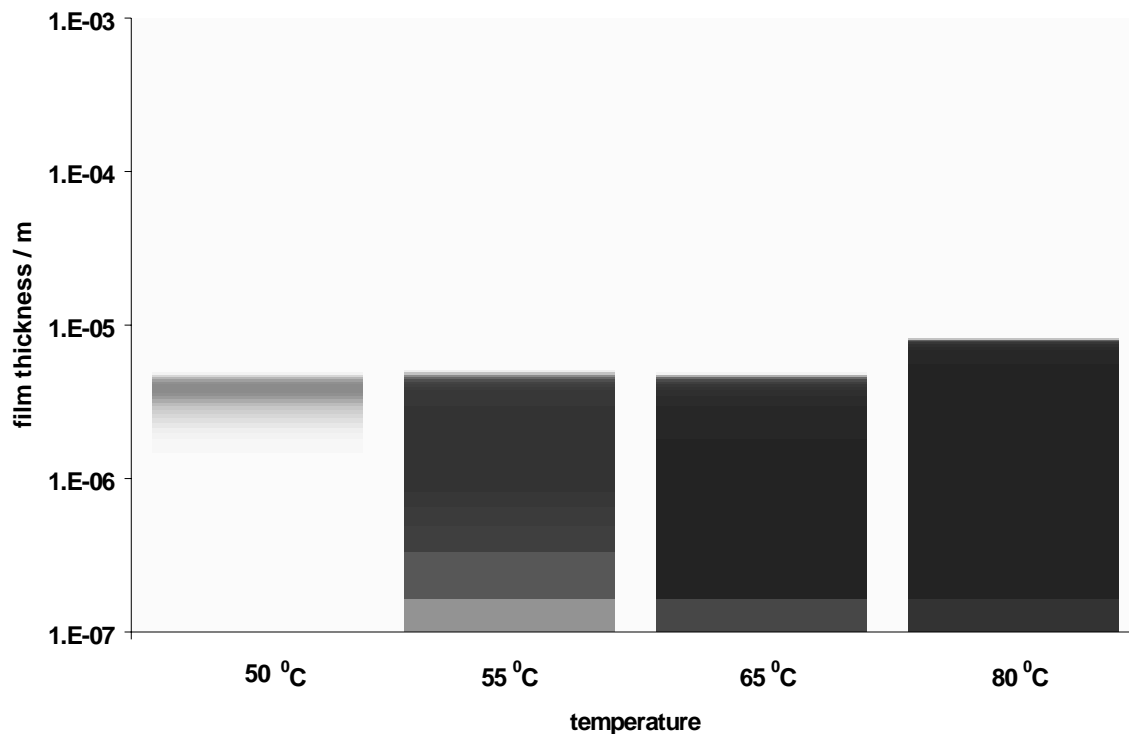


Figure 29. The predicted film thickness and porosity as a function of temperature after 30 hours of exposure at pH 6.6, $P_{CO_2}=0.54$ bar, $c_{Fe^{2+}}=250$ ppm, $v=1$ m/s. Black depicts a 100% dense ($\varepsilon=0$) iron carbonate film and white means no film ($\varepsilon=1$). The corresponding corrosion rate curves are shown in Figure 28. Predicted supersaturation and scaling tendency are listed in Table 8.

5.4.6 The effect of CO₂ partial pressure

In the case of free CO₂ corrosion, an increase of CO₂ partial pressure (P_{CO_2}) typically leads to an increase in the corrosion rate. However, when other conditions are favourable for formation of iron carbonate films, increased P_{CO_2} can help. At a constant pH, higher P_{CO_2} leads to an increase in CO₃²⁻ concentration and a higher supersaturation (given the pH is high enough), what accelerates precipitation and film formation. The effect of P_{CO_2} on the corrosion rate in the presence of iron carbonate precipitation is illustrated in Figure 30 for the baseline case.

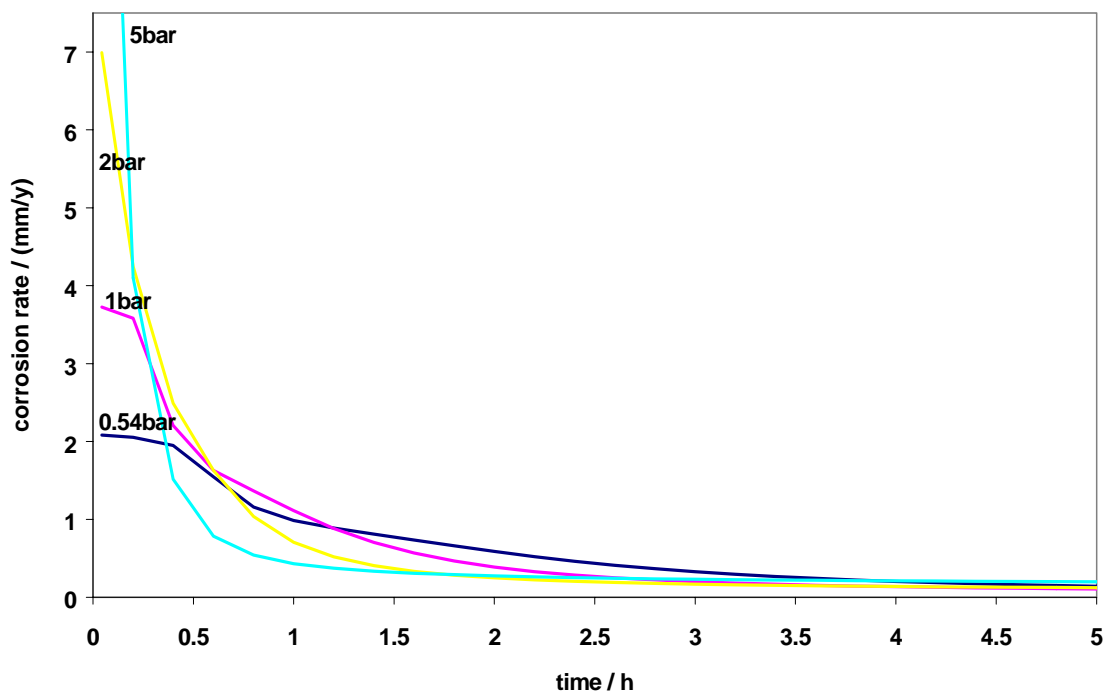


Figure 30. The predicted effect of CO₂ partial pressure on the corrosion rate for T=80°C, pH 6.6, $c_{Fe^{2+}} = 250$ ppm, $v=1$ m/s. Corresponding film thickness and porosity are shown in Figure 31. Predicted supersaturation and scaling tendency are listed in Table 9.

Prior to film formation, increased P_{CO_2} leads to a rapid rise in corrosion rate. However, protective films form even for the lowest P_{CO_2} = 0.54 bar (given the pH 6.6), any increase in P_{CO_2} leads to formation of even more protective films - and this happens faster. Data are presented only for the first 5 hours of corrosion as very low, almost indistinguishable corrosion rates are obtained beyond. One could expect such behaviour just by looking at the high supersaturations and scaling tendencies shown in Table 9.

Table 9. Predicted supersaturation, scaling tendency, film thickness and corrosion rate at various CO_2 partial pressures for $T=80^\circ C$, pH 6.6, $c_{Fe^{2+}}=250$ ppm, $v=1$ m/s.

P_{CO_2} in bar	Supersaturation (prior to any film formation)		Scaling Tendency (prior to any film formation)		Film thickness* (after 5 hours) in μm	Corrosion rate* (after 5 hours) in mm/y
	Surface	bulk	Surface	Bulk		
0.54	1595	576	9.70	3.35	2.47	0.14
1	3078	1069	10.77	3.59	3.5	0.11
2	5881	2142	11.75	4.13	5.6	0.12
5	11800	5422	12.26	5.66	11.4	0.2

* Film thickness as well as porosity are shown in Figure 31.

* Corresponding corrosion rate vs. time curves are shown in Figure 30.

By inspecting Figure 31 it can be concluded that somewhat denser and clearly thicker films form at higher P_{CO_2} .

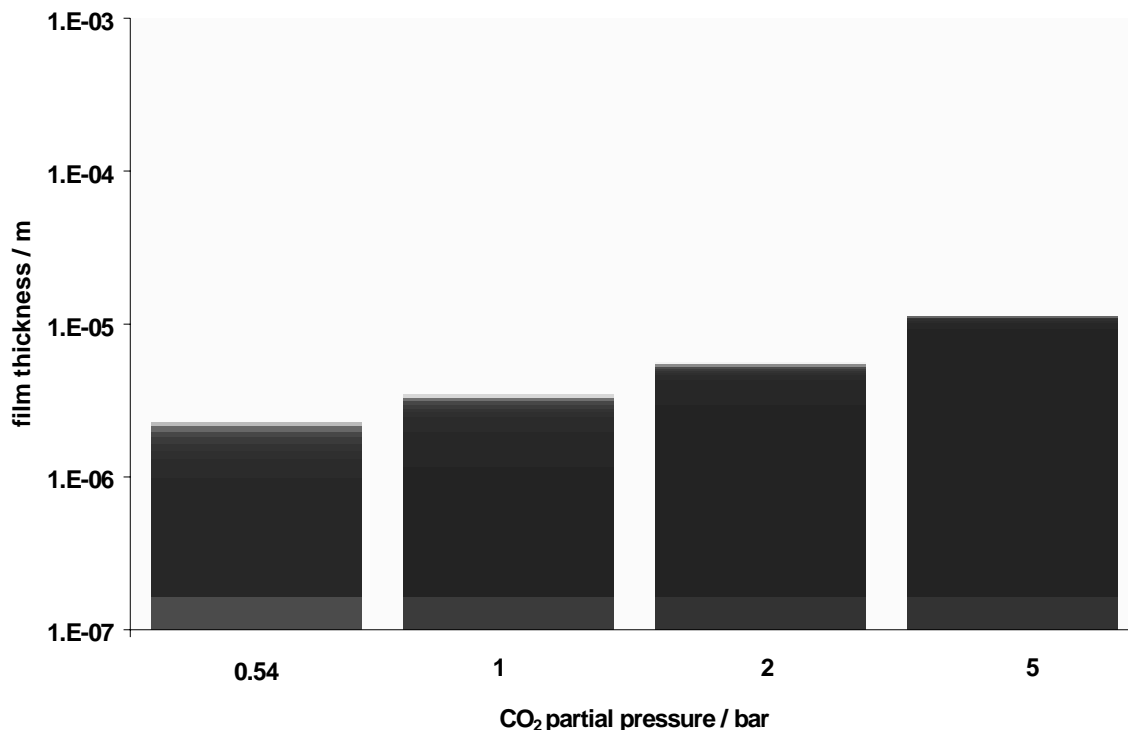


Figure 31. The predicted film thickness and porosity as a function of CO₂ partial pressure after 5 hours of exposure at T=80°C, pH 6.6, $c_{Fe^{2+}}=250$ ppm, $v=1$ m/s. Black depicts a 100% dense ($\varepsilon=0$) iron carbonate film and white means no film ($\varepsilon=1$). The corresponding corrosion rate curves are shown in Figure 30. Predicted supersaturation and scaling tendency are listed in Table 9.

5.4.7 The effect of Fe^{2+} concentration

The concentration of Fe^{2+} ions in the solution ($c_{Fe^{2+}}$) is another important factor that contributes to film formation. The increase of $c_{Fe^{2+}}$ results in higher supersaturation, which consequently accelerates the precipitation rate and leads to higher surface scaling tendency. In Figure 32 the effect of $c_{Fe^{2+}}$ on the rate of corrosion rate reduction due to iron carbonate film formation is shown for the baseline case.

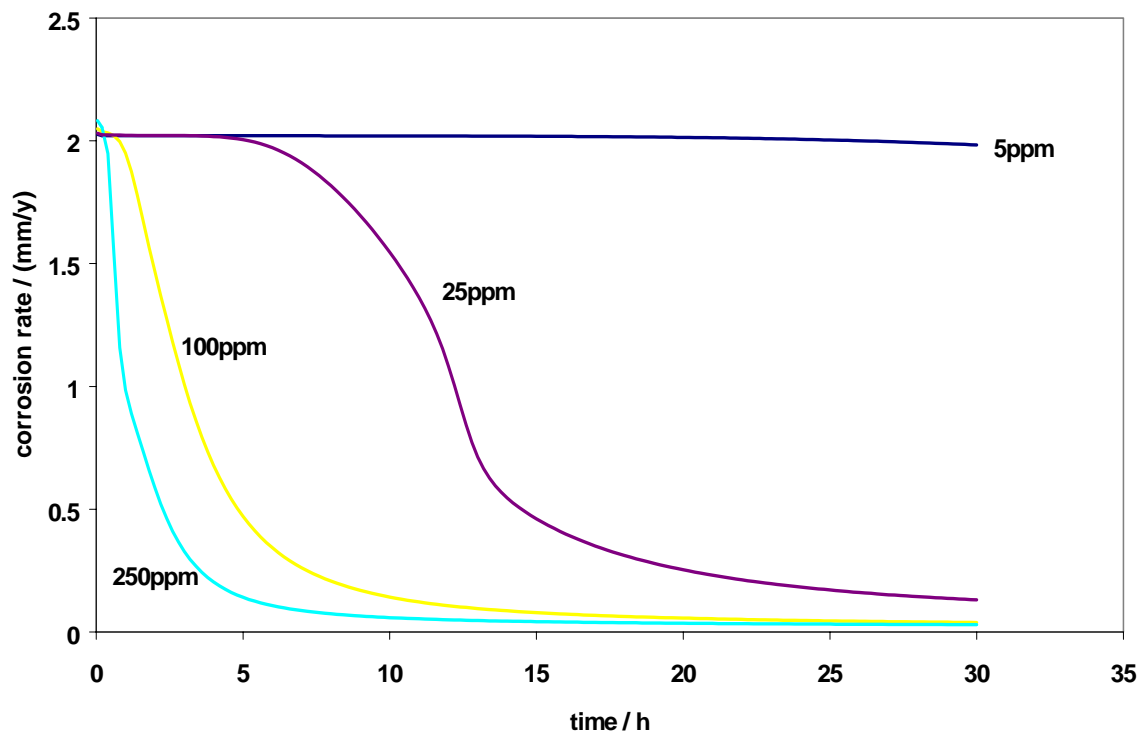


Figure 32. The predicted effect of Fe^{2+} concentration on the corrosion rate for $T=80^\circ\text{C}$, $\text{pH } 6.6$, $P_{\text{CO}_2} = 0.54 \text{ bar}$, $v=1 \text{ m/s}$. Corresponding film thickness and porosity are shown in Figure 33. Predicted supersaturation and scaling tendency are listed in Table 10.

The $c_{\text{Fe}^{2+}}$ does not affect the corrosion rate if there are no iron carbonate films (at the beginning of the simulation). When $c_{\text{Fe}^{2+}}=5\text{ppm}$, supersaturation is achieved however the surface scaling tendency is much less than unity (see Table 10) and one cannot expect protective films to form.

Table 10. Predicted supersaturation, scaling tendency, film thickness and corrosion rate at various Fe^{2+} concentrations for $T=80^{\circ}C$, $pH\ 6.6$, $P_{CO_2} = 0.54\ bar$, $v=1\ m/s$.

$c_{Fe^{2+}}$ in ppm	Supersaturation (prior to any film formation)		Scaling Tendency (prior to any film formation)		Film thickness [♦] (after 30 hours) in μm	Corrosion rate [♥] (after 30 hours) in mm/y
	Surface	bulk	Surface	Bulk		
5	51	11	0.27	0.05	7.1	1.98
25	185	58	1.1	0.32	5.7	0.13
100	671	230	3.90	1.31	6.0	0.04
250	1595	576	9.70	3.35	8.4	0.03

♦ Film thickness as well as porosity are shown in Figure 33.

♥ Corresponding corrosion rate vs. time curves are shown in Figure 32.

This is confirmed as corrosion rate is not reduced significantly even after 30 hours (see Figure 32). The iron carbonate film which forms is very porous and unprotective (see Figure 33 but also the comparison case #2 - Figure 22 - Figure 25). At higher concentrations more protective, dense and thick films form as shown in Figure 32 and Figure 33.

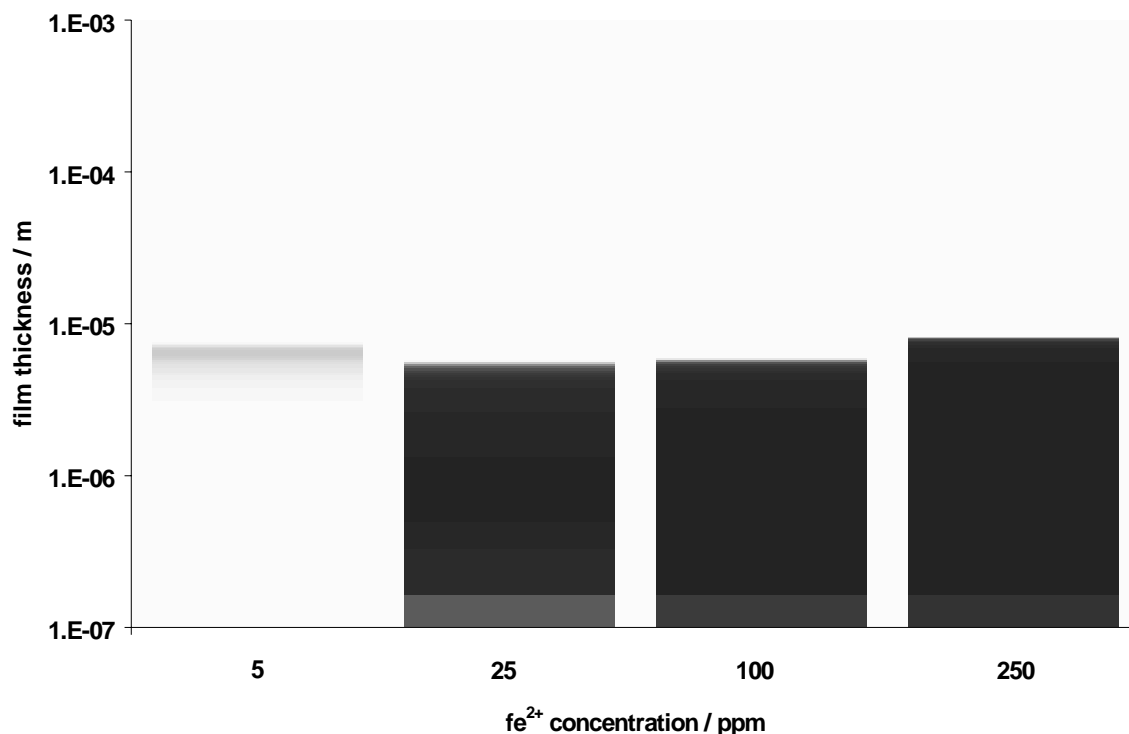


Figure 33. The predicted film thickness and porosity as a function of Fe^{2+} ion concentration after 30 hours of exposure at $T=80^\circ\text{C}$, $\text{pH } 6.6$, $P_{\text{CO}_2}=1 \text{ bar}$, $v=1 \text{ m/s}$. Black depicts a 100% dense ($\varepsilon=0$) iron carbonate film and white means no film ($\varepsilon=1$). The corresponding corrosion rate curves are shown in Figure 32. Predicted supersaturation and scaling tendency are listed in Table 10.

5.5 Summary

A mechanistic model of iron carbonate film growth in CO_2 corrosion of carbon steel was created and coupled with the overall corrosion prediction model. The model relies on accurate prediction of the solution chemistry at the metal surface. It includes two principle mechanisms which determine the kinetics of growth and the resulting morphology of the iron carbonate films: precipitation and undermining of the film by

ongoing corrosion. The morphology is described by the distribution of porosity throughout the film.

The model is capable of predicting the kinetics of iron carbonate film growth, the change in morphology of the film with respect to space and time as well as the resulting corrosion rate time evolution.

The model has been successfully calibrated against limited experimental data. Further adjustment of the model will be done as more accurate data on CO₂ corrosion in the presence of iron carbonate films emerge.

Parametric testing of the model has been done in order to gain insight into the effect of various environmental parameters on iron carbonate film formation. The trends shown in the predictions agreed well with the general understanding of the CO₂ corrosion process in the presence of iron carbonate films.

The present model confirms that the concept of scaling tendency is a good tool for predicting the likelihood of protective iron carbonate film formation. It was found that protective films formed when the surface scaling tendency was larger than unity, otherwise porous and unprotective film formed irrespective of the level of supersaturation. If bulk scaling tendency is used, the critical value is 0.6 - 0.7, which is close to the experimentally observed value by van Hunnik et al.⁴⁶.

CHAPTER 6: MODELING OF CO₂/H₂S CORROSION IN FILM FREE CONDITIONS

6.1 Introduction

Dissolved H₂S is a mild acid and can be treated as another cathodic species given that the concentrations are high enough. Moreover, the presence of H₂S can lead to formation of various forms of iron sulfide films that can be either very protective or causing localized attack. In order to extend the mechanistic CO₂ corrosion model described above and to cover the effect of H₂S, two main building blocks are necessary:

1. The electrochemistry of CO₂/H₂S corrosion on mild steel in film free conditions (covered in the present Chapter 6);
2. The modelling of iron sulfide film growth and its effects on CO₂/H₂S corrosion (covered in the following Chapter 7).

A systematic approach is taken in which the effect of trace amount of H₂S on CO₂ corrosion in the film-free conditions is investigated initially, deliberately avoiding the complex issues associated with formation of iron sulfide films, which will be further studied once the mechanisms of CO₂/H₂S corrosion in film-free conditions are grasped.

In order to determine the mechanism for CO₂/H₂S corrosion in film-free conditions, numerous experiments were conducted by the present author in the absence of film precipitation and qualitative explanations were deduced from experiments, which are discussed in the following subsection

6.2 Physico-Chemical Model

The investigation on electrochemical kinetics of CO₂/H₂S corrosion takes into account the reactions on the surface of the metal, partial cathodic and anodic processes are investigated and combined to compute corrosion rates in the framework of the mixed potential theory. In addition, the mechanisms and the missing physical constants can be determined during the process.

Essentially, there are three kinds of mechanisms that govern the process of H₂S/CO₂ corrosion, namely, charge transfer, mass transfer and chemical reactions. One needs to determine which of these mechanisms governs the corrosion process under given conditions before investigating further on the finer details and the missing physical constants of the specific mechanism. For instance, if charge transfer governs the corrosion process, then one needs to determine the Tafel slopes of anodic and cathodic reactions in order to find to the corrosion current via Tafel analysis. On the other hand, if the corrosion process is mass transfer controlled, then one needs to investigate further on the limiting current, the presence of film, whether it leads to diffusion control or coverage control. Furthermore, when the corrosion process is governed by chemical reactions, then the reaction rate needs to be determined.

In order to determine the mechanism and the missing physical constants for H₂S/CO₂ corrosion, numerous experiments were conducted in a flow loop⁸² to study the corrosion mechanism with no protective films present (pH 4). In these experiments the corrosion process was monitored with different electrochemical measuring techniques: potentiodynamic sweep and linear polarization resistance as shown in Figure 34 below:

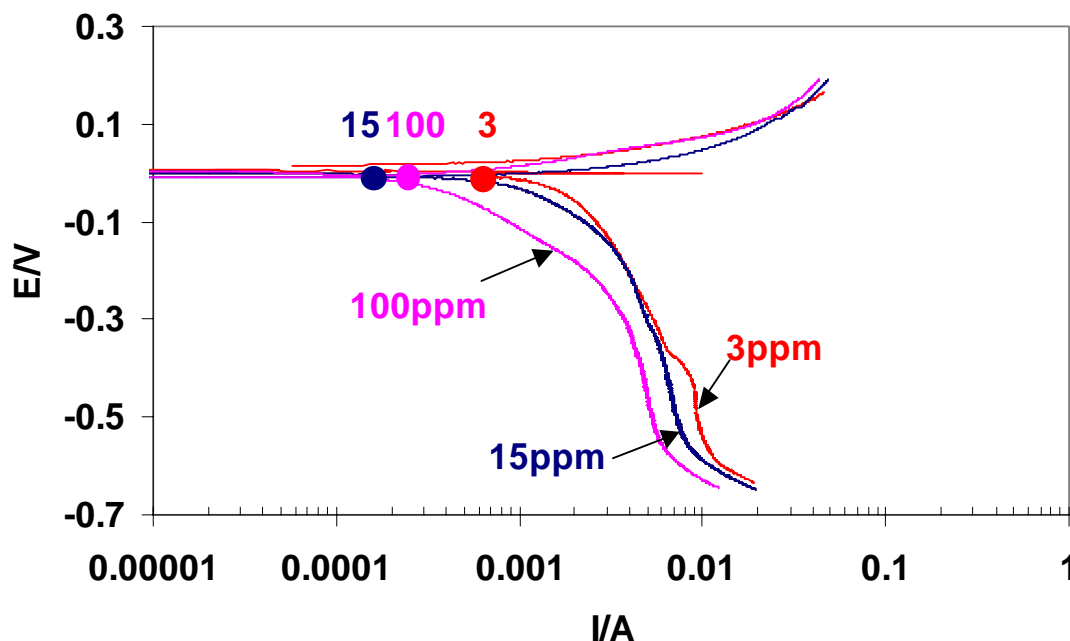


Figure 34. Effect of H_2S concentration in single phase flow for $T=60^\circ\text{C}$, $p(\text{CO}_2)=7.7$ bar, $\text{pH}4$, $v=1.92\text{m/s}$, $V_{\text{sg}}=3.0$ m/s. Data taken from Brown and Lee.⁸²

However, there were major inconsistencies between the corrosion rate obtained from the LPR technique and Tafel analysis from potentiodynamic sweep technique. Moreover, the shape of the cathodic sweeps were difficult to interpret, as there appeared to be a Tafel region with a slope of 300-500 mV/decade. From a theoretical point of view this is almost impossible to justify and therefore it has been concluded that the cathodic sweeps were unreliable. It is hypothesized that during the cathodic sweep, as the pH increased, accelerated surface film buildup occurred and an artificial reduction of the currents was recorded. This is the reason for unrealistically high apparent cathodic Tafel slopes and the observed inconsistency between LPR and sweep measurements.

Overall it can be summarized that potentiodynamic sweep measurements were not a sufficiently sensitive tool for studying the mechanisms of CO₂/H₂S corrosion and therefore need to be complemented in the future with other less intrusive electrochemical techniques such as AC impedance.

Therefore a transient electrochemical technique such as Electrochemical Impedance Spectroscopy (EIS) was used to study CO₂/H₂S corrosion because it is less intrusive than the potentiodynamic sweep technique. The underlying principle of EIS is to disturb the reaction from the steady state by applying a small amplitude, sinusoidal perturbation to the electrochemical system forcing the system to relax to a new steady state. As the various elementary processes change at different rates, the responses can be obtained at different frequencies in a single experiment. Therefore, it is a powerful diagnostic method for analyzing CO₂/H₂S corrosion mechanisms involving multiple charge transfer steps with adsorbed intermediates at the metal surface. No systematic studies of CO₂/H₂S corrosion have been made previously using the EIS technique. Since significant data processing is often required for EIS data, a mechanistic EIS analytical model was therefore developed in order to provide mechanistic information. Detailed derivation of the mechanistic EIS analytical tool is described in Appendix C.

6.2.1 Experiments

In order to determine the mechanism and the missing physical constants for H₂S/CO₂ corrosion, experiments were conducted in a glass cell on API 5L X65 carbon steel at film free conditions shown in Figure 35 below. In these experiments the

corrosion process was monitored with two different electrochemical measurement techniques: Electrochemical Impedance Spectroscopy (EIS) and Linear Polarization Resistance (LPR). Experiments for each H₂S concentration were conducted at least twice to make sure the result was reproducible and reliable.

6.2.2 Experimental equipments

A three-electrode set-up was used in the electrochemical experiments. A rotating cylinder electrode with a speed control unit was used as the working electrode. A concentric graphite ring was used as a counter electrode. A saturated Ag/AgCl reference electrode was used and was externally connected to the cell via a Luggin capillary and a porous wooden plug. The pH was followed with an electrode directly immersed into the electrolyte. H₂S and CO₂ gases were scrubbed by gas absorbent. Electrochemical measurements were made with a Gamry Instruments, Inc. potentiostat connected to a PC Pentium III computer.

A schematic diagram of glass cell experimental setup is shown below:

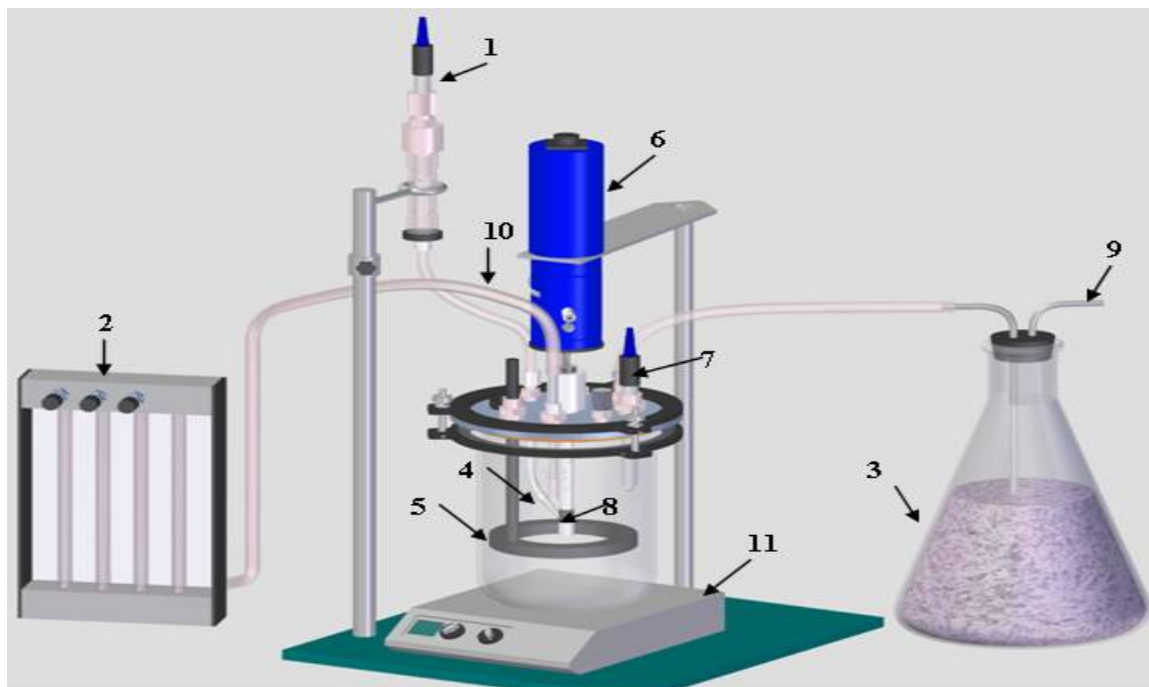


Figure 35 Schematic of the experimental test cell: 1-Ag/AgCl reference electrode, 2-gas rotameter, 3-H₂S scrubber (gas absorbent) , 4-Luggin capillary, 5-graphite counter electrode, 6-rotator, 7-pH electrode, 8-working electrode, 9-gas out, 10-gas in, 11-temperature control unit/stirrer.

6.2.3 Material

A typical construction API 5L X65 carbon steel was tested. The chemical composition of the steel is given in Table 1. The working electrode was machined from the parent material into a cylinder 12 mm in diameter and 14.3 mm long. The exposed area of the specimen was 5.4 cm².

Table 11. Chemical composition of the API 5L X65 carbon steel used for the working electrode (mass%)

C	Mn	Si	Nb	V	Fe	P	S	Cr	Cu	Ni	Mo	Al
0.150	1.34	0.24	0.03	0.055	Balanced	0.011	0.004	0.011	0.01	0.02	0.103	0.032

6.2.4 Experimental Procedure

The glass cell was filled with 2 liters of electrolyte: de-ionized distilled water + 3 mass% NaCl. Initially CO₂ gas was bubbled through the electrolyte (at least one hour prior to experiments) in order to saturate and deaerate the solution. Monitoring of pH was used to determine whether the solution is in equilibrium. NaHCO₃ was deaerated before being added to adjust the solution to pH 5. In different experiments various concentrations of H₂S in CO₂ gas were then bubbled through the electrolyte (at least 1 hour) in order to saturate the solution. The H₂S concentration can be maintained precisely by adjusting the flow rate ratio of CO₂ to H₂S with gas rotameter. The gaseous concentration of H₂S was verified by colorimetric tube before the experiment was conducted. The steel working electrode surface was then polished with 220 and 600 grit silicon carbide paper, washed with alcohol, mounted on the specimen holders, and immersed into the electrolyte. The free corrosion potential was followed immediately after immersion. The Linear Polarization Resistance (LPR) technique was used to measure the polarization resistance R_p .

After 20 minutes of immersion at the free corrosion potential, EIS measurements were conducted by applying an oscillating potential $\pm 5\text{mV}$ around the free corrosion potential to the working electrode using the frequency range 0.001 Hz to 5000 Hz. The experimental conditions are listed in Table 12.

Table 12. Experimental conditions for CO₂/H₂S film-free corrosion study

Test solution	Water + 3 mass% NaCl
Test material	API 5L X65 Carbon steel
Temperature	20°C
Pressure	1 bar
pH	5
Fe ²⁺	<1 ppm
Velocity	1000 rpm
Gaseous H ₂ S concentration in CO ₂	0, 3, 15, 40, 100, 340 ppm
Sweep rate	0.125 mV/s
Polarization resistance	From -5 to +5 mV vs. E _{oc}
Potentiostatic EIS	
DC current	0 mV vs. E _{corr}
AC potential	±5 mV
Frequency range	0.001 – 5000 Hz
Test duration	4 – 48 hours

6.2.5 Results and discussion of mechanisms

Before any experiments were conducted using the EIS technique in slightly sour environments, a number of baseline experimental results needed to be established in the absence of H₂S to serve as reference points in order to better understand the role of H₂S on the corrosion of carbon steel.

Figure 36 demonstrates the effect of 3 ppm H₂S concentration on the characteristics of the impedance plots at the corrosion potential. For carbon steel X65 in the pH 5 H₂S-free saturated CO₂ solution at corrosion potential, the impedance diagram exhibits a depressed semi-circle at high frequencies indicating a double-layer capacitance, as well as an inductive loop at lowest frequencies. A depressed semi-circle is not uncommon for iron dissolution in acidic media and it was suggested in the literature that the

heterogeneous surface roughness and the nonuniform distribution of current density on the surface may be related to it.^{127,128} The Nyquist impedance diagram showed no mass transfer controlled impedance under these conditions; however, it was not a pure charge transfer controlled process either because the inductive loop at low frequencies indicated that the iron dissolution mechanism might occur in two steps involving an adsorbed intermediate. According to Keddam et al.,^{129,130} the inductive loop at the low frequency was related to the relaxation time of the intermediate adsorbed species, $(\text{FeHCO}_3)^+_{\text{ad}}$. Moreover, the characteristics of the impedance diagram did not change after 4 hours of immersion.

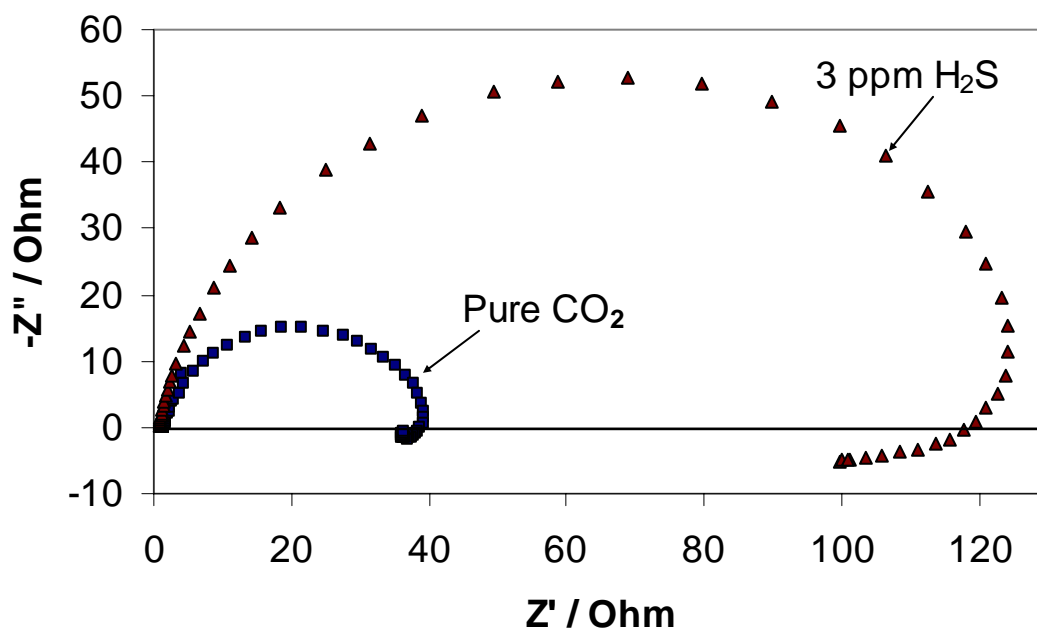


Figure 36. Effect of 3 ppm gaseous H_2S on the Nyquist impedance diagram for carbon steel X65 in pH 5 saturated CO_2 solution of water + 3% NaCl, $p = 1$ bar, $t = 20^\circ\text{C}$, $\omega = 1000$ rpm at corrosion potential (vs. Ag/AgCl).

With the addition of 3 ppm gaseous H₂S, the steady-state impedance diagram at corrosion potential demonstrated a larger depressed semi-circle with similar characteristics. Moreover, the polarization resistance (R_p) values that intercepted the real axis of the Nyquist plot are three times larger than that of the H₂S free solution, matching a lower corrosion rate of 0.28 mm/year measured by LPR (Figure 38). These results suggest that the mechanism is still charge-transfer controlled in the presence of 3 ppm gaseous H₂S, but the sulfide film detected on the electrode surface (using EDS)¹³¹ had inhibited the corrosion rate by a coverage effect.

In order to investigate the effect of very small H₂S concentrations, other sets of experiments were conducted by saturating the solution with 15 ppm, 40 ppm, 160 ppm and 340 ppm of gaseous H₂S in CO₂, while keeping all other conditions the same. The steady-state Nyquist plot shown in Figure 37 demonstrates that the diameter of depressed semi-circle increases with increasing H₂S concentration, while maintaining similar characteristics and exhibits only charge-transfer controlled behavior. On the other hand, the increase in polarization resistance R_p from EIS measurements also indicated the decrease in corrosion rate with increasing H₂S concentration. The R_p from both EIS and LPR measurements were converted into corrosion rate and a good agreement was reached between the two techniques (Figure 38). From the above evidence, it can be concluded that the sulfide film did not act as a diffusion barrier, but rather had inhibited the corrosion by a coverage effect under these experimental conditions. Although the surface coverage effect strongly depends on H₂S concentration, the inhibition of corrosion rate

reaches plateau at 0.06 mm/year and ceases to decrease significantly beyond 160 ppm of H_2S concentration.

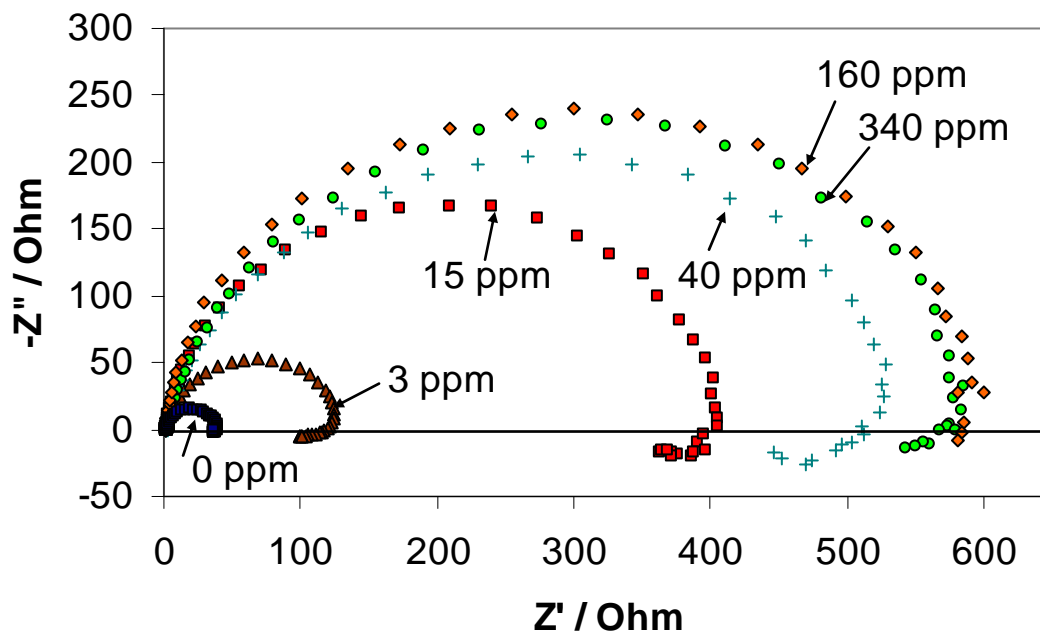


Figure 37. Effect of gaseous H_2S concentration on the steady-state Nyquist impedance diagram for carbon steel X65 in pH 5 saturated CO_2 solution of water + 3% NaCl, $p = 1$ bar, $t = 20^\circ\text{C}$, $\omega = 1000$ rpm at corrosion potential.

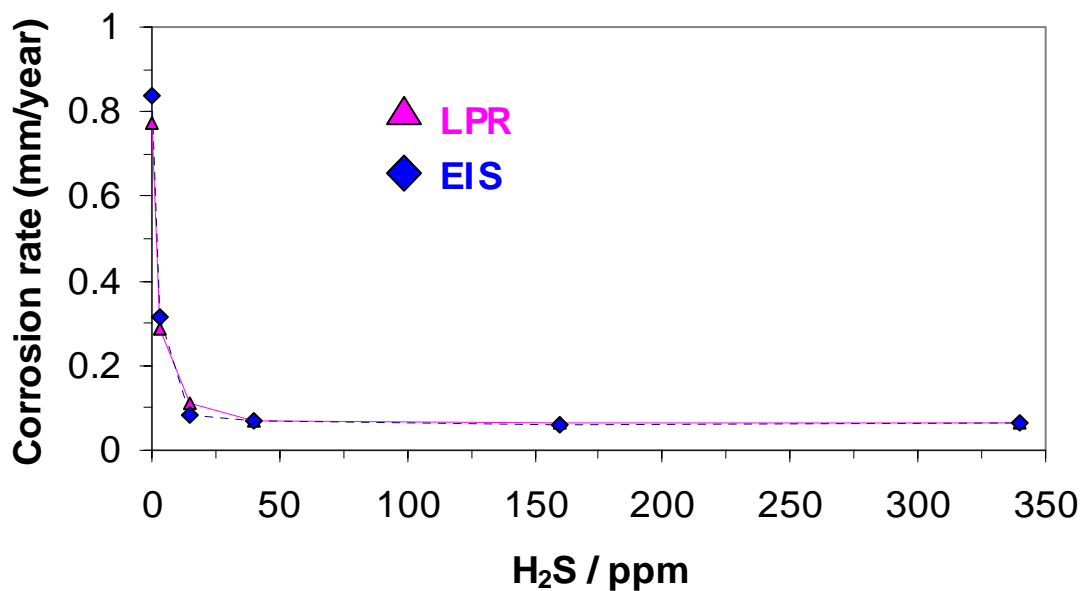


Figure 38. Effect of H₂S gaseous concentration on the final stabilized corrosion rate (measured by LPR and EIS) of carbon steel X65 in pH 5 saturated CO₂ solution, water + 3% NaCl, p = 1 bar, t = 20 °C, ω = 1000 rpm. Experiments were repeated for each H₂S concentration.

Moreover, a large number of carefully controlled corrosion experiments has been conducted in flow loop under different temperatures (60 °C and 80 °C), partial pressures of CO₂ (7.7 bar) and velocities (stagnant to 3 m/s) in both single and multiphase flow.⁸² The results obtained from the flow loop experiments (under high temperature and high pressure) have very similar trends compared to that of glass cell experiment (low temperature and low pressure). All the experimental data clearly indicate that the presence of even very small amounts of H₂S (10 ppm in the gas phase) leads to rapid and drastic reduction in the corrosion rate. However, this trend is slowed down or even somewhat reversed at higher H₂S concentration. The effect seems to be universal and depend only on the H₂S concentration because all the data obtained at very different

conditions follow the same trend, as shown in Figure 39. The corrosion rate in Figure 39 was normalized with the pure CO₂ corrosion rate that was obtained in the absence of H₂S.

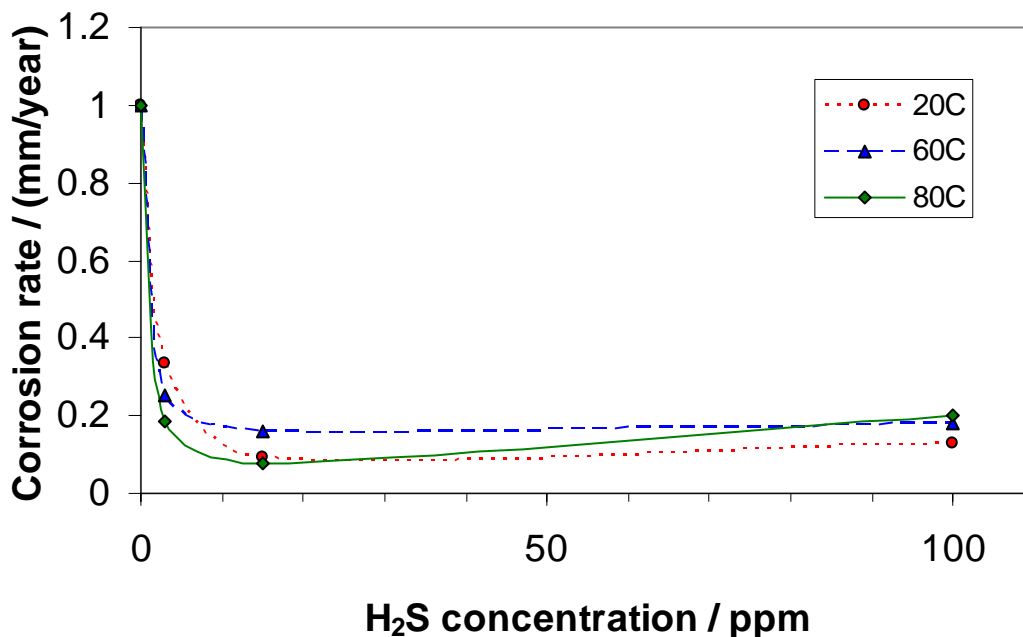


Figure 39. Normalised corrosion rate obtained under various environmental parameters in film free conditions: pH<5 p = 1 to 7 bar, t = 20-80°C, v=stagnant to 3 m/s.

On the other hand, from the EIS plot one can observe how the depressed semi-circle increases in diameter over time in Figure 40, which demonstrates the transient characteristics of the Nyquist impedance diagram in the presence of 340 ppm gaseous H₂S. The initial EIS measurement (taken after 20 minutes of immersion) suggests that a protective thin sulfide film had formed via solid state formation²⁷ at the electrode surface immediately after immersion. The low-frequency data (of the initial EIS measurement) that drifts below the x-axis is not of instrumental error, but indicates the transient increase of polarization resistance (R_p) during the long EIS measurement, hence illustrating the

increase of surface coverage over time. By the end of first EIS measurement, the electrode had been immersed in the solution for 4 hours and the lowest frequency ($f=0.001$) data point indicated that R_p was already 394 ohm (denoted by the larger marker), matching a low corrosion rate of 0.08 mm/year (measured by LPR). Comparing to the corrosion rate of H_2S -free solution (0.84 mm/year), this result suggests that mackinawite film had achieved a ten-fold inhibition of corrosion rate within 4 hours of immersion under the experimental condition. The characteristics of the impedance diagram stopped changing after 36 hours of immersion indicating that the sulfide film had reached an equilibrium and the corrosion rate remained constant throughout the rest of the experiment.

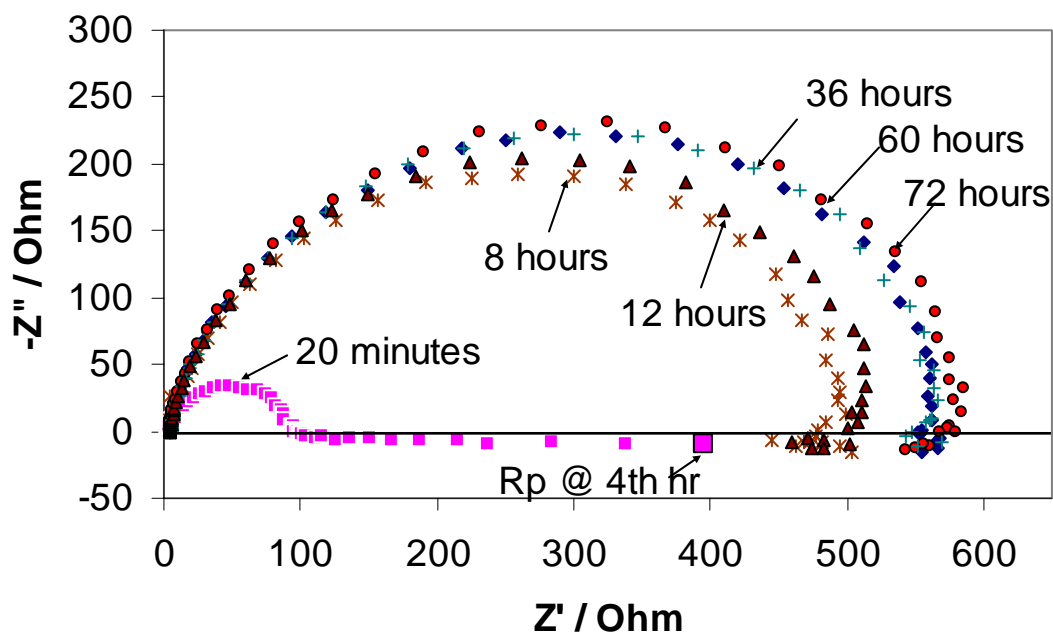


Figure 40. Effect of immersion time on Nyquist impedance diagram of carbon steel X65 in pH 5 saturated CO_2 solution with 340 ppm gaseous H_2S , water + 3% NaCl, $p = 1$ bar, $t = 20^\circ C$, $\omega = 1000$ rpm at corrosion potential.

6.2.6 Surface Analysis

In order to ascertain the property of the transparent thin film that caused the retardation of CO₂ corrosion rate in the presence of H₂S, a thin film analysis was necessary. X-ray photoelectron spectra were obtained with a Kratos Ultra Axis electron energy analyzer using an Al K α non-monochromatic source (1486.6 eV) at Ohio State University. The base pressure in the analytical chamber was of the order of 10⁻⁹ mbar. The energy scale was calibrated using the Ag(3d_{5/2})(368.2 eV) lines. Survey and narrow XPS spectra were obtained with an analyzer pass energy of 80 and 20 eV, respectively. Raw spectra were smoothed before being fitted using a Shirley base line and a Gaussian-Lorentzian shape peak. The aliphatic adventitious hydrocarbon C(1s) peak at 284.6 eV was adopted as a check for surface charging.

The XPS survey scan of the sample (retrieved after 72 hours of immersion in a saturated CO₂ solution with gaseous concentration of 340 ppm H₂S and 3% NaCl) indicated the presence of O, C, Na, Cl, Fe and S at the sample surface (shown in Figure 41). Even by taking precautions during the preparation of the sample for analysis, it was not possible to completely eliminate oxygen that adsorbed at the surface. Otherwise, carbon was an ubiquitous contaminant.

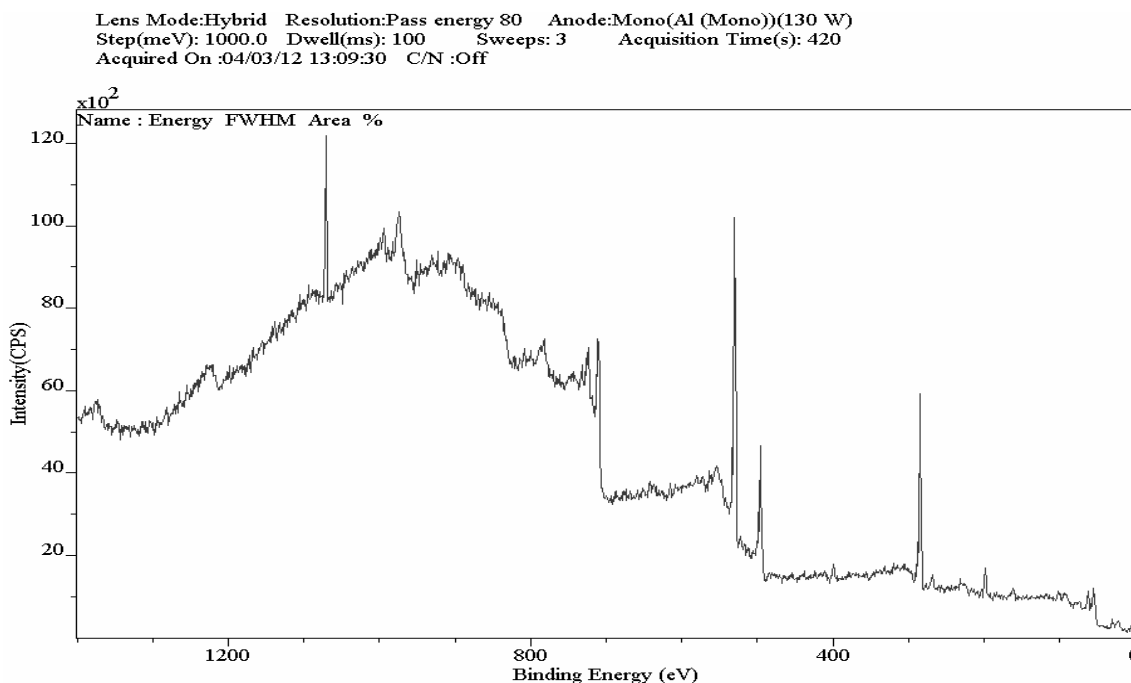


Figure 41. Survey scan on the carbon steel X65 surface after 72 hours of immersion in pH 5 saturated CO₂ solution with 340 ppm gaseous H₂S, water + 3% NaCl, p = 1 bar, t = 20°C, ω = 1000 rpm.

The narrow region spectra for Fe(2p_{3/2}) and S(2p) are shown in Figure 42 and Figure 43, respectively. No charge correction was necessary. The Fe(2p_{3/2}) spectrum consists of two major contributions occurring at 710.4eV and 712.1eV, the second peak corresponds to the chemical shift in the photoelectron binding energy of Mackinawite from elemental iron Fe.^{132,133} On the other hand, the S(2p) spectrum presents a major contribution which has peak occurring at 162.3 eV, which also matches the shift in photoelectron binding energy of Mackinawite from elemental sulfur S.^{132,133} Furthermore, the semi-quantitative surface composition (±10%) was calculated from the peak areas and theoretical cross-sections,¹³⁴ giving Fe:S atomic mass concentration ratio of 1 to 0.847, which matches the chemical composition of Mackinawite (FeS_{1-x})^{135,136,137}

and supports the analysis of the spectra. Hence, it can be concluded that Mackinawite film had inhibited the corrosion by a coverage effect under these experimental conditions.

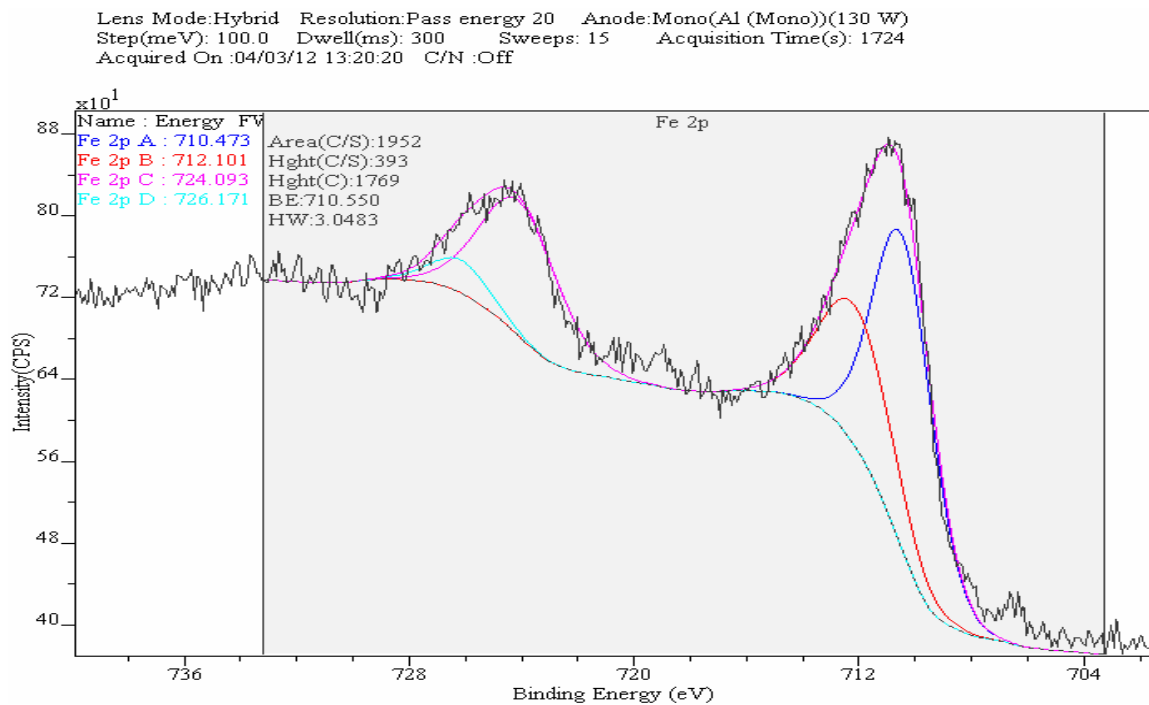


Figure 42. Narrow scans of Fe(2p_{3/2}) spectrum on the carbon steel X65 surface after 72 hours of immersion in pH 5 saturated CO₂ solution with 340 ppm gaseous H₂S, water + 3% NaCl, p = 1 bar, t = 20°C, ω = 1000 rpm , including fitted curves.

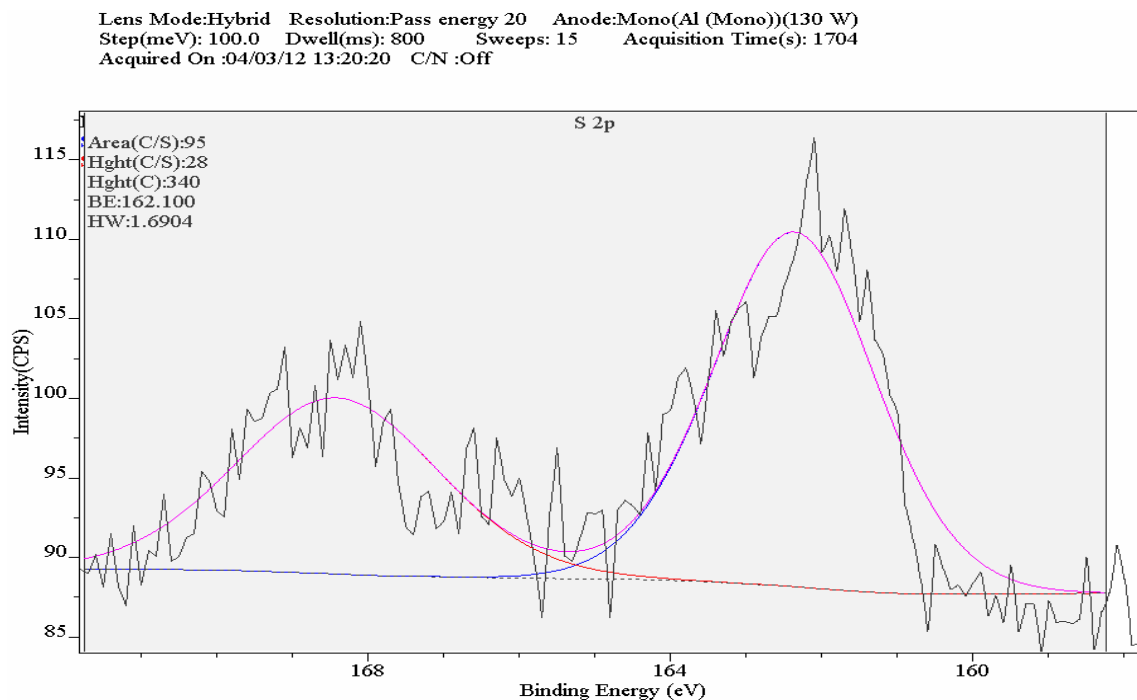


Figure 43. Narrow scans of S(2p) spectrum on the carbon steel X65 surface after 72 hours of immersion in pH 5 saturated CO₂ solution with 340 ppm gaseous H₂S, water + 3% NaCl, p = 1 bar, t = 20°C, ω = 1000 rpm, including fitted curves.

6.3 Mathematical Model

The above mentioned experimental results suggest that iron sulfide films such as Mackinawite can form on the surface of the steel via solid state reaction regardless of whether supersaturation is exceeded or not, which agreed with previous research done by Shoesmith et al.²⁷ These iron sulfide films have two effects: they inhibit the corrosion process by surface coverage of Mackinawite (dominant at very low H₂S concentrations) and have a catalytic effect at higher H₂S concentrations, e.g. by providing an increased area for the cathodic reaction. From EIS measurements, it was observed that the mechanism is not of mass-transfer control, but rather charge-transfer controlled. In order to account for the inhibition of a charge transfer reaction at the electrode surface, an

equation including a simple Langmuir type adsorption isotherm and a first order catalytic effect was successfully used to model the decrease of the corrosion rate:

$$1 - \theta_{H_2S} = \frac{1}{1 + K_{a/d} c_{H_2S}} + k_c c_{H_2S} \quad (63)$$

where $K_{a/d}$ = the adsorption/desorption constant for sulfide species

k_c = the catalytic rate constant.

6.4 Verification

This model was verified by comparing the predictions with experimental results as illustrated in Figure 44

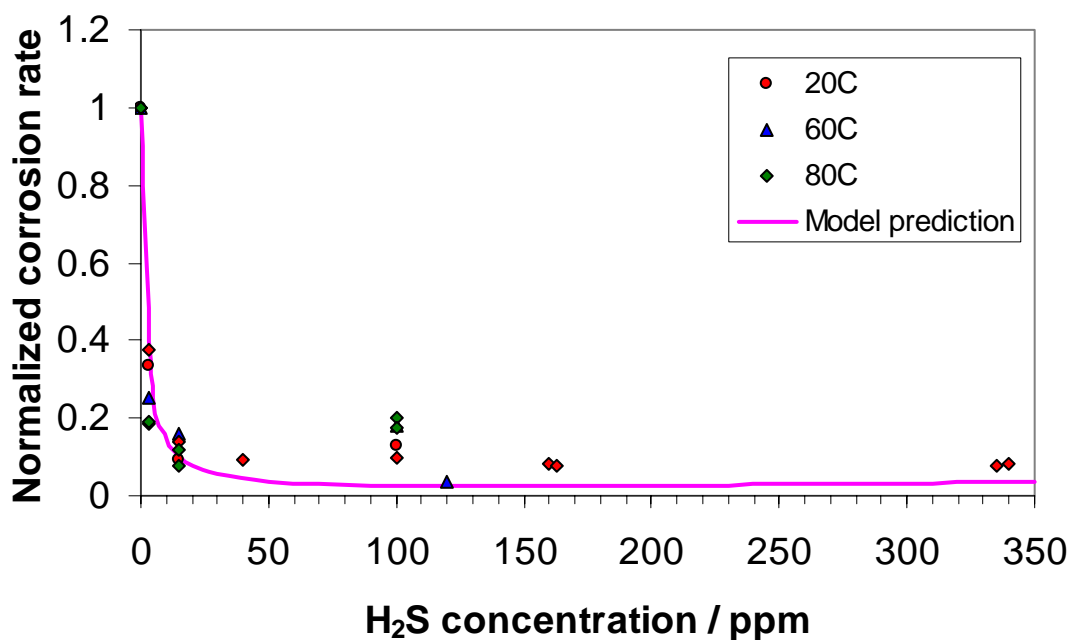


Figure 44. Comparison between model prediction and experimental data on the effect of trace amount of H₂S on CO₂ corrosion rate in the absence of iron sulfide films. ppm refers to the concentration in the gas phase.

6.5 Summary

- XPS analysis confirmed the presence of mackinawite (FeS_{1-x}) on the electrode surface under these experimental conditions.
- Mackinawite was formed immediately on the electrode via solid state formation in CO_2 solution with trace amount of H_2S .
- Under these experimental conditions, the Mackinawite film did not act as a diffusion barrier, but rather had inhibited the corrosion by a coverage effect.
- At higher H_2S concentrations, it is hypothesized that iron sulfide films may provide an increased area for the cathodic reaction.
- Langmuir type adsorption isotherm and a first order catalytic effect was successful in modeling the effect of trace amount of H_2S in the absence of iron sulfide precipitation.

**CHAPTER 7: MECHANISTIC MODEL OF CO₂/H₂S CORROSION
ACCOMPANIED BY SIMULTANEOUS IRON CARBONATE AND IRON
SULFIDE FILM GROWTH**

7.1 Introduction

After the groundwork on CO₂/H₂S corrosion modelling in film-free conditions has been laid (as described in the previous Chapter 6), the modelling of iron sulfide film growth and its complex interaction with CO₂/H₂S corrosion is discussed in this chapter.

The addition of iron sulfide film growth to the mechanistic CO₂/H₂S corrosion model is the final piece of work that completes this Ph.D. study. Using iron carbonate film growth model (Chapter 5) as a template, a similar methodology will be followed to model the formation of iron sulfide films.

7.2 Physico-Chemical Model

In CO₂ corrosion of carbon steel, when the concentrations of Fe²⁺ and CO₃²⁻ ions exceed the solubility limit, they can precipitate to form solid iron carbonate according to:



Similarly, in the presence of trace amount of H₂S, when the concentrations of Fe²⁺ and S²⁻ ions exceed the solubility limit, they can precipitate to form solid iron sulfide according to:



When films precipitates at the steel surface, it can slow or stop the corrosion process by presenting a diffusion barrier for the species involved in the corrosion process. Film growth depends primarily on the precipitation rate of either iron carbonate or iron sulfide or both (R_{FeCO_3} or R_{FeS}). The film grows in density as well as thickness as it precipitates. However, the steel surface corrodes under the film, continuously creating a “void” between the film and the steel surface (here called “film undermining”). As soon as it is created, the void starts filling by the ongoing precipitation. The competitive effect between undermining and precipitation of pure iron carbonate films has been extensively discussed in Chapter 5.

The proposed equation describing the simultaneous iron carbonate and iron sulfide film growth kinetics are obtained by writing mass balances for the solid iron carbonate and iron sulfide:

$$\underbrace{\frac{\partial c_{FeCO_3(s)}}{\partial t}}_{\text{local change}} = \underbrace{R_{FeCO_3(s)}}_{\text{precipitation rate}} - \underbrace{CR \frac{\partial c_{FeCO_3(s)}}{\partial x}}_{\text{undermining rate}} \quad (66)$$

$$\underbrace{\frac{\partial c_{FeS(s)}}{\partial t}}_{\text{local change}} = \underbrace{R_{FeS(s)}}_{\text{precipitation rate}} - \underbrace{CR \frac{\partial c_{FeS(s)}}{\partial x}}_{\text{undermining rate}} \quad (67)$$

expressing the fact that the amount of solid iron carbonate and iron sulfide found at any location, $c_{FeCO_3(s)}$, $c_{FeS(s)}$ in kmol/m^3 will increase over time because of precipitation and/or will decrease due to the undermining effect.

The last term on the right hand side (rhs) in equation (66) and (67) has the same meaning as already described in Section 5.

It is convenient to express the combined morphology of the mixed iron carbonate / iron sulfide film via the distribution of volumetric porosity ε since it is used as the principal film parameter affecting transport of species. In this case volumetric porosity is defined as:

$$\varepsilon = \frac{V_{\text{void}}}{V_{\text{total}}} = \frac{(V_{\text{total}} - V_{\text{FeCO}_3(s)} - V_{\text{FeS}})}{V_{\text{total}}} = 1 - \frac{V_{\text{FeCO}_3(s)}}{V_{\text{total}}} - \frac{V_{\text{FeS}(s)}}{V_{\text{total}}} \quad (68)$$

where V_{void} = volume occupied by void within control volume;

V_{total} = total volume of each individual control volume;

V_{FeCO_3} = volume occupied by FeCO_3 in a control volume;

V_{FeS} = volume occupied by FeS in a control volume

Rearranging and combining film growth equation (66) and (67) to express it in terms of porosity yields:

$$\frac{\partial \varepsilon}{\partial t} = - \frac{M_{\text{FeCO}_3(s)}}{\rho_{\text{FeCO}_3(s)}} R_{\text{FeCO}_3(s)} - \frac{M_{\text{FeS}(s)}}{\rho_{\text{FeS}(s)}} R_{\text{FeS}(s)} - CR \frac{\partial \varepsilon}{\partial x} \quad (69)$$

where $M_{\text{FeCO}_3(s)}$ = the molecular mass of iron carbonate (115.847 kg/kmol).

$\rho_{\text{FeCO}_3(s)}$ = the density of iron carbonate (3900 kg/m³).

$M_{\text{FeS}(s)}$ = the molecular mass of iron sulfide (87.9 kg/kmol).

$\rho_{\text{FeS}(s)}$ = the density of iron sulfide (2500 kg/m³).

The iron carbonate kinetics $R_{\text{FeCO}_3(s)}$ is previously described in chapter 5. Similar to $R_{\text{FeCO}_3(s)}$, the rate of iron sulfide precipitation R_{FeS} in equation (69) can also be

described as a function of supersaturation S , solubility limit K_{sp} , temperature T , and surface area-to-volume ratio A/V :⁴⁸

$$R_{FeS(s)} = \exp\left(16.2584 \frac{9520.648}{T}\right) \cdot \frac{A}{V} \cdot [(S_{FeS})^{0.5} - 1]^2 \quad (70)$$

Since the local concentration of Fe^{2+} and S^{2-} ions can be obtained from the model, supersaturation for iron sulfide film can be calculated via:

$$S_{FeS} = \frac{c_{Fe^{2+}} c_{S^{2-}}}{Ksp_{(FeS)}} \quad (71)$$

where the solubility product for FeS is defined as:⁴⁸

$$Ksp_{(FeS)} = \exp\left(-81.369 + \frac{12391.7}{T}\right) \quad (72)$$

with temperature(T) in Kelvin.

The expression describing the kinetics of iron sulfide precipitation shown above was proposed by Harmandas and Koutsoukos⁴⁸ and is used in conjunction with the film growth model, because it is the only reference that had published the precipitation kinetics of iron sulfide. Within the context of the present model, the surface area-to-volume ratio A/V for R_{FeS} is assumed to be the same as that of $R_{FeCO_3(s)}$. When the concentrations of Fe^{2+} and S^{2-} ions exceed the solubility limit, additional Fe^{2+} and S^{2-} concentration sinks were implemented in the corrosion model to account for the consumption of these ions due to the formation of iron sulfide films reaction, which also

affects the fluxes and concentration gradients for both the ions and all other sulfide species..

Equation (66) and (67) that describe the mass balance for the solid iron carbonate and iron sulfide can also be rearranged to express in terms of volume occupied by either iron carbonate or iron sulfide films, respectively:

$$\underbrace{\frac{\partial V_{FeCO_3(s)}}{\partial t}}_{\text{local change}} = \underbrace{\frac{M_{FeCO_3}}{\rho_{FeCO_3}} R_{FeCO_3(s)}}_{\text{precipitation rate}} - CR \underbrace{\frac{\partial V_{FeCO_3(s)}}{\partial x}}_{\text{undermining rate}} \quad (73)$$

$$\underbrace{\frac{\partial V_{FeS(s)}}{\partial t}}_{\text{local change}} = \underbrace{\frac{M_{FeS}}{\rho_{FeS}} R_{FeS(s)}}_{\text{precipitation rate}} - CR \underbrace{\frac{\partial V_{FeS(s)}}{\partial x}}_{\text{undermining rate}} \quad (74)$$

Knowing the ratio of volume occupied by iron carbonate and iron sulfide enables us to predict the composition of mixed films at different locations by using the following expressions:

$$vol\%_{FeCO_3(s)} = \frac{V_{FeCO_3(s)}}{V_{FeCO_3(s)} + V_{FeS(s)}} \times 100 \quad (75)$$

$$vol\%_{FeS(s)} = \frac{V_{FeS(s)}}{V_{FeCO_3(s)} + V_{FeS(s)}} \times 100 \quad (76)$$

7.3 Verification and Parametric Study

At the initial stage, the growth of iron sulfide has been modeled in the same way as that of iron carbonate due to the lack of quantitative information iron sulfide formation, especially the kinetics of iron sulfide precipitation. Observations from experiments in film forming conditions can be used to assist the understanding of the mechanism and thus improve the model. CO₂/H₂S corrosion experiments were conducted in supersaturated conditions in the flow loop by Bruce Brown.¹²⁶ Experiments were conducted in a 1% NaCl solution at 60°C, pH 6.0, 0.77MPa partial pressure CO₂, with trace amounts of H₂S in both single phase flow ($V_{sl} = 1$ m/s) and multiphase flow ($V_{sg}=3$ m/s, $V_{sl}= 1$ m/s). Corrosion testing was conducted in the region of low supersaturation values for iron carbonate ($SS_{FeCO_3} < 10$) and three different supersaturation values for iron sulfide ($2.5 < SS_{FeS} < 125$) through adjustment of the partial pressure of H₂S for three 30 day exposures. Under the conditions tested, both iron carbonate and mackinawite films were observed as adherent corrosion product films. The results obtained by Brown from these experiments were used to compare against the model prediction in order to verify and fine tune the model. The experimental test matrix is shown below:

Table 13. Experimental Test Matrix for CO₂/H₂S flow loop in film-forming conditions

Parameter	Conditions
CO ₂ partial pressure	0.77MPa (7.7 bar)
Solution	1% NaCl solution, pH6
Corrosion Rate Measurement	Weight loss (C1018 and X-65) Linear Polarization Resistance
Single-phase flow	$V_{sl} = 1$ m/s
Temperature	60°C
Test Time	25 days
H ₂ S gaseous concentration	120 ppm
Fe ²⁺ concentration	17 ppm

7.3.1 Corrosion rate comparison

Since the composition of films was described in detail for the experiment 3 from Brown's study¹²⁶, it was used to verify the model. The initial corrosion was observed to be 0.65mm/year, which was low due to the retardation by the Mackinawite film via solid state formation, then the corrosion rate decreased further due to the precipitation of mixed film. Figure 45 indicates that both the initial corrosion rate and the transient change of corrosion rate can be somewhat captured by the model. It should be noted that this is the first attempt to compare the experimental results against a model that adapts the kinetics of iron sulfide precipitation⁴⁸ without any modification.

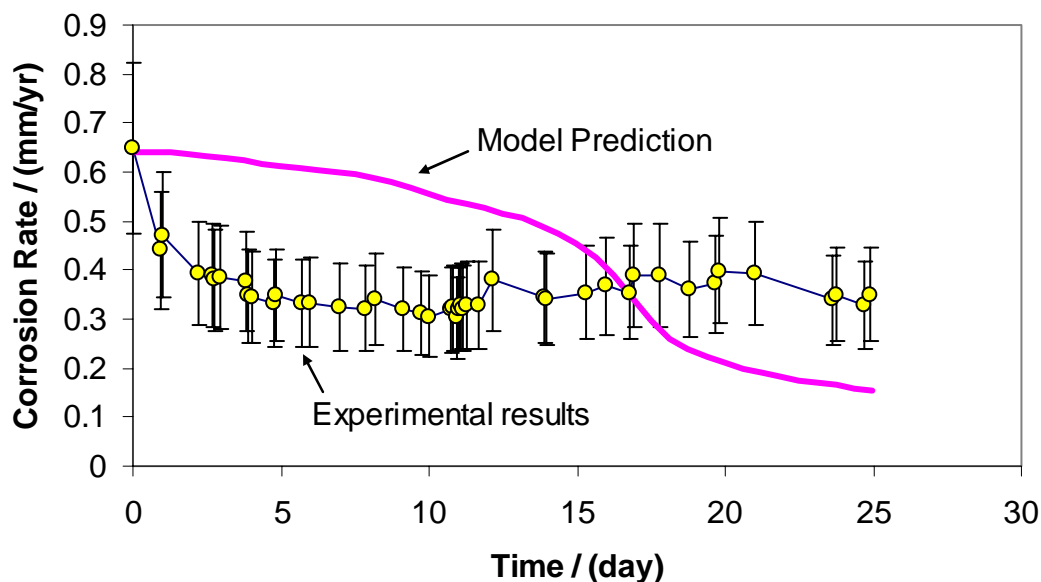


Figure 45. First attempt at the comparison between the model prediction and the measured corrosion rate from the flow loop experiment in the presence of trace amount of H_2S at film forming conditions: pH 6 saturated CO_2 solution with 120 ppm gaseous H_2S , water + 1% NaCl, $P_{\text{CO}_2} = 7.7$ bar, $t = 60^\circ\text{C}$, $\text{Fe}^{2+} = 17\text{ppm}$.

7.3.2 Film comparison

The film developed after the 25 day exposure to system conditions in multiphase flow was analyzed by EDS. A cross-sectional view of the coupon in Figure 46 shows three layers of film developed on the surface. From the surface of the coupon outward, the first 60 μm layer was analyzed with EDS and found to have 0% Sulfur, 32.4% Iron, 13.4% Carbon, and 26.5% Oxygen. The next 60 μm layer was found to have 15% Sulfur, 31.2% Iron, 20.8% Carbon, and 11.2% Oxygen. The outermost 30 μm layer was found to have 11% Sulfur, 33% Iron, 22% Carbon, and 13% Oxygen.

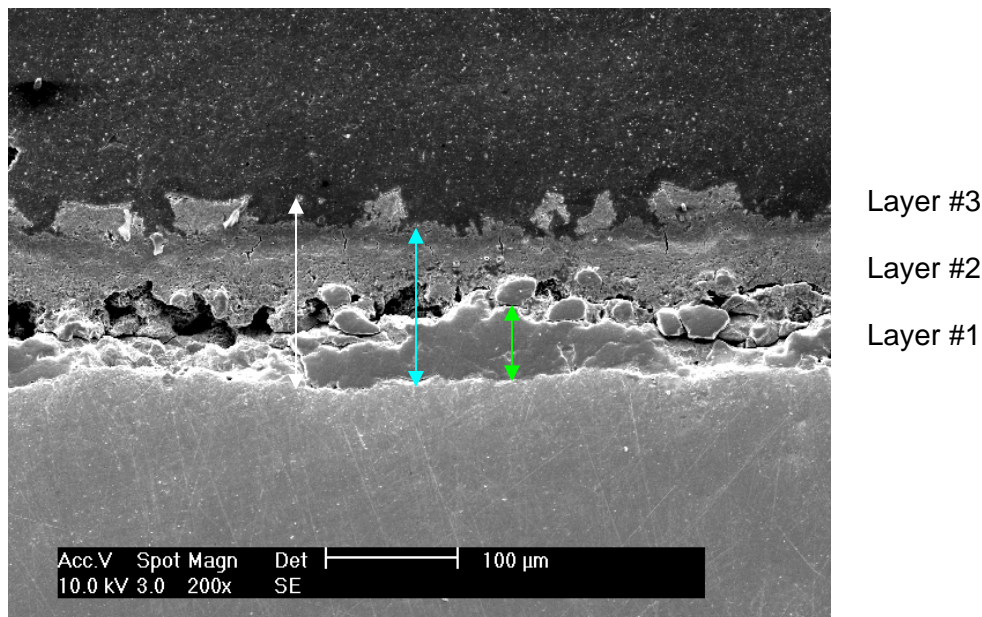


Figure 46. Cross section MP 25 day exposure of X65(2) coupon, (next to metal surface) layer #1: 60 μm, layer #2: 60 μm, and layer #3: 30 μm. Layer #1 EDS is [32.4% Fe, 0.0% S, 13.4% C, 26.5% O], the interface between layer #1 and layer #2 EDS is [35.4% Fe, 12.9% S, 14.0% C, 9.5% O], and the EDS of layer #2 is [31.2% Fe, 15.0% S, 20.8% C, 11.2% O].

The porosity with respect to distance predicted by the model is shown in Figure 47 below, which indicates that approximately 30 μm of mixed film has been formed after 25 days of exposure, which is much less than the experimental observation. On the other hand, it also predicts that first 10 μm layer is consisted of mainly iron sulfide and the outer layer is consisted of mostly iron carbonate, which is completely in contrary with the experimental observation.

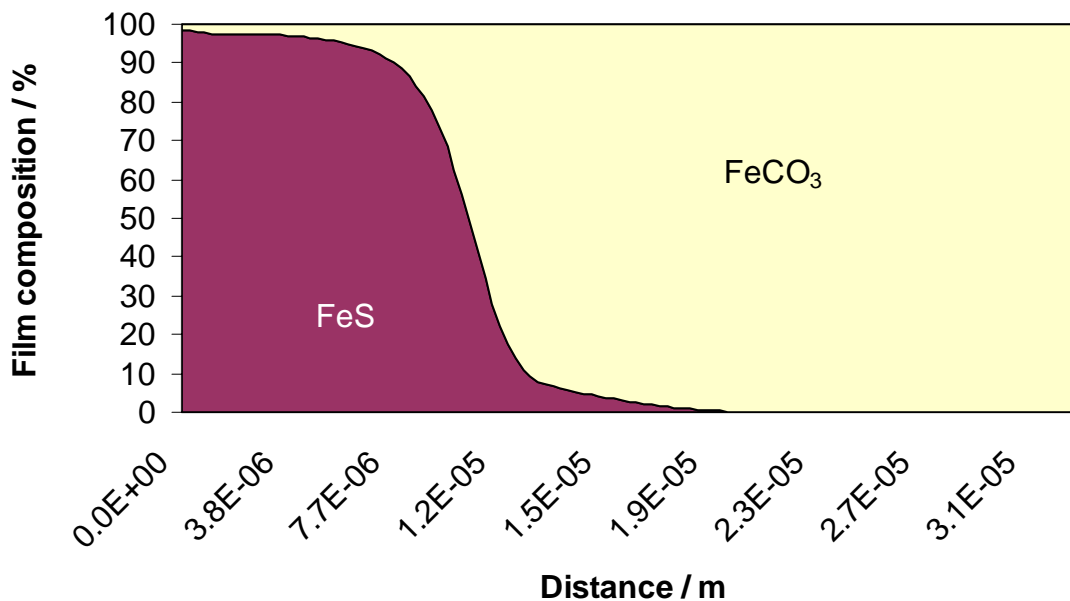


Figure 47. First attempt at predicting film thickness and composition of film without modification of kinetics of iron sulfide precipitation. After 25 days of exposure at $c_{H_2S}=120$ ppm, $T=60^\circ\text{C}$, $P_{CO_2}=7.7\text{bar}$, pH 6.0, $c_{Fe^{2+}}=17$ ppm, $v=1$ m/s.

Since the model prediction was not able to match the morphology and the composition of mixed films from experimental observation, it can be concluded that the kinetics of iron sulfide precipitation proposed by Harmandas and Koutsoukos⁴⁸ is not suitable for the model and should be modified.

In order to match the composition and morphology of mixed films, the surface area-to-volume ratio A/V for iron sulfide precipitation in equation (70) needs to be modified. It was concluded that A/V for iron carbonate precipitation is a function of porosity as shown in equation (62) and $A/V=0$ when porosity $\varepsilon=1$. However, experimental observation in chapter 6.2.6 and literature review in chapter 2.10.2 both indicate a thin layer of mackinawite is initially produced at the metal surface by solid state formation.²⁷

Hence it can be proposed that this initial layer of mackinawite will always provide a surface area at the metal surface for iron sulfide to precipitate upon, even if porosity $\varepsilon=1$ next to the metal surface. Thus A/V for iron sulfide precipitation at the metal surface was modified to make sure A/V will never be zero at the metal surface in the presence of H_2S . This modification initiates the precipitation of iron sulfide on the metal surface, even when porosity $\varepsilon=1$ on the metal surface. Moreover, the solubility product for iron sulfide in equation (72) was adjusted to give higher supersaturation, thus higher precipitation rate for iron sulfide:

$$K_{sp_{(FeS)}} = \exp\left(-81.369 + \frac{12091.7}{T}\right) \quad (77)$$

After the kinetics of iron sulfide precipitation has been modified, the model was then able to match the thickness, morphology and the composition of mixed films as shown Figure 48 and Figure 49.

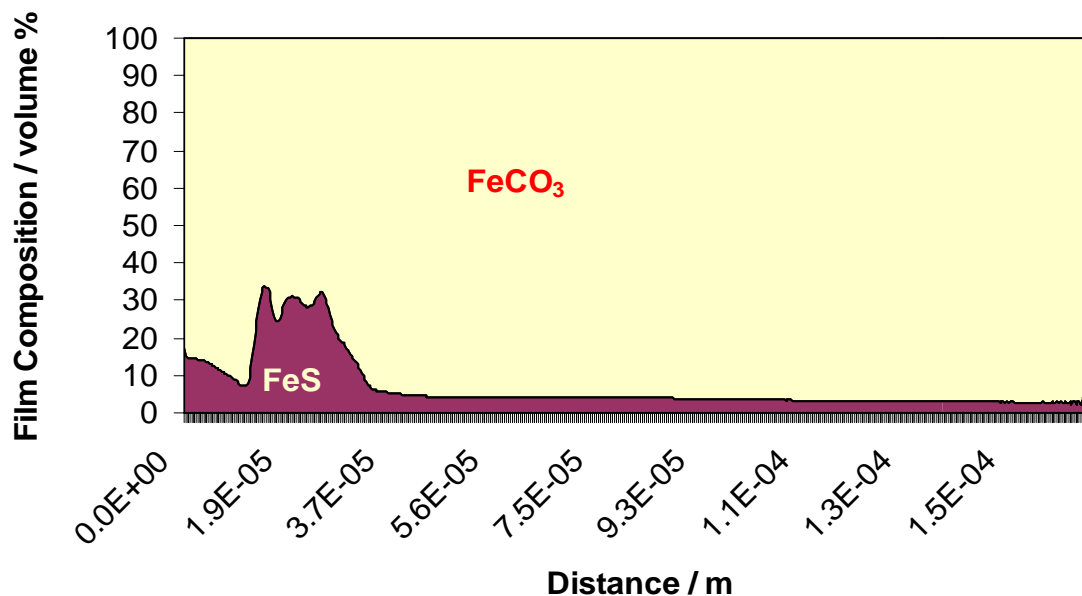


Figure 48. Second attempt at predicting film thickness and composition of film after modification of kinetics of iron sulfide precipitation. 25 days of exposure at $c_{H_2S}=120$ ppm, $T=60^\circ\text{C}$, $P_{CO_2}=7.7\text{bar}$, pH 6.0, $c_{Fe^{2+}}=17$ ppm, $v=1$ m/s.

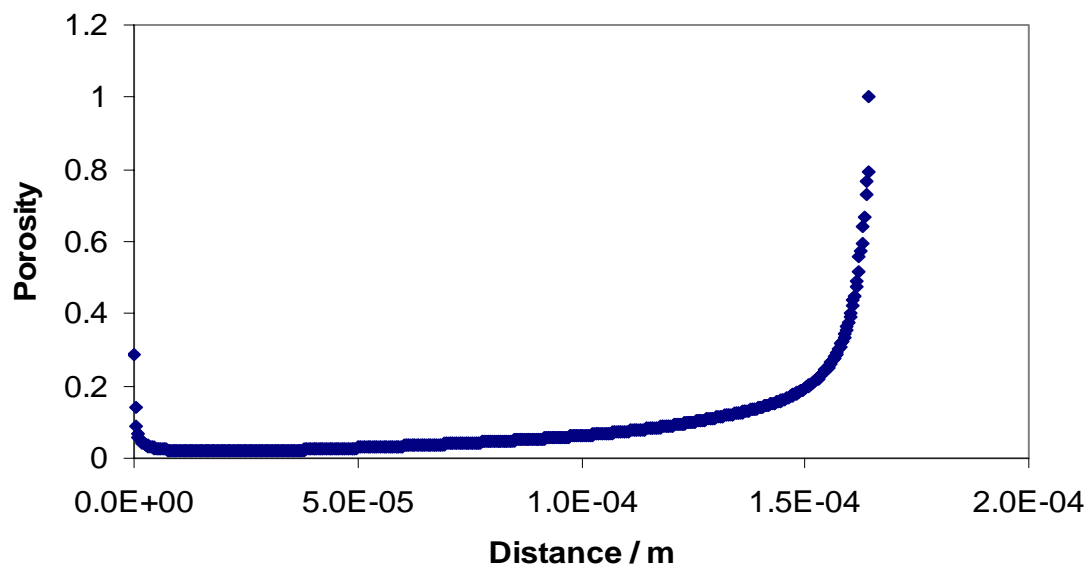


Figure 49. Second attempt at predicting film thickness and porosity of film after modification of kinetics of iron sulfide precipitation. 25 days of exposure at $c_{H_2S}=120$ ppm, $T=60^\circ\text{C}$, $P_{CO_2}=7.7\text{bar}$, pH 6.0, $c_{Fe^{2+}}=17$ ppm, $v=1$ m/s. Porosity $\varepsilon=1$ means no film.

Having modified the kinetics of iron sulfide precipitation, the model predicts a thickness of 160 micron of mixed films with three layers of different compositions. First 10 micron layer consists of mainly iron carbonate, the second 20 micron layer consists of 70% iron carbonate and 30 % iron sulfide and the third 130 micron layer is made up of mostly iron carbonate. Given the complexity of the process, the film morphology can be predicted reasonably well. Furthermore, the resulting corrosion rate prediction was also matched as shown in Figure 50.

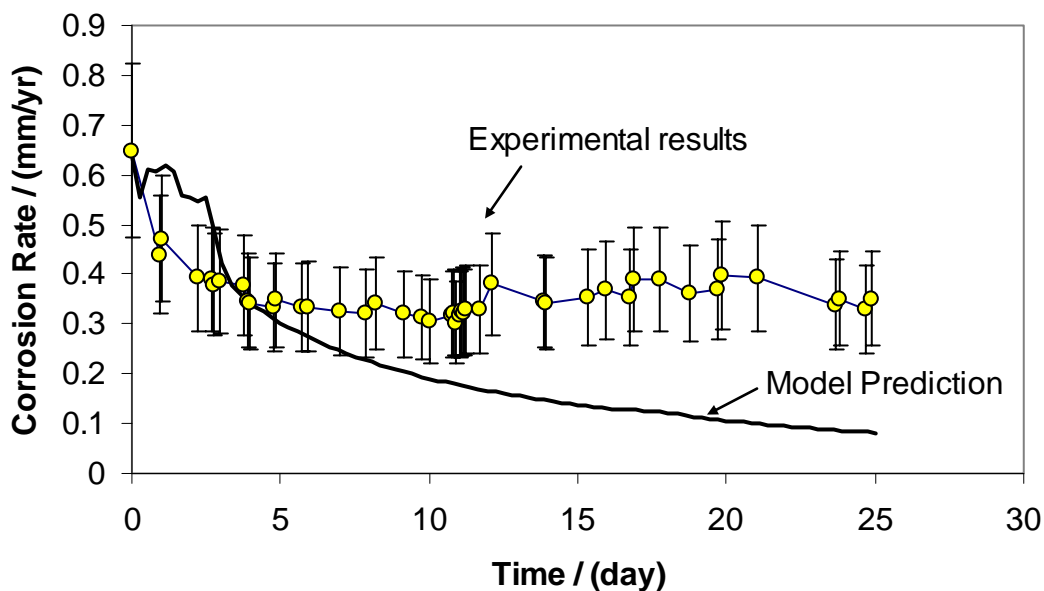


Figure 50. After modification of iron sulfide precipitation kinetics, second attempt at the comparing the model prediction and the measured corrosion rate from the flow loop experiment in the presence of trace amount of H_2S at film forming conditions: pH 6 saturated CO_2 solution with 120 ppm gaseous H_2S , water + 1% NaCl, $P_{CO_2} = 7.7$ bar, $t = 60^\circ C$, $Fe^{2+} = 17$ ppm.

7.4 parametric testing

In this section the model will be used to predict CO_2 corrosion under varying environmental conditions in order to establish its more general applicability. No direct

comparisons with experiments will be made in this section, however performance of the model will be contrasted against the general understanding of the CO₂/H₂S corrosion process in the presence of mixed iron carbonate and iron sulfide films. The same conditions for verification at T=60°C, pH=6.0, $P_{CO_2} = 7.7$ bar, $c_{H_2S} = 120$ ppm, $c_{Fe^{2+}} = 17$ ppm, $v = 1$ m/s will be used as a baseline case when varying the different parameters, one at a time.

7.4.1 The effect of H₂S concentration

The concentration of H₂S in the solution is an important factor that contributes not only to iron sulfide film formation, but also the overall morphology and thickness of the mixed film. The increase of c_{H_2S} results in higher supersaturation, which consequently accelerates the precipitation rate of FeS. However, the formation of FeS and FeCO₃ both requires the same Fe²⁺ ions in the solution and the competition between the kinetics of FeS and FeCO₃ may lead to variety of interesting scenarios. In Figure 51 the effect of c_{H_2S} on the rate of corrosion rate reduction due to mixed film formation is illustrated. In pure CO₂ conditions (0 ppm H₂S), the initial high corrosion rate of 15 mm/year is rapidly reduced to final corrosion rate of 0.4 mm/year due to the formation of a protective, dense FeCO₃ film that has a thickness of 40 μm (Figure 52). On the other hand, in the presence of H₂S, the c_{H_2S} also affects the corrosion rate by coverage effect due to solid-state formation of Mackinawite even if there are no films (at the beginning of the simulation). When $c_{H_2S} = 50$ ppm, the initial corrosion rate is immediately reduced to 0.54 mm/year due to surface coverage of Mackinawite. However, the corrosion rate did not change much with respect to time because only a thin unprotective film has been

formed (Figure 52 and Figure 54). This thin film is consisted of 50% iron sulfide and 50% iron carbonate in the first 6 μm layer and the content of iron carbonate gradually increases in the second layer as shown in Figure 53. As c_{H_2S} increases, not only does the thickness of the film increase, but also the morphology and the composition of the films will change as illustrated in Figure 55 to Figure 58.

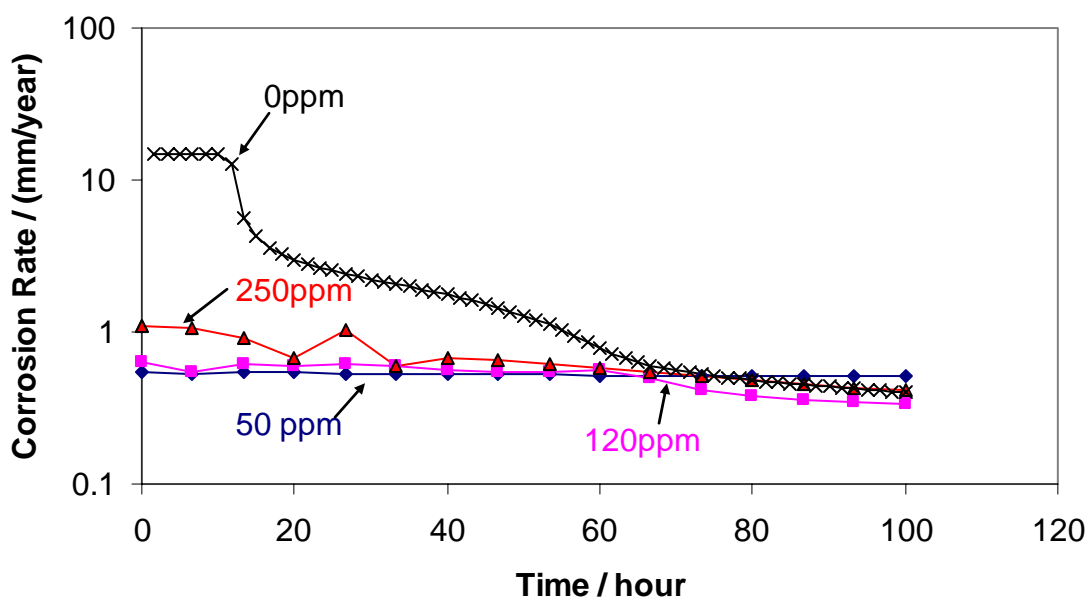


Figure 51. The predicted effect of H_2S concentration on the corrosion rate for $T=60^\circ\text{C}$, $\text{pH } 6.0$, $P_{CO_2} = 7.7 \text{ bar}$, $c_{Fe^{2+}} = 17 \text{ ppm}$, $v=1 \text{ m/s}$. Corresponding film thickness and porosity are shown in Figure 52.

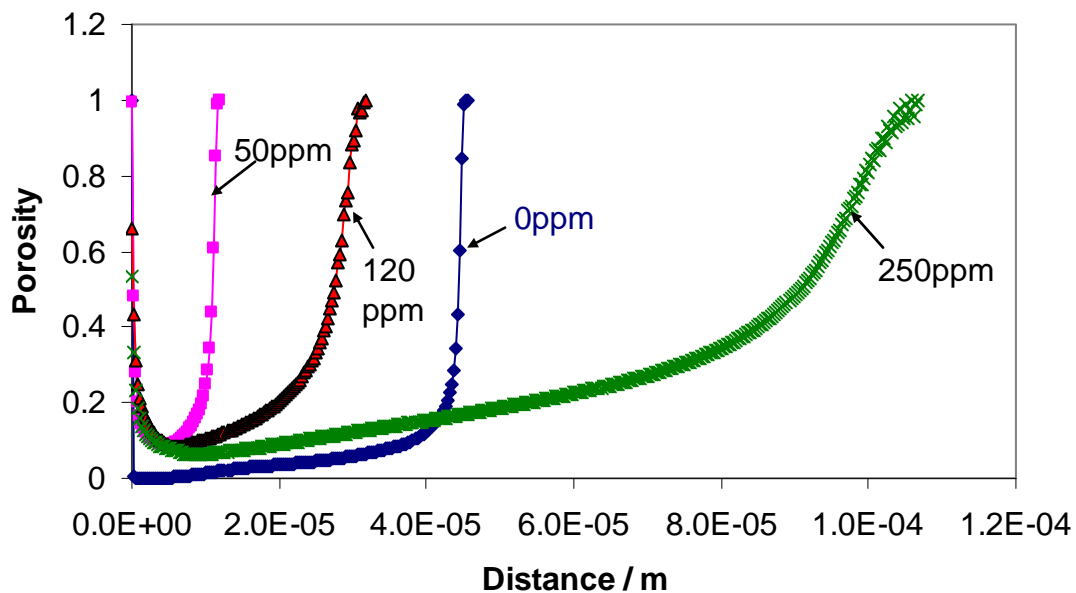


Figure 52. The predicted effect of H_2S concentration on the film thickness and porosity after 100 hours of exposure at $T=60^\circ C$, $P_{CO_2} = 7.7\text{bar}$, $\text{pH } 6$, $c_{Fe^{2+}} = 17\text{ ppm}$, $v=1\text{ m/s}$. Porosity $\varepsilon=1$ means no film.

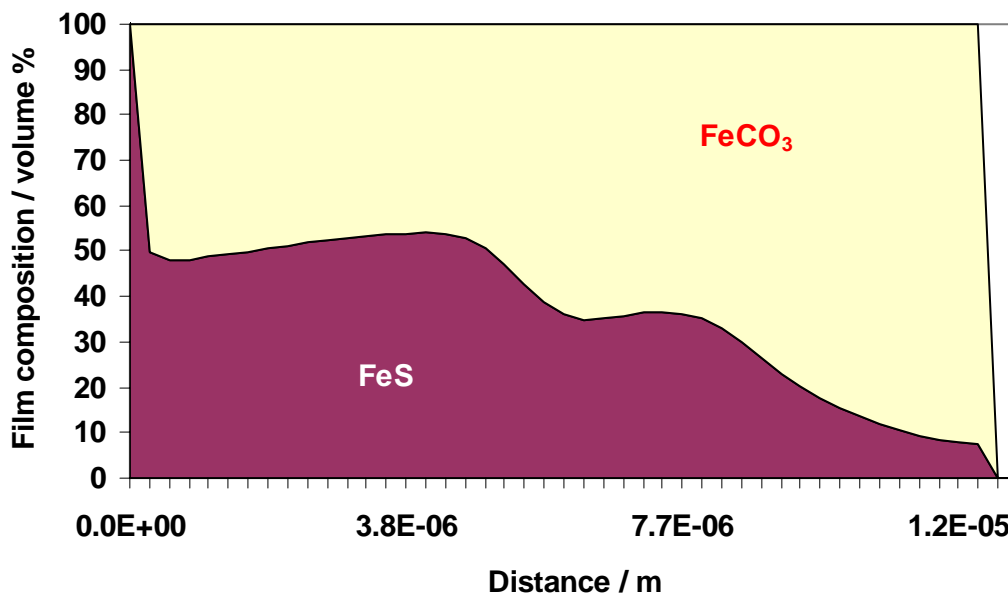


Figure 53. The predicted film thickness and composition of film after 100 hours of exposure at $c_{H_2S} = 50\text{ ppm}$, $T=60^\circ C$, $P_{CO_2} = 7.7\text{bar}$, $\text{pH } 6.0$, $c_{Fe^{2+}} = 17\text{ ppm}$, $v=1\text{ m/s}$.

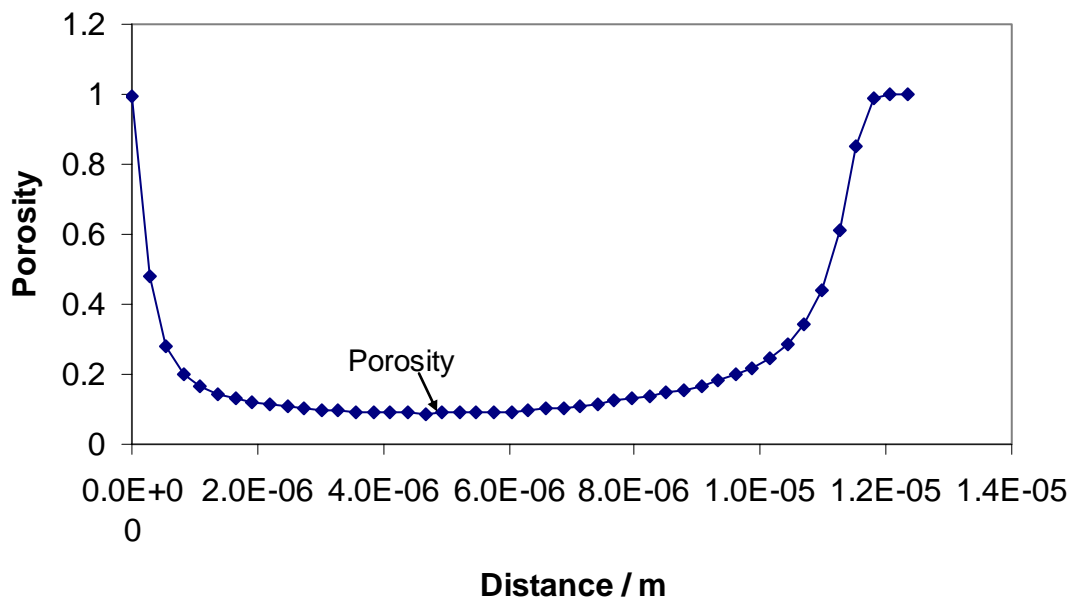


Figure 54. The predicted film thickness and porosity of film after 100 hours of exposure at $c_{H_2S}=50$ ppm, $T=60^\circ\text{C}$, $P_{CO_2}=7.7\text{bar}$, $\text{pH } 6.0$, $c_{Fe^{2+}}=17$ ppm, $v=1$ m/s. Porosity $\varepsilon=1$ means no film.

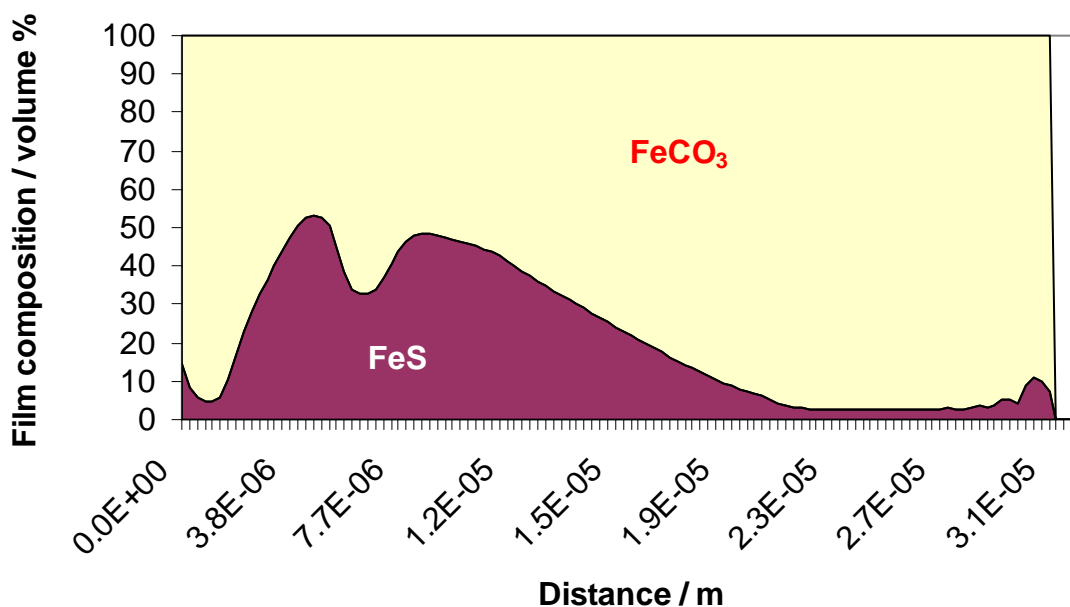


Figure 55. The predicted film thickness and composition of film after 100 hours of exposure at $c_{H_2S}=120$ ppm, $T=60^\circ\text{C}$, $P_{CO_2}=7.7\text{bar}$, $\text{pH } 6.0$, $c_{Fe^{2+}}=17$ ppm, $v=1$ m/s. Porosity $\varepsilon=1$ means no film.

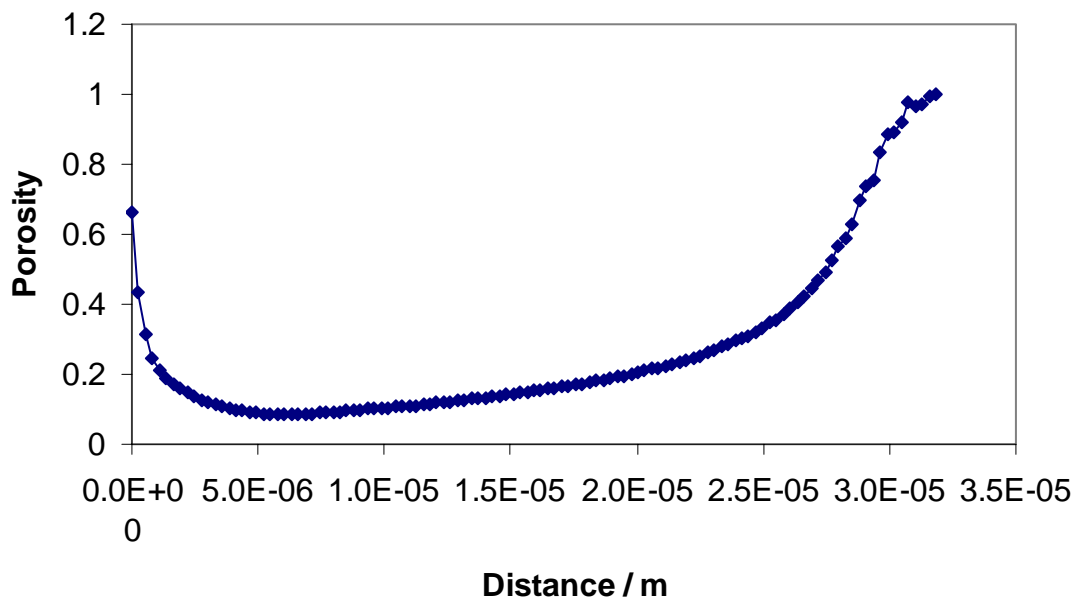


Figure 56. The predicted film thickness and porosity of film after 100 hours of exposure at $c_{H_2S}=120$ ppm, $T=60^\circ\text{C}$, $P_{CO_2}=7.7\text{bar}$, $\text{pH} 6.0$, $c_{Fe^{2+}}=17$ ppm, $v=1$ m/s. Porosity $\varepsilon=1$ means no film.

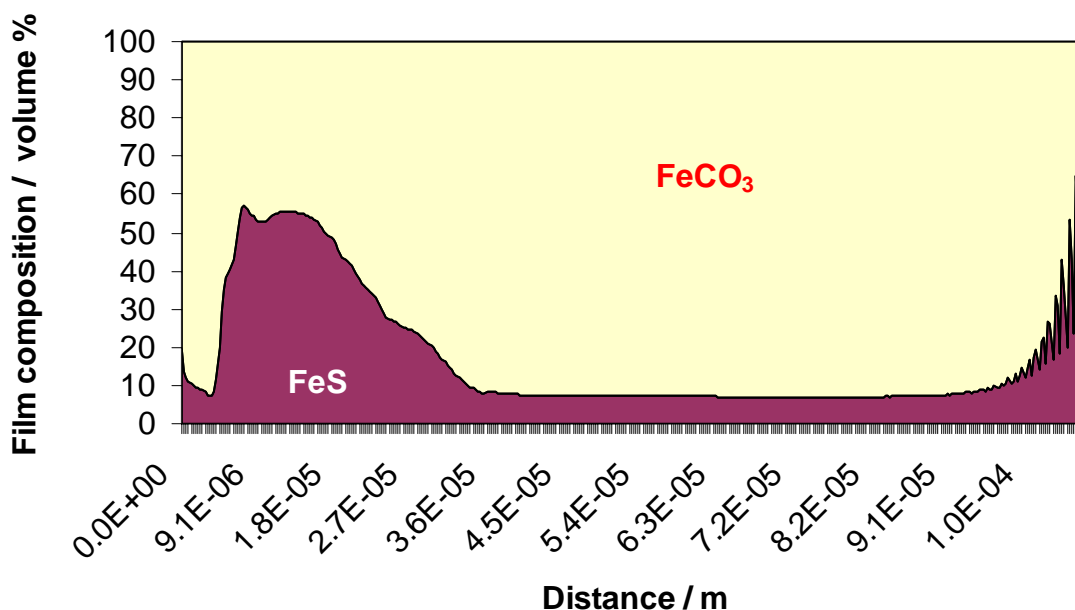


Figure 57. The predicted film thickness and composition of film after 100 hours of exposure at $c_{H_2S}=250$ ppm, $T=60^\circ\text{C}$, $P_{CO_2}=7.7\text{bar}$, $\text{pH} 6.0$, $c_{Fe^{2+}}=17$ ppm, $v=1$ m/s. Porosity $\varepsilon=1$ means no film.

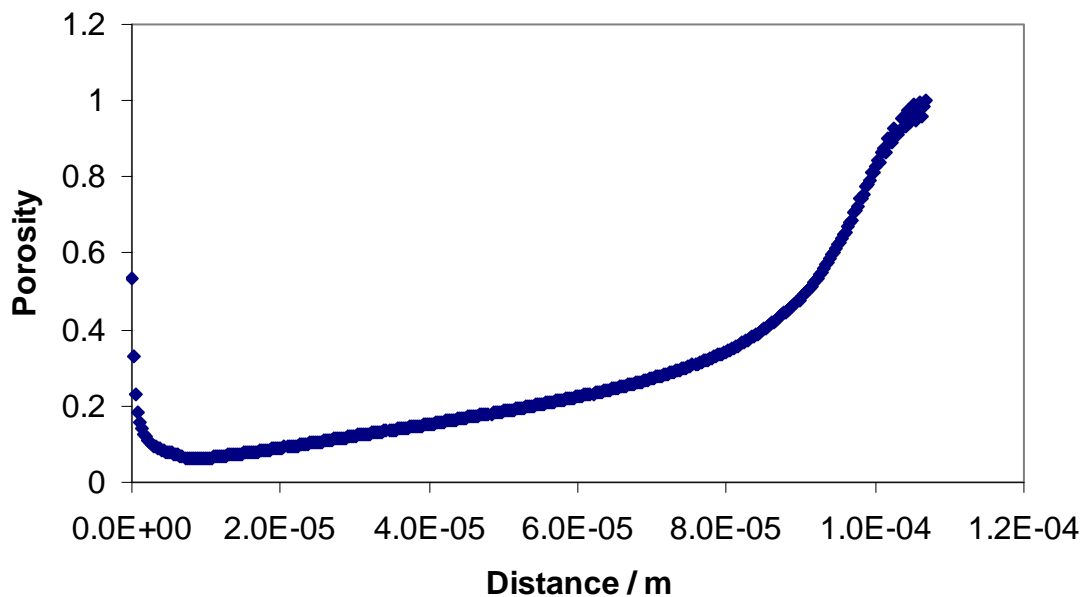


Figure 58. The predicted film thickness and porosity of film after 100 hours of exposure at $c_{H_2S}=250$ ppm, $T=60^\circ\text{C}$, $P_{CO_2}=7.7\text{bar}$, $\text{pH} 6.0$, $c_{Fe^{2+}}=17$ ppm, $v=1$ m/s. Porosity $\varepsilon=1$ means no film.

7.4.2 The effect of pH

It was shown in previous chapters that pH has a strong influence on the conditions leading to the formation of iron carbonate films. High pH results in a increased concentration of $c_{S^{2-}}$ and $c_{CO_3^{2-}}$, which leads to increased supersaturation and consequently higher precipitation rate and faster formation of protective films. The effect of pH on the corrosion rate is demonstrated in Figure 59.

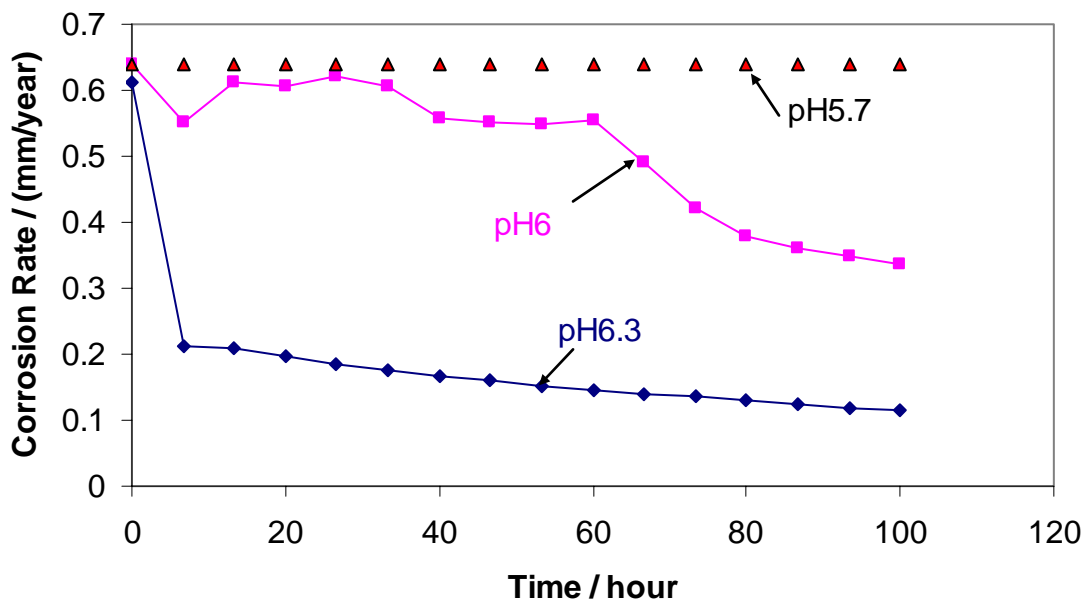


Figure 59. The predicted effect of pH on the corrosion rate for $T=60^{\circ}\text{C}$, $c_{H_2S}=120$ ppm, $P_{CO_2}=7.7$ bar, $c_{Fe^{2+}}=17$ ppm, $v=1$ m/s. Corresponding film thickness and porosity are shown in Figure 60.

Figure 60 illustrates that films will become denser and thicker at higher pH. Corrosion rate is not reduced at pH 5.7, because only a thin porous film will be formed. Whereas at pH 6.3, corrosion rate was reduced significantly by a dense protective film that is consisted of mostly iron carbonate (Figure 61).

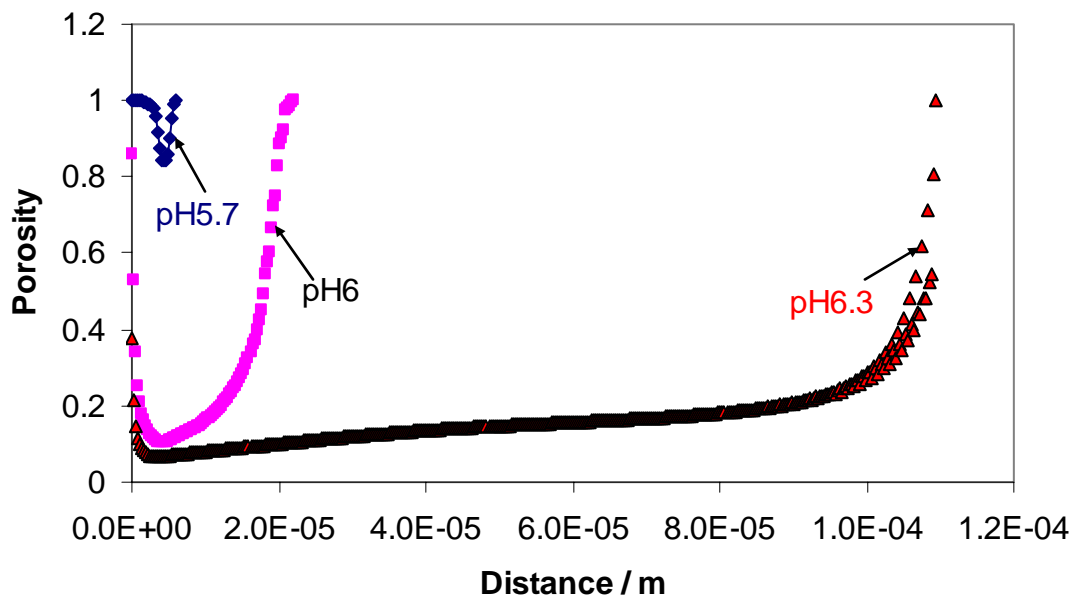


Figure 60. The predicted effect of pH on the film thickness and porosity after 66 hours of exposure at $T=60^{\circ}\text{C}$, $c_{\text{H}_2\text{S}}=120$ ppm, $P_{\text{CO}_2}=7.7$ bar, $c_{\text{Fe}^{2+}}=17$ ppm, $v=1$ m/s. Porosity $\varepsilon=1$ means no film.

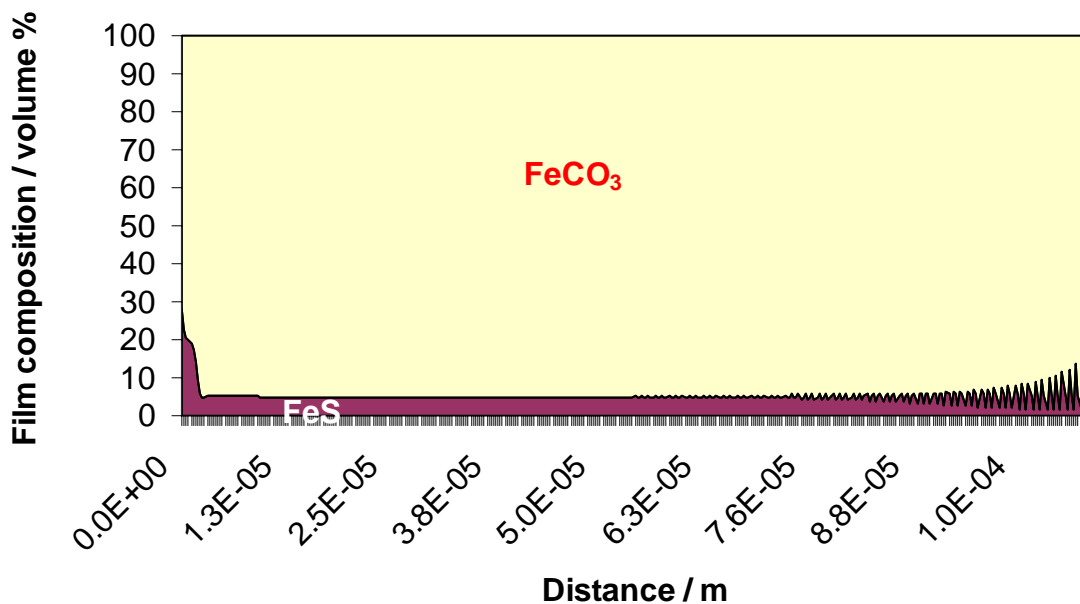


Figure 61. The predicted film thickness and composition of film after 66 hours of exposure at pH 6.3, $c_{\text{H}_2\text{S}}=120$ ppm, $T=60^{\circ}\text{C}$, $P_{\text{CO}_2}=7.7$ bar, $c_{\text{Fe}^{2+}}=17$ ppm, $v=1$ m/s.

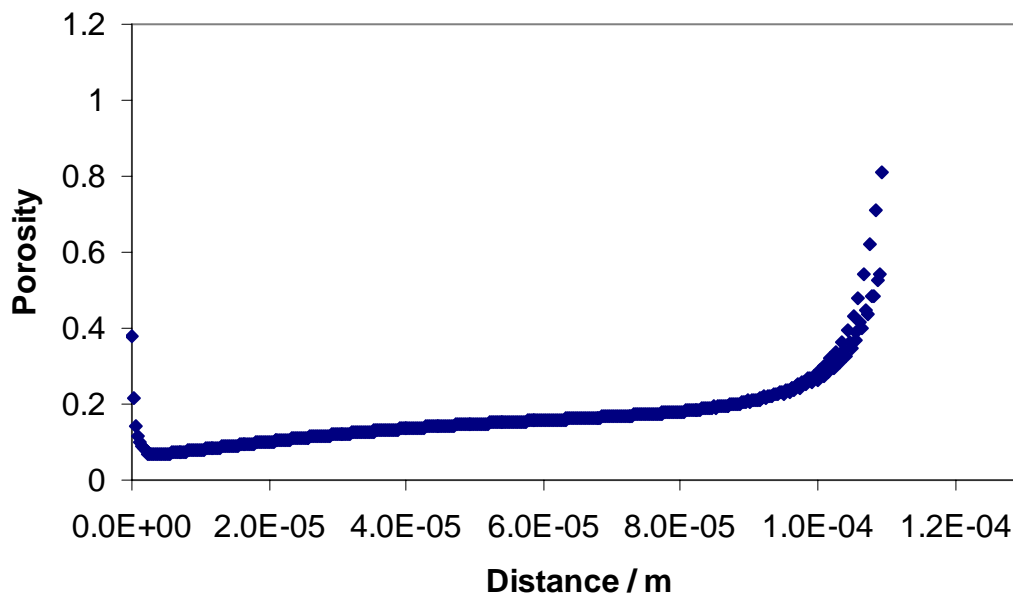


Figure 62. The predicted film thickness and porosity of film after 66 hours of exposure at pH 6.3, $c_{H_2S}=120$ ppm, $T=60^\circ\text{C}$, $P_{CO_2}=7.7$ bar, $c_{Fe^{2+}}=17$ ppm, $v=1$ m/s. Porosity $\varepsilon=1$ means no film.

On the other hand, the film is no longer dominated by iron carbonate at pH 6, but rather evenly mixed with iron carbonate and iron sulfide as shown in Figure 63. The undulating profile of film composition is caused by the fact that sulfide species are only present in small quantities ($\approx 10^{-16}$ kmol/liter) in this condition, thus it is easily exhausted/depleted by the precipitation of iron sulfide. Once the sulfide species is exhausted or depleted, supersaturation for FeS will be reduced significantly or even become undersaturated. Thus the precipitation of iron sulfide will slow down or stop, until sulfide species is replenished by either transportation or dissociation from HS^- ions.

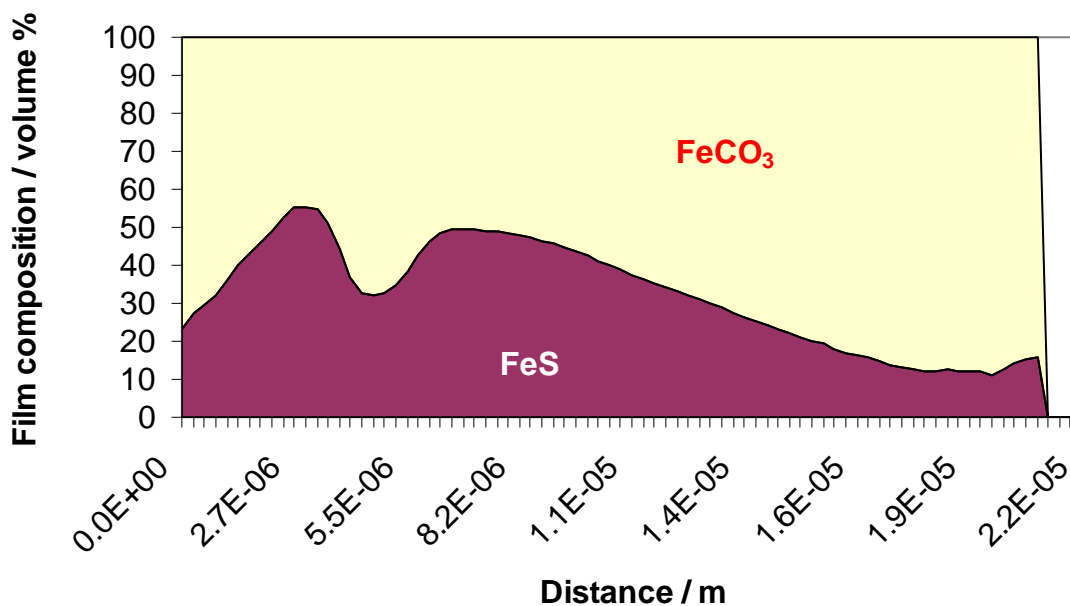


Figure 63. The predicted film thickness and composition of film after 66 hours of exposure at pH 6, $c_{H_2S}=120$ ppm, $T=60^\circ\text{C}$, $P_{CO_2}=7.7$ bar, $c_{Fe^{2+}}=17$ ppm, $v=1$ m/s.

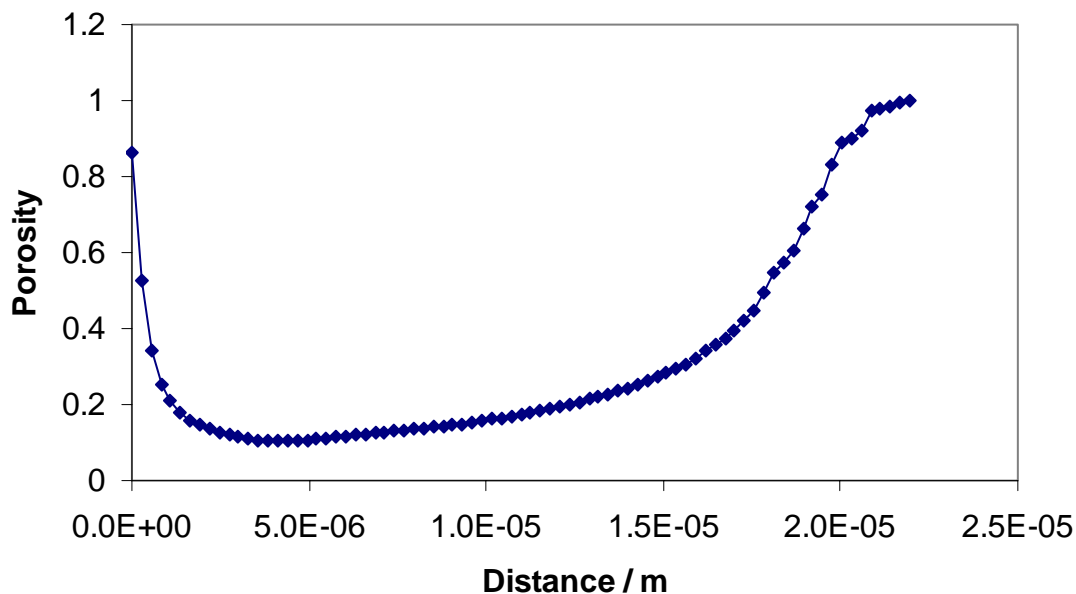


Figure 64. The predicted film thickness and porosity of film after 66 hours of exposure at pH 6, $c_{H_2S}=120$ ppm, $T=60^\circ\text{C}$, $P_{CO_2}=7.7$ bar, $c_{Fe^{2+}}=17$ ppm, $v=1$ m/s. Porosity $\varepsilon=1$ means no film.

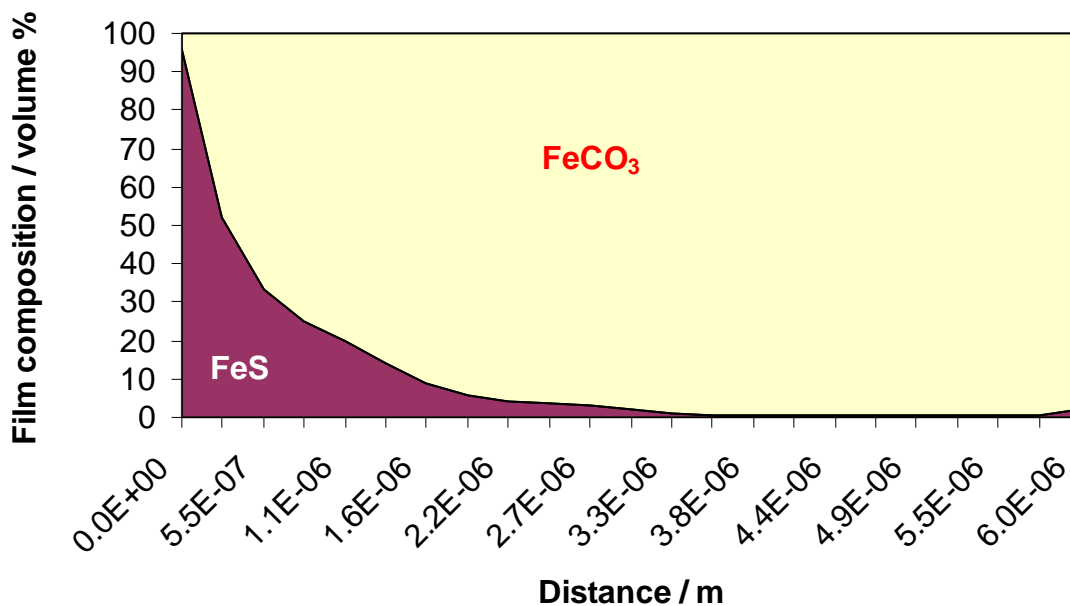


Figure 65. The predicted film thickness and composition of film after 66 hours of exposure at pH 5.7, $c_{H_2S}=120$ ppm, $T=60^\circ\text{C}$, $P_{CO_2}=7.7$ bar, $c_{Fe^{2+}}=17$ ppm, $v=1$ m/s.

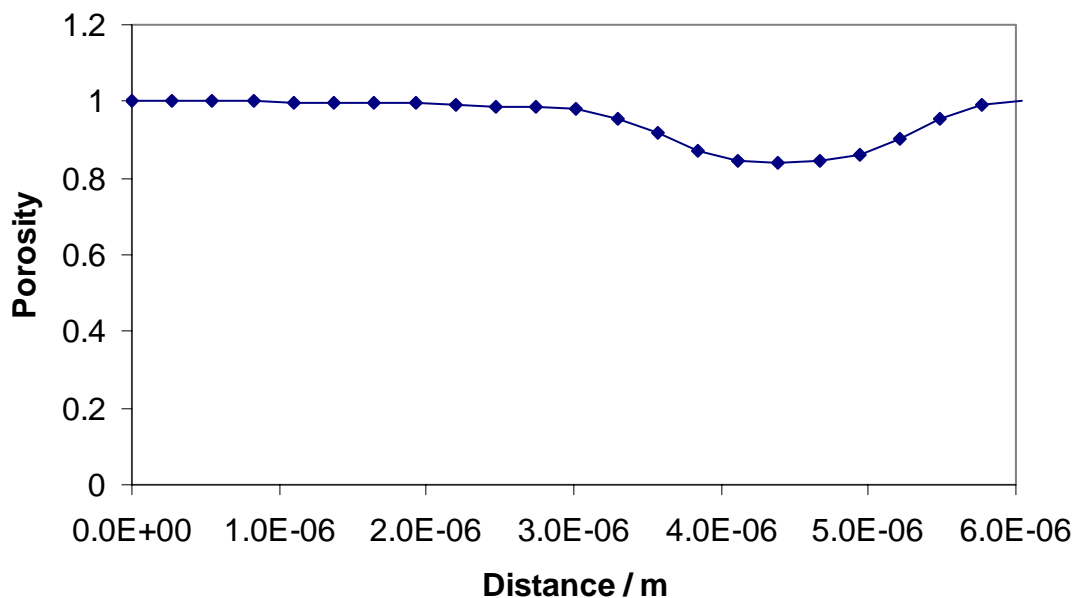


Figure 66. The predicted film thickness and porosity of film after 66 hours of exposure at pH 5.7, $c_{H_2S}=120$ ppm, $T=60^\circ\text{C}$, $P_{CO_2}=7.7$ bar, $c_{Fe^{2+}}=17$ ppm, $v=1$ m/s. Porosity $\varepsilon=1$ means no film.

7.4.3 The effect of CO₂ partial pressure

In the case of film-free CO₂ corrosion, an increase of CO₂ partial pressure (P_{CO_2}) typically leads to an increase in the corrosion rate. However, when other conditions are favorable for formation of iron carbonate and iron sulfide films, increased P_{CO_2} can help to retard the corrosion rate as shown in chapter 5.5.3. At a constant pH, higher P_{CO_2} leads to an increase in CO₃²⁻ concentration and a higher supersaturation (given the pH is high enough), which accelerates precipitation and film formation of FeCO₃. The effect of P_{CO_2} on the corrosion rate in the presence of iron carbonate and iron sulfide film is illustrated in Figure 67 for the baseline case.

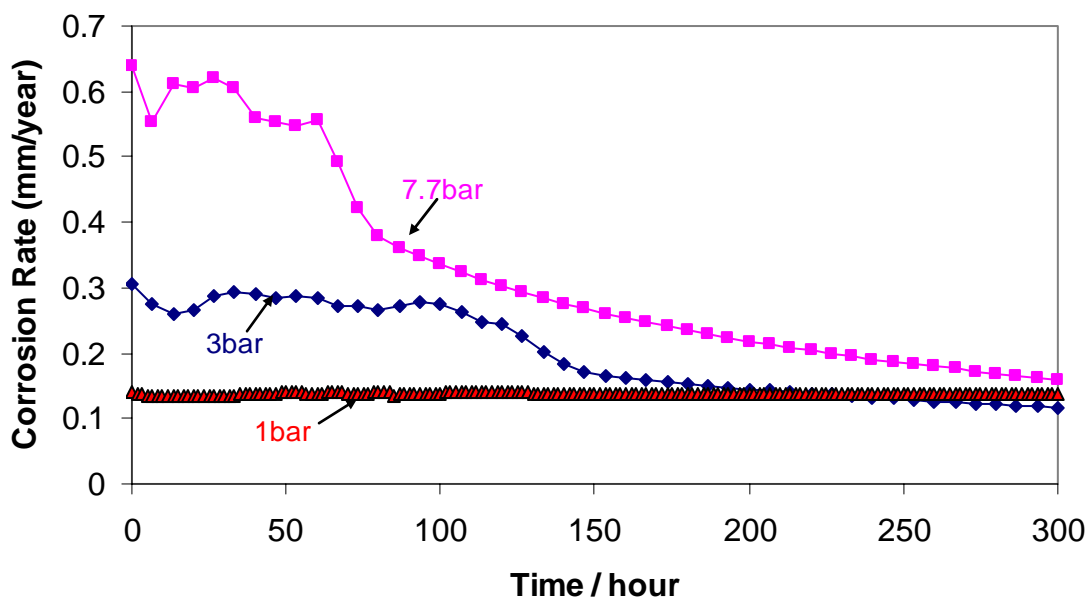


Figure 67. The predicted effect of P_{CO_2} on the corrosion rate for $T=60^{\circ}C$, $c_{H_2S}=120$ ppm, $pH=6$, $c_{Fe^{2+}}=17$ ppm, $v=1$ m/s. Corresponding film thickness and porosity are shown in Figure 68.

With the presence of 120ppm of H_2S in the gas phase, the initial corrosion rates are immediately reduced by approximately ten times from their respective H_2S -free corrosion rates. Although the final corrosion rates for each P_{CO_2} end up the same, the reasons behind each scenario are different. It is illustrated in Figure 68 that films become denser at higher P_{CO_2} , while the thickness of films is unaffected by P_{CO_2} .

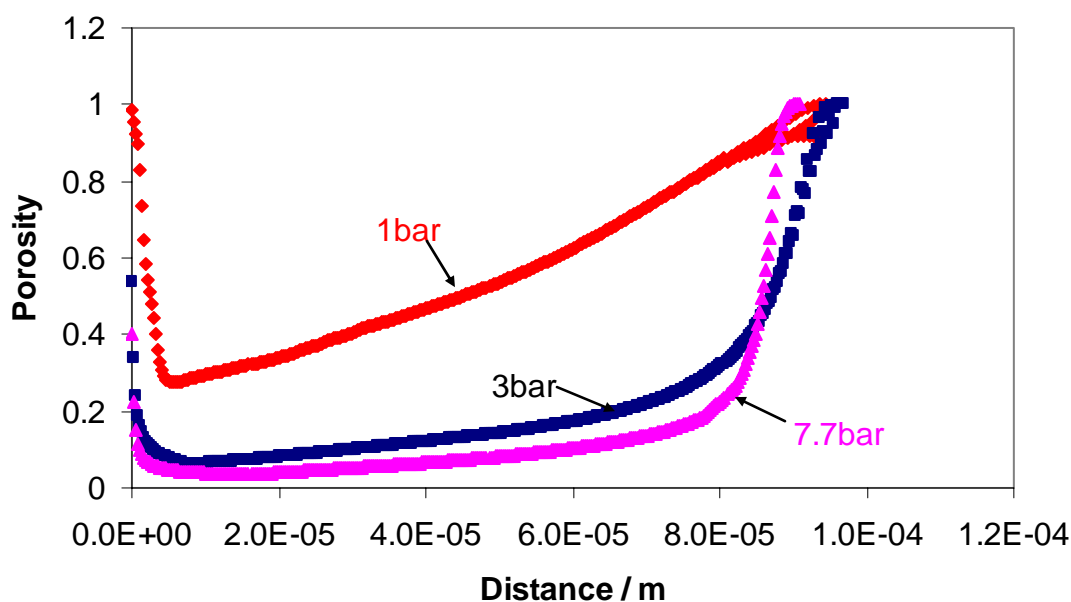


Figure 68. The predicted effect of P_{CO_2} on the film thickness and porosity after 300 hours of exposure at $T=60^{\circ}C$, $c_{H_2S}=120$ ppm, $pH=6$, $c_{Fe^{2+}}=17$ ppm, $v=1$ m/s. Porosity $\varepsilon=1$ means no film.

The initial corrosion rate for $P_{CO_2}=1$ bar is low (0.14mm/year) and the corrosion rate stays constant throughout the simulation because the porous film formed under this condition (Figure 70) can not reduce the corrosion rate further. Whereas denser films formed at higher P_{CO_2} helps to reduce the corrosion rate even further. On the other hand,

it should be noted that as P_{CO_2} increases, the composition of films will be gradually dominated by iron carbonate, which is evident in Figure 71 and Figure 73.

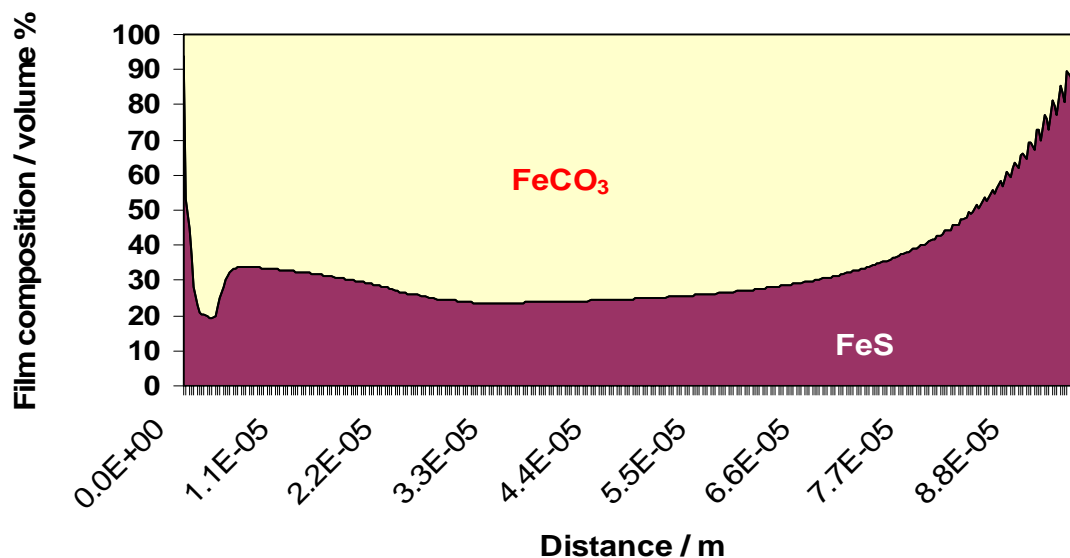


Figure 69. The predicted film thickness and composition of film after 300 hours of exposure at $P_{CO_2} = 1$ bar, $c_{H_2S} = 120$ ppm, $T = 60^\circ\text{C}$, pH 6, $c_{Fe^{2+}} = 17$ ppm, $v = 1$ m/s.

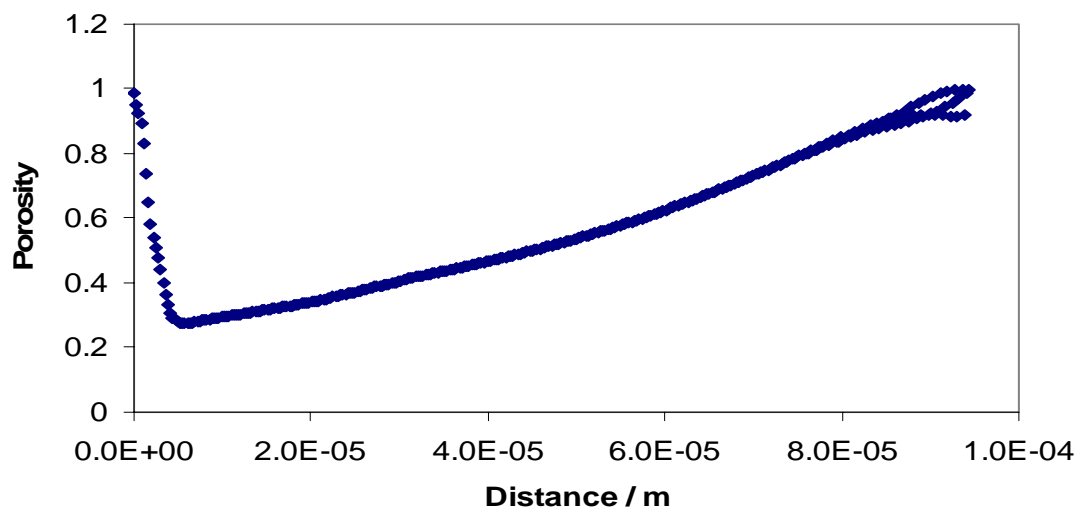


Figure 70. The predicted film thickness and porosity of film after 300 hours of exposure at $P_{CO_2} = 1$ bar, $c_{H_2S} = 120$ ppm, $T = 60^\circ\text{C}$, pH 6, $c_{Fe^{2+}} = 17$ ppm, $v = 1$ m/s. Porosity $\varepsilon = 1$ means no film.

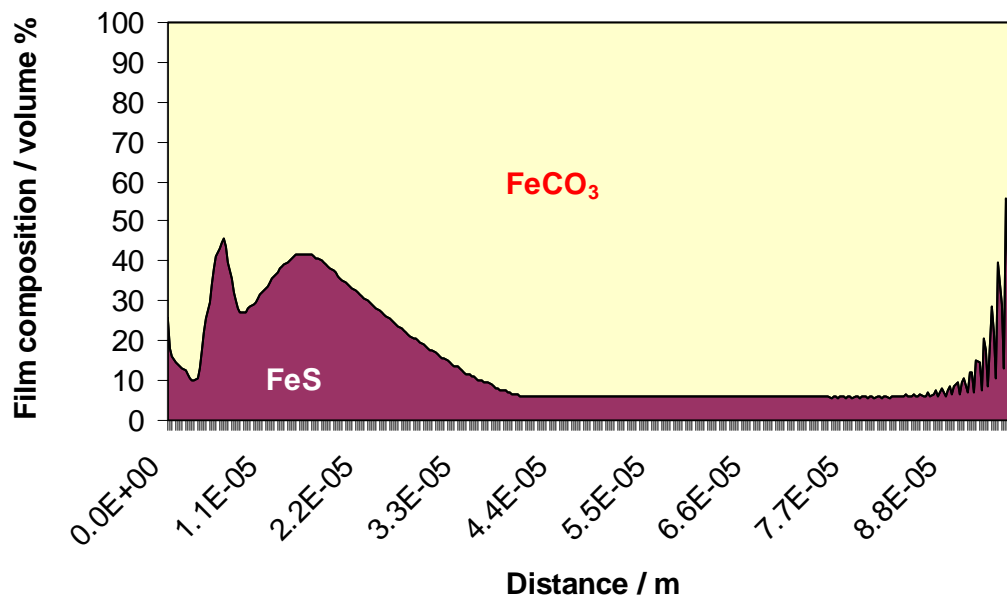


Figure 71. The predicted film thickness and composition of film after 300 hours of exposure at $P_{CO_2} = 3$ bar, $c_{H_2S} = 120$ ppm, $T = 60^\circ\text{C}$, $\text{pH} = 6$, $c_{Fe^{2+}} = 17$ ppm, $v = 1$ m/s.

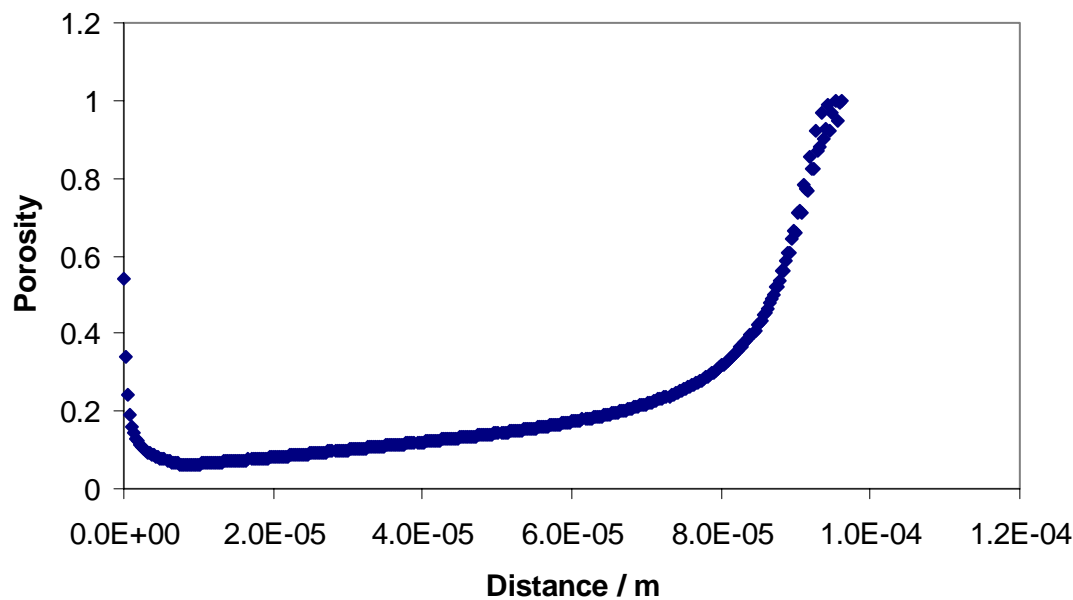


Figure 72. The predicted film thickness and porosity of film after 300 hours of exposure at $P_{CO_2} = 3$ bar, $c_{H_2S} = 120$ ppm, $T = 60^\circ\text{C}$, $\text{pH} = 6$, $c_{Fe^{2+}} = 17$ ppm, $v = 1$ m/s. Porosity $\varepsilon = 1$ means no film.

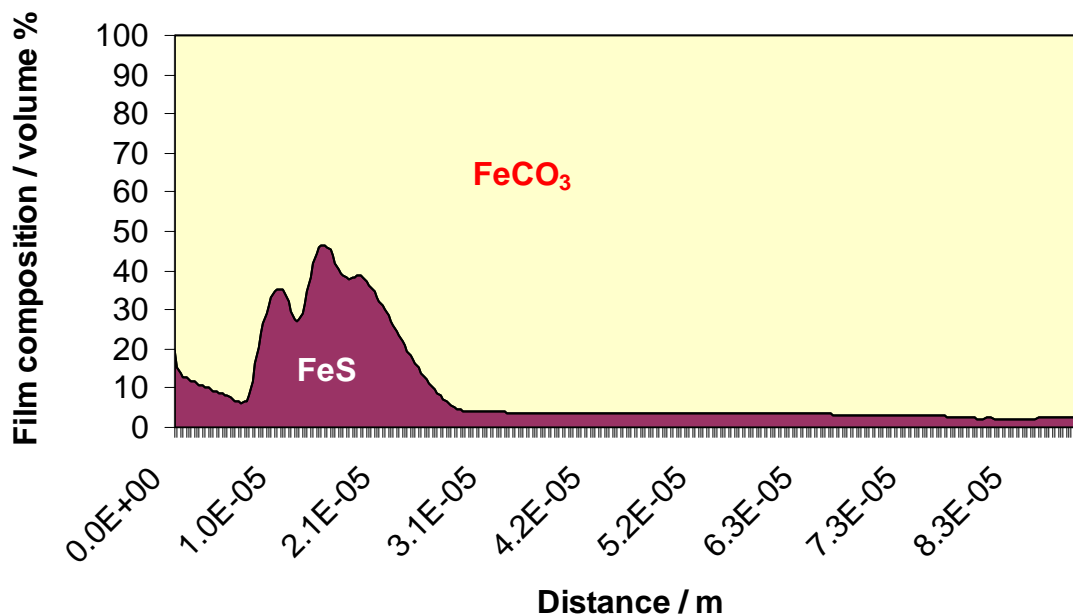


Figure 73. The predicted film thickness and composition of film after 300 hours of exposure at $P_{CO_2} = 7.7$ bar, $c_{H_2S} = 120$ ppm, $T = 60^\circ\text{C}$, pH 6, $c_{Fe^{2+}} = 17$ ppm, $v = 1$ m/s.

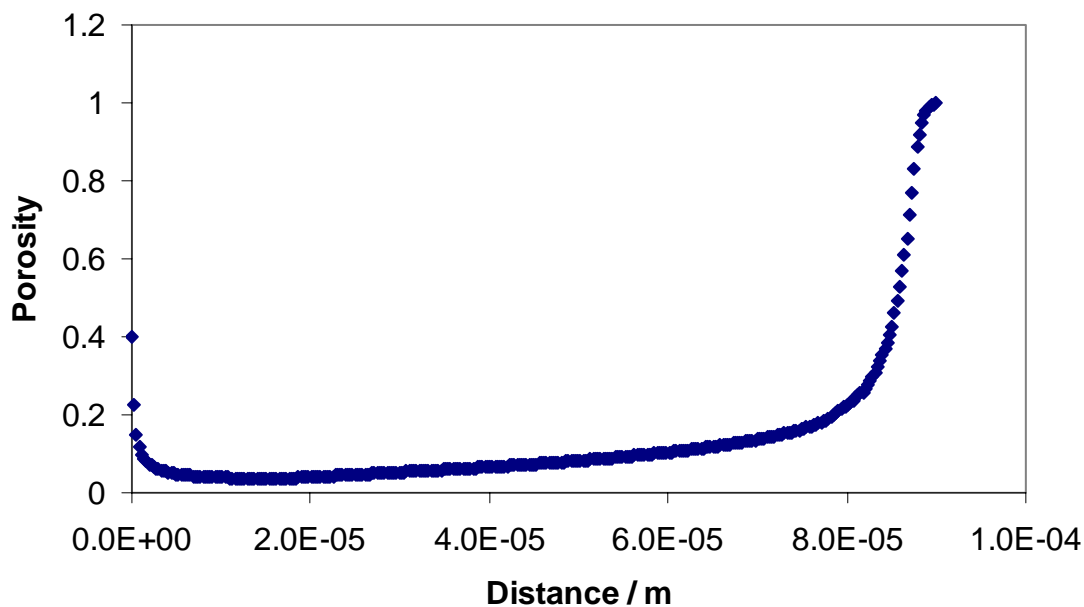


Figure 74. The predicted film thickness and porosity of film after 300 hours of exposure at $P_{CO_2} = 7.7$ bar, $c_{H_2S} = 120$ ppm, $T = 60^\circ\text{C}$, pH 6, $c_{Fe^{2+}} = 17$ ppm, $v = 1$ m/s. Porosity $\varepsilon = 1$ means no film.

CHAPTER 8: CONCLUSIONS

A mechanistic model CO₂/H₂S corrosion of mild steel in the presence of trace amount of H₂S was developed. Essentially, a mechanistic model that predicts the formation of iron sulfide film together with iron carbonate film in CO₂ corrosion of carbon steel was created and coupled with the overall CO₂ corrosion prediction model. The model relies on accurate prediction of the solution chemistry at the metal surface. It includes two principle mechanisms which determine the kinetics of growth and the resulting morphology of the iron carbonate films: precipitation and undermining of the film by ongoing corrosion. Morphology of the film is described by the distribution of porosity throughout the film.

The model is capable of predicting the kinetics of iron sulfide and iron carbonate film growth, the change in morphology of the film with respect to space and time, as well as the resulting corrosion rate time evolution. Furthermore, the model is capable of predicting the transient and spatial composition of the film by calculating the ratio of volume occupied by iron sulfide over total film volume and the ratio of iron carbonate volume over total film volume.

The model has been successfully calibrated against data from a large number of carefully controlled corrosion experiments under different environmental parameters in film free conditions, as well as against limited experimental data in film forming conditions. Parametric testing of the model has been done in order to gain insight into

the effect of various environmental parameters on mixed iron carbonate and iron sulfide films formation. The trends shown in the predictions agreed well with the general understanding of the CO₂/H₂S corrosion process in the presence of iron carbonate and iron sulfide films.

CHAPTER 9: RECOMMENDATION AND FUTURE WORK

Further adjustment of the model will be done as more accurate data on CO₂/H₂S corrosion in the presence of iron carbonate and iron sulfide films emerge. It is speculated that at high H₂S concentration (in % range), dissolved H₂S can be directly reduced and increase the corrosion rate. Thus CO₂/H₂S corrosion experiments in both film-free and film-forming conditions at higher concentration of H₂S needs to be performed.

Currently, the kinetics of FeS precipitation adopted from the literature⁴⁸ has not been independently verified. Therefore, a more accurate study on the kinetics of FeS precipitation needs to be conducted in a carefully controlled environment.

There are various types of iron sulfide films and the mechanism of formation of these films remains unclear and requires further investigation. Once the mechanisms are grasped, various types iron sulfide films can be included in the mechanistic model.

REFERENCES

1. C. de Waard and D.E Milliams, Corrosion, 31 (1975): p.131.
2. C. de Waard and D.E Milliams, "Predictive Model for CO₂ Corrosion Engineering in Wet Natural Gas Pipelines", Paper No.577, CORROSION/91.
3. C. de Waard and U Lotz, "Prediction of CO₂ corrosion of carbon steel", Paper No.69, CORROSION/93.
4. C. de Waard, U Lotz, and A Dugstad, "Influence of liquid flow velocity on CO₂ corrosion: a semi-empirical model", Paper No.128, CORROSION/95.
5. M. R. Bonis, J-L. Crolet, "Basics of the prediction of the risks of CO₂ corrosion in oil and gas wells", CORROSION/89, paper no. 466, (Houston Texas: NACE International, 1995).
6. Y.M. Gunaltun. "Combining research and field data for corrosion rate prediction". CORROSION/96, paper no. 27. (Houston Texas: NACE International, 1996).
7. C.D. Adams, J.D. Garber, R.K. Singh, "Computer modelling to predict corrosion rates in gas condensate wells containing CO₂", CORROSION/96, paper no. 31, (Houston Texas: NACE International, 1996).
8. S. Srinivasan, R.D. Kane, "Prediction of Corrosivity of CO₂/ H₂S production environments", CORROSION/96, paper no.11, (Houston Texas: NACE International, 1996).
9. R.C. John, K.G. Jordan, S.D. Kapusta, A.L. Young and W.T. Thompson, "SweetCor: An information system for the analysis of corrosion of steels by water and carbon dioxide", CORROSION/98, paper no.20, (Houston Texas: NACE International, 1998).
10. W.P. Jepson, C. Kang, M. Gopal and S. Stitzel, "Model for sweet corrosion in horizontal multiphase slug flow", CORROSION/97, paper no.11, (Houston Texas: NACE International, 1997).
11. R.Zhang, M.Gopal and W.P. Jepson, "Development of a mechanistic model for predicting corrosion rate in multiphase oil/water/gas flows", CORROSION/97, paper no.601, (Houston, TX: NACE International, 1997).
12. B.F.M. Pots, "Mechanistic models for the prediction of CO₂ corrosion rates under multi-phase flow conditions", paper no. 137, CORROSION/95.

13. S. Nestic, J. Postlethwaite and S. Olsen, "An Electrochemical Model for Prediction of CO₂ Corrosion", paper no.131, CORROSION/95.
14. E. Dayalan, F.D. deMoraes, J.R. Shadley, S. A. Shirazi, E. F. Ribicki, "CO₂ corrosion prediction in pipe flow under FeCO₃ scale-forming conditions", CORROSION/98, paper no. 51, (Houston, TX: NACE International, 1998).
15. S. Nestic, M. Nordsveen, R. Nyborg and A. Stangeland, "A Mechanistic Model for CO₂ Corrosion with Protective Iron Carbonate Films", CORROSION/2001, paper no. 40, (Houston, TX: NACE International, 2001).
16. S. Nestic and K.J. Lee, "The mechanistic model of iron carbonate film growth and the effect on CO₂ corrosion of mild steel", Paper No.237, CORROSION/02.
17. A. Anderko and R. Young, "Simulation of CO₂/ H₂S corrosion using thermodynamic and electrochemical models", Paper No.31, CORROSION/99.
18. E.C. Greco, W.B. Wright, Corrosion, v.18, p. 119t-124t (1962).
19. J.B. Sardisco, W. B. Wright, E. C. Greco, Corrosion, v.19, p. 354t (1963).
20. S.P. Ewing, "Electrochemical studies of the hydrogen sulfide corrosion mechanism", Corrosion 11 (1955): p.51.
21. K.Videm, J. Kvarekval, Corrosion, v.51, p.260-269 (1995).
22. A.Ikeda, M.Ueda and S. Mukai, "Influence of environmental factors on corrosion in CO₂ source well", advance in CO₂ corrosion.
23. D.R. Morris, L.P. Sampaleanu, D.N. Veysey, "The corrosion of steel by aqueous solutions of hydrogen sulfide", J. Electrochem. Soc., v. 127, p. 1228-1235 (1980).
24. Z.A. Iofa, V. V. Batrakov, Cho-Ngok-ba, Electrochim. Acta, V. 9, p. 1645 (1964).
25. D.W. Shoesmith, P. Taylor, M.G. Bailey, B.Ikeda, Electrochim. Acta, v. 23, p. 903-916 (1978).
26. D.W. Shoesmith, M.G. Bailey, B.Ikeda, Electrochim. Acta, v.23, p. 1329-1339 (1978).
27. D.W. Shoesmith, P. Taylor, M.G. Bailey, D. Owen, J. Electrochem. Soc., v. 127, p. 1007-1015 (1980).

28. T.A. Ramanarayanan and S.N. Smith, "Corrosion of iron in gaseous environments and in gas-saturated aqueous environments", *Corrosion* v. 46 no.1 p.66 (1990).
29. S.N. Smith, "A proposed mechanism for corrosion in slightly sour oil and gas production", 12th international corrosion congress, Houston, TX, September 1993.
30. H.Vedage, T.A. Ramanarayanan, J.D. Mumford and S.N. Smith, "Electrochemical growth of iron sulfide films in H₂S-saturated chloride media", *Corrosion*, v. 49, no.2, p.114-121 (1993).
31. S.N. Smith and E.J. Wright, "Prediction of minimum H₂S levels required for slightly sour corrosion", Paper NO.11, CORROSION/94.
32. D.W. Shoesmith, "Formation, Transformation and Dissolution of phases formed on surfaces", Electrochemical Society Meeting, Ottawa, 1981.
33. D.D. MacDonald and J.B. Hyne, "The thermodynamics of the iron/sulphur/water system", Whiteshell Nuclear Research Establishment, 1979.
34. H.Y. Ma, X.L. Cheng, S.H. Chen, C. Wang, J.P. Zhang. H.Q. Yang, J. *Electroanal. Chem.* 451 (1998) 11.
35. X.L. Cheng, H.Y. Ma, J.P.Zhang, X.Chen, S.H. Chen, H.Q. Yang, *Corrosion* 54 (1998) 369.
36. H.Y. Ma, X.L. Cheng, S.H. Chen, G.Q. Li, X. Chen, S.B. Lei, H.Q. Yang, *Corrosion* 54 (1998) 634.
37. H.Y. Ma, X.L. Cheng, S.H. Chen, G.Q. Li, Z.Quan, S. Zhao, L. Niu, *Corrosion Sci.* 42 (2000) 1669-1693.
38. B. E. Roberts and P.R. Tremaine, "Vapour Liquid Equilibrium Calculations for Dilute Aqueous Solutions of CO₂, H₂S, NH₃ and NaOH to 300°C", *The Canadian Journal of Chemical Engineering*, 63, (1985): p.294-300.
39. R.D. Deshmukh and A.E. Mather, "A Mathematical Model for Equilibrium Solubility of Hydrogen Sulfide and Carbon Dioxide in Aqueous Alkanolamine Solutions", *Chemical Engineering Science*, 36, (1980): p.355-362.

40. A. Miyasaka, "Thermodynamic Estimation of pH of Sour and Sweet Environments as Influenced by the Effects of Anions and Cations", CORROSION/92, paper no. 247.
41. A. Dugstad, "Mechanism of Protective Film Formation During CO₂ Corrosion of Carbon Steel", CORROSION/98, paper no. 31, (Houston, TX: NACE International, 1998).
42. R. Nyborg, "Initiation and Growth of Mesa Corrosion Attack During CO₂ Corrosion of Carbon Steel ", CORROSION/98, paper no. 48, (Houston, TX: NACE International, 1998).
43. R. Nyborg, A. Dugstad, "Mesa Corrosion Attack in Carbon Steel and 0.5 % Chromium Steel", CORROSION/98, paper no. 29, (Houston, TX: NACE International, 1998).
44. L. G. S. Gray, B. G. Anderson, M. J. Danysh and P. R. Tremaine, "Mechanism of Carbon Steel Corrosion in Brines Containing Dissolved Carbon Dioxide at pH 4", Corrosion/89, paper no. 464, (Houston, TX: NACE International, 1989).
45. L. G. S. Gray, B. G. Anderson, M. J. Danysh and P. R. Tremaine, "Effect of pH and Temperature on the Mechanism of Carbon Steel Corrosion by Aqueous Carbon Dioxide", Corrosion/90, paper no. 40, (Houston, TX: NACE International, 1990).
46. E. W. J. van Hunnik, B. F. M. Pots and E. L. J. A. Hendriksen, "The Formation of Protective FeCO₃ Corrosion Product Layers in CO₂ Corrosion". CORROSION/96, paper no. 6, (Houston, TX: NACE International, 1996).
47. E. Gulbrandsen, S. Nesic, A. Strangeland, T. Buchardt, B. Sundfaer, "Effect of precorrosion on the performance of inhibitors for CO₂ corrosion of carbon steel", CORROSION/98, paper no. 013, (Houston, TX: NACE International, 1998).
48. N.G. Harmandas and P.G. Koutsoukos, "The formation of iron sulfides in aqueous solutions", Journal of Crystal Growth, 1996, p.719.
49. D. M. Drazic, "Iron and its Electrochemistry in an Active State", Modern Aspects of Electrochemistry, Vol 19, p.79, Plenum Press, 1989.
50. W. Lorenz and K Heusler, "Anodic Dissolution of Iron Group Metals", in Corrosion Mechanisms, ed. F. Mansfeld, Marcel Dekker, New York, 1987.

51. M. L. Johnson and M. B. Tomson, "Ferrous Carbonate Precipitation Kinetics and Its Impact on CO₂ Corrosion", CORROSION/91, paper no. 268, (Houston, TX: NACE International, 1991).
52. M. Kermani and A. Morshed "Carbon dioxide corrosion in oil and gas production-a compendium" Corrosion , Vol.59, No.8 (2003): p659.
53. R.H. Hausler, H.P. Goddard, eds., Advances in CO₂ Corrosion, vol. 1 (1985) and 2 (1986) (Houston, TX: NACE).
54. B. Kaasa, T. Ostvold, "Prediction of pH and Mineral Scaling in Waters with Varying Ionic Strength Containing CO₂ and H₂S for 0<T(°C)<200 and 1<p(bar)<500", CORROSION/98, paper no. 62 (Houston, TX: NACE, 1998).
55. J. L. Crolet, M. Pourbaix, A. Pourbaix, "The Role of Trace Amount of Oxygen on the Corrosivity of H₂S media", CORROSION/91, paper no. 22 (Houston, TX: NACE, 1991).
56. K. Videm and J. Kvarekvaal, Corrosion 51, 4 (1995): p.260-269.
57. A.Ikeda, M. Ueda, S. Mukai, "Influence of Environmental Factors on Corrosion, Advances in CO₂ corrosion", vol. 2, Proc. CORROSION/84 and CORROSION/85 Symp. On CO₂ Corrosion in the Oil and Gas Industry (Houston, TX: NACE 1985).
58. B. F. M. Pots, R. C. John, Improvements on de- Waard Milliams Corrosion Prediction and Applications to Corrosion Management, Corrosion/02, Paper No. 02235, NACE International, Houston, Texas, 2002.
59. Personal communication, S. Nestic, IFE, Norway, presently affiliated with Ohio University, 2004.
60. IUPAC: Chemical Data Series No. 21, Stability constants of Metal-Ion Complexes. Par A: Inorganic ligands. Pergamon Press.
61. J. S. Smith and J. D. A. Miller, Nature of Sulfides and Their Corrosive Effect on Ferrous Metals: A Review, Br. Corros. J., Vol 10, No. 3, 136-143, 1975.
62. L. A. Taylor and L. W. Finger, Structure Refinement and Composition of Mackinawite, Carnegie Inst. Wash. Year Book, 69, 318-323, 1971.
63. M. Mullet, S. Boursiquot, M. Abdelmoula, et al. Surface Chemistry and Structural properties of Mackinawite Prepared by Reaction of Sulfide Ions with Metallic Iron, Geochimica et Cosmochimica Acta, Vol. 66, No. 5, 829-836, 2002.

64. F. H. Meyer, O. L. Riggs, *ibid.*, 1958, 14, 109t.
65. P.H. Tewari, G. Wallace and A.B. Campbell, Atomic Energy of Canada Limited Report, AECL-5960 (1978).
66. R.A. Berner, "Thermodynamic stability of sedimentary iron sulfides". *Am. J. Sci.* Vol. 265, (1967) p. 773-785.
67. S. Takeno, H. Zoka and T. Niihara, *Am. Mineral.*, 55, 1639 (1970).
68. R. de Medicis, *Science*, 170, 1191 (1970); *Rev. Chim. Miner.* 7, 723 (1970).
69. R.A. Berner, *Science*, 137, 669 (1962).
70. A.G. Wikjord, T.E. Rummery, F.E. Doern and D.G. Owen, Submitted to *Corros. Sci.*
71. R.A. Berner, *Am. J. Sci.*, 265, 773 (1967).
72. A. Anderko, P. J. Shuler, A Computational Approach to Predicting the Formation of Iron Sulfide Species Using Stability Diagrams, *Computers & Geosciences*, Vol. 23, No. 6, 647-658, 1997.
73. A. Anderko, P. J. Shuler, Modeling the Formation of Iron Sulfide Scales Using Thermodynamic Simulation, *Corrosion/98*, Paper No. 64, NACE International, Houston, Texas, 1998.
74. L. G. Benning, R. T. Wilkin, H. L. Barnes, Reaction Pathways in the Fe-S System Below 100°C, *Chemical Geology*, Vol. 167, 25-51, 2000.
75. S. N. Smith, J. L. Pacheco, Prediction of Corrosion in Slightly Sour Environments, *Corrosion/02*, Paper No. 02241, NACE International, Houston, Texas, 2002.
76. S. N. Smith, Predicting Corrosion in Slightly Sour Environments, *Materials Performance*, 2002.
77. E.H. Schot, J. Ottermann and P. Omenettor, *Rend. Soc. Ital. Mineral. Petrol.*, 28, 241 (1972).
78. H.T. Evans, Jr., C. Milton, E.C.T. Chao, I. Adler, C. Mead, B. Ingram and R.A. Berner, Art. 133 in *U.S. Geol. Survey Prof. Paper* 475-D, pp. D64-D69 (1964).
79. J.O.M. Bockris, D. Drazic and A. R. Despic, *Electrochim. Acta*, 4 (1961): p.325.

80. G. Schmitt and B. Rothman, *Werkstoffe und Korrosion*, 28 (1977): p.816.
81. S. Nestic, B. F. M. Pots, J. Postlethwaite and N. Thevenot, "Superposition of Diffusion and Chemical Reaction Limiting Currents – Application to CO₂ Corrosion", *Journal of Corrosion Science and Engineering*, Vol.1, Paper No. 3, World Wide Web, http://www.cp.umist.ac.uk/JCSE/Vol1/PAPER3/V1_p3int.htm, The Corrosion Information Server, The Corrosion & Protection Centre at UMIST, Manchester, UK, 1995.
82. B. Brown, K-L J. Lee, Apr. 2002, Institute for Corrosion and Multiphase Technology Board Meeting report, Ohio University.
83. K-L J. Lee and S. Nestic, "EIS Investigation on the Electrochemistry of CO₂/H₂S corrosion", *Corrosion/04*, paper no. 728 (New Orleans: NACE International, 2004).
84. K-L J. Lee, Sept. 2003, Institute for Corrosion and Multiphase Technology Board Meeting report, Ohio University.
85. K-L J. Lee, Apr. 2004, Institute for Corrosion and Multiphase Technology Board Meeting report, Ohio University.
86. K-L J. Lee, Sept. 2004, Institute for Corrosion and Multiphase Technology Board Meeting report, Ohio University.
87. K-L J. Lee, Apr. 2005, Institute for Corrosion and Multiphase Technology Board Meeting report, Ohio University.
88. S. Nestic, N. Thevenot and J. L. Crolet, "Electrochemical Properties of Iron Dissolution in CO₂ solutions – basics revisited", *Corrosion/96*, paper no. 3, (Houston, TX: NACE International, 1996).
89. E. Eriksrud and T. Sontvedt, "Effect of Flow on CO₂ Corrosion Rates in Real and Synthetic Formation Waters", *Advances in CO₂ Corrosion*, Vol. 1. Proceedings of the Corrosion /83 Symposium on CO₂ Corrosion in the Oil and Gas Industry, Editors: R.H. Hausler, H. P. Goddard, p. 20, (Houston, TX: NACE, 1984).
90. P. Delahay, *J. Am. Chem. Soc.*, 74 (1952): p.3497.
91. J. E. Oddo, M. B. Tomson, "Simplified Calculation of CaCO₃ Saturation at High Temperatures and Pressures in Brine Solutions". *SPE of AIME*, (1982): p. 1583.
92. IUPAC. *Chemical Data Series*, No. 21. *Stability Constants of Metal-Ion Complexes. Part A: Inorganic Ligands*. Pergamon Press.

93. B. Sundman, "Thermo-Calc Version L, Users' Guide", Dept. of Materials Science and Engineering, Royal Institute of Technology, Stockholm, Sweden, 1997.
94. Y. K. Kharaka et al., "Solmineq 88: A Computer Program for Geochemical Modelling of Water-Rock Interactions", Alberta Research Council, Menlo Park, California, 1989.
95. D. A. Palmer, R. van Eldik, *Chem. Rev.*, 83, (1983): p. 651.
96. *Comprehensive Chemical Kinetics*, Vol. 6, pp. 283-284 (Elsevier Publishing Company, Amsterdam, The Netherlands, 1972).
97. R. H. Perry, D. Green, *Perry's Chemical Engineers' Handbook*, 50th edition (McGraw-Hill, 1984).
98. J. Kvarekvål, "A Kinetic Model for Calculating Concentration Profiles and Fluxes of CO₂-Related Species Across the Nernst Diffusion Layer", *CORROSION/97*, paper no 5, (Houston, TX: NACE International, 1997).
99. D. R. Lide, "CRC Handbook of Chemistry and Physics", 75th edition, (CRC Press, 1995).
100. K. J. Vetter, *Electrochemical Kinetics, Theoretical Aspects*, Sections 1, 2 and 3 of *Electrochemical Kinetics: Theoretical and Experimental Aspects*, translation from German, (New York: Academic Press, 1967): p.235.
101. J. S. Newman, "Electrochemical Systems", Second Edition, Part C, Prentice Hall, 1991.
102. J. Bear, *Dynamics of Fluids in Porous Media*, (Dover Publications, New York, 1972).
103. J. T. Davies, *Turbulence Phenomena*, (Academic Press, 1972).
104. H. Press, *Numerical recipes in FORTRAN : the art of scientific computing*, 2nd edition, (Cambridge University Press, Cambridge 1992).
105. S. Netic, S. Wang, J. Cai, Y. Xiao, "Integrated CO₂ Corrosion - Multiphase Flow Model", *Corrosion/04*, paper no. 626, (Houston, TX: NACE International, 2004).
106. S. Netic, G.T. Solvi, and J. Enerhaug,, *Corrosion*, 51 (1995) p. 773.

107. S. Wang, K. George, S. Netic, " High Pressure CO₂ Corrosion Electrochemistry and the Effect of Acetic Acid ". CORROSION/2004, Paper No. 375 (Houston, TX: NACE International, 2004).
108. K. George, S. Netic, C. deWaard, "Electrochemical Investigation and Modeling of CO₂ Corrosion of Mild Steel in the Presence of Acetic Acid". CORROSION/2004, Paper No. 379 (Houston, TX: NACE International, 2004).
109. I. Nainville, A. Lemarchand and J.P. Badiali, "Growth and morphology of thick films formed on a metallic surface", *Electrochim. Acta*, Vol 41, No11/12, (1996): p. 1855.
110. M. Lafage, V. Russier and J.P. Badiali, "Simulation of growth and corrosion during the formation of a passive layer", *J. Electroanal. Chem.*, 450, (1998): p. 203.
111. A. Taleb, J. Stafiej, A. Chausse, R. Messina and J.P. Badiali, "Simulation of film growth and diffusion during the corrosion process", *J. Electroanal. Chem.*, 500, (2001): p. 554.
112. Nakayama and F. Kuwahara, "Numerical Modeling of Convective Heat Transfer in Porous Media Using Microscopic Structures", *Handbook of Porous Media*. (Marcel Dekker Publication, New York, 1995).
113. L. Latour, P. Mitra, R. Kleinberg and C. Sotak, "Time-Dependent Diffusion Coefficient of Fluids in Porous Media as a Probe of Surface-to-Volume Ratio", *Journal of Magnetic Resonance. Series A* 101, (1993): p.342.
114. J. W. Mullin, *Crystallization*, 3rd edition, (Oxford, 1993).
115. K. Hoffmann, S. Chiang, "Computational Fluid Dynamics for Engineers - Volume 1", fourth print, (A Publication of Engineering Education System, Kansas, USA, 1997).
116. B.P. Leonard, "A Stable and Accurate Convective Modelling Procedure based on Quadratic Upstream Interpolation", *Computer methods in applied mechanics and engineering*, 19, (1979): p. 59. (North-Holland Publishing Company, 1977).

117. B. Koren, "A robust upwind discretization method for advection, diffusion and source terms", Numerical methods for advection-diffusion problems, Vieweg, Braunschweig, (1993): p117.
118. A. Dugstad, "The Importance of FeCO_3 Supersaturation on the CO_2 Corrosion of Carbon Steels. CORROSION/92, paper no. 14, (Houston, TX: NACE International, 1992).
119. K. J. Vetter, Electrochemische Kinetik, p 406-429 (Springer-Verlag, Berlin, 1961).
120. P. Taylor, The Stereochemistry of Iron Sulfides-a Structural Rationale for the Crystallization of Some Metastable Phases from Aqueous Solution, Am. Mineral., Vol. 65, 1026-1030, 1980.
121. J.O.M, Bockris and Reddy Modern Electrochemistry : an introduction to an interdisciplinary area (A.K.N 1970).
122. G.L. Cooper, ASTM STP908, "Corrosion Monitoring in Industrial Plants", p.237-250 (1986).
123. G.R. Cameron, L.G. Coker, ASTM STP908, "Corrosion Monitoring in Industrial Plants", p.251-265 (1986).
124. M.W. Joosten, K.P. Fisher, R. Strommen and K.C. Lunden, Material Performance, p.44-48, April 1995.
125. S.W. Dean, ASTM STP908, "Corrosion Monitoring in Industrial Plants", p.197-218 (1986).
126. B. Brown, "CO₂/H₂S corrosion in supersaturated conditions" Oct. 2004, Institute of Corrosion and Multiphase Technology Board Meeting report, Ohio University.
127. E. McCafferty, Corros. Sci. 39 (1997) 243.
128. D.D. MacDonald, M.C.H. Mckubre, J.O.M. Bockris, B.E. Conway, R.E. White (Eds.), Modern Aspects of Electrochemistry, vol. 14, Plenum Press, New York, 1982, p.61.
129. M. Keddam, O.R. Mattos, H. Takenouti, J. Electrochem. Soc. 128 (1981) p.257.
130. M. Keddam, O.R. Mattos, H. Takenouti, J. Electrochem. Soc. 128 (1981) p.266.

131. B. Brown, Srdjan Nesic and Shilpha Reddy Parakala, "CO₂ Corrosion in the presence of Trace Amounts of H₂S", paper 736, (New Orleans, LA: NACE International, 2004).
132. H. Binder, *Z. Naturforsch* (1973). B28, p.256.
133. Y. Limouzin-Maire, *Y. Bull. Soc. Chim. Fr.* (1981) I. p.340.
134. J.H. Scofield, *Electron. Spectrosc. Related Phenom.* 8 (1976), p.129-137.
135. D.T. Rickard, "The Chemistry of iron sulfide formation at low temperatures". *Stockholm Contrib. Geol.* 26 (1969), p. 67-95.
136. R.E. Sweeney, I.R. Kaplan, "Pyrite framboid formation: laboratory synthesis and marine sediments". *Geology.* Vol. 68, (1973) p. 618-634.
137. A.R. Lennie and D.J. Vaughan, "spectroscopic studies of iron sulfide formation and phase relations at low temperatures", *Mineral Spectroscopy: A tribute to R.G. Burns.* 5 (1996), p.117-131.
138. J. Heyrosky, *Rec. Trav. Chim. Pays-Bas* 44, 499 (1925).
139. J. Tafel, *Z. Physik, Chem.* 50, (1905): p641.
140. J.O.M. Bockris, D. Drazic and A.R. Despic, *Electrochim. Acta*, 4 (1961): p.325.
141. H. Gerischer and W. Mehl, *Z. physik. Chem* (1955): p.1049.
142. E. Warburg, *Wied. Ann.* 67, (1899): p.493.
143. M. Sluyters-Rembach and J.H. Sluyters, in *Electroanalytical Chemistry*, Vol. 4 (A. J. Bard, ed.), Marcel Dekker, New York, 1970.
144. J.E. Ferrer, L. Victori, *Electrochim. Acta* 39 (1994) p 581.

APPENDIX A: CORROSION MONITORING TECHNIQUES

Introduction

Corrosion monitoring techniques can be classified into two major categories: non-electrochemical techniques and electrochemical techniques. Traditionally the non-electrochemical techniques such as weight loss and electrical resistance are widely used throughout the industry due to their simplicity, robustness and reliability. However, information obtained by these non-electrochemical techniques do not reveal any details about the mechanism of corrosion process. On the other hand, the use of electrochemical techniques offer a great deal more with regard to the mechanistic details in corrosion process.

Corrosion is an electrochemical process, therefore electrochemical methods are well suited for monitoring corrosion. A broad range of electrochemical techniques can be used to monitor corrosion process. Some of the most commonly used electrochemical techniques are: Linear Polarization Resistance (LPR), potentiodynamic sweep, Electrochemical Impedance Spectroscopy (EIS) and Electrochemical Noise (EN). Each technique has its strengths and limitations, therefore each technique is best suited for specific applications.

The advantages and drawbacks of each technique (both non-electrochemical and electrochemical type) are briefly compared and contrasted in Appendix A.

Non-electrochemical techniques

Weight loss method

For over thirty years, weight loss coupons have been used in industrial processes to measure corrosion rates. This simple and reliable technique provides an accurate measure of corrosion rate in any environment. However, it requires an extended exposure time in order to yield meaningful result. The corrosion rate from a weight loss coupon method is determined as follows:

$$CR_{average} = \frac{WL \times 24 \times 36 \times 365 \times 10}{\rho A t}$$

Where $CR_{average}$ = average corrosion rate in mm/year;

WL = coupon weight loss in grams;

ρ = density of the coupon in gram/cm³

A = exposed coupon surface area in cm²

t = exposed time in hours

Ideally one is interested in extracting as much information from an experiment as possible to gain a complete understanding of the influence of various parameters. However, weight loss method provides only an average corrosion rate over a given interval of the experiment and some visual clues of a type of corrosion.

Electrical Resistance method

Electrical Resistance (ER) technique provides the way to electrically transmit and record corrosion rate by measuring the increase in electrical resistance of a metal sensor

element as its cross-section is reduced by corrosion, compared to a protected reference element. The electrical resistance of a metal or alloy element is given by:

$$R = \frac{\rho L}{A}$$

where ρ = specific resistance of the metal or alloy

L = length of the probe

A = cross sectional area.

Hence, the reduction (i.e. metal loss) in the cross sectional area due to corrosion attack will be accompanied by a proportional increase in the electrical resistance of the probe.

ER technique is essentially a metal loss measurement technique; therefore it is applicable in almost any environment.¹²² Only sulfide environments present difficulties for the electrical resistance technique, iron sulfide film is conductive and it will cause underestimation of metal loss. In some extreme cases where a metal gain would be recorded due to excessive amount of iron sulfide film.¹²³

The fundamental drawback of ER technique is the lengthy response time. Removal of sufficient metal for a measurable resistance increase to happen can take days or even weeks.^{122,124}

Solution Analysis method

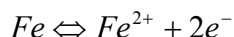
The concentration of the ion (typically Fe^{2+}) in the solution is measured prior and after the experiment. Based on the exposed surface area of the coupon and the volume of

the solution, the integrated corrosion rate of the coupon over the exposure time can be estimated. However, similar to other non-electrochemical techniques, this technique can not determine the instantaneous corrosion rate. Therefore, it is not suitable for on-line corrosion monitoring application.

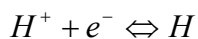
Electrochemical techniques

Potentiodynamic sweep

Nearly all metal corrosion occurs via electrochemical reactions at the interface between the metal and an electrolyte solution. Corrosion proceeds at a rate determined by equilibrium between opposing electrochemical reactions. One reaction is the anodic dissolution of the iron to iron ions, in which metal is oxidized, releasing electrons into the metal:



The other is the cathodic reaction, in which a solution species is reduced; removing electrons from the metal, one of the most common cathodic reactions is the hydrogen evolution:



When these two reactions are in equilibrium, the flow of electrons from each reaction is balanced and no net electron flow occurs. Except when an external instrument such as a potentiostat is used to remove or supply free electrons from the metal.

The current response of a corroding metal to a voltage is determined in potentiodynamic sweep technique. If free electrons are supplied, then the potential is shifted negatively and the cathodic reaction rate is accelerated, whereas the anodic reaction rate is decelerated. Since the anodic and cathodic reactions are no longer balanced, a net current will flow from the electronic circuit into the metal sample and measured by the potentiostat.

$$I_{\text{applied,c}} = i_c - i_a$$

where i_c is the current density for the cathodic reduction reaction, i_a is the current density for the anodic oxidation reaction and $i_{\text{applied,c}}$ is the applied cathodic current density, all at the same potential. If enough electrons are supplied to shift the potential far away from corrosion potential, the current from the anodic reaction will be negligible and the measured current will be a measure of the cathodic reaction alone.

On the other hand, if free electrons are removed, then the anodic reaction is driven in the forward direction and the cathodic reaction is driven in the reverse direction. At strong enough positive potentials the anodic current dominates the cell current. Similarly, the applied anodic current density is given by :

$$I_{\text{applied,a}} = i_a - i_c$$

In some cases, potential can be varied to passivate the metal and causing pitting corrosion, however, it is not within the scope of this report.

The value of either the anodic or cathodic current at corrosion potential is the corrosion current, i_{corr} . The corrosion rate of the metal can be determined if i_{corr} can be

measured. Unfortunately i_{corr} can not be measured directly; one must estimate it from a polarization curve using the Tafel extrapolation method as shown in **Figure 75**.

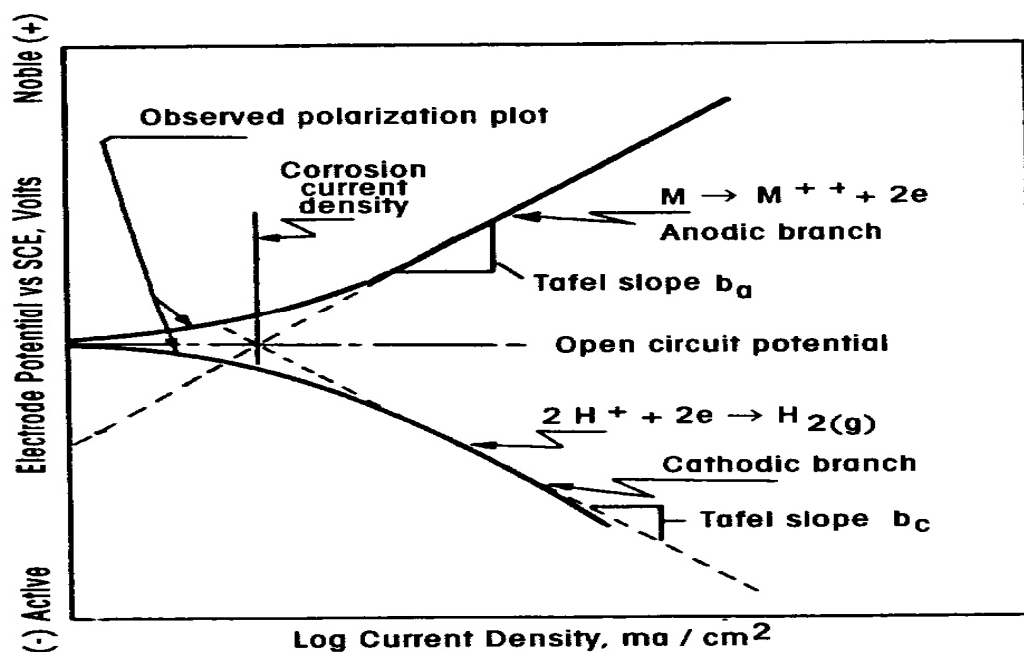


Figure 75. Polarization curve from potentiodynamic sweep technique. Source: DC electrochemical test methods from Corrosion testing made easy series. NACE

Faraday's law states that the electrochemical reactions either produce or consume electrons and the rate of electron flow to or from a reacting interface is a direct indication of electrochemical reaction rate. Hence, corrosion rate can be determined from corrosion current i_{corr} as given below:

$$CR = \frac{i_{\text{corr}} MW_{\text{iron}}}{nF\rho_{\text{iron}}}$$

where CR = corrosion rate (mm/year)

MW_{iron} = molecular weight of iron

n = number of electrons transferred during the reaction

F = Faraday's constant (96500 coulombs/equivalent)

ρ_{iron} = density of iron

The major advantage of potentiodynamic sweep technique is the capability to study the mechanism of corrosion. This technique enables one to determine whether the corrosion process is charge transfer, mass transfer or chemical reaction controlled. Moreover, once the mechanism has been identified, the kinetic rate constants such as exchange current density, Tafel slopes and chemical reaction rate can be determined using this technique.

However, the major disadvantage is that the electrode must be polarized far from its corrosion potential in order to obtain the Tafel portions in the anodic and cathodic regions.

When the electrode is cathodically polarized far away from corrosion potential, H^+ will be consumed at the electrode surface and an artificial corrosion product may form due to low pH. On the other hand, if the electrode is anodically polarized too far away from corrosion potential, the electrode surface will be damaged by excessive artificial corrosion and the solution will be contaminated by too much iron ions. Due to the destructive nature of potentiodynamic sweep, this technique is unsuitable for on-line corrosion monitoring applications.

Linear Polarization Resistance (LPR)

This technique is based on the fact that the free electrons required to produce a small shift in the potential of a corroding electrode is proportional to the corrosion current density, which can be converted to corrosion rate.

R_p is defined as dE/di at the corrosion potential and may be easily measured by plotting a potential on a linear graph vs. current over a small potential range near corrosion potential as shown in Figure 76. The slope of the resulting line tangent to the curve at $i=0$ is equal to R_p .

Once R_p has been estimated, the corrosion rate can be obtained from Stern-Geary approximation, which assumes the polarizing current changes linearly with a change in the potential in a region that is within a few (10-20) mV of the corrosion potential. From this linear approximation, the corrosion current can be estimated as shown below:

$$i_{corr} = \frac{\beta_a \beta_c}{2.303(\beta_a + \beta_c)} \frac{1}{R_p}$$

where β_a = the anodic Tafel slope (V/decade)

β_c = the cathodic Tafel slope (V/decade)

i_{corr} = corrosion current density (A/cm²)

R_p = polarization resistance (Ohm cm²)

Linear Polarization Resistance (LPR) technique almost overcomes the destructive nature of potentiodynamic sweep because only the small overpotential with respect to corrosion potential is applied. Another advantage is that it enables corrosion rate to be obtained relatively fast (2-10 minutes) compared to non-electrochemical techniques.

LPR has been widely used throughout industry for more than forty years. However, it is

restricted to use in continuous electrolytes.¹²⁵ Multiphase, discontinuous, corrosive fluids such as emulsions, condensing vapors, thin moisture films and condensates prove rather difficult, if not impossible, to monitor using this technique. Moreover, Low conductive electrolyte also causes IR-drop error that is difficult for LPR to manage.

Another disadvantage of LPR technique is that the Tafel slope constants need to be assumed a priori. This may be problematic when the mechanism is unknown. In order to avoid assuming Tafel constants, potentiodynamic sweep technique can be incorporated to determine the Tafel slope.

The fundamental drawback of this technique is that it gives no information about the corrosion mechanism.

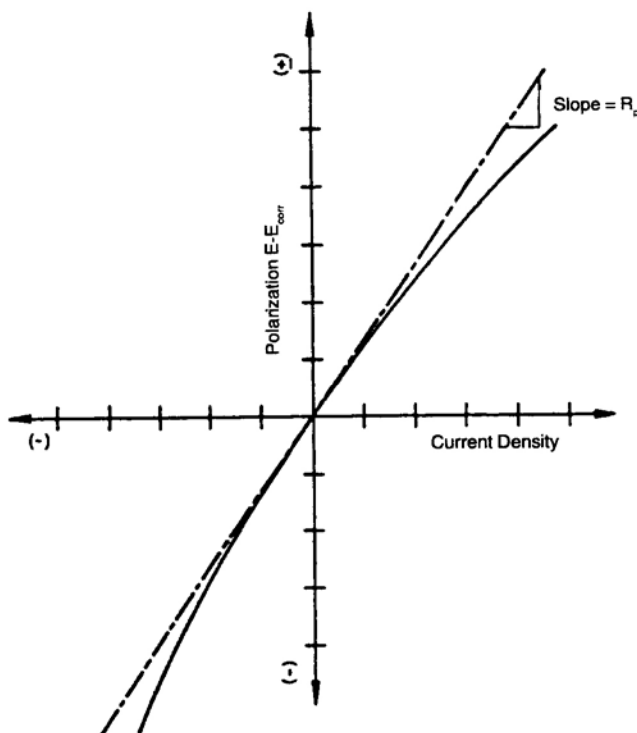


Figure 76. Obtaining R_p from Linear Polarization Resistance technique. Source: DC electrochemical test methods from Corrosion testing made easy series. NACE

Electrochemical Impedance Spectroscopy (EIS)

EIS is an electrochemical technique in which an external AC signal is applied to a corroding metal, and the response is then measured. Typically a small sinusoidal voltage perturbation is applied at various frequencies and the resulting AC current response is measured.

EIS involves only little external perturbation to the system, which makes it non-destructive in nature. On the other hand, alternating current measurements at different frequencies enable different processes to be identified and measured. For instance, the solution resistance can be measured at high frequencies, whereas polarization resistance can be determined at the lower frequencies. At even lower frequencies, different types of process occur over different time scales at different frequencies, which enables diffusion effects and adsorption/desorption phenomena to be identified.

In EIS, the double layer capacitance and solution resistance can be obtained. Therefore, it can be used to study high impedance systems such as coatings and linings. EIS also enables one to investigate a system in a low conductive solution because the error caused by solution resistance can be compensated.

However, major disadvantages are the difficulty in interpreting EIS data and the time required to obtain a full impedance diagram also may impose a serious limitation in on-line corrosion monitoring applications. A mechanistic analytical model is developed in order to interpret EIS data and is shown in Appendix C.

APPENDIX B: VAPOR-LIQUID EQUILIBRIUM MODEL

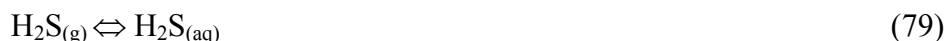
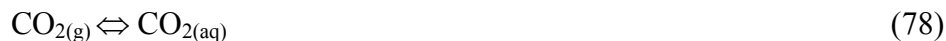
The CO₂/H₂S/H₂O vapor-liquid equilibrium model for dilute aqueous solutions of CO₂/H₂S at different temperature is developed with the aim to calculate the species concentrations in the presence of H₂S. Although similar model has been built previously^{38,39,40} It is essential to develop a model of our own to provide more flexibility and applicability of input and output because the equilibrium concentrations are used as initial and boundary conditions for the mechanistic corrosion model. The equilibrium model is also a practical tool for experiments as it enables important parameter such as pH and H₂S concentration to be compared and verified against the experimental measurements.

The model has been built to simulate two different environments: an open system simulating a situation with a constant partial pressure of CO₂ and H₂S, and a closed system simulating an autoclave or a closed flow loop system with varying gas/liquid volume ratios. The model is based on the vapor-liquid equilibria of gaseous species and the dissociation equilibria for dissolved species. The difference in modeling an open system and a closed system will be illustrated in the following section:

Open system conditions

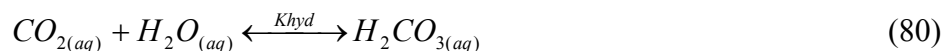
In an open system there is a constant partial pressure of carbon dioxide and hydrogen sulfide gaseous species applied on the surface of the water, this results in

carbonic and sulfide species dissolves in water. Vapor-liquid equilibrium of carbon dioxide and hydrogen sulfide reactions are described as follow:

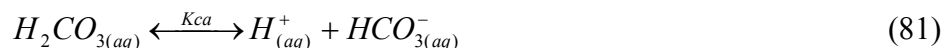


Once carbon dioxide dissolves in water, $\text{CO}_{2(aq)}$ is involved in a sequence of chemical reactions as follows:

Hydration of aqueous carbon dioxide:



Dissociation of carbonic acid:



Dissociation of bicarbonate ion:



On the other hand, when hydrogen sulfide dissolves in water, it does not need to hydrate with water to form an acid in order to dissociate hydrogen ions, since it is already acidic, the series of dissociation that sulfide species proceeds in the aqueous solution are:

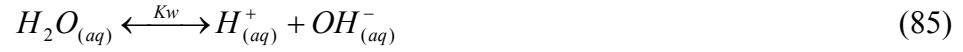
Dissociation of hydrogen sulfide:



Dissociation of HS^- ion:



Since all these processes occur in water, self-ionization of water is also involved :



Since the partial pressures of both gaseous species are known in an open system, Henry's law can be applied in order to calculate the composition of vapor-liquid equilibrium:

$$M_{CO_2} H_{CO_2} = P_{CO_2} \quad (86)$$

$$M_{H_2S} H_{H_2S} = P_{H_2S} \quad (87)$$

Where M_{CO_2} and M_{H_2S} is the concentration of carbon dioxide and hydrogen sulfide in solution, respectively, and H is the Henry's constant. P_{CO_2} and P_{H_2S} is the partial pressure of carbon dioxide and hydrogen sulfide, respectively.

Once the concentration of dissolved carbon dioxide and dissolved hydrogen sulfide are determined, all the reactions above can be solved by corresponding equilibrium constants, therefore the concentrations of each species can be calculated as follows:

$$K_{hyd} = \frac{[H_2CO_3]}{[CO_2][H_2O]} \quad (88)$$

$$K_{ca} = \frac{[H^+][HCO_3^-]}{[H_2CO_3]} \quad (89)$$

$$K_{bi} = \frac{[H^+][CO_3^{2-}]}{[HCO_3^-]} \quad (90)$$

$$K_1 = \frac{[H^+][HS^-]}{[H_2S]} \quad (91)$$

$$K_2 = \frac{[H^+][S^{2-}]}{[HS^-]} \quad (92)$$

$$K_w = \frac{[H^+][OH^-]}{[H_2O]} \quad (93)$$

The K 's, as a function of the temperature, are available in the open literature³⁸

Since the solution cannot have a net charge, electroneutrality relation is required.

Mathematically, this is expressed as:

$$M_{H^+} + M_{Na^+} = M_{HS^-} + 2 \times M_{S^{2-}} + M_{HCO_3^-} + 2 \times M_{CO_3^{2-}} + M_{Cl^-} \quad (94)$$

When dealing with a base or an acid, additional ions such as Na^+ and Cl^- also needs to be considered in this equation.

Closed system conditions

Once the system is closed, the partial pressure of gases is no longer constant and the concentration of H_2S and CO_2 in gaseous phase becomes an unknown when the vapor-liquid equilibrium is disturbed (i.e. change of pH). However, total amount of carbonic and sulfide species are kept constant in a closed system. Hence, two extra mass conservation equations for both species are added in order to model the closed system.

$$\Sigma M_{\text{carbonic species}} = M_{CO_{2(g)}} + M_{CO_{2(aq)}} + M_{H_2CO_3} + M_{HCO_3^-} + M_{CO_3^{2-}} \quad (95)$$

$$\Sigma M_{\text{sulfide species}} = M_{H_2S_{(g)}} + M_{H_2S_{(aq)}} + M_{HS^-} + M_{S^{2-}} \quad (96)$$

Numerical techniques

There are eleven species exist in the system: $\text{CO}_{2(\text{g})}$, $\text{CO}_{2(\text{aq})}$, H_2CO_3 , HCO_3^- , CO_3^{2-} , $\text{H}_2\text{S}_{(\text{g})}$, $\text{H}_2\text{S}_{(\text{aq})}$, HS^- , S^{2-} , H^+ , OH^- . Therefore there are eleven unknowns to be solved in eleven equations in a closed system: two vapor-liquid equilibria (86,87), six chemical equilibria(88,89,90,91,92,93), an electroneutrality equation(94) and two mass balance equations(95,96). Newton-Raphson's method was chosen for solving this system of non-linear algebraic equations. A FORTRAN program for the calculation of the equilibrium compositions was written. The sequence of calculation is as follows:

1. The temperature, total pressure, desired H_2S concentration in gas phase, initial concentration of the salt and the volume of the gaseous and aqueous phase in the system are specified.
2. The partial pressure of water vapor, H_2S and CO_2 are calculated.
3. The preliminary estimate is refined using Newton-Raphson's method for the solution of non-linear equations.
4. The Equilibrium composition is determined from the converged solution.

pH can be adjusted by setting the H^+ concentration to the desired value, this leaves 10 unknowns with eleven equations, therefore the additional unknown is introduced here as the concentration of the additive(e.g. NaHCO_3) that needs to be added in electroneutrality equation(94) in order to change the pH.

Results and discussion

In order to verify the performance of the newly developed model, the OLI Systems Stream Analyzer, a thermodynamic model that is commonly used by the oil and gas industry, has been used. For an open system, predictions for species concentrations made by the two models agree very well except for the case of the S^{2-} as shown in Figure 77. This is due to the fact that the value of the dissociation constant for the HS^- is not consistent in the literature and is yet to be confirmed.^{38,39} Therefore in the current stage of development, this discrepancy is not of major concern.

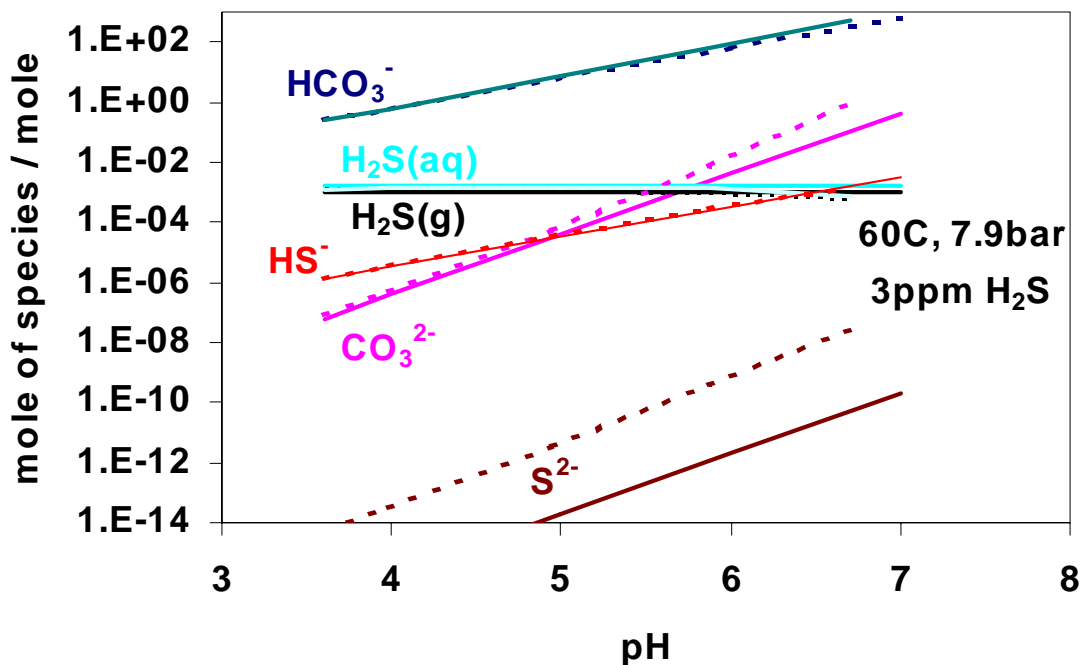


Figure 77. Comparison between our model and OLI model prediction on the species concentration with respect to pH in open system, solid line = our model, dash line = OLI model prediction.

Simulation of a hypothetical closed system showing the effect of pH on the carbonic species concentration is shown in Figure 78. Note that this is a simulation for pure CO_2 condition. More HCO_3^- and CO_3^{2-} are produced by dissociation as pH increases while the concentration of $\text{CO}_{2(\text{aq})}$ and H_2CO_3 decreases. At high pH ($\text{pH} > 10$), the concentration of HCO_3^- starts decreasing. Eventually most of the carbonic species would be converted into CO_3^{2-} , because it obeys the law of conservation of carbonic species in a closed system.

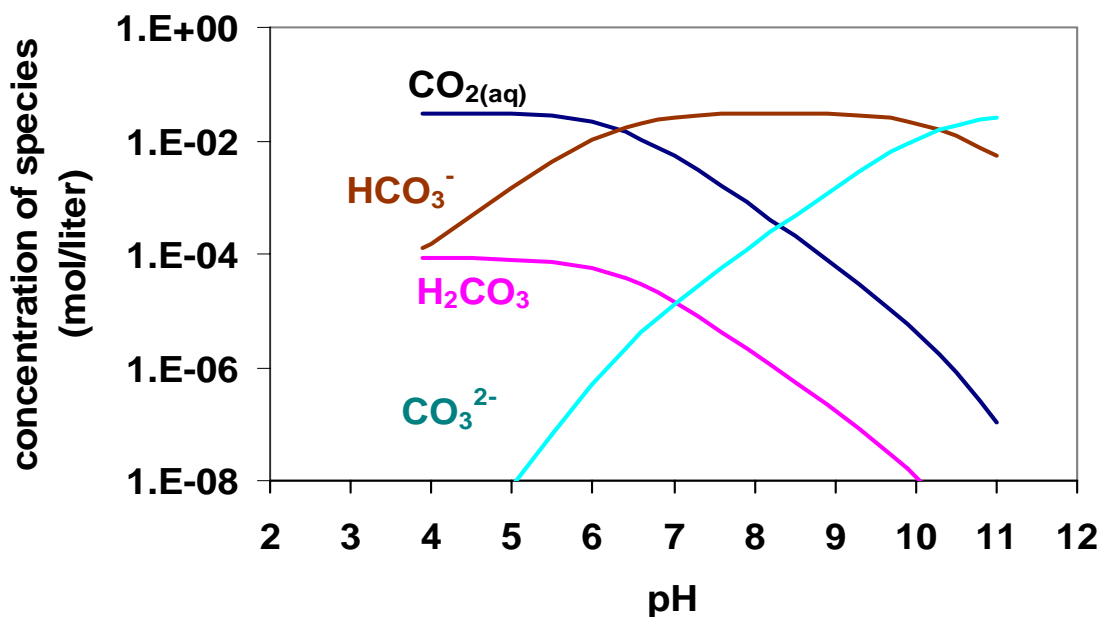


Figure 78. pH effect on the concentration of carbonic species for 25°C, atmospheric pressure in closed system

The equilibrium model has been built with the flexibility to take into account various gas to liquid volumetric ratios and Figure 79 illustrates a comparison between an

open system and hypothetical closed system with gas to liquid ratio of 100:1. In the interested pH range of 4-6, there is no difference in concentration of carbonic species between two systems. Only at the high pH the deviation of concentrations between the two systems is evident.

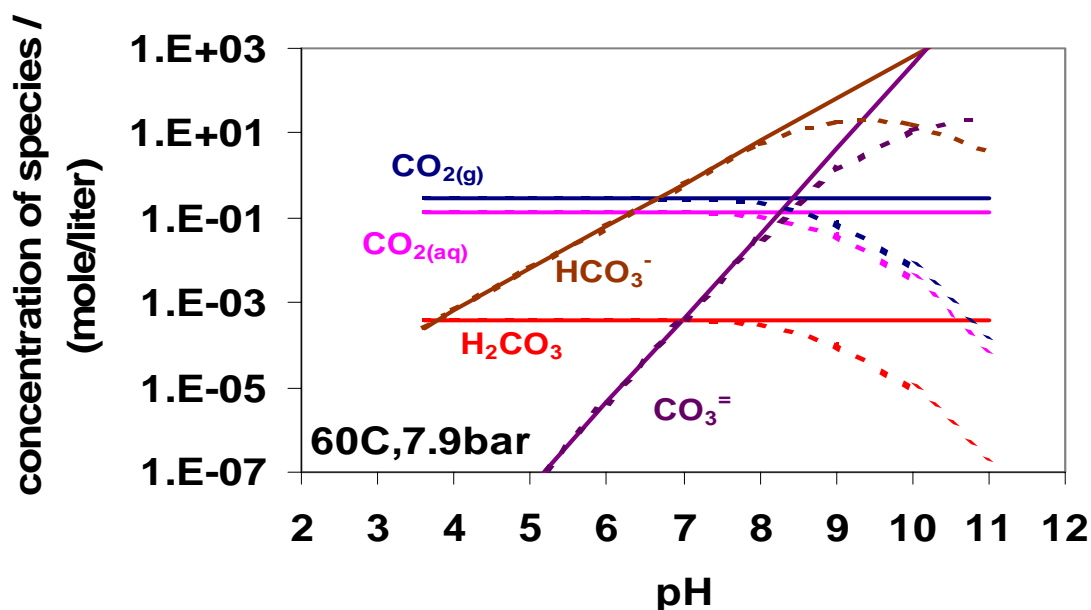


Figure 79. Comparison of open system and closed system with gas to volume ratio 100:1 at 60°C and 7.9bar

The next test for the model was to simulate the equilibrium chemistry in the H₂S flow loop system at Ohio University. The following parameters were used: 60°C, pH 4, p(CO₂)= 7.7 bar, 3 ppm H₂S in the gas phase and system gas to liquid ratio of 1004:946. By using the model the amount of H₂S that was required to achieve certain gaseous concentration can be pre-determined under these environmental conditions. The

calculated values were verified within 10% of error by the experimental measurement using a gas chromatograph on the sample gas withdrawn from the system after the addition. Figure 80 demonstrates the comparison between the equilibrium in the H₂S flow loop system and a hypothetical open system over the wide range of pH in the presence of 3 ppm of H₂S in the system. By comparing the sulfide species only, the concentrations in the two systems are the same over the pH range of 4-6. The concentrations only deviate at pH>6. Since the hypothetical open system simulates the field condition with limitless gaseous supply, this proves that the H₂S flow loop system is capable of simulating the field condition in the pH range between 4-6.

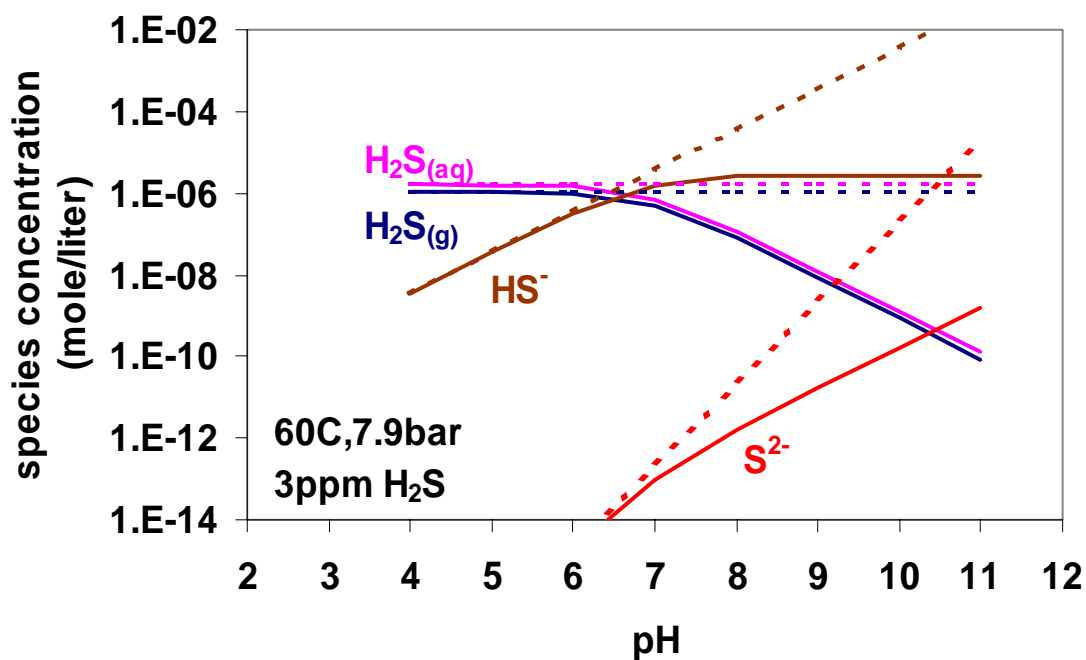


Figure 80. Effect of pH on the concentration of sulfuric species, solid line=H₂S flow loop system with gas to liquid volume ratio of 1004:946, dash line = open system.

In order to illustrate the amount of sulfide species in relation to the carbonic species, Figure 81 shows all the species concentrations for the same parameters as described in the paragraph above. Note that the y-axis is in log scale and the carbonic species is greater than the sulfide species by several orders of magnitude. Therefore the concentration of carbonic species is not altered by the presence of 3 ppm of H_2S in the system.

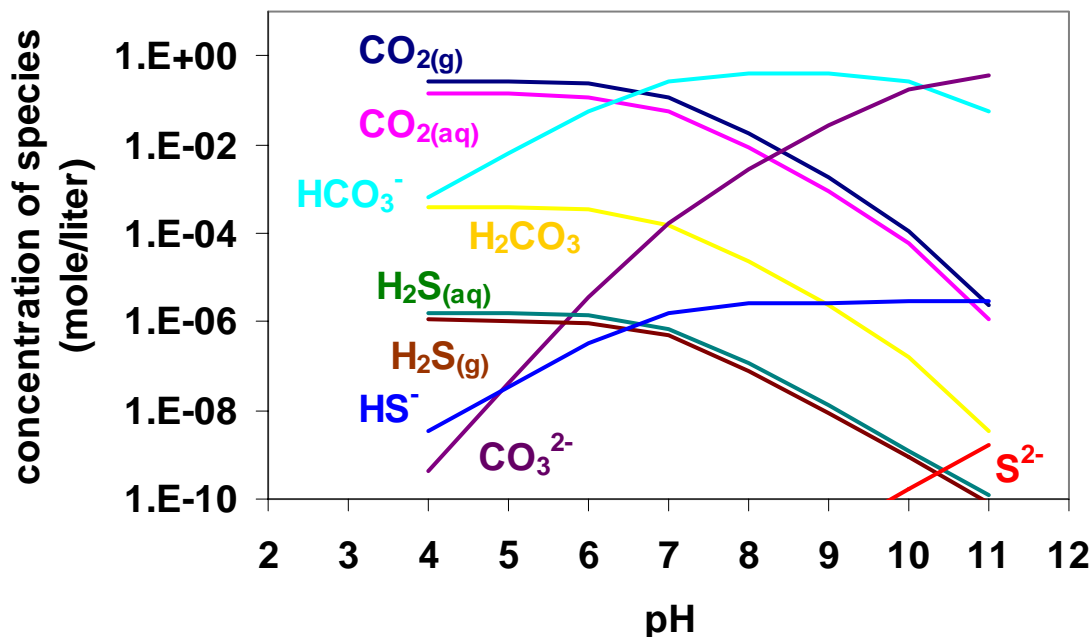


Figure 81. H_2S flow loop system concentration of all the species in the presence of 3 ppm H_2S at $T=60^\circ\text{C}$, $p(\text{CO}_2)=7.9$ bar with gas to liquid ratio of 1004:946

Similar calculations have been conducted for different low concentrations of H_2S (10 ppm, 100 ppm and 300 ppm) with similar results, i.e. showing that the carbonic species concentration is practically not affected by the presence of H_2S at these low

concentration. However, from the theory one knows that the carbonic species would eventually be affected by the presence of sulfide species, given that the concentrations of sulfide species are high enough. Therefore a hypothetical high gaseous concentration of H_2S has been selected to test how the model performs at the other extreme end. Figure 82 illustrates the concentrations of all the species for 20% of H_2S in the system. Figure 83 shows that at this high concentration of H_2S , the concentration of carbonic species in the flow loop system is significantly reduced when compared to the one without H_2S , which qualitatively made sense.

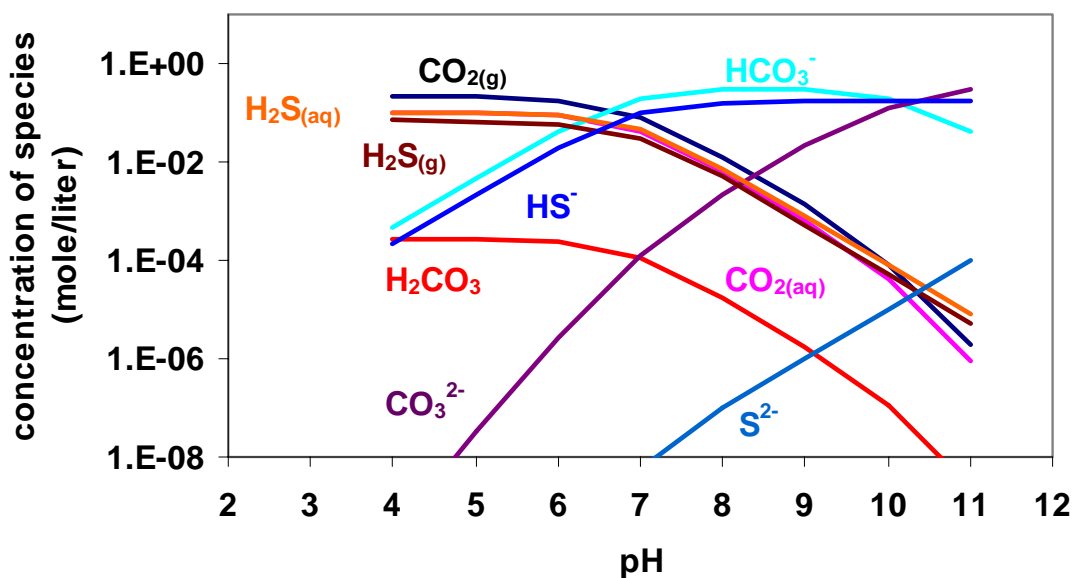


Figure 82. Closed flow loop system concentration of all the species in the presence of 20%(200000ppm) H_2S at $T=60^\circ\text{C}$, $p(\text{CO}_2)=7.7$ bar with gas to liquid ratio of 1004:946

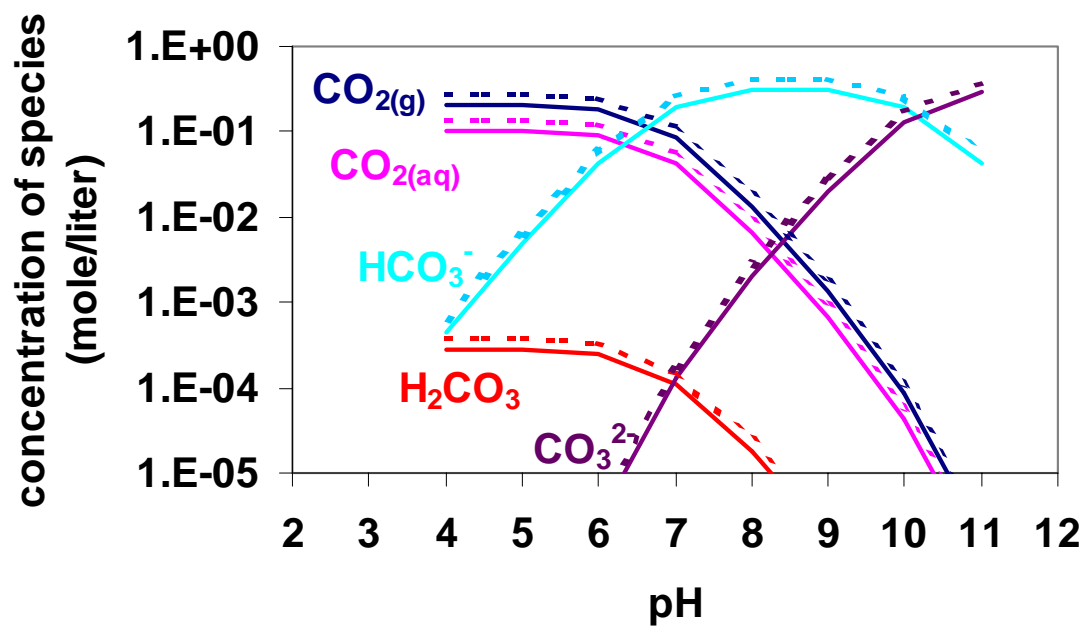


Figure 83. Effect of 20% H₂S concentration on the carbonic species, solid line= 20% H₂S in the system, dash line = no H₂S presence.

APPENDIX C: MECHANISTIC EIS ANALYTICAL MODEL

Introduction

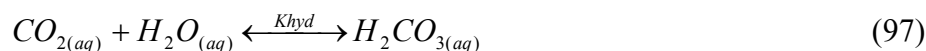
Due to its difficulty in extracting meaningful physical information from the Nyquist plot produced by using EIS technique, an analytical tool is required in order to interpret the mechanism. Traditionally, equivalent circuit analysis was commonly used to interpret the information from the Nyquist plot by fitting the data with a combination of capacitors, resistors and inductors. However, this approach is not conclusive in determining the mechanism because various combinations of equivalent circuit can all lead to a similar result. Furthermore, equivalent circuit analysis provides very limited information on the underlying physico-chemical process because it is not based on any knowledge of chemistry within the system. Therefore, a mechanistic approach was pursued and a model that gives an electrochemical impedance response was established based on fundamental equation of electrochemistry on the surface, transport and water chemistry in the bulk of the solution. This model is able to capture complicated EIS curves to provide qualitative information of the underlying CO₂/H₂S corrosion process.

Modeling

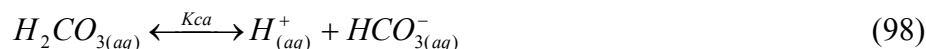
Physical model of Cathodic reaction

The mechanistic model of electrochemical impedance response is based on following fundamental reactions in CO₂ corrosion proposed by previous studies in the field¹³⁻¹⁶:

When CO_2 is dissolved in water, hydration of aqueous carbon dioxide takes place to form carbonic acid:



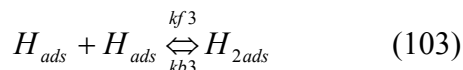
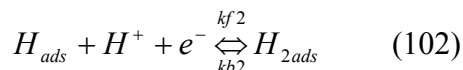
The carbonic acid H_2CO_3 is then dissociated in two steps:



It is proposed that carbonic acid provides a reservoir of H^+ ions at a given pH. Therefore hydrogen evolution is assumed to be the most dominant cathodic reaction. Whereas the other possibility of direct carbonic acid reduction is not considered in this particular EIS model: ¹



When hydrogen ions diffuse through the diffusion boundary layer to the metal surface, hydrogen evolution involving intermediate adsorbed hydrogen atom will take place as shown below:



When the hydrogen ion is being reduced (120), the resulting adsorbed hydrogen atom H_{ads} can either recombine with another adsorbed hydrogen atom to form H_{2ads} (103),

or it has the possibility to undergo another charge transfer step by reacting with a hydrogen ion and an electron to form H_{2ads} (102). This additional charge transfer reaction (102) is first proposed by Heyrosky¹³⁸ and is also known as Heyrosky's reaction. On the other hand, the slow recombination reaction (103) assumed by Tafel¹³⁹ is the best-known rate determining chemical reaction.

Mathematical model

In order to develop a mechanistic EIS model that gives an electrochemical impedance response, both charge transfer and mass transfer of H^+ need to be taken into consideration. Moreover, hydration of carbon dioxide (117), being the slowest chemical reaction in CO_2 solution, which contributes partly to the current limitation, is also included in the model. The resistance resulting from the current and the overvoltage is impedance and the total impedance response is described as:

$$Z_{total} = \frac{\eta_{total}}{i} = \frac{\eta_{d,B.L.,r} + \eta_t}{i} \quad (104)$$

where

$$i = I \sin(\omega t)$$

I = current amplitude

$$\omega = 2\pi f$$

f = frequency (Hz)

$\eta_{d,B.L.,r}$ = diffusion overvoltage taking account of finite-thickness boundary layer and limiting chemical reaction (117).

η_t = charge transfer overvoltage

Charge-transfer overvoltage

Charge transfer overvoltage arises when charge transfer reaction is rate determining when current flows. Therefore one needs to determine the relationship between current and overvoltage resulting from charge transfer reaction. The two-step charge transfer process with two possible paths of hydrogen evolution as shown above can be modeled by mathematical equations. The reaction for the reduction of hydrogen ions on the bare metal surface (120) can be modeled by the following relationship:

$$i_1 = (1 - \theta)i_{0,1}10^{(-\eta/b_1)} \quad (105)$$

where

θ = coverage factor , percentage of H_{ad} covered on the metal surface ($0 \leq \theta \leq 1$)

$i_{0,1}$ = exchange current density for hydrogen ion reduction on fully uncovered electrode at equilibrium potential $\approx 1.58 \times 10^{-2}$ A/m² for 20°C and pH5^{13,140}

η = overvoltage = $\varepsilon - \varepsilon_0$

ε_0 = equilibrium potential

b_1 = Tafel slope = $2.303RT/\alpha_1F$

α_1 =Symmetry factor, according to Bockris et al.¹⁴⁰, for hydrogen evolution,

$\alpha_1=0.5$ giving $b_1=0.108$ at 20°C.

On the other hand, Heyrosky's reaction (102) requires an adsorbed hydrogen atom to react with a hydrogen ion and an electron. Since this is an electrochemical reaction involving charge transfer, it can be described similarly as above:

$$i_2 = \theta i_{0,2} e^{(-\eta/b_2)} \quad (106)$$

The recombination of H_{ad} is a chemical reaction requiring two adsorbed hydrogen atoms, therefore rate of reaction (103) is modeled as:

$$K_3 = 2Fk_{f3}\theta^2 \quad (107)$$

The rate of change of H_{ad} adsorption coverage θ on the metal surface is described by the fact that reaction of hydrogen ion reduction (120) increases the H_{ad} adsorption coverage, whereas the Heyrosky's reaction (102) and recombination chemical reaction (103) decrease the adsorption coverage:

$$\frac{d\theta}{dt} = \frac{i_1 - i_2 - K_3}{C_H} \quad (108)$$

where C_H is the constant linking the fraction of the adsorbed surface θ and the surface concentration of adsorbed species expressed in mol/cm². It is also called adsorption capacitance and it is considered to be equal to 10⁻⁸ mol/cm², which corresponds to about one monolayer for the case of one intermediate bonding to one surface metal atom.¹²⁹

Combining equation (105), (106), (107) and (108) with the initial condition: $t=0$; $\theta=0$, adsorption coverage can be determined as a function of time $\theta(t)$. Therefore the individual current i_1, i_2 is a function of overvoltage and adsorption coverage, which is a function of time. The total current resulting from the cathodic charge transfer of hydrogen evolution is the sum of individual current:

$$i_{total} = i_1 + i_2 \quad (109)$$

When small amplitude of sinusoidal alternating current is induced, a relationship between charge transfer overvoltage and current was derived by Gerischer and Mehl:¹⁴⁴

$$\eta_t = \frac{I \sin(\omega t)}{L_D - \frac{ab}{b^2 + C_H^2 \omega^2} + \frac{aC_H \omega}{b^2 + C_H^2 \omega^2} j} \quad (110)$$

Where

$$j = \text{imaginary component} = \sqrt{-1}$$

$$L_D = \frac{F(\alpha_1 i_1' + \alpha_2 i_2')}{RT}$$

$$a = \frac{F(i_2 - i_1)(\alpha_2 i_2' - \alpha_1 i_1')}{RT}$$

$$b = i_1 + i_2 + 2F\theta' k_{f3}$$

i_1', i_2' and θ' are values at equilibrium potential.

It is seen in equation (110) that real and imaginary component are both frequency dependent. This frequency dependence was evoked by periodic change of adsorption

coverage θ . This charge transfer overvoltage has a phase shift with respect to the alternating current, that's why there is an imaginary component. This imaginary component can be both capacitive ($a>0$) and inductive ($a<0$) and it depends on which way the adsorption coverage θ change with the fluctuation of overpotential and whether it increases or decreases the current.

Diffusion overvoltage

Diffusion overvoltage appears when the supply of reactants at the electrode or the removal of the reaction products is rate determining when current flows. When applying a sinusoidal alternating current, a relationship between diffusion overvoltage and sinusoidal alternating current is found by Warburg¹⁴⁴:

$$\eta_w = \frac{RT}{n^2 F^2} \frac{v^2}{\sqrt{\omega} [H^+]_{bulk} \sqrt{D_{H^+}}} I \sin(\omega t - \frac{\pi}{4}) \quad (111)$$

where

v = stoichiometric constant

$[H^+]_{bulk}$ = concentration of H^+ ions in the bulk

D_{H^+} = diffusion coefficient for H^+ ions = 9.312×10^{-5} cm²/sec, according to Newman¹⁰¹

The diffusion overvoltage lags behind the current by a phase angle of $\pi/4=45^\circ$ and the so-called Warburg Impedance can be determined by:

$$Z_w = \frac{\eta_w}{i} \quad (112)$$

where $i = I \sin(\omega t)$

However, the Warburg impedance is derived assuming an infinite-thickness boundary layer resulting from a stagnant condition, which is rarely encountered in oil and gas field. Therefore diffusion overvoltage with a finite-thickness boundary layer is more appropriate for the model and it was derived by Sluyters et al¹⁴⁴:

$$\eta_{d,bl} = \frac{RT}{n^2 F^2} \frac{1-i}{[H^+]_{bulk} \sqrt{2\omega D_{H^+}}} \tanh \left[\delta \sqrt{\frac{i\omega}{D_{H^+}}} \right] I \sin \omega t \quad (113)$$

where

δ = boundary layer thickness

Equation (113) shows that the phase shift is no longer constant, but is a function of the frequency and the thickness of diffusion boundary layer. Figure 84 demonstrated that the characteristics of the impedance plot for a finite-thickness boundary layer is very different to that of infinite-thickness boundary layer and is strongly dependent on the thickness of boundary layer as shown in Figure 85.

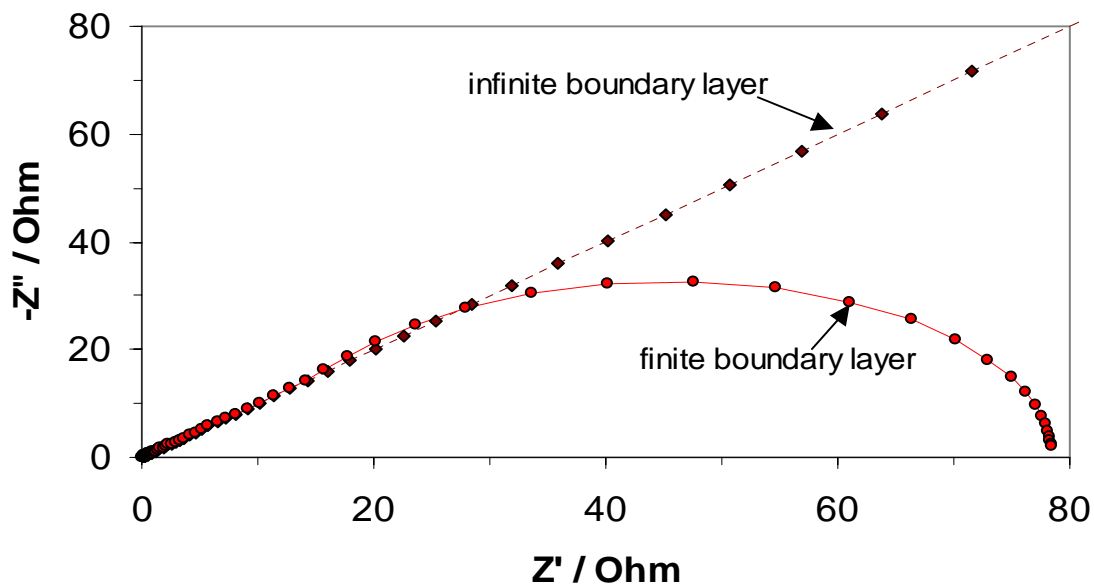


Figure 84. Comparison between calculated electrochemical impedance of H^+ ions for a finite-thickness diffusion boundary layer, $\delta_{B.L.}=0.003\text{m}$ and infinite-thickness diffusion boundary layer, also known as Warburg impedance, for $T=20^\circ\text{C}$, $[H^+]_{bulk}=1\times 10^{-5}$ mol/liter.

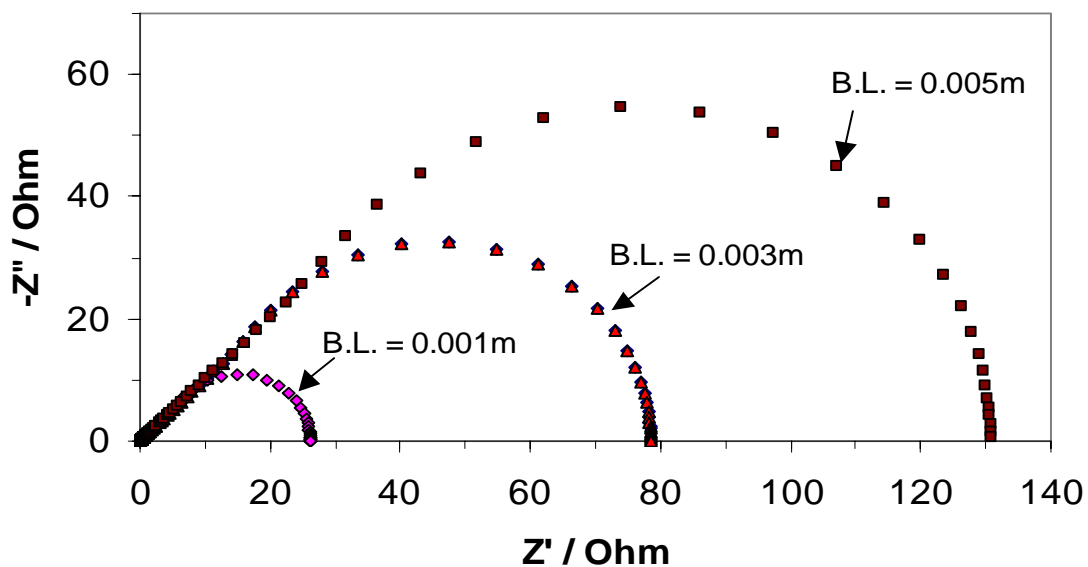


Figure 85. Effect of the thickness of diffusion boundary layer on the characteristics of electrochemical impedance of H^+ ions for $T=20^\circ\text{C}$, $[H^+]_{bulk}=1\times 10^{-5}$ mol/liter.

Reaction overvoltage

Reaction overvoltage is a phenomenon resulting from the existence of a slow (rate determining) chemical step in the overall reaction. In the case of CO₂ corrosion, the slow Hydration of CO₂ (117) contributes partly to the limiting current and previous studies¹⁴⁴ suggested that the superposition of diffusion and chemical reaction controlled limiting current is legitimate. Therefore the influence of diffusion and reaction-rate control are treated simultaneously when alternating current is induced and diffusion overvoltage with reaction η_r is obtained by Vetter:¹⁴⁴

$$\eta_r = \frac{RT}{n^2 F^2} \frac{v^2}{\sqrt{\omega} [H^+]_{bulk} \sqrt{2D_{H^+}}} \sqrt{\frac{1 + \left(\frac{k}{\omega}\right)^2 + \frac{k}{\omega}}{1 + \left(\frac{k}{\omega}\right)^2}} I \sin \omega t - \frac{RT}{n^2 F^2} \frac{v^2}{\sqrt{\omega} [H^+]_{bulk} \sqrt{2D_{H^+}}} \sqrt{\frac{1 + \left(\frac{k}{\omega}\right)^2 - \frac{k}{\omega}}{1 + \left(\frac{k}{\omega}\right)^2}} I \cos \omega t \quad (114)$$

This diffusion overvoltage with reaction has a phase shift with respect to alternating current that is not constant, but is a function of the frequency ω and the rate of the reaction k . Equation (114) without the square root expression would be a diffusion overvoltage (111) that was related to transport of hydrogen ion H⁺. It is this expression that takes into account the formation and depletion of H⁺ as a result of the rate-

determining step. However, equation (114) was derived for the case of infinite boundary layer condition, because Vetter assumed that the fluid is well mixed and in equilibrium only when $x \rightarrow \infty$, which is a good assumption for laminar flow and stagnant solutions. Whereas for a high enough velocity and turbulent flow, one need to assume that the edge of the mass transfer boundary layer at $x = \delta$ is the point where everything is well mixed and all reactions are in equilibrium. Therefore reaction overvoltage for mass transfer involving rate-determining reaction in turbulent flow conditions is derived (derivation is shown in a separate section below)

$$\eta_{\delta,r} = \frac{RT}{n^2 F^2 [H^+]_{bulk} D_{H^+} \lambda} \tanh(\lambda \delta) I \sin \omega t \quad (115)$$

$$\text{where } \lambda = \sqrt{\frac{i\omega + k}{D_{H^+}}}$$

Combining equation (104), (110) and (115), the total electrochemical impedance Z_{total} for the cathodic reaction in CO₂ corrosion is obtained.

Double layer capacitance

From the impedance spectrum, the semi circle at high frequency that contains information about double layer capacitance, is commonly modeled by a capacitor in a parallel configuration with the total impedance. However, in order to obtain more accurate fit results, the constant phase element (CPE) is substituted for capacitors. The

so-called CPE is an element whose impedance value is a function of the frequency and its phase is independent of the frequency. Its impedance is defined as:¹⁴⁴

$$Z_{CPE} = \frac{1}{Y_o} (j\omega)^{-n} \quad (116)$$

where Y_o = modulus of CPE,

$$\omega = \text{angular frequency} = 2\pi f$$

n = phase.

The reason that CPE is used instead of capacitors when one analyses the impedance spectra is that most impedance curves measured in experiments are not ideal semi-circles, but are depressed due to heterogeneous surface roughness and the nonuniform distribution of current density on the surface.^{127,128} The depression degree depends on the phase n of the CPE.¹⁴⁴

Therefore CPE is the only element in the model that is not mechanistic and it is assumed to be in a parallel configuration with total impedance Z_{total} as shown in Figure 86.

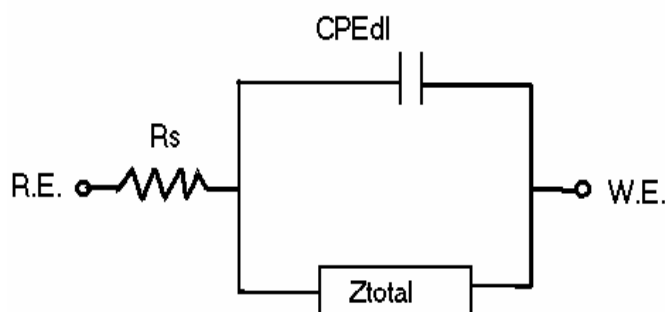


Figure 86. The equivalent circuit of the EIS model. R_s = solution resistance, CPE_{dl} = constant phase elements describing double layer capacitance, Z_{total} = total impedance, R.E. = reference electrode, W.E. = working electrode

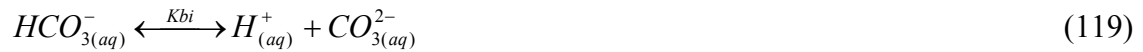
Derivation of reaction impedance in a finite boundary layer

In order to derive reaction impedance with a finite boundary layer, one needs to consider the following sequence of reactions:

When CO₂ is dissolved in water, hydration of aqueous carbon dioxide takes place to form carbonic acid:



The carbonic acid H₂CO₃ is then dissociated in two steps:



It is proposed that carbonic acid provides a reservoir of H⁺ ions at a given pH. Therefore hydrogen evolution is assumed to be the most dominant cathodic reaction.



The hydrogen ions H⁺ discharged in the cathodic evolution of hydrogen gas (120) are replaced by dissociation of the carbonic acid. Although the dissociation reactions (118) (119) are inherently fast, the formation of carbonic acid via the hydration step of aqueous carbon dioxide (117) is rate determining and causes the overvoltage of homogeneous reaction.

Hence Fick's second law in the form

$$\frac{\partial c}{\partial t} = D \frac{\partial^2 c}{\partial x^2} + v \quad (121)$$

is applied for the change with time (t) and distance (x) of H^+ concentration as a result of the diffusion and reaction processes.

Vetter¹⁴⁴ proposed the relation for formulation of the homogeneous reaction rate v ,

$$v = v_0 \left[1 - \left(\frac{c}{\bar{c}} \right)^p \right] \quad (122)$$

with reaction order p , concentration c and bulk concentration \bar{c} . For the evaluation of the reaction impedance only the current and overvoltage range in which a linear relationship exists between current i and overvoltage η is of interest. This is true only for relatively small concentration changes¹⁴⁴.

Since

$$\left(\frac{c}{\bar{c}} \right)^p = \left(1 + \frac{c - \bar{c}}{\bar{c}} \right)^p \approx 1 + p \frac{c - \bar{c}}{\bar{c}} \quad (123)$$

the following is approximately valid:

$$v = -\frac{v_0 p}{\bar{c}} \Delta c = -k \Delta c \quad (124)$$

where $\Delta c = c - \bar{c}$ and $k = \frac{v_0 p}{\bar{c}}$

The reaction order in this case is $p=1$. v_0 is the rate at which the two opposing reactions meet to establish equilibrium and may therefore be designated as the reaction exchange rate.

Substituting equation (124) for the reaction rate into equation (121) gives the partial differential equation

$$\frac{\partial \Delta c}{\partial t} = D \frac{\partial^2 \Delta c}{\partial x^2} - k \Delta c \quad (125)$$

for the concentration difference $\Delta c(x, t) = c(x, t) - \bar{c}$ where \bar{c} = bulk concentration (=H⁺ in this case)

An alternating current density of frequency $\omega/2\pi$, i.e.

$$i = I \sin \omega t \quad (126)$$

which satisfies the boundary condition at the surface

$$\left(\frac{\partial \Delta c}{\partial x} \right)_{x=0} = - \frac{1}{nFD} I \sin \omega t \quad (127)$$

In addition, a boundary condition for a finite diffusion boundary layer is also satisfied

$$\Delta c_{x=\delta} = 0 \quad \text{where } \delta = \text{diffusion boundary layer} \quad (128)$$

As well as the initial condition

$$\Delta C(x,0) = 0 \text{ for all } x \quad (129)$$

Using separation of variable method, one starts by looking for product solutions of the form

$$\Delta c(x,t) = X(x)T(t) \quad (130)$$

where $X(x)$ is a function of x alone and $T(t)$ is a function of t alone. Plugging into the modified partial differential equation of Fick's second law (125), one obtains

$$XT' = DX''T - kXT \quad (131)$$

After separating the variables, the equation is now in the form of

$$\frac{T'}{T} = \frac{DX''}{X} - k \quad (132)$$

For the equality to hold, one must have

$$\frac{T'}{T} = \alpha \text{ and } \frac{DX''}{X} - k = \alpha$$

where α is the separation constant. From these equations, one obtains two ordinary differential equations

$$T' - \alpha T = 0 \quad (133)$$

and

$$DX'' - (k + \alpha)X = 0 \quad (134)$$

Separating variables in the boundary condition(128), one get

$$X(\delta)T(t) = 0 \quad (135)$$

If $X(\delta) \neq 0$, then $T(t)$ must be 0 for all t, if so, $\Delta c(x,t) = X(x)T(t)=0$. To avoid trivial solutions we set

$$X(\delta) = 0 \quad (136)$$

Hence one obtains the boundary value problem in X:

$$DX'' - (k + \alpha)X = 0, \quad X(\delta) = 0$$

with characteristic equation

$$D\lambda^2 - (k + \alpha) = 0 \quad (137)$$

one obtains the distinct real characteristic roots of $\lambda_1 = \sqrt{\frac{(k + \alpha)}{D}}$ and $\lambda_2 = -\sqrt{\frac{(k + \alpha)}{D}}$

Therefore the general solution of X of this differential equation is given as

$$X = C_1 e^{\lambda x} + C_2 e^{-\lambda x} \quad (138)$$

By applying the boundary condition(128),

$$0 = C_1 e^{\lambda\delta} + C_2 e^{-\lambda\delta} \quad (139)$$

$$C_1 e^{\lambda\delta} = -C_2 e^{-\lambda\delta} \quad (140)$$

$$C_1 = -C_2 \frac{e^{-\lambda\delta}}{e^{\lambda\delta}} \quad (141)$$

substitute C_1 into the general solution(138) for space domain, one obtains

$$X(x) = -C_2 \frac{e^{-\lambda\delta}}{e^{\lambda\delta}} e^{\lambda x} + C_2 e^{-\lambda x} \quad (142)$$

$$X(x) = -C_2 \frac{e^{-\lambda\delta}}{e^{\lambda\delta}} e^{\lambda x} + C_2 e^{-\lambda x} \frac{e^{\lambda\delta}}{e^{\lambda\delta}} \quad (143)$$

$$X(x) = \frac{C_2}{e^{\lambda\delta}} \left(e^{\lambda(\delta-x)} - e^{-\lambda(\delta-x)} \right) \quad (144)$$

On the other hand, for the time domain,

$$T' - \alpha T = 0 \quad (145)$$

let's set $\alpha = i\omega$, one obtains

$$T' - i\omega T = 0 \quad (146)$$

The general solution for the above differential equation for time domain is then given as

$$T(t) = Ae^{i\omega t} \quad (147)$$

Combining the two general solutions together, one obtains the general solution of equation (125)

$$\Delta c = X(x)T(t) = \frac{C_2}{e^{\lambda\delta}} \left(e^{\lambda(\delta-x)} - e^{-\lambda(\delta-x)} \right) Ae^{i\omega t} \quad (148)$$

By partial differentiation of the above equation with respect to x and t , and by substituting into partial differential equation (125) of the modified Fick's second law, the coefficient λ can be obtained

$$\begin{aligned} i\omega \frac{C_2}{e^{\lambda\delta}} \left(e^{\lambda(\delta-x)} - e^{-\lambda(\delta-x)} \right) Ae^{i\omega t} &= D\lambda^2 \frac{C_2}{e^{\lambda\delta}} \left(e^{\lambda(\delta-x)} - e^{-\lambda(\delta-x)} \right) Ae^{i\omega t} \\ &\quad - k \frac{C_2}{e^{\lambda\delta}} \left(e^{\lambda(\delta-x)} - e^{-\lambda(\delta-x)} \right) Ae^{i\omega t} \end{aligned} \quad (149)$$

After canceling out the Δc term from the above equation, one obtains

$$i\omega = D\lambda^2 - k \quad (150)$$

Thus

$$\lambda = \sqrt{\frac{i\omega + k}{D}} \quad (151)$$

On the other hand, separating variables in the initial condition, one gets

$$X(x)T(0) = 0 \quad (152)$$

Since $X(x) \neq 0$, $T(0) = 0$

$$0 = Ae^0 \quad (153)$$

If $A=0$, $T(t)=0$ and $\Delta c=0$. To avoid trivial solution, one need to make use of Euler's identity

$$Ae^{i\omega t} = A(\cos \omega t + i \sin \omega t) \quad (154)$$

Now applying the initial condition, one obtains

$$0 = A(\cos 0 + i \sin 0) \quad (155)$$

In order for the above equation to hold true, the $\cos \omega t$ term must be omitted.

$$T(t) = i A \sin \omega t \quad (156)$$

However, for the purpose of mathematical simplicity, the general solution of $T = Ae^{i\omega t}$ is used for the determination of the coefficient C_2 , which can be obtained by applying the boundary condition at the surface(127)

$$\frac{C_2}{e^{\lambda\delta}} \left(-\lambda e^{\lambda(\delta-x)} - \lambda e^{-\lambda(\delta-x)} \right)_{x=0} Ae^{i\omega t} = -\frac{1}{nFD} I \sin \omega t \quad (157)$$

$$-\lambda \frac{C_2}{e^{\lambda\delta}} \left(e^{(\lambda\delta)} + e^{-(\lambda\delta)} \right) Ae^{i\omega t} = -\frac{1}{nFD} I \sin \omega t \quad (158)$$

After applying the hyperbolic identity $\cosh(x) = \frac{e^x + e^{-x}}{2}$ and canceling $I \sin \omega t$ term on

both sides (since $Ae^{i\omega t} = I \sin \omega t$), C_2 is then obtained

$$C_2 = \frac{e^{\lambda \delta}}{\lambda n F D 2 \cosh(\lambda \delta)} \quad (159)$$

Finally, substituting the coefficients C_2 and applying the hyperbolic identity

$\sinh(x) = \frac{e^x - e^{-x}}{2}$ into the general solution in equation (148)

$$\Delta c = \frac{\sinh[(\delta - x)\lambda]}{\lambda n F D \cosh(\delta\lambda)} I e^{i\omega t} \quad (160)$$

where $\lambda = \sqrt{\frac{i\omega + k}{D}}$

The objective of the above concentration derivation is to calculate $c(0,t)/\bar{c}$ at the surface. It was assumed that $|\Delta c|/\bar{c} \ll 1$ and thus $c/\bar{c} \approx 1$. Therefore the following relation for the reaction overvoltage is approximately valid¹⁴⁴

$$\eta_r = \varepsilon - \varepsilon_0 = \frac{RT}{nF} \ln \frac{c(0,t)}{\bar{c}} \approx \frac{RT}{nF} \frac{\Delta c(0,t)}{\bar{c}} \quad (161)$$

After Substituting equation (160) for Δc with $x=0$ into the above equation (161) and applying the trigonometric identity $\tanh(x)=\sinh(x)/\cosh(x)$, the reaction overvoltage is obtained:

$$\eta_r = \frac{RT}{n^2 F^2 \bar{c} D \lambda} \tanh(\lambda \delta) I \sin \omega t \quad (162)$$

$$\text{where } \lambda = \sqrt{\frac{i\omega + k}{D}}$$